Faculty of Engineering
Department of Mechanical Engineering

8th INTERNATIONAL SCIENTIFIC CONFERENCE ON ADVANCES IN MECHANICAL ENGINEERING (ISCAME 2022)

10-11 November, 2022 Debrecen, Hungary

CONFERENCE PROCEEDINGS
(BOOK OF EXTENDED ABSTRACTS)

organized by
Department of Mechanical Engineering
Faculty of Engineering, University of Debrecen
and
Working Commission in Mechanical Engineering
Specialized Committee in Engineering
Regional Committee in Debrecen, Hungary Academy of Science

Edited by **Márton HOMOLYA, Tamás MANKOVITS**

Publisher: **Department of Mechanical Engineering**
Faculty of Engineering
University of Debrecen
2-4 Ótemető str. Debrecen, Hungary
Phone: +36 52 512 900
Web page: https://mecheng.unideb.hu/

ISBN 978-963-490-448-9

CONFERENCE PROCEEDINGS (BOOK OF EXTENDED ABSTRACTS)

8th INTERNATIONAL SCIENTIFIC CONFERENCE ON ADVANCES IN MECHANICAL ENGINEERING (ISCAME 2022)

10-11 November, 2022
Debrecen, Hungary

Chair of ISCAME 2022

Tamás MANKOVITS, University of Debrecen, Hungary

Scientific Program Committee of ISCAME 2022

Piroska AILER, University of Debrecen, Hungary
Sándor BODZÁS, University of Debrecen, Hungary
Gábor BOHÁCS, Budapest University of Technology and Economics, Hungary
István BUDAI, University of Debrecen, Hungary
Levente CZÉGÉ, University of Debrecen, Hungary
János Péter ERDÉLYI, University of Miskolc, Hungary
Lajos FAZEKAS, University of Debrecen, Hungary
Sándor HAJDU, University of Debrecen, Hungary
György JUHÁSZ, University of Debrecen, Hungary
Gábor KALÁCSKA, Hungarian University of Agricultural and Life Sciences (MATE), Hungary
Ferenc KALMÁR, University of Debrecen, Hungary
Imre KOCSIS, University of Debrecen, Hungary
Ákos LAKATOS, University of Debrecen, Hungary
Daniel LATES, SC IRUM SA, Romania
Stanislav LEGUTKO, Poznan University of Technology, Poland
János LÍSKA, John von Neumann University, Hungary
Zoltán MAJOR, Johannes Kepler University Linz, Austria
József MENYHÁRT, University of Debrecen, Hungary
Ljubica MILOVIC, University of Belgrade, Serbia
Imre Norbert ORBULOV, Budapest University of Technology and Economics, Hungary
Sándor PÁLINKÁS, University of Debrecen, Hungary
Tibor POÓS, Budapest University of Technology and Economics, Hungary
Milan RACKOV, University of Novi Sad, Serbia
Istvánné RÁTHY, Óbuda University, Hungary
Tamás SZABÓ, University of Miskolc, Hungary
Edit SZŰCS, University of Debrecen, Hungary
György THALMAIER, Technical University of Cluj-Napoca, Romania
Zsolt TIBA, University of Debrecen, Hungary
László TÓTH, University of Debrecen, Hungary
Matej VESENJAK, University of Maribor, Slovenia
Zoltán WELTSCH, John von Neumann University, Hungary
László ZSIDAI, Hungarian University of Agricultural and Life Sciences (MATE), Hungary

Technical Assistance of ISCAME 2022

Szandra SITKU, University of Debrecen, Hungary
Lilla CSONKÁNÉ DÓRÓ, University of Debrecen, Hungary

CONTENTS

ÁDÁM Balázs
INVESTIGATION OF NON-ISOTHERMAL CRYSTALLIZATION KINETICS OF MELAMINE-BASED FLAME RETARDANT PLA *9-10*

ALKENTAR Rashwan, MANKOVITS Tamás
DESIGN OF PATIENT SPECIFIC FEMORAL STEM USING LATTICE STRUCTURES *11-12*

ALSALAMAH Bassel, KUZSELLA László
THE EFFECT OF TEMPERATURE ON THE HOT COMPRESSION TEST OF ALSI7 ALUMINUM ALLOY *13-14*

ANGELI Eliza, KOLTAI László, SZENTGYÖRGYVÖLGYI Rozália
INFLUENCE OF CARDBOARD SURFACE SIZING ON SOLVENT RETENTION *15-16*

ANTAL Tamás, NAGY János
CHANGES IN PHYSICAL AND MECHANICAL PROPERTIES OF DRIED SWEET POTATOES DURING STORAGE *17-18*

ARADI Attila, VARGA Attila Károly
DEEP LEARNING BASED CLASSIFICATION OF SOUNDS RECORDED BY HYDROPHONE IN A TANK FOR LEAK DETECTION AND MONITORING OF PUMP CONDITIONS *19-20*

BÍRÓ Nóra, MOLNÁR Dániel, FEGYVERNEKI György
THERMAL ANALYSIS – THEORY AND APPLICATION *21-22*

BODZÁS Sándor
GEOMETRIC DESIGN OF FORM TOOLS FOR TURNING TECHNOLOGIES *23-24*

BUDAI István, SZOBOSZLAI András
DEVELOPMENT OF CELLULAR MARTIX DROG FORMULA *25-26*

CS. TÓTH Annamária, PREKLET Edina, BÖRCSÖK Zoltán, HORVÁTH Brigitta, HALÁSZ Katalin
CHARACTERIZATION OF A BIODEGRADABLE EDIBLE FILM OBTAINED FROM PSYLLIUM HUSK FLOUR *27-28*

DAKHEL Ahmad Yasser, LUKÁCS János
FULL-SCALE TESTS OF PIPELINE GIRTH WELDS UNDER COMPLEX CYCLIC INTERNAL PRESSURE AND STATIC BENDING LOADING CONDITIONS *29-30*

DESSIE Jemal Ebrahim, LUKÁCS Zsolt
A NUMERICAL STUDY ON SPRINGBACK PREDICTION WITH SYSTEMATIC PROCESS IMPROVEMENT *31-32*

DOMOKOS Tatiane, BAKSA Attila, SZÁVAI Szabolcs
PREDICTION OF FLD USING GURSON MODEL FOR SIMPLE FLAT SPECIMEN *33*

ECSEDI István, BAKSA Attila, LENGYEL Ákos József, GÖNCZI Dávid
ON THE TORSIONAL RIGIDITY OF ORTHOTROPIC BEAMS WITH RECTANGULAR CROSS SECTION *34*

ECSEDI István, BAKSA Attila, LENGYEL Ákos József, GÖNCZI Dávid
AN ANALYTICAL SOLUTION FOR THE TWO-LAYERED COMPOSITE BEAM-COLUMN WITH INTERLAYER SLIP AND CONSTANT AXIAL LOAD *35*

GYARMATI Gábor, KÉRI Zoltán, MOLNÁR Dániel
ANALYSIS OF THE QUALITY OF INCOMING ALUMINUM ALLOY INGOTS *36-37*

HABBACHI Marwen
NUMERICAL MODELLING AND SIMULATION OF SHEET METAL FORMING PROCESS *38-39*

HALÁPI Dávid, VARGA László
ULTRASONIC POWDER ATOMISATION FOR ADDITIVE MANUFACTURING *40-41*

HASAN Mustafa, HRICZÓ Krisztián
PREDICTION OF ENERGY EFFICIENCY OF A SOLAR AIR COLLECTOR USING ARTIFICIAL NEURAL NETWORK TECHNIQUE *42-43*

HORVÁTH Dániel, POÓS Tibor
DIMENSIONAL ANALYSIS OF MIXING POWER REQUIREMENT IN AGITATED DRUM *44-45*

HUNYADY Gergely, FODOR Dénes
TRANSFORMATION OF AN INTERNAL COMBUSTION ENGINE VEHICLE TO AN AUTONOMOUS ONE THROUGH MODULAR SYSTEM DESIGN *46-47*

JAWABREH Anas, SEPSI Máté, BARKÓCZY Péter
EFFECTS OF ELEVATED TEMPERATURE ON THE MECHANICAL BEHAVIOR OF ACSR TYPE CONDUCTORS *48-49*

KARAMAN Ömer Faruk, HÉGELY László, LÁNG Péter
OPTIMISATION OF METHANOL RECOVERY BY SURROGATE MODELS: INFLUENCE OF PRICES *50-51*

KHALILI NAJAFABADI Mohsen, HRICZÓ Krisztián, BOGNÁR Gabriella
HEAT TRANSFER CHARACTERISTICS OF WATER-CUO NANOFLUID FLOW INSIDE 2D PIPE *52-53*

KLAPCSIK Kálmán
BUBBLE POSITION CONTROL BY PHASE-CONTROLLABLE ULTRASONIC STANDING WAVE *54-55*

KÖLÜS Martin László, BORBÉLY Richárd, SZŐKE Dániel, BÉRES Gábor József
EFFECT OF THE FLOW CURVE DETERMINATION ON THE THINNING OF DRAWN PARTS *56-57*

KOROKNAI László, KUZSELLA László, PÓR Gábor
THE IMPORTANCE OF PERPENDICULARITY DURING THE SCANNING ULTRASOUND EXAMINATION *58-59*

KOVÁCS Péter Zoltán, JÓNÁS Szabolcs
TUBE-TO-TUBE JOINING BY FORMING *60-61*

KOVÁCS Sándor Endre, VARGA László
MECHANICAL TESTING OF 3D PRINTED STAINLESS STEEL SPECIMENS *62-63*

LADÁNYI Ramóna, BODZÁS Sándor
DESIGN OF AN UNIQUE CLAMPING DEVICE FOR THE DEVELOPMENT OF PRESSING TECHNOLOGY *64-65*

LATES Daniel, ALFIANU Calin
ANALYSIS OF STRUCTURAL STRENGTHS FOR THE CABLEWAY GROUP *66-67*

MOHAMMED SAHIB Mortda, KOVÁCS György, SZÁVAI Szabolcs
USING ARTIFICIAL NEURAL NETWORK IN THE DESIGN OF COMPOSITE SANDWICH STRUCTURES *68-69*

NAGY Viktor, KOVÁCS Gábor
EXPERIMENTAL ANALYSIS OF BUS DRIVER BEHAVIOR AND COGNITIVE LOAD *70-71*

NEMES Dániel, HAJDU Sándor
A SOLUTION FOR CREATING A SUBMODEL OF AN ELECTRIC MOTOR IN A VEHICLE DYNAMICS MODEL BY USING MATLAB SIMULINK *72-73*

OMLE Issa, ASKAR Ali Habeeb, KOVÁCS Endre
INVESTIGATING THE EFFECT OF SURFACE ROUGHNESS TYPE ON THE CONVECTION AND RADIATION HEAT TRANSFER INSIDE THE ENCLOSURE *74-75*

POLYÁKNÉ KOVÁCS Annamária, TAMÁSI Kinga, SZABÓ Tamás József
EXAMINATION OF HYDROLYSIS-RESISTANT POLYKETONE AND ITS APPLICATION POSSIBILITIES IN THE INDUSTRY *76-77*

POÓS Tibor, SZÁVICS Nikolett
CONTINUOUS CONCENTRATION MEASUREMENT OF ORGANIC AIR POLLUTANT COMPONENTS IN GAS STREAM *78-79*

POÓS Tibor, SZABÓ Viktor, RASHED Rashed
CHARACTERISTIC FUNCTIONS OF A BATCH, CONVECTIVE DRYING *80-81*

QASEM Rabea Hussein Mohammed
EFFECT OF SURFACE-MODIFIED NANOPARTICLES ON OIL RECOVERY EFFICIENCY AND THE MECHANISM UNDERLIES THIS EFFECT *82-83*

ROY Atosi, BODZÁS Sándor
GEOMETRIC ANALYSIS OF SPLINE SHAFTS USING SURFACE ROUGHNESS PROFILOMETER AND 3D SCANNER *84-85*

SKORIC Branko, TEREK Pal, KOVACEVIC Lazar, TEREK Vladimir, BOBIC Zoran, KUKURUZOVIC Dragan
INFLUENCE OF ION IMPLANTATION ON TOOL STEEL *86-87*

STRAKA Ľuboslav, KUCHTA Patrik
EFFICIENCY OF MACHINING CURVED SURFACES THROUGH ELECTRICAL DISCHARGE TECHNOLOGY *88-89*

STRAKA Ľuboslav, KUCHTA Patrik
MACHINING OF CARBIDE METALS BY ELECTRICAL DISCHARGE TECHNOLOGY *90-91*

SZABÓ Kristóf
COMPONENT DEVELOPMENT USING TOPOLOGICAL METHODS *92-93*

SZABÓ Kristóf
APPLICATION OF TOPOLOGICAL METHODS IN THE DEVELOPMENT OF VEHICLE COMPONENTS *94-95*

SZODRAI Ferenc
ASSESSMENT OF PULSATING FLOW *96*

TAJTI Ferenc, BERCZELI Miklós
INVESTIGATION OF THE ADHESION PROPERTIES OF POTTINGS *97-98*

TAMÁSI Kinga, POLYÁKNÉ KOVÁCS Annamária, BORDÁS Viktor, SIMON Andrea
CELLULAR CERAMIC AND POLYMERIC MATERIALS FOR DEFENCE AND MILITARY APPLICATIONS- A REVIEW *99-100*

THALMAIER Gyorgy, VIDA-SIMITI Ioan, SECHEL Niculina, BATIN Gabriel
CREATING POROUS METAL PARTS BY FUSED DEPOSITION MODELING AND SINTERING *101-102*

TÖRŐCSIK Dávid, NAGY Attila
TORQUE MEASUREMENT ON A CYLINDER TYPE MAGNETORHEOLOGICAL CLUTCH USING STRAIN GAUGES *103-104*

TUGYI Levente, SIMÉNFALVI Zoltán, SZEPESI L. Gábor
PROPANE GAS DIFFUSION FOR PROPANE-PROPYLENE SEPARATION COLUMNS WITH DIFFERENT OUTFLOW DIRECTIONS *105-106*

VARGA Attila Károly
EXPERT INVESTIGATION OF THE INSTALLATION AND MAINTENANCE OF A COMMUNICATION CABLE CUT WITH AN AGRICULTURAL MACHINE *107-108*

VARJU Evelin, POÓS Tibor
INVESTIGATION OF HEAT TRANSFER COEFFICIENT AT EVAPORATION FROM A HEATED VESSEL *109-110*

WINDISCH Márk, MALOVECZKY Anna, VERES Miklós, RIGÓ István,FÜRJES Péter, DANKHÁZI Zoltán, VIDA Ádám
APPLICATION OF LASER SURFACE TREATMENT IN SURFACE-ENHANCED RAMAN SPECTROSCOPY *111-112*

ZAKIYYA Hanna, KÉKESI Tamás
POTENTIODYNAMIC STUDY OF THE EFFECTS OF NICKEL ON THE ELECTRODEPOSITION OF ZINC FROM CHLORIDE MEDIA *113-114*

TAKÁCS Zoltán, KÁLLAI Imre
APPLICATION OF ADDITIVE MANUFACTURING TECHNOLOGY FOR THE PRODUCTI OF INJECTION MOLDING TOOLS IN ORDER TO REDUCE THE CYCLE TIME *115-116*

INVESTIGATION OF NON-ISOTHERMAL CRYSTALLIZATION KINETICS OF MELAMINE-BASED FLAME RETARDANT PLA

ÁDÁM Balázs
Polymer Technology Research Group, Department of Innovative Vehicles and Materials, GAMF Faculty of Engineering and Computer Science, John von Neumann University, Hungary
E-mail: adam.balazs@gamf.uni-neumann.hu

Keywords: environmental pollution, PLA, DSC, nucleation, crystallization

Environmental pollution is one of the most serious problems that humanity has to face today. More studies and publications say that less than a hundred companies have been causing the greatest destruction to the environment for a little more than a century. These include large oil companies and large food manufacturing companies that package their products in plastic. [1] The sorting and recycling of selectively collected plastic waste could be solved, the main problem is the lack of proper collection, so a lot of otherwise recyclable plastic ends up in landfills. [2] One of the possible solutions to reduce the amount of waste is to make plastics degradable or to use biodegradable polymers. One of the most intensively researched biopolymers is PLA (Poly-Lactic Acid). PLA can be produced from natural materials and is a biodegradable polymer under industrial conditions, by composting. PLA is a thermoplastic, semi-crystalline polyester with good mechanical properties (tensile strength of 60 MPa, elastic modulus of 3 GPa). [3] One of disadvantages of PLA is it catch fire easily, so for safety reasons it is worth, or even necessary, to be provided with a flame retardant additive. Another disadvantages of PLA is its crystallization is slow, so with the usual processing technologies and technological settings, it is difficult to achieve the appropriate degree of crystallinity when using pure material. There are overlaps between flame retardant and nucleating additives, such as montmorillonite (MMT), which is a commonly used nucleating material, but is also used as a flame retardant. [4] In this paper, the effect of the amount of halogen-free flame retardant on the crystallization of PLA was investigated by DSC under non-isothermal conditions. Naturework Ingeo 7032D was chosen as the matrix material, which is a PLA used for bottle blowing, so it can be suitable to replace the traditional PET bottle. The halogen-free flame retardant is the melamine-based Melapur MC25, which was developed by CIBA mainly for polyamides and thermoplastic polyurethanes. We received the flame retardant additive in granule form from the staff of the Department of Polymer Engineering at the University of Miskolc, who tested its flame retardant ability when mixed with PET. [5] On the samples received from them we examined the effect of Melapur on the crystallization of PET in anisothermic and isothermal conditions and found that Melapur behaves as a nucleating agent. [6, 7] Based on these, we chose Melapur as a flame retardant, but also as a possible nucleating agent, to be mixed with PLA.

The blends were prepared by Brabender Plastograph and IDMX mixer. The blends contained 1, 4 and 8 weight% Melapur MC25. Before extrusion, PLA was drying at 60°C and 4 hours long. The temperatures of the feeding Brabender extruder were 190, 200, 210, 220°C (from the hopper to the die) and the rate of the extruder was 40 rpm. The temperature of the mixer was 210°C, and the rate of the mixer was 12.5 rpm.

The preparing of the blends were done in the Laboratory of Polymer Technology Research Group, Department of Innovative Vehicles and Materials, at John von Neumann University.

DSC (Differential Scanning Calorimetry) tests were performed on the blends by TA Q200 instrument. The blends were subjected to a non-isothermal analysis at cooling rates of 2.5, 5, and 10°C/min. The temperature range was between 30°C and 200°C. After each cooling, the heating rate was 20°C/min. The tests were performed under a nitrogen atmosphere. The weight of the samples were about 5 mg. The DSC measurements were analyzed with the TA Universal Analysis software. The measurements were done in the accredited Material Testing and Measurement Techniques Laboratory at John von Neumann University.

During crystallization, an exothermic peak can be seen on the DSC curve. The area under the curve is the enthalpy change of crystallization, or in other words the heat of crystallization (its symbol ΔH_c - unit of measure J/g), from which we can deduce the amount of the crystallized material. T_{ic} is the initial temperature of crystallization, and T_{fc} is the final temperature of crystallization, but their exact values are difficult to determine, so extrapolated values are used instead. T_{eic} is the extrapolated initial temperature of crystallization, while T_{efc} is the extrapolated final temperature of crystallization. The maximum rate of crystallization is indicated by the peak crystallization temperature, T_{pc}. [8] When testing the effectiveness of nucleating agent, the change in the initial temperature of crystallization is monitored. Since crystallization can start sooner, it shifts towards higher temperatures. [9, 10].

It can be observed that by increasing the cooling rate, the peak temperatures of crystallization shift to lower and lower values, and the interval of crystallization also widens. Due to the ever-faster cooling rate, the material has less and less time for crystallization, so the amount of the crystalline fraction decreases.

By increasing the amount of Melapur, the peak crystallization temperatures shift towards higher and higher values, and this happens regardless of the magnitude of the cooling rate, because it occurs in all cases.

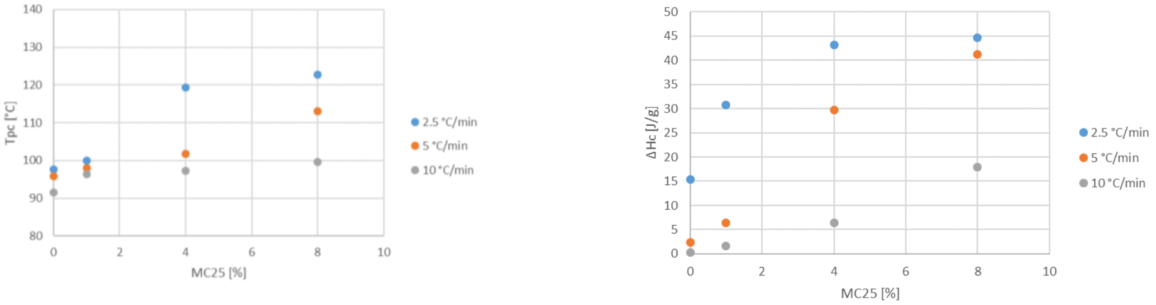

Figure 1 Peak temperatures (T_{pc}) and enthalpy changes (ΔH_c) of crystallization

While in the case of the extrapolated initial temperatures the effect of Melapur was clear only at the slowest speed of 2.5°C/min, in the case of the peak temperatures of crystallization the change is already clearly visible. Increasing the Melapur content increases the peak temperature at all cooling rates.

In addition to the temperatures, the enthalpy change of crystallization also provides valuable information about the change in the amount of the crystalline fraction. From the measured values, we can see that by increasing the amount of Melapur, we get higher and higher J/g values, that is, the amount of the crystalline fraction also increases. However, the effect of the cooling rate is also significant. If 1% Melapur was mixed with PLA, but the cooling rate is faster, 5 or 10°C/min, it cannot be achieved as much crystalline fraction as if we cooled the pure material at a slower rate at 2.5°C/min. Of course, it should be noted here that the cooling rates of the processing technologies exceed the cooling rates used in the research, however, in order to detect the nucleation effect, it was essential to use the slowest possible rates.

Summarizing the results, it can be said that during the measurements, the effect of the cooling rate and the amount of halogen-free flame retardant mixed with the PLA base material on the crystallization of PLA were investigated at the same time.

As a result of increasing the cooling rate, the temperatures of crystallization and the heats of crystallization decreased in all cases. As a result of rapid cooling, there is not enough time for the formation of crystalline phases, so their quantity decreases.

Increasing the amount of flame retardant is just the opposite, we have seen an increase in crystallization temperatures and heats of crystallization. The increase in the initial temperature of crystallization is usually a characteristic effect of nucleating agent, which we were able to detect with DSC analysis, but it is also worth checking with additional measurements, for example X-ray diffraction or some kind of microscopic tests. It is also worth continuing the DSC studies with isothermal crystallization kinetics.

REFERENCES

[1] Ekwurzel, B. (2017), *The rise in global atmospheric CO2, surface temperature, and sea level from emissions traced to major carbon producers*, Climatic Change, 144:579–590.

[2] Ronkay, F., Dobrovszky, K., Toldy, A. (2014) *Műanyagok újrahasznositása*, egyetemi tankönyv, Printer kiadó, Budapest.

[3] Lim, L.-T., Auras, R., Rubino, M. (2008), *Processing technologies for poly(lactic-acid)*, Progress in Polymer Science 33, 820-852.

[4] Wang, Y.M., Gao, J.P., Ma, Y.Q., Agarwal, U.S. (2006), *Study on mechanical properties, thermal stability and crystallization behavior of PET/MMT nanocomposites*, Composites Part B-Engineering, 37, 399-407.

[5] Czél Gy., Kelemen A., Sólyom D. (2010) *Flame retardant polyethylene terephthalate fibers added with melamine based FR additive*, Materials Science Forum Vol. 659, pp. 135-140

[6] Ádám, B., Nagy, D. (2017) *Halogénmentes égésgátló hatása PET kristályosodására*, Gradus 4:2 pp. 367-372.

[7] Ádám, B. (2018) *Isothermal crystallization kinetics of flame retardant PET containing melamine based FR*, IOP Conference Series: Materials Science and Engineering, 448, 012041.

[8] Ehrenstein, G. W., Riedel, G., Trawiel, P. (2004) *Thermal Analysis of Plastics, Theory and Practice*, Hanser Publishers, Munich, Hanser Gardner Publications, Cincinnati.

[9] Belina, G., Menyhárd, A., Juhász, P., Belina, K. (2001) *Heterogén gócképzők hatékonysága PET hulladékban*, Műanyag és Gumi, 38(12), 441-446.

[10] Belina G., Menyhárd A., Juhász P., Belina K. (2001) *Gócképzők hatékonysága különböző szerkezetű polipropilénekben*, Műanyag és Gumi, 38. évf. 7. szám, 255-259.o.

DESIGN OF PATIENT SPECIFIC FEMORAL STEM USING LATTICE STRUCTURES

[1,2]ALKENTAR Rashwan, [2]MANKOVITS Tamás
[1]Doctoral School of Informatics, University of Debrecen, Hungary
E-mail: rashwan.alkentar@eng.unideb.hu
[2]Department of Mechanical Engineering, Faculty of Engineering, University of Debrecen, Hungary
E-mail: tamas.mankovits@eng.unideb.hu

Keywords: Unit cells, finite element method, lattice structures.

Nowadays, much research is dedicated to the improvement of the biomedical implants. The most researched area is related to the design and structure of the implant in order to have the best biomechanical properties. Consequently, the deficiencies are reduced and the life span of the implant is increased. Many types of lattice structures are applied to the body of the hip implant. The aim of this research is to investigate the effect of each type of the unit cells on the biomechanical properties of the total prosthesis. Three types of unit cells were investigated in a previous study [1], and each type's Young's modulus was calculated to match the unit cell type with the close-in-strength bone of the human body. The investigation comprised finite element analysis on the specimens and validation of the results using the laboratorial compression test. In this research, Samples of the total hip implant will be 3D printed to be tested on compression in the lab. The same types of unit cells will be applied to the hip implant design.. However, the design parameters of the unit cells are to be optimized to get the best values that creates a lattice-structured body which is most suitable to the osseointegration. The three applied types of unit cells are 3D lattice infill, Double pyramid lattice and face diagonals and the Octahedral lattice two. Figure 1 shows the three types of unit cells applied to a part of the hip implant in comparison to the original design. The geometry of each unit cell is also shown. ANSYS software (Canonsburg, PA, USA) with 2021 R2 version is used to design the implants and simulate the compression test.

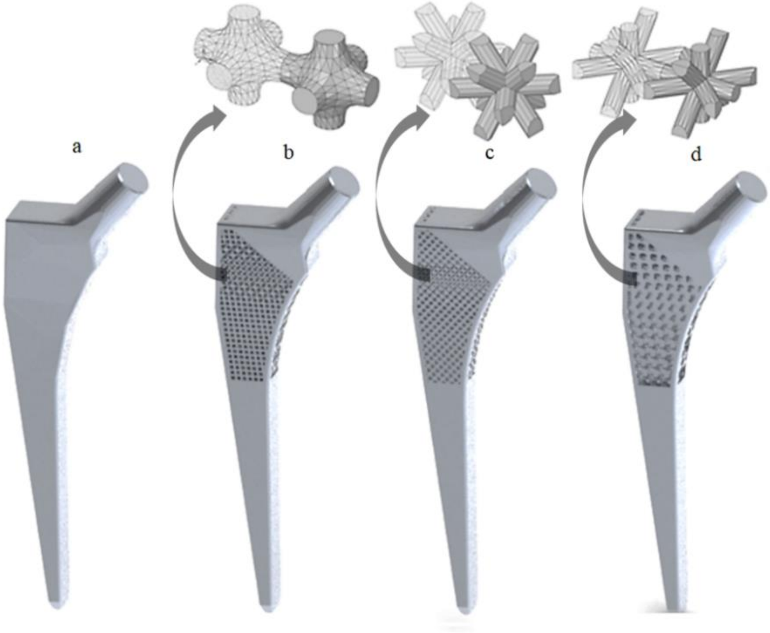

Figure 1 Hip implant designs and the application of unit cells: a) bulk hip implant design, b) 3D lattice infill, c) Double pyramid lattice and face diagonals, d) Octahedral lattice 2

After optimizing the parameters of the unit cells to be applied on the design of the hip implants with the help of the Support-Vector-Regression (SVR) method, EOS M 290 (electro optical systems, Germany) 3D-printing machine will be used to manufacture the implants to be tested. INSTRON 8801 Servo-hydraulic Fatigue testing machine (USA) will be used to conduct the laboratory compression test with a compression rate of 1mm/min and a maximum force of 2300 N. Finite element analysis is to be performed on the implants to make a comparison with the lab results. Mesh convergence analysis will be performed to reach the best most optimized results. Figure 2 shows the loading and boundary conditions to be applied on the implant according to the ISO 7206-4:2010 standard [2].

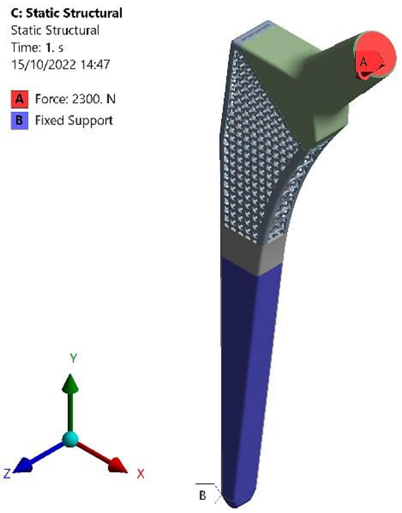

Figure 2 Loading and boundary condition on the hip implant

Based on its good biomechanical properties (low density, high strength, and high corrosion resistance), the titanium alloy Ti6Al4V grade 23 was used as the main material for the printed samples. Ti6Al4V can also reduce the contact pressure between the human bone and the implant surface [3]. Table 1 shows the chemical composition of the alloy used.

Table 1. Chemical composition of Ti64 Powder [4]

Element	**Al**	**V**	**O**	**N**	**C**	**H**	**Fe**	**Y**	**Other elements each**	**Other element total**
Chemical composition percentage %	5.50 - 6.50	3.50 - 4.50	0.13	0.05	0.08	0.012	0.25	0.005	0.1	0.4

The main mechanical properties of the material used were determined by the authors to guarantee the usage of the practical values. The calculated properties are listed in Table 2.

Table 2 Material properties used in the FEM

Property	**Value**	**Unit**
Elastic modulus	106247	MPa
Mass Density	4.4	g/cm^3
Poisson's ratio	0.34	-

The research seeks finding the optimized parameters of the unit cells and the generation of a patient-specific hip implant design with good biomechanical properties. The designed hip implants will be tested numerically and in the laboratory in order to validate the performance of the implants under the real loads.

REFERENCES

[1] R. Alkentar, M. File, and T. Mankovits, "Investigation of the Performance of Ti6Al4V Lattice Structures Designed for Biomedical Implants Using the Finite Element Method," *Materials (Basel).*, vol. 15, no. 18, pp. 1–14, 2022, doi: 10.3390/ma15186335.

[2] Y. E. Delikanli and M. C. Kayacan, "Design, manufacture, and fatigue analysis of lightweight hip implants," *J. Appl. Biomater. Funct. Mater.*, vol. 17, no. 2, p. 2280800019836830, Apr. 2019, doi: 10.1177/2280800019836830.

[3] J. Jamari, M. I. Ammarullah, G. Santoso, S. Sugiharto, T. Supriyono, and E. van der Heide, "In Silico Contact Pressure of Metal-on-Metal Total Hip Implant with Different Materials Subjected to Gait Loading," *Metals* , vol. 12, no. 8. 2022, doi: 10.3390/met12081241.

[4] EOS GmbH, "EOS Titanium Ti64 - Material data sheet," 2017, [Online]. Available: https://www.eos.info/material-m.

THE EFFECT OF TEMPERATURE ON THE HOT COMPRESSION TEST OF ALSI7 ALUMINUM ALLOY

ALSALAMAH Bassel, KUZSELLA László
Mechanical Technology Institute Department, Institute of Material Structure and Materials Technology, University of Miskolc, Hungary
E-mail: metbasel@uni-miskolc.hu , kuzsella@uni-miskolc.hu

Keywords: Physical Simulation, Aluminum Alloy, GLEEBLE 3500, Forming Rates

The aim is to perform physical simulation tests to investigate the formability of aluminum alloys. This paper presents the process and results of these tests, from a detailed description of the equipment used to the shape of the test specimen that emerges from the device and is deformed by stress. One of the study's primary subjects is the influence of the sample orientation of the specimen on the final result under the same forming conditions. After the test, the specimen's shape was not circular, as was expected. It was more like an ellipsoid. Therefore, we started to observe the effect of the orientation of the machining. From this aspect, three kinds of directions can be distinguished. One is the same as a rolling direction, the other is perpendicular to the rolling direction in the same plane, and the third is the normal direction. As it was found, the samples machined in the normal direction were the only circular shaped. Five temperatures and four forming rates were studied. The temperatures and the forming rate were chosen concerning the hot rolling technology of this alloy. Therefore, the temperatures were 350, 400, 450, 500, and 550°C. The forming rates were 0.001, 0.01, 0.1 and 1 s-1 .This publication details the effect of the temperature in the case of different forming rates. The device with which the research can be carried out is the GLEEBLE 3500, At the University of Miskolc, Institute of Materials Science and Technologies exists the GLEEBLE 3500 which is a fully integrated, digitally controlled thermomechanical testing scheme with Windows-based software computer support that allows extensive thermo-mechanical simulation and testing.

Figure 1 GLEEBLE 3500 thermo-mechanical simulator and the testing space

The GLEEBLE can be divided into three main units: mechanical, thermal unit and digital control system. When a simulation or a scan takes place, the results are automatically inserted into the Origin software, which is a part of a compelling and flexible data analysis platform that comes with GLEEBLE 3500. Origin offers numerous built-in math functions for data analysis and includes the LabTalk coding language that can be used to evaluate and process comparative, comprehensive simulations, and test data.

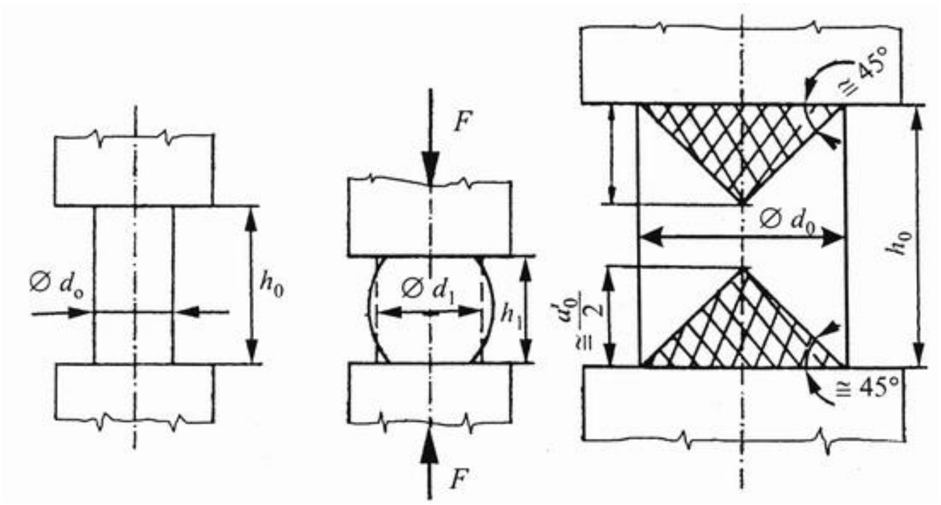

Figure 2 The presentation of the compression test with the phenomenon of barrelling in the middle

REFERENCES

[1] Adonyi Y.: Heat-Affected Zone Characterization by Physical Simulations, Welding Journal (October 2006) p. 42-47.
[2] Dunaújváros regional material science and research knowledge center Duratt 25-DRTT/2009 — irt.: 2009/10/1 15th February, 2009, Dunaújváros
[3] Adonyi Y.: Heat-Affected Zone Characterization by Physical Simulations, Welding Journal (October 2006) p. 42-47.

INFLUENCE OF CARDBOARD SURFACE SIZING ON SOLVENT RETENTION

[1]ANGELI Eliza, [2]KOLTAI László, [2]SZENTGYÖRGYVÖLGYI Rozália
[1]GAMF Faculty of Engineering and Computer Science, John von Neumann University, Hungary
E-mail: eliza.angeli@gamf.uni-neumann.hu
[2]Rejtő Sándor Faculty of Light Industry and Environmental Engineering, Óbuda University, Hungary
E-mail: koltai.laszlo@uni-obuda.hu , szentgyorgyvolgyi.rozsa@rkk.uni-obuda.hu

Keywords: folding boxboard, surface sizing, solvent retention, gravure printing, gas chromatography

INTRODUCTION

Packaging has nowadays become a critical part of the food product. Solvent residues in gravure printed cartonboard packaging can alter the taste and flavour of packaged products. In order to avoid off-taste and off-flavour effects, solvent retention values have to be measured and kept as low as possible. This study is part of a series of research studies where important to investigate the cartonboard manufacturing factors related to the solvent retention of cellulose-based folding boxboard (FBB) type packaging materials for the food industry, produced by gravure printing. In this study, the influence of surface sizing on solvent (ethanol and ethyl acetate) retention and release of gravure printed fibre-based packaging was evaluated.

LITERATURE REVIEW

The chemical substances can potentially migrate from packaging substrates (such as paper, cardboard, or plastics) to food products. Where the contamination does occur, it usually results from inks and solvents with the paperboard was printed or chemicals in coatings or adhesives [1]. Prints are almost always applied to the outer surface of a food packaging and are not intended to come into direct contact with food. However, low molecular weight substances in ink easily migrate (permeate) through the packaging material into the food. Only a few packaging materials, such as glass and aluminium foil, prevent all the substances in the ink from migrating. Fibrous materials and most plastics are not barriers to migrants. Solvents in particular can easily pass through packages made of paper, cardboard or plastic.[2]. Solvent-based gravure and flexo inks used in packaging always retain some amounts of solvents in the final package. Excess solvent retention might cause the package to have an odour and can spoil the taste of food products [3].

During the gravure printing process of polymer materials, the inks and adhesive formulations used are diluted or dissolved in organic solvents that are later removed through evaporation as the printed films are passed through dryers. Printing solvents that are retained on the packaging films after the drying process at significant residual levels is called solvent retention. The solvents used in printing consist of alcohols, hydrocarbons, glycol ethers, ketones, and esters [4]. Regularly used solvents, such as ethanol and ethyl acetate are considered as volatile organic compounds (VOCs) and can be detected by gas chromatography (GC) method.[5].

FBB type cartonboard is a cellulose-based packaging material used for many packaging and non-packaging solutions worldwide in the grammage range of 160-450 g/m2. Folding boxboard is a multiply cartonboard, typically made of three pulp plies: top ply – chemical pulp; middle ply – mechanical pulp or CTMP (chemi-thermo-mechanical pulp); back ply – chemical pulp. Depending on the end-use requirements, top side of FBB can be single, double or triple coated, while back side can be single coated or uncoated. In the papermaking process, the first step is to produce the cellulose fibres from wood to make the pulp where individual fibres are separated either mechanically or chemically. Papermaking process steps: headbox, wire section, press section, dryer section, surface sizing, coating section, calendering.[6][7][8].

Sizing is a process, which is mainly used for improving the strength properties of paperboard, but many other paper properties can also be improved like reduced dusting, desired absorption properties, reduced porosity, reduced dimensional variation, smoothness. There are two different types of sizing: internal sizing and surface sizing. Surface sizing is commonly used for fine papers, coated base papers and paperboards, and also for reducing penetration of the aqueous solutions to the finished product. Starch is the most common material used in the surface sizing.[8][9].

EXPERIMENTAL

FBB type cartonboard samples produced with surface sizing (Board B-MC6.9TC3) and without surface sizing (Board H-SS0), then printed by gravure. The production profiles of both test materials were the same, differing only in the surface sizing. The retained solvent amount was measured by GC method at three interval times: right after, 1 day and 7 days after printing. Solvent retention ratio was than normalised in order to see the solvent emission characteristic.

Ethanol retention ratio

Ethanol retention of test board samples with and without surface sizing were investigated. Figure 1 clearly shows, that in case of test material had no surface sizing applied on board surface, 6% more ethanol could evaporate in 1 day than from cardboard with surface sizing, so the starch layer did not obstruct the ethanol emission. By day 7, the ethanol emission accelerated for both test cartons, more than four-fifths of the remaining ethanol had evaporated from both samples, at this stage minor deviation was detectable between the analysed test boards.

Two process phases of ethanol emission were observed: the first, one-day long quick phase, when the ethanol emission was intensive and exponential; the second, 6-day long slow phase, which might also be a diffusion controlled process when ethanol left the cardboard linearly.

Ethyl acetate retention ratio

The effect of surface sizing on ethyl acetate retention of two test boards was examined. Based on the results that can be seen on Figure 2, 1 day and also 7 days after printing, Board H-SS0 without surface sizing had less retained ethyl acetate compared to Board B-MC6.9TC3 with surface sizing. The application of starch layer during surface sizing inhibited also the evaporation of ethyl acetate, same as in the case of ethanol. Notable, that two evaporation process phases - slow/exponential and fast/linear - could also be observed, however, it was also found that the second, diffusion controlled process was slowed down and the result correlated with the slower evaporation rate of ethyl acetate.

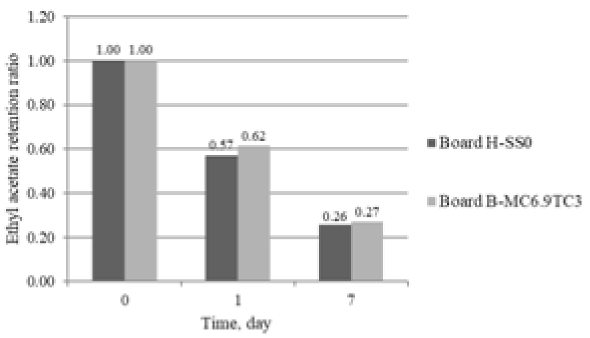

Figure 1 Normalised ethanol retention ratio of cardboard with surface sizing (Board B-MC6.9TC3) and without surface sizing (Board H-SS0), measured at different interval times

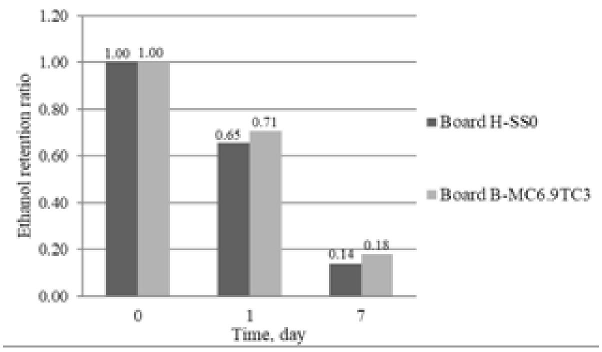

Figure 2 Normalised ethyl acetate retention ratio of cardboard with surface sizing (Board B-MC6.9TC3) and without surface sizing (Board H-SS0), measured at different interval times

CONCLUSIONS

The aim of this study was to evaluate the role and influence of surface sizing on solvent (ethanol and ethyl acetate) retention and emission of gravure printed fibre based packaging materials. FBB type cartonboard samples with and without surface sizing layers were investigated. Samples were printed by gravure then solvent retention was measured by gas chromatography at 3 different interval times. The results were then normalised in order to see the solvent emission characteristic. It was found that cartonboard sample without surface sizing had lower ethanol and ethyl acetate retention and higher emission, the applied starch layer might obstruct the solvent evaporation. It could also be noted that two process phases of solvent emission were observed: the first, one-day long quick phase, when the solvent emission was intensive and exponential; the second, 6-day long slow phase, which might be a diffusion controlled process when the solvent left the cardboard linearly. It can be concluded that surface sizing has an impact on the solvent retention of FBB type gravure printed cartonboard packaging.

REFERENCES

[1] M. S. Alamri et al., “Food packaging’s materials: A food safety perspective,” Saudi J. Biol. Sci., vol. 28, no. 8, pp. 4490–4499, Aug. 2021, doi: 10.1016/J.SJBS.2021.04.047.
[2] K. Barnes, R. Sinclair, and D. Watson, “Chemical migration and food contact materials,” Chem. Migr. Food Contact Mater., pp. 302–344, 2006, doi: 10.1533/9781845692094.
[3] D. Argent, “Solvent Retention in Packaging,” Paper, Film & Foil Converter, 2008. Accessed: Jun. 01, 2022. [Online]. Available: https://www.pffc-online.com/process-management/6603-solvent-retention-packaging-1008
[4] G.L. Robertson, Food Packaging - Principles and Practice. Taylor & Francis Group, 2012. Accessed: May 31, 2022. [Online]. https://www.academia.edu/19121118/Food_Packaging_Principles_and_Practice_3rd_Edition_Robertson_2012_
[5] W. F. Dong, W.L., Li, Y.J., Zhang, “Migration detection of residual solvents from composite packaging film to food by GC-MS,” Adv. Mater. Res., pp. 218–221, 2012.
[6] H. Paulapuro, Paper & Board Grades. 2000.
[7] K. Niskanen, Mechanics of Paper Products Edited by Kaarlo Niskanen. 2011.
[8] H. Holik, “Handbook of paper and board,” 2013.
[9] G. A. Smook, Handbook for Pulp & Paper Technologists. Angus Wilde Publications, Vancouver, 1994.

CHANGES IN PHYSICAL AND MECHANICAL PROPERTIES OF DRIED SWEET POTATOES DURING STORAGE

ANTAL Tamás, NAGY János
Institute of Engineering and Agricultural Sciences, University of Nyíregyháza, Hungary, Nyíregyháza
E-mail: antal.tamas@nye.hu , nagy.janos@nye.hu

Keywords: sweet potato, combined drying, color, texture, vacuum packaging, storage.

Dehydration is one of the oldest techniques for extending food shelf life. The food industry faces a constant challenge to meet rapidly changing consumer tastes and the demand for healthier foods with a longer shelf life, free from traditional chemical preservatives [1]. Raw sweet potatoes have a relatively high water content and are very susceptible to microbial spoilage and enzymatic browning, so dehydration and proper storage are essential [2]. The color as physical characteristic is an important quality factors of dehydrated foods, as it affects consumer acceptability [3]. Modifications in mechanical characteristics are related to the textural attributes of the food. Hence, it is important to determine the texture of the dried products [4]. Rehydration is the process of wetting dry material. If drying does not cause any damage to the material, rehydration can be treated as a process that can be reversed by dehydration [5].
The aim of the research is to determine the effect of shelf life on the physical and mechanical properties of the product. In addition, to find out which of the different drying solutions gives the least variation in color, texture and rehydration.

MATERIAL AND METHODS

The sweet potato material (*Ipomoea batatas* L.) was dried by various drying methods, i.e., lyophilization (FD), vacuum pre-drying and freeze post-drying (VD-FD), mid-infrared freeze-drying (MIR-FD) and hot-air pre-drying and freeze post-drying (HAD-FD). The following parameters were used for drying: FD (T=-25 - 20°C, p=50-80 Pa, dt=23 h), VD-FD (pre-drying: T=60°C, p=7 kPa, dt=3 h; post-drying: T=-25 - 20°C, p=50-80 Pa, dt=12 h), MIR-FD (pre-drying: T=60°C, p= 1 bar, dt=5 min; post-drying: T=-25 - 20°C, p=50-80 Pa, dt=12 h) and HAD-FD (pre-drying: T=60°C, p= 1 bar, dt=3 h; post-drying: T=-25 - 20°C, p=50-80 Pa, dt=11 h), respectively. The drying was carried out to a constant weight of the material. The moisture content of the samples at the end of the drying process: FD – 2,41% (w.b.), 3hVD-FD – 2,39% (w.b.), 5minMIR-FD – 2,69% (w.b.) and 3hHAD-FD – 2,07% (w.b.), respectively. Moisture content of the dried sweet potato dices was determined by the gravimetric method (LP306, LaborMIM, Hungary). For each drying method, 50-50 g samples were used. Weighing was performed on a digital balance (JKH-500, Jadever Co., Taiwan). The raw samples used in the experiment are cube-shaped – smooth surface – with an average of 10 mm each.
The dried materials were placed in vacuum packaging (Laica VT3112, LAICA, Italy). The packs were stored at room temperature (t=20-22 °C) for 3 months and the color difference (ΔE) (ColorLite sph900 spectrophotometer, ColorLite GmbH, Katlenburg-Lindau, Germany), hardness (compression test using CT3-4500 texture analyzer, Brookfield Engineering Laboratories, Middleboro, USA) and rehydration (in distilled water at 30 °C for 10 minutes) of the finished product were measured weekly. All tests were repeated three times.

RESULTS

Figure 1 shows the value of rehydration rate (RR) of the dried sweet potatoes placed in vacuum packaging during the investigated period, i.e. the storage time (12 weeks).

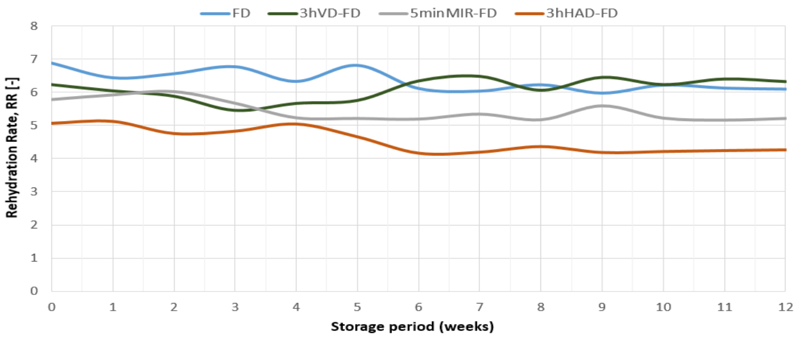

Figure 1 Change in rehydration value of the dried product under storage

From the rehydration rate curves (Fig. 1), it can be observed that the RR value of the product dried by different methods fluctuated slightly from week to week, and was stable by the end of the examination. Only the RR of the material produced by the VD-FD method increased at the end of the storage test.
Table 1 provides information on the results of the color and hardness test of dried sweet potatoes placed in vacuum packaging over a period of 12 weeks.

Table 1 Changes in color and texture during the storage period

Designation	0-12 weeks												
Color difference ΔE	0	1	2	3	4	5	6	7	8	9	10	11	12
FD	-*	1.34	1.55	2.12	1.55	3.55	4.69	3.26	4.89	5.22	5.83	5.22	5.34
3hVD-FD	4.36	4.55	5.78	6.22	5.99	6.84	7.23	7.15	8.22	9.11	8.46	8.26	8.48
5minMIR-FD	7.11	6.65	7.33	7.62	8.22	8.03	9.56	10.33	10.16	9.77	10.33	10.88	10.77
3hHAD-FD	9.22	10.26	10.66	11.25	11.05	10.82	12.09	11.86	12.34	12.97	13.44	13.73	13.88
Texture, N	0-12 weeks												
FD	1.21	1.02	1.30	1.65	1.39	1.87	1.22	1.38	1.88	2.04	2.18	2.16	2.20
3hVD-FD	4.98	5.22	4.67	4.78	4.77	5.28	5.89	5.16	4.36	4.92	5.06	4.55	4.62
5minMIR-FD	3.82	3.33	3.58	4.02	4.44	4.48	4.88	4.19	4.56	4.83	4.45	4.79	4.56
3hHAD-FD	6.50	6.23	6.77	7.21	7.76	8.14	8.05	8.27	8.43	8.21	8.38	8.24	8.49

*Freeze-dried (FD) samples are the standard.
„0" data include the value of the dried product before packaging.

The color difference (ΔE) of the samples in vacuum packs shows an increase during the storage period (Table 1). This was mainly due to fading of the product (increase of the L^* parameter). For samples dried by combined methods (VD-FD, MIR-FD and HAD-FD), the ΔE increased slightly over the 12 weeks, but increased 4-fold for lyophilized material (FD). The color difference between the MIR-FD and HAD-FD samples is already in the range of significant deviation [6].

The texture of the packaged products also shows a slight increase, mostly negligible, except for VD-FD sweet potatoes (stable texture). The increase in texture of the product means that the material becomes harder (increase in resistance of the material, N). The largest change - negative - in texture is observed for the HAD-FD product.

CONCLUSIONS

Freeze-dried and combined dried sweet potato cubes were vacuum packed at room temperature and the color, rehydration and texture of the product were monitored week by week over a 12-week storage period. It was found that vacuum packaging was suitable for packaging lyophilized and hybrid dried product with hygroscopic characteristics. During the storage test, the product with the most favorable physical and mechanical properties was prepared by the vacuum pre- and freeze post-drying methods (3hVD-FD).

ACKNOWLEDGMENTS

This paper was supported by the János Bolyai Research Scholarship of the Hungarian Academy of Sciences.

REFERENCES

[1] Cantalejo, M. J., Zouaghi, F., Pérez-Arnedo, I. (2016), *Combined Effects of Ozone and Freeze-Drying on the Shelf-life of Broiler Chicken Meat.* LWT-Food Science and Technology, 68, 400-407.

[2] Xiao, H. W, Lin, H, Yao, X. D, Du, Z. L, Lou, Z., Gao, Z. J. (2009), *Effects of Different Pretreatments on Drying Kinetics and Quality of Sweet Potato Bars Undergoing Air Impingement Drying*. International Journal of Food Engineering 5(5), Article 5.

[3] Joardder, M. U., Karim, A., Kumar, C. (2013), *Effect of Temperature Distribution on Predicting Quality of Microwave Dehydrated Food.* Journal of Mechanical Engineering and Sciences, 5, 562-568.

[4] Guiné, R. P., Barroca, M. J. (2012), *Effect of Drying Treatments on Texture and Color of Vegetables (pumpkin and green pepper*). Food and Bioproducts Processing, 90(1), 58-63.

[5] Lewicki, P. P. (1998*), Effect of Pre-Drying Treatment, Drying and Rehydration on Plant Tissue Properties: A Review.* International Journal of Food Properties, 1(1), 1-22.

[6] Araujo, C. D. S., Corrêa, J. L. G., Dev, S., Macedo, L. L., Vimercati, W. C., Rodrigues de Oliveira, C., Pio, L. A. S. (2022), *Influence of Pretreatment with Ethanol and Drying Temperature on Physicochemical and Antioxidant Properties of White and Red Pulp Pitayas Dried in Foam Mat.* Drying Technology, 40(3), 484-493.

DEEP LEARNING BASED CLASSIFICATION OF SOUNDS RECORDED BY HYDROPHONE IN A TANK FOR LEAK DETECTION AND MONITORING OF PUMP CONDITIONS

[1]ARADI Attila, [2]VARGA Attila Károly
[1]Hatvany József Doctoral School of Information Science, University of Miskolc, Hungary
E-mail : aradi.attila@gmail.com
[2]Institute of Automation and Infocommunication , Faculty of Mechanical Engineering and Informatics, University of Miskolc, Hungary
E-mail : attila.varga@uni-miskolc.hu

Keywords: acoustic, hydrophone, machine-learning, artificial-intelligence, sensor system engineering

Deep-learning techniques are widely used to classify sounds [1]. A measurement and data acquisition system and a computer program have been developed to record, process, and classify sounds recorded by an underwater microphone (hydrophone) using deep-learning techniques (artificial intelligence). From a practical point of view, one possible condition monitoring possibility is the phenomenon of cavitation. Vibrations caused by cavitation and erosion of the pipes are potential damaging factors in the following cases piping systems. To prevent damage, a detection method should be developed [2]. The detection of cavitation phenomena is particularly desirable in power plants occurrence from outside the pipelines during operation [3]. In this study, pump sound phenomena were investigated experimentally using microphones placed inside a tank. Another example is a low-cost leak detection system that is fast, accurate, traceable, and automated.

Figure 1 Experimental setup with tank, pump, and hydrophone system

However, by using acoustic sensors, the system eliminates the drawbacks of current techniques in the industry that require manual labor and are operator dependent. In this approach, hydrophones are used to listen to the sounds produced by gas escaping from pressurized tanks. When pressurized gas leaks from a tank, it generates an acoustic signal that can travel through the liquid medium. By interpreting the acoustic data, and some future applications that could improve the management of pump maintenance [4]. We outline what could be the potential of novel, real-time method to detect and address problems in a timely manner. Rolling bearings are key components of centrifugal pumps bearings reduce friction and maintain the impeller rotor. In proper alignment with stationary parts under the action of the crank wheel radial and transverse loads. Efficient fault detection of bearings allows appropriate preventive measures to be taken in good time if and improve performance. An easy to implement yet effective method for bearing detection and diagnose pump bearing failures. To achieve this, we plan on using different neural network architectures such as Multi-Layer Perceptrons (MLPs) and Convolutional Neural Networks (CNNs) [5,6,7,8]. Here we show the evaluation metric of the problem will be "classification accuracy", defined as follows the percentage of correct predictions. Accuracy = correct classifications / number of classifications. Classification accuracy is considered the optimal metric, since we assume that the that the data set will be relatively symmetric, and that this is a multiclass classifier, where the classes of the target data will be of generally uniform size. Other metrics such as Precision, Recall (or, combined, F1-score) are excluded as they are more applicable to classification challenges that involve relatively small target classes in an unbalanced data set. Our results demonstrate the zero-crossing rate is the rate at which the sign changes with the signal, this feature is used extensively in both speech recognition and music information retrieval. Spectral centroid indicates where the "centre of mass" of a sound is located and is calculated as the weighted average of the frequencies present in the sound. Spectral rolloff a measure of the shape of a signal. It indicates the frequency below which a certain percentage of the total spectral energy is present, e.g. 85%. The Mel-frequency cepstral coefficients (MFCC) of a signal are a small number (usually 10-20) of features that succinctly describe the general shape of the spectral envelope.

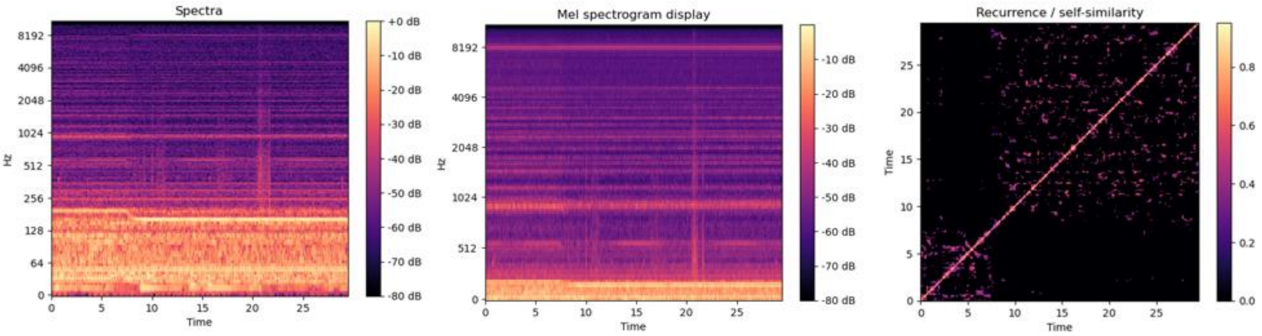

Figure 2 Underwater microphone recordings by hydrophone in the tank during pump operation

We anticipate our system to be starting point for more sophisticated machine learning based sound classification of underwater sounds in tank due to pump or leakage. Furthermore, this is a major target of artificial intelligence-based sensor system development will be relevant for such developments.

ACKNOWLEDGMENTS

The described work was carried out as part of a project supported by ION-technik Kft., ION Alkalmazott Kutatási NonProfit Kft., Gábor Pap and Mátyás Pap.

REFERENCES

[1] Simone Scardapane, Michele Scarpiniti, Marta Bucciarelli, Fabiola Colone, Marcello Vincenzo Mansueto, Raffaele Parisi (2015) Microphone array-based classification for security monitoring in unstructured environments, AEU - International Journal of Electronics and Communications, Volume 69, Issue 11, 2015, Pages 1715-1723, ISSN 1434-8411, https://doi.org/10.1016/j.aeue.2015.08.007.

[2] Yukinori Nagaya, Michio Murase (2012) Detection of cavitation with directional microphones placed outside piping, Nuclear Engineering and Design, Volume 249, 2012, Pages 140-145, ISSN 0029-5493, https://doi.org/10.1016/j.nucengdes.2011.08.045.

[3] M. Cudina (2003) Detection of cavitation phenomenon in a centrifugal pump using audible sound. Mechanical Systems and Signal Processing (2003) 17(6), 1335–1347 https://doi:10.1006/mssp.2002.1514

[4] Seyed Farshid Chini, Hassan Rahimzadeh, Mohsen Bahrami (2005) Cavitation detection of a centrifugal pump using noise spectrum. Proceedings of IDETC/CIE 2005 ASME 2005 International Design Engineering Technical Conferences & Computers and Information in Engineering Conference September 24-28, 2005, Long Beach, California, USA

[5] Vinay Arora, Rohan Leekha , Raman Singh and Inderveer Chana (2019) Heart sound classification using machine learning and phonocardiogram Modern Physics Letters BVol. 33, No. 26, 1950321 (2019)

[6] N. Dutta, S. Umashankar, V. K. A. Shankar, S. Padmanaban, Z. Leonowicz and P. Wheeler (2018) Centrifugal Pump Cavitation Detection Using Machine Learning Algorithm Technique. 2018 IEEE International Conference on Environment and Electrical Engineering and 2018 IEEE Industrial and Commercial Power Systems Europe (EEEIC / I&CPS Europe), 2018, pp. 1-6, https://doi.org/10.1109/EEEIC.2018.8494594.

[7] Primož Potočnika, Borja Olmosa, Lučka Vodopivecb, Egon Susičb, Edvard Govekar (2021) Condition classification of heating systems valves based on acoustic features and machine learning Applied Acoustics Volume 174, March 2021, 107736

[8] Orrù, P.F.; Zoccheddu, A.; Sassu, L.; Mattia, C.; Cozza, R.; Arena, S. (2020) Machine Learning Approach Using MLP and SVM Algorithms for the Fault Prediction of a Centrifugal Pump in the Oil and Gas Industry. Sustainability 2020, 12, 4776. https://doi.org/10.3390/su12114776

THERMAL ANALYSIS – THEORY AND APPLICATION

BÍRÓ Nóra, MOLNÁR Dániel, FEGYVERNE György
Foundry Institute, University of Miskolc, Hungary
E-mail : bironora1991@gmail.com , daniel.molnar@uni-miskolc.hu , dr.fegyverneki@gmail.com

Keywords: Thermal analysis, Al-Si alloys, Casting

Cast parts of the automotive industry have to meet several strict requirements that have to be proven during the entire production process. In order to ensure these requirements, different examinations have to be carried out during different stages of the production process. These examinations can be destructive or non-destructive methods.
Thermal analysis is a non-destructive method, which based on the analysis of cooling curves of the alloys. With this method the metallurgical and metallography properties of castings can be predicted and optimized. Thermal analysis methods are used since 1931 in case of cats iron alloys. As a result of the continuous developments it has started to use in case of aluminium alloys in the 1980s. There are two methods for the thermal analysis: the so called one-thermocouple method, and the two- thermocouple method.
In case of the one-thermocouple method, which is called the “classic method”, the measurement is carried out with one thermocouple, which is positioned in the middle of the test specimen. The data of cooling curve are recorded, after that the first and second derivatives are determined.

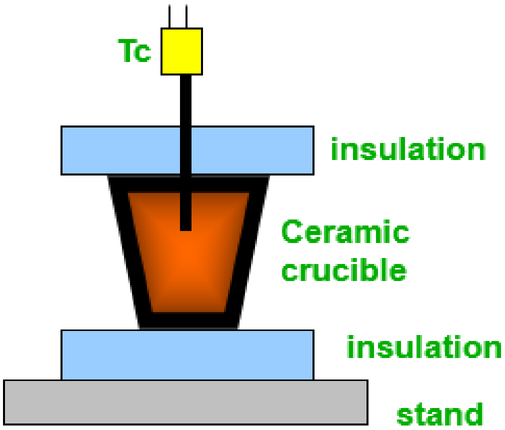

Figure 1 One-thermocouple method

In case of the two-thermocouple method the measurement is carried out with two thermocouples. One thermocouple is positioned in the middle of the test specimen and another one is positioned near the wall of specimen. The data of cooling curves are recorded, and the first and second derivatives are determined similar to the previous method. In addition the temperature difference of the two thermocouples are recorded too and based on this, the dendrite coherency and rigidity points can be determined.

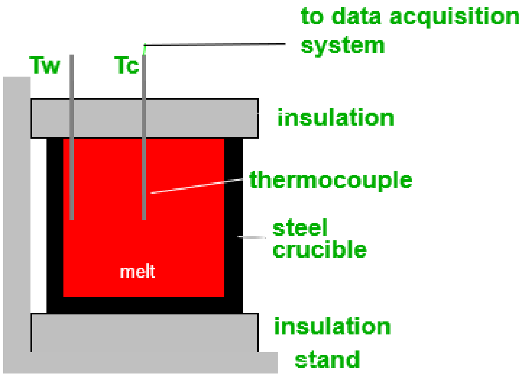

Figure 2 Two-thermocouple method

One of the most important application of thermal analysis is the determination of the efficiency of the grain refinement. By the help of the method, the undercooling of liqvidus temperature can be measured. If this calculated value is smaller the grain refinement is more effective.

One of the most harmful contaminants of Al-Si castings is iron, which can appear in the form of iron contained intermetallic phases: for example Al_8Fe_2Si (Chinese script shaped α-phase), Al_5FeSi (needle shaped β-phase) and $Al_8FeMg_3Si_6$ (π-phase). The iron contained intermetallic phases have negative effects on the mechanical properties of castings. In case of the high iron content aluminum alloys the iron contained intermetallic phases can be determined by thermal analysis.

REFERENCES

[1] Mile B. Djurdjevic, Gerhard Huber (2014), *Determination of Rigidity point/temperature using thermal analysis method and mechanical* technique, Journal of Alloys and Compounds 590, 500–506.

[2] Iban Vicario Gómez, Ester Villanueva Viteri, Jessica Montero, Mile Djurdjevic, and Gerhard Huber (2018), *The Determination of Dendrite Coherency Point Characteristics Using Three New Methods for Aluminum Alloys*, Applied -sciences 8-(8):1236.

[3] Mile B. Djurdjevic (2014), *Present and Future Application of the Thermal Analysis in Aluminum Casting Industry*, Revista de Metalurgia 50(1).

[4] A. Loizaga, A. Niklas, A.I. Fernandez-Calvo, J. Lacaze (2009), *Thermal analysis applied to estimation of solification kinetics of Al-Si aluminium alloys,* International Journal of Cast Metals Research vol 22, 345-352.

[5] D. Emadi, L.V. Whiting, S. Nafisi, R. Ghomashchi (2005), *Application of thermal analysis in quality control of solidification processes*, Journal of Thermal Analysis and Calometry, Vol 81, 235-242.

[6] D.A. Sparkman (2011), *Microstructure by Thermal Analysis,* AFS Transactions 2011, 413-420.

[7] John A. Taylor (2012), Iron-containing phases in Al-Si based casting alloys, Procedia Materials Science 1, 19-33.

GEOMETRIC DESIGN OF FORM TOOLS FOR TURNING TECHNOLOGIES

BODZÁS Sándor
Department of Mechanical Engineering, University of Debrecen, Hungary
E-mail: bodzassandor@eng.unideb.hu

Keywords: flat, circular, tangentional, tool, workpiece

Supposing serial or quantity production for a shaft or other body of revolution having complex geometry manufacturing and cost analysis is recommended before the manufacturing design.

The application of the standardized tools with CNC technology is favourable in case of unit production since the cutting time is long.

Form tools are usable for the reduction of the cutting time and enhancement of the surface roughness of the cutting surface. In addition the application of those tools are independent from the workers' competence. The disadvantages are the tool design and manufacturing time and costs that we have to consider for the cost calculation. We can simply move the tool perpendicularly for the axis of rotation of the workpiece to manufacture the complex geometric section on the workpiece. One tool geometry is applicable for one given complex workpiece geometry. It means each complex workpiece geometry means different type of form tools.

According to type of the manufacturing strategy of the workpiece there are two main groups of form tools: radial cutting tool and tangentional cutting tool.

In case of radial cutting tool (flat form tool or circular form tool) the feed direction of the tool point intersects the axis of rotation of the workpiece. The angle which is closed by the feed direction and the axis of rotation is 90°.

In case of tangential cutting tool the feed direction of the tool point and the axis of rotation of the workpiece are bypass but perpendicular for each other.

The aim of this research is the geometric analysis, mathematical and geometric design of form tools in general way for manufacturing development of body of revolutions having complex geometries.

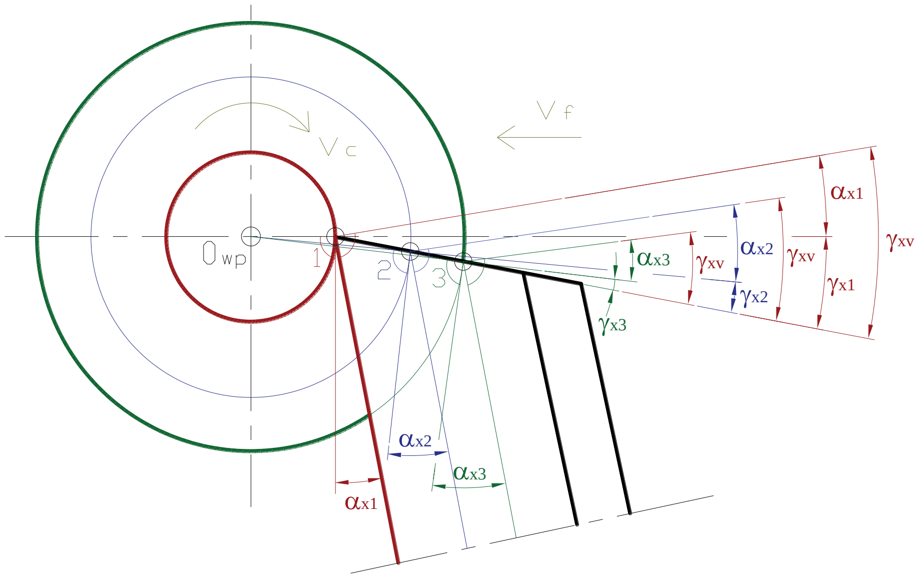

Figure 1 The position of the angles on a flat form tool

Table 1. The properties of the form tools based on the position of the tool rakes and tool clearances on the tool setting system

Flat form tool	Circular form tool	Tangentional form tool
$\alpha_{x1} < \alpha_{x2} < \alpha_{x3}$	$\alpha_{x1} < \alpha_{x2} < \alpha_{x3} < \alpha_{x4}$	$\alpha_{xA} > \alpha_{xC} > \alpha_{xB}$
$\gamma_{x1} > \gamma_{x2} > \gamma_{x3}$	$\gamma_{x1} > \gamma_{x2} > \gamma_{x3} > \gamma_{x4}$	$\gamma_{xA} < \gamma_{xC} < \gamma_{xB}$
$\gamma_{xv} = constant$	$\gamma_{xv1} > \gamma_{xv2} > \gamma_{xv3} > \gamma_{xv4}$	$\xi_{xA} > \xi_{xC} > \xi_{xB}$

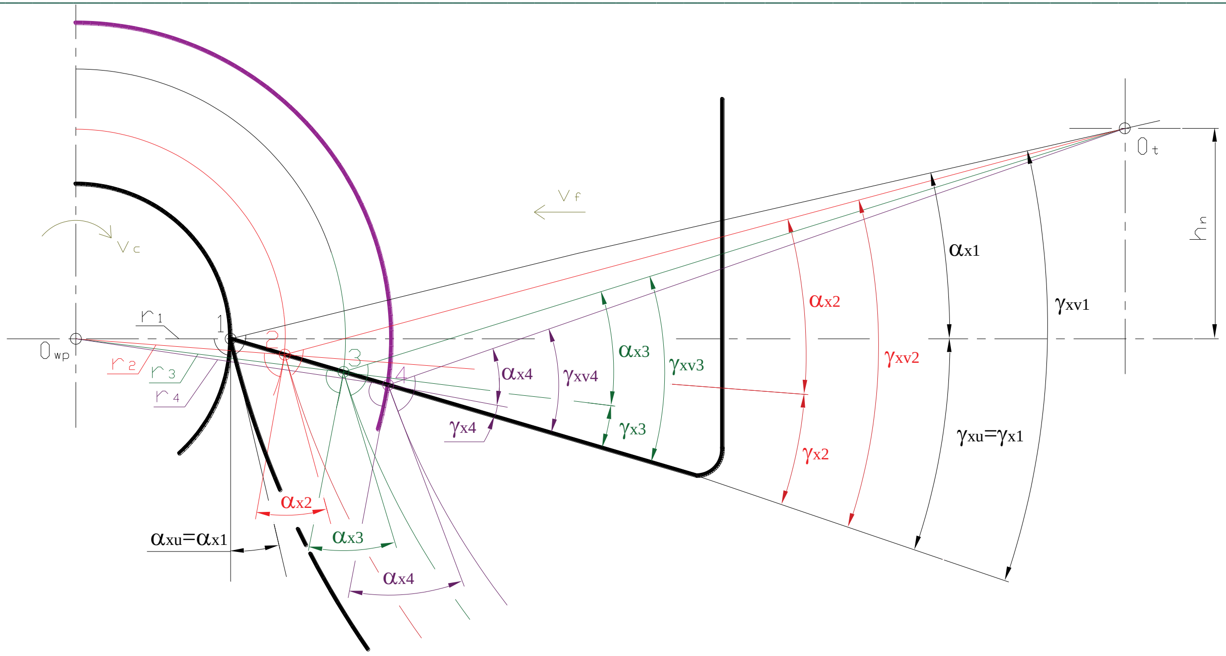

Figure 2 The position of the angles on a circular form tool

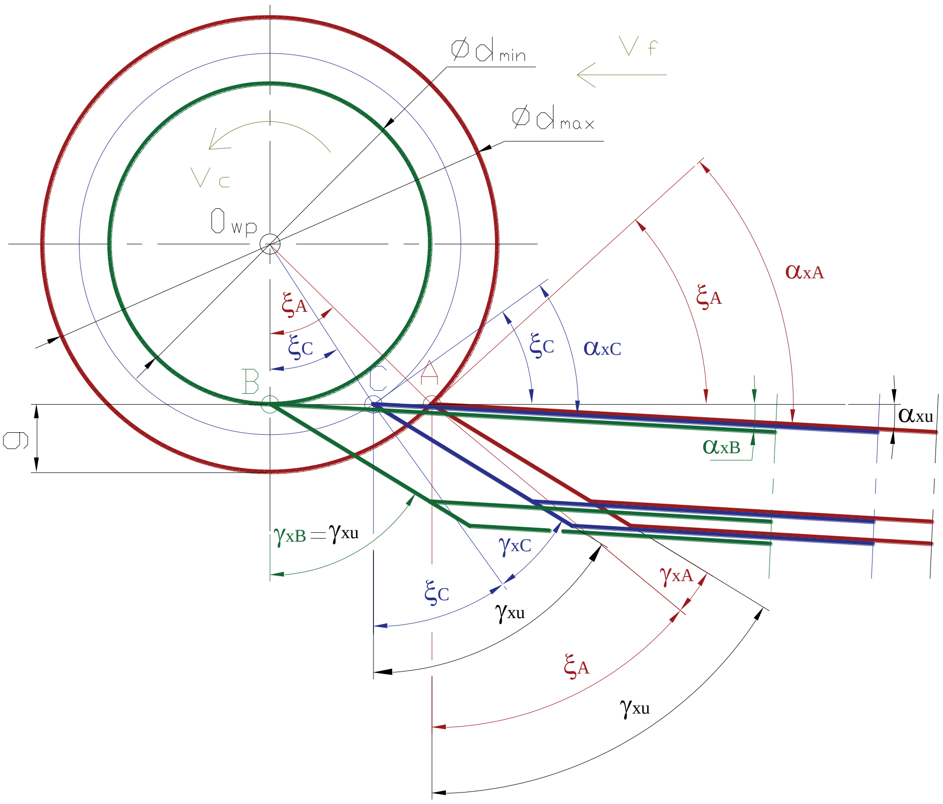

Figure 3 The position of the angles on a tangentional form tool

ACKNOWLEDGEMENT

Project no. TKP2020-NKA-04 has been implemented with the support provided from the National Research, Development and Innovation Fund of Hungary, financed under the 2020-4.1.1-TKP2020 funding scheme.

REFERENCES

[1] Gorski E. (1976), Alakos megmunkáló szerszámok, Kések, Üregelőtüskék, Marók, Műszaki Könyvkiadó, Budapest, 1976, ISBN 963 10 1182 8

DEVELOPMENT OF CELLULAR MARTIX DROG FORMULA

BUDAI István, SZOBOSZLAI András
Institute University of Debrecen Faculty of Engineering, Hungary
E-mail: budai.istvan@eng.unikdeb.hu , andras.szoboszlai@neopac.com

Keywords: polysaccharide, pharmaceutical formulation, cellular structure, solid foam capsule.

The pharmaceutical industry is constantly working to develop the most optimal drug delivery media. We have been working to develop a material that can replace the gelatine capsules used today. We saw this as necessary because gelatine carrier capsules have some undesirable properties that could be eliminated. In addition, gelatine is made from animal collagen which makes its use in certain lifestyles and religions not beneficial. Today's in the modern world, more and more companies are trying to reduce the use of animal-based raw materials. In their manufacturing processes and plant-based products are becoming more common. The use of a natural polysaccharide matrix can replace the commonly used polyethylene glycol (PEG), which causes allergic reactions in some patients. The composite is also positive for patients by reducing the side effects caused by the carriers of the drugs. The cellular structure helps to use fewer active ingredients and absorb them more efficiently. This has led to a number of important in many diseases, as individualised dosing enhances therapeutic efficacy. Our aim was to produce a stable floating formula by foaming. Among the matrix components, pectin proved to be suitable. This matrix was heated to 60°C to produce a dispersion of the active ingredient and then foamed with air at atmospheric pressure using an ultrasonic homogenizer. The structure of the moulded solid foam was investigated by microCT. Our experiments showed that a stable foam could be produced by rapid homogenization without surfactant and other additives. The durability and disintegration in the gastric environment of the solid foam capsules produced were investigated, as well as the release of the active ingredient.

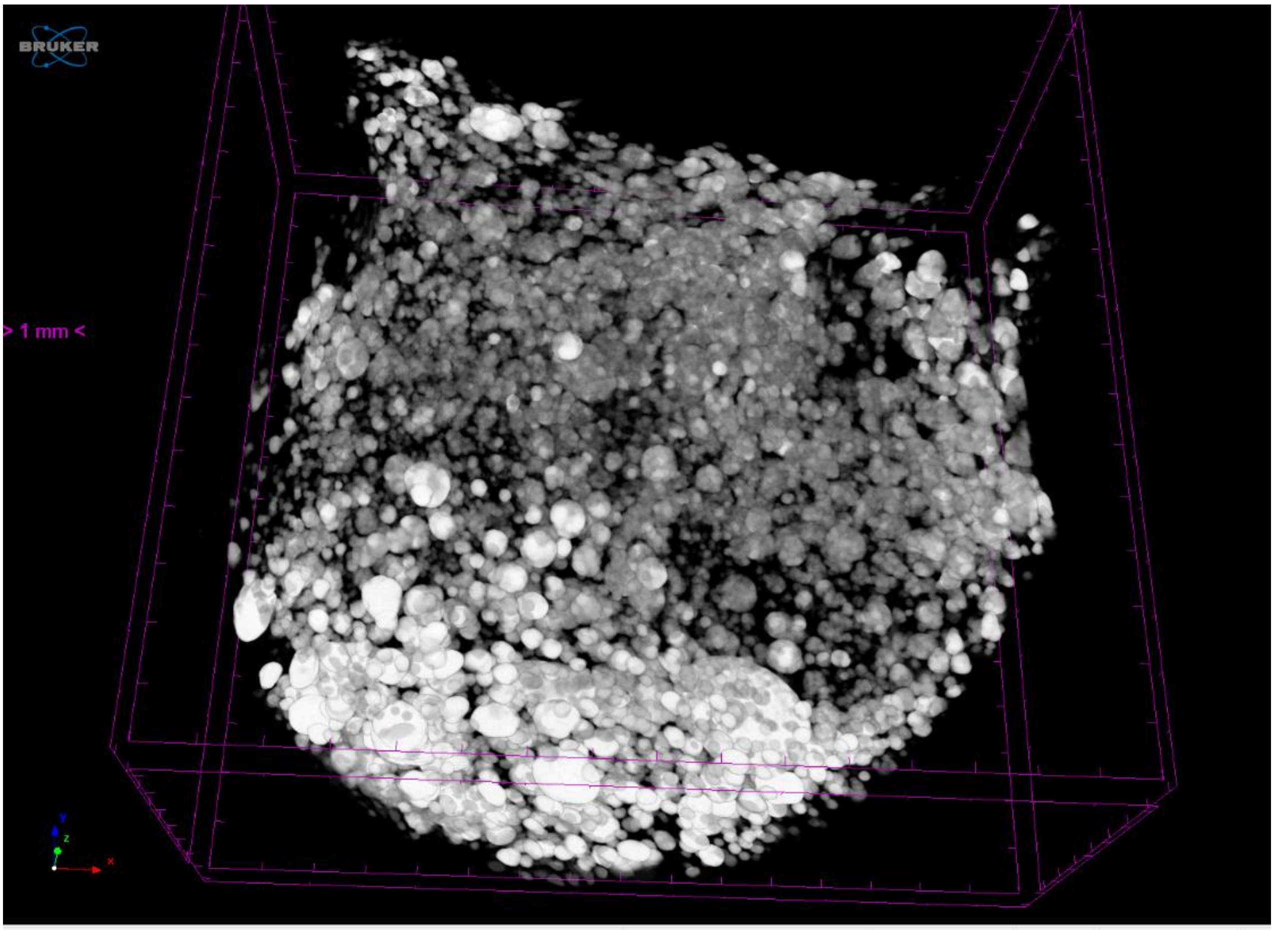

Figure 1 MicroCT image of bubbles trapped in a pectin capsule.

ACKNOWLEDGMENTS

This project was supported by the János Bolyai Research Scholarship of the Hungarian Academy of Sciences (BO/00517/20/6). „SUPPORTED BY THE ÚNKP-22-5 NEW NATIONAL EXCELLENCE PROGRAM OF THE MINISTRY FOR CULTURE AND INNOVATION FROM THE SOURCE OF THE NATIONAL RESEARCH, DEVELOPMENT AND INNOVATION FUND."

REFERENCES

[1] D. Weaire, S. Hutzler, (2001), *The Physics of Foams*, Oxford, Oxford University Press, ISBN: 978-0198510970.

[2] Y. Bienvenu, (2014), "*Application and future of solid foams,*" Comptes Rendus Physique, pp. 719-730, doi: 10.1016/j.crhy.2014.09.006

[3] Singh, A. Bhadauria, P. Kumar, H. Bera, S. Saha, (2019), *2 - Bioactive and drug-delivery potentials of polysaccharides and their derivatives* In: Maiti S, Jana S, Polysaccharide carriers for drug delivery, pp: *19-48, doi: 10.1016/B978-0-08-102553-6.00002-7. doi: 10.1016/j.nano.2015.02.018.*

[4] Haimhoffer, Á.; Fenyvesi, F.; Lekli, I.; Béresová, M.; Bak, I.; Czagány, M.; Vasvári, G.; Bácskay, I.; Tóth, J.; Budai, I. (2021), *Preparation of Acyclovir-Containing Solid Foam by Ultrasonic Batch Technology. Pharmaceutics*, 13, 1571. https://doi.org/10.3390/pharmaceutics13101571

CHARACTERIZATION OF A BIODEGRADABLE EDIBLE FILM OBTAINED FROM PSYLLIUM HUSK FLOUR

[1]CS. TÓTH Annamária, [2]PREKLET Edina, [2]BÖRCSÖK Zoltán, [3]HORVÁTH Brigitta, [2]HALÁSZ Katalin
[1]Mechanical Engineering in the Agriculture and Food Industry Institute, University of Nyíregyháza, Hungary
E-mail: toth.annamaria@nye.hu
[2]Faculty of Wood Engineering and Creative Industries, University of Sopron, Hungary
E-mail: joobne.preklet.edina@uni-sopron.hu
[3]Faculty of Health Science, University of Debrecen, Hungary
E-mail: horvath.brigitta@foh.unideb.hu

Keywords: *active packaging, psyllium, edible packaging, ultrasonic cavitation*

Every year more and more waste is generated worldwide. The massive use and uncontrolled disposal of plastics has become a habit over the past four decades that needs to be changed immediately. In 2017, around 15 million metric tons of plastic packaging waste was generated in the European Union alone [1]. In the general packaging sector, food packaging has the highest demand for plastic [1]. The need for plastic in Europe is several tens of millions of tons per year [4], of which almost half is used to produce plastic packaging material and almost 1/5 of it is used for food packaging material [1] [2] [4].

The development and production of new types of food packaging materials (active packaging materials, intelligent packaging materials, edible packaging materials and packaging materials produced from 100% natural, degradable polymers and their combination) is very important nowadays. Within this, the various edible packaging materials, which are usually films, can even form an airtight seal on the surface of the packaged food, or with its active components, as well as the diffusion of active components into the food or its immediate environment, the shelf life of the food can be increased, safely, with zero waste. Their use can be easily integrated into the production chains of currently used packaging materials.

In this study, an edible film was produced from psyllium husk flour. A film containing a control and a plasticizer was also produced. During the tests, the physical, mechanical, thermogravimetric water vapor permeability, water vapor binding properties, and antioxidant capacity of the edible film coating were studied.

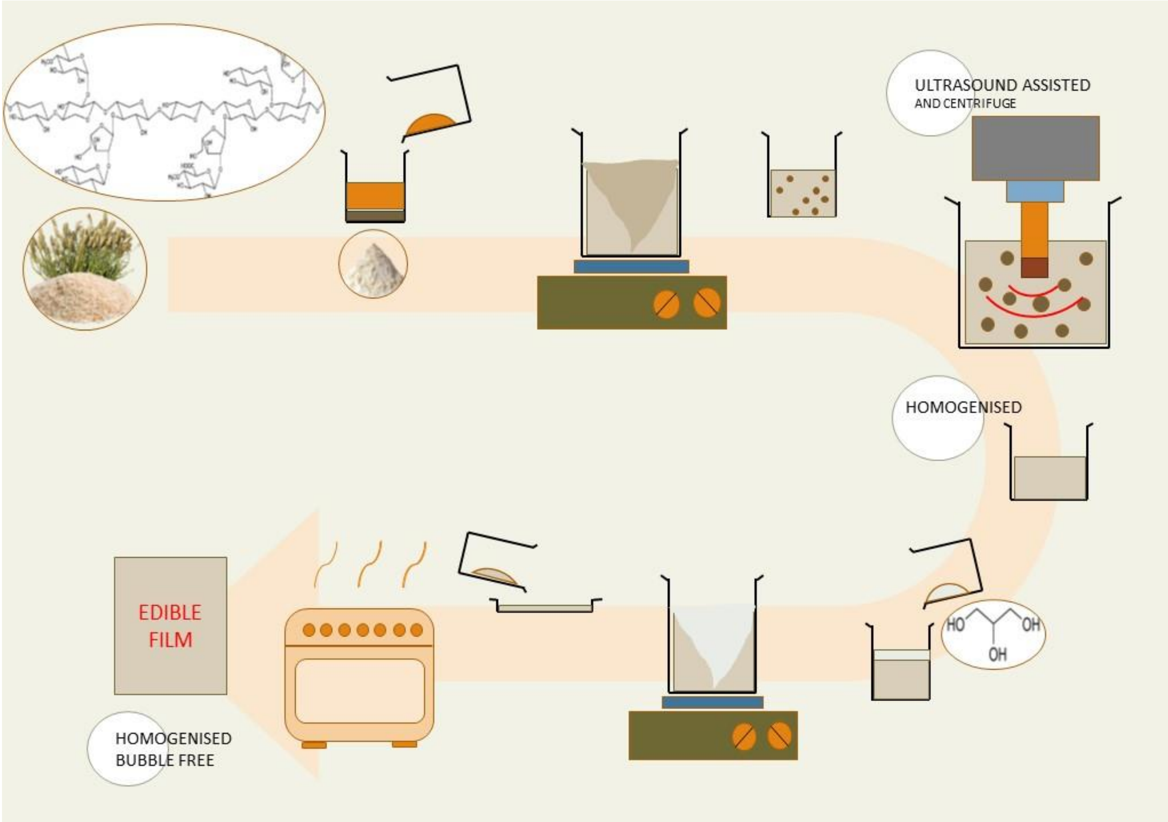

Figure 1 The production of the film from Psyllium husk flour

RESULT

During the production of the film (Figure 1), the psyllium mucilage was treated using ultrasonic cavitation, which affected the structure of the arabinoxylan macromolecules containing the psyllium husk flour: by changing it, it drastically reduced the viscosity of the psyllium mucilage, which helped the production of the film [3]. The mechanical properties of the film determine its durability and suitability for coatings or films. The film produced from mucilage without plasticizer was more brittle and did not show a high value for plastic deformation.

CONCLUSION

Based on the mechanical results, the produced composite films may be suitable for the production of edible film coating, of course, during further examination of the films, the antibacterial, antifungal, and antimicrobial effects of the films can be determined in vivo and in vitro, which is an important property for use as food packaging material.

REFERENCES

[1] Athanassiou, A. (2020). Preface. In A. A. (Ed.), Sustainable Food Packaging Technology. John Wiley & Sons.
[2] Data for the year 2018 From ING Economics Department, D. (without date). By: https://www.statista.com/statistics/282732/global-production-of-plastics-since-1950/
[3] Halász, K., Tóth, A., Börcsök, Z., & Preklet, E. (2022). Edible, Antioxidant Films from Ultrasonically Extracted Plantago psyllium Seed Husk Flour Mucilage. Journal of Polymers and the Environment, 1-10.
[4] Plastics, E. (2019). Plastics - the Facts 2018: An analysis of European plastics production. Brussels.

FULL-SCALE TESTS OF PIPELINE GIRTH WELDS UNDER COMPLEX CYCLIC INTERNAL PRESSURE AND STATIC BENDING LOADING CONDITIONS

DAKHEL Ahmad Yasser, LUKÁCS János
Institute of Materials Science and Technology, University of Miskolc, Hungary
E-mail: yaser.dakhel@gmail.com , janos.lukacs@uni-miskolc.hu

Keywords: gas transporting pipeline, full-scale test, girth weld, complex loading condition.

High pressure pipelines are used to transport different media (crude oil, natural gas, etc.) worldwide. These piping systems can contain a large number of girth welded joints (more than 730,000 on the Hungarian system alone) which must be evaluated at the design stage to assess their fatigue resistance. The repeating startup and shutdown events, the changes in the internal pressure values, furthermore the external impacts (e.g. seismic, dynamic) result in cyclic loads, having a characteristic effect on the lifetime of the girth welds. Unfortunately, during the construction of pipelines, it is not uncommon to encounter external influences that result in excess bending stresses in the girth welds. Defects and/or discontinuities occurring in gas pipelines, frequently in the welds, can lead to propagating cracks, and these pipeline cracks may cause catastrophic fractures. Full-scale fatigue and burst test are the best ways of assessing the crack propagation resistance of a natural gas pipeline, especially in cases of the girth welds. In the case where we can superimpose external bending stress on the cyclic internal pressure, we can model the real loading conditions of the pipelines well.

The aims of our research and this paper are to introduce our full-scale pipeline fatigue and burst tests applying cyclic internal pressure and superimposed external bending stress on girth welds, furthermore, attracting the importance and the applicability of the investigation results.

A unique test system has been developed for the complex loading of pipeline sections by cyclic internal pressure and external bending. In the three-point bending arrangement, the tested girth weld was positioned in the middle of a nominal 4 meters long pipeline section; the bending load was set via a load cell and checked by means of a deflection meter. The experimental setup is shown in Figure 1, where water was used as the internal test medium.

a) Load cell and deflection meter b) Transfer of external load c) The whole pipeline section

Figure 1 Experimental setup for cyclic internal pressure and external bending

The investigated pipeline sections were made of P355NH steel with a nominal diameter of DN100 (114.3 mm) and a nominal wall thickness of 5.6 mm. The tested girth welds were made by manual metal arc welding and were inspected by visual, liquid penetrant, and radiographic tests (VT, PT, and RT, respectively).

Three pipeline sections were tested in the first phase of the full-scale tests. The first pipeline section (Y3) was only subjected to a burst test without fatigue testing and external bending loading. The second pipeline section (Y2) was subjected to the burst test after 100,000 cycles of internal pressure loading, both without external bending loading. The cyclic internal pressure varied between 60% and 100% of the operational pressure (64 bar). For the third section of the pipeline (Y5), external bending loads were applied during the cyclic loading (100,000 cycles) and the burst test. The applied stress from bending was twice the axial stress from the maximum internal pressure. After the fatigue tests, the radiographic examination (RT) of the examined girth welds were performed again.

During the fatigue tests, where the applied frequency was 0.2 Hz, the change in the internal pressure value and the deflection value and its variation were continuously monitored. These values were recorded every 5,000-8,000 cycles, with a time interval of 50-60 cycles (250-300 s).

Figure 2 illustrates the internal pressure vs. burst test time diagrams of the investigated pipeline sections, where the arrows indicate the burst points (burst pressures): Y3 – 447 bar, Y2 – 447 bar, and Y5 – 446 bar. The pressure drop parts of the diagrams demonstrate the volume expansions of the pipeline sections. During the time with decreasing pressure, the test system took water from the external water network. Figure 3 shows the investigated pipeline sections at the moment of failure, where the water burst with huge force through the split area.

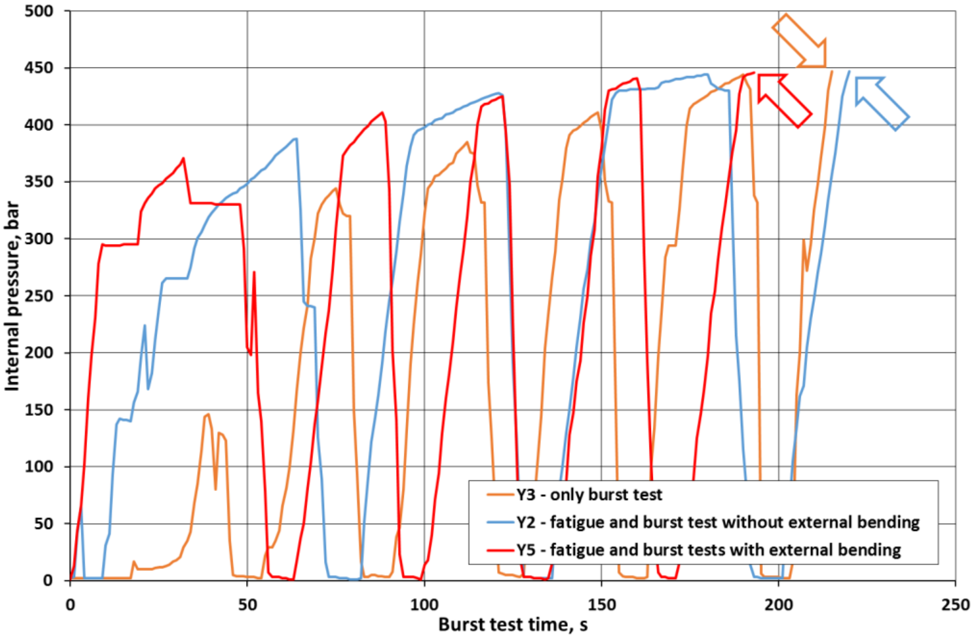

Figure 2 Internal pressure vs. burst test time diagrams during the burst tests of the pipeline sections

a) Y3 b) Y2 c) Y5

Figure 3 The investigated pipeline sections at the moment of their failures

The full-scale tests have confirmed the high load-bearing capacity of the girth welds produced to the required quality. The failure of the tested pipeline sections occurred similarly, but in none of the cases in a girth weld, with failure pressures significantly higher than the operating pressure. Neither the cyclic loading nor the cyclic loading and applied external bending load (in this magnitude) significantly affect the pipeline sections' failure (Y2, Y5). However, further full-scale tests are needed, both under higher axial stresses from the external bending and using artificial girth weld defects on the tensile bending stress side of the pipeline section.

ACKNOWLEDGMENTS

This research was supported by the European Union and the Hungarian State, co-financed by the European Structural and Investment Funds in the framework of the GINOP-2.3.4-15-2016-00004 project, aimed to promote the cooperation between the higher education and the industry.

A NUMERICAL STUDY ON SPRINGBACK PREDICTION WITH SYSTEMATIC PROCESS IMPROVEMENT

DESSIE Jemal Ebrahim, LUKÁCS Zsolt
Institute of Materials Science and Technology, Faculty of Mechanical Engineering, University of Miskolc, Hungary
E-mail: metjemal@uni-miskolc.hu , metzsolt@uni-miskolc.hu

Keywords: AutoForm, high strength aluminium alloy, Springback, Systematic process improvement, U-bending

Springback is a technical challenge in the automotive industry. AutoForm FEM package uses a material parameter expressing the reduction of the initial tangent modulus γ, the saturation constant χ, and the strain distance affecting the steepness of the reverse stress curve K to predict springback. To validate such types of material parameters, conducting a physical experiment is mandatory. Stretch bending tests are the most common method to study springback using U-shaped bending testing tools. In addition to the material behavior of the sheet metal, springback is also affected by friction coefficient, blank holder force, die, and punch radius. If so, before going to conduct a physical experiment, it needs a numerical study using acceptable FEM code to determine the range and the most influential parameters. In this study, a cold U-shaped bending test of AA 6181-T4 was numerically investigated using AutoForm. Different ranges of die radius (Rd) and punch radius (Rp), coefficient of friction, and blank holding force (BHF) has been considered. The Systematic process improvement (SPI) was applied to easily identify which design parameters influence the springback and to what extent at different levels. The most important parameters, to what extent, to predict springback amount to stretch U-bending of high strength aluminum alloy (HSAA) have been numerically studied. Even though all considered parameters affect the geometrical deviations from the intended shape, but the die radius (Rd) is the most influential one. The range of die and punch radius which would be free from distortion and warpage has been leveled. Finally, the number of designs of the experiment matrix required is confirmed for further physical study.
In the AutoForm finite element analysis material card, the reduction of the tangent modulus to analyze the kinematic hardening behavior of the material is expressed as:

$$E_l = E_0[1 - \gamma(1 - e^{\chi p})]$$

Where E_0 initial tangent modulus, E_l is deformation-dependent tangential modulus, γ is a material parameter called young's reduction factor and χ is saturation constant.
The non-linear reverse strain is approximated with an inverse hyperbolic tangent function and for the sum of linear and non-linear reverse strain the following expression can be written:

$$\varepsilon_r = \varepsilon_{rl} + \varepsilon_{rn} = \frac{\sigma_r}{E_1(p)} + Karctanh^2\left(\frac{\sigma_r}{2\sigma_h(p)}\right)^2$$

where $\sigma_\mathrm{h}(\mathrm{p})$ is the isotropic stress depending on the reverse plastic strain and K is a material parameter representing a typical strain distance affecting the steepness of the reverse stress curve (σ_r). ε_r is total reverse strain, ε_rl is linear reverse strain, ε_rn is nonlinear reverse strain. Therefore, γ, χ, and K will play essential roles in the physical experiment to analyse springback. This study takes into account those parameters directly from the material library found in AutoForm finite element package for the specific material
AutoForm uses systematic process improvement (SPI) and multiple stamping simulations are carried out automatically. SPI enables engineers to improve the forming process systematically. Systematic process improvement brings transparency to the forming process by showing which design parameters influence the part quality and to what extent. The acceptable and defect-free design parameters for the simulation of stretch U-bending of high-strength aluminum alloy are listed in *Table 1*.

Table 1 Design parameters for simulation

Geometrical parameters	Considered Value	Accepted value
Die radius (Rd)	3-10 mm	5,6,7,8, 9 & 10 mm
Punch radius (Rp)	3-10 mm	3,4,5,6,7,8 & 9 mm
Blank holding force (BHF)	3,4,5,6,7,8, & 9 kN	
coefficient of friction (μ)	0.01, 0.05, 0.1 & 0.15	

The effect of die radius on a different level of constant punch radius and vis versa on the flange springback θ1 is shown in *Figure 1*. *Figure 2* also demonstrated the effect of BHF and coefficient of friction to flange springback θ1 on the constant of coefficient of friction and BHF respectively.

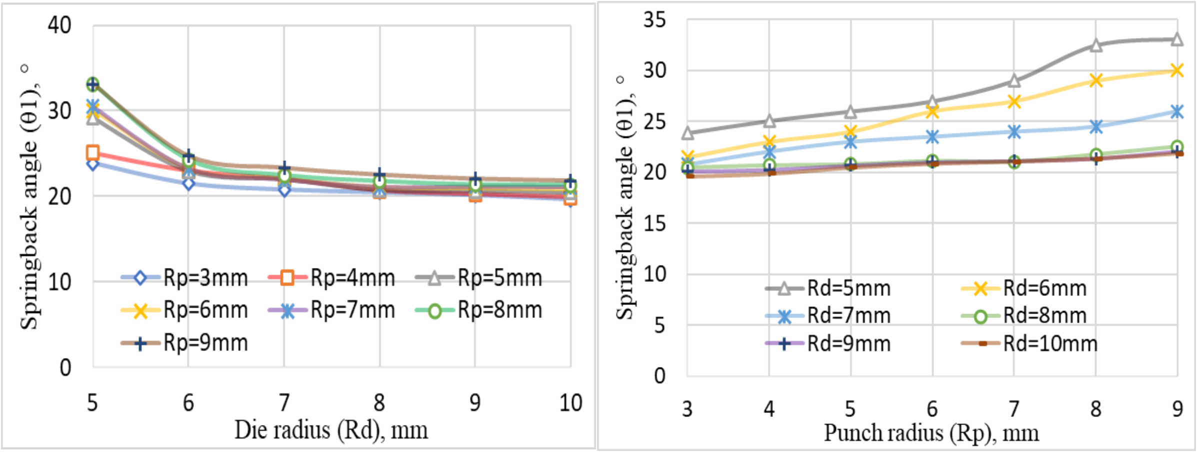

(a) (b)

Figure 1 The effect of die and punch radius on flange springback: (a) constant punch radius; (b) constant die radius

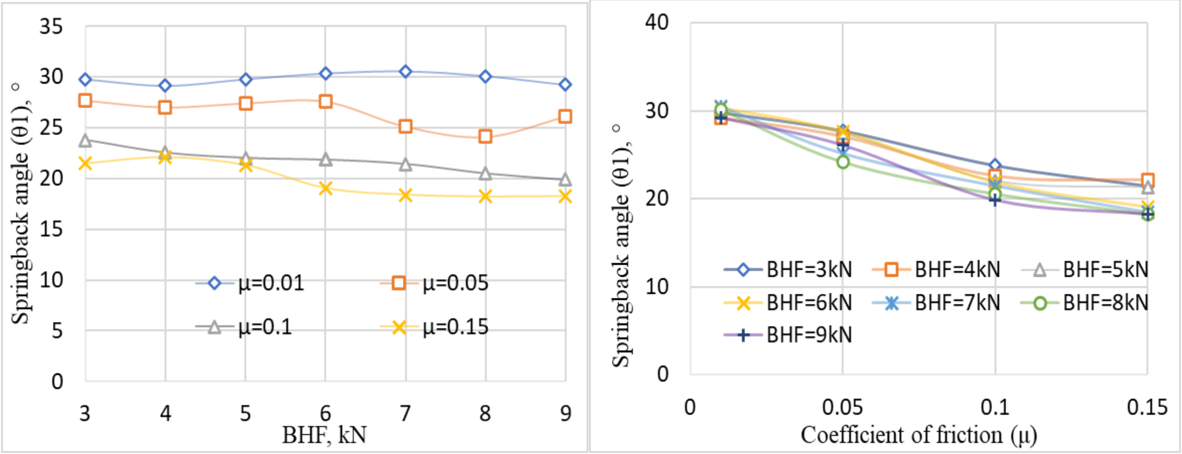

(a) (b)

Figure 2 The effect of BHF and coefficient of friction on flange springback: (a) constant coefficient of friction; (b) constant BHF

REFERENCES

[1] Tisza, M., & Lukács, Z. (2014). Springback analysis of high strength dual-phase steels. Procedia Engineering, 81, 975-980.

[2] Systematic process improvement, https://www.autoform.com, 18.10.2022

PREDICTION OF FLD USING GURSON MODEL FOR SIMPLE FLAT SPECIMEN

[1]DOMOKOS Tatiane, [1]BAKSA Attila, [2]SZABOLCS Szávai
[1]Intsitute of Applied Mechanics, University of Miskolc, Hungary
E-mail: metwadas@uni-miskolc.hu , attila.baksa@uni-miskolc.hu
[2]Institute of Machine and Product Design, University of Miskolc, Hungary
E-mail: szavai.szabolcs@uni-miskolc.hu

Keywords: Forming limit diagram (FLD) - Gurson model - FLD - Abaqus - metal forming

In the past century, the prediction of ductile damage and fracture of metal materials under complex loadings has always been an important topic in many industries like the metal forming industry.

The GTN model is one of the most classical damage models regarding damage mechanics, which has a wide application and perfect development in studies of fracture of metal ductile. GTN was originated from Gurson and later improved by Tvergaard and Needleman. The improvement consists on introducing an equivalent void volume fraction f and two more parameters called q_1 and q_2 into the yield function of Gurson's model to model the complete loss of load-carrying capacity at a realistic void volume fraction.

The yield function of the GTN model can be expressed as

$$(\sigma, f) = \left(\frac{\sigma_{eq}}{\bar{\sigma}_m}\right)^2 + 2q_1 f^* \cos h\left(\frac{3}{2}\frac{q_2\,\sigma_m}{\bar{\sigma}_m}\right) - 1 - (q_1 f^*)^2 = 0$$

Where σ_m is the mean stress, σ_{eq} is the macroscopic von Mises equivalent stress; $\sigma_m = \frac{\sigma_{ii}}{3}$ is the mean stress; $\bar{\sigma}_m$ is the equivalent stress of the matrix material; q_1 and q_2 are adjustment parameters introduced by Tvergaard; the equivalent void volume fraction f is a function of the current void volume fraction f:

$$f^* = \begin{cases} f & f \leq f_c \\ f_c + k_f(f - f_c) & f > f_c \end{cases}$$

The Gurson-Tvergaard-Needleman (GTN) model, is widely used to predict the failure of materials based on lab specimens and its direct identification is not so easy to acquire, where time and financial investiment are needed. The Gurson model is based on micro-mechanical behavior of ductile fracture, where void nucleation, growth and coalescence are contained. To determine the GTN parameters, the most used method is the combination betwwen the experimentals tests results and the FEM results.

In this work it is presented a comparison between different parameters and tests results for flat specimen based on the fracture of traction and compress test.

One of the major issue of the GTN model is the accurate identification of GTN parameters, making not possible to perform experiments for their evaluation. In order to estimate the material parameters of the GTN it is made an inverse procedure aimed to estimate the material parameters of the GTN porosity-based plastic damage model by means of RSM method is represented. Results are showed with agreement between experimental and predicted FLD when determined GTN parameters were utilized. For the FE - Simulation Abaqus software is used to predict FLDs.

The predicted FLDs are compared with experiments involving aluminum alloys.

ACKNOWLEDGMENTS

This research work started in the framework of TÁMOP-4.2.1.B-10/2/KONV-2010-0001 project and is continued in the project entitled Material Developments for the Automotive Industry within the project TÁMOP-4.2.2.A-11/1/KONV-2012-0029. Both projects are supported by the New Hungarian Development Plan and jointly financed by the European Union and European Social Fund.

REFERENCES

[1] Chahboub, Y., Szavai, S., Bezi, Z. (2019), *Determination of GTN Parameters of Sent Specimen During Ductile Fracture* – MultiScience – XXXIII. MicroCAD International Multidisciplinary Scientific Conference – University of Miskolc, Hungary 23-24 May, 2019, ISBN 978-963-358-177-3

[2] Abbasi, M., Ketabchi, M., Izadkhah, H., Fatmehsaria, D.H., Aghbash, A.N., (2011), *Identification of GTN Model Parameters by Application of Response Surface Methodology*. Science Direct. Procedia Engineering 10 (2011) 415-420.

[3] Zao, H., Hao Z., Yumei, H., (2021), *An Improved Shear Modified GTN Model for Ductile Fracture of Aluminium Alloys Under Different Stress States and its Parameters Identification*. International Journal of Mechanical Sciences 192 (2021), 106081.

ON THE TORSIONAL RIGIDITY OF ORTHOTROPIC BEAMS WITH RECTANGULAR CROSS SECTION

ECSEDI István, BAKSA Attila, LENGYEL Ákos József, GÖNCZI Dávid
Institute of Applied Mechanics, University of Miskolc, Hungary
E-mail: mechecs@uni-miskolc.hu, mechab@uni-miskolc.hu, mechlen@uni-miskolc.hu, mechgoda@uni-miskolc.hu

Keywords: Orthotropic Beam, Saint-Venant torsion, torsional rigidity.

The paper deals with the torsional rigidity of homogenous and orthotropic beam with rectangular cross section. The torsional rigidity of the considered beam is defined in the framework of the Saint-Venant theory of uniform torsion. Exact and approximate solutions are given to the determination of the torsional rigidity. The shape of cross section is determined which gives maximum value of the torsional rigidity for a given cross-sectional area. The dependence of torsional rigidity as a function of the ratio shear moduli of beam is also studied.
Figure 1 shows the beam with rectangular cross section which is subjected to torsional load. The material of the beam is elastic, homogenous and Cartesian orthotropic with shear moduli $G_{xz} = G_x$ and $G_{yz} = G_y$. Although the exact solution is known for the twisted orthotropic beam with a rectangular cross section [1,2,3,4], the basic formulae are given for the simplicity, which are directly connected to the torsional stiffness.

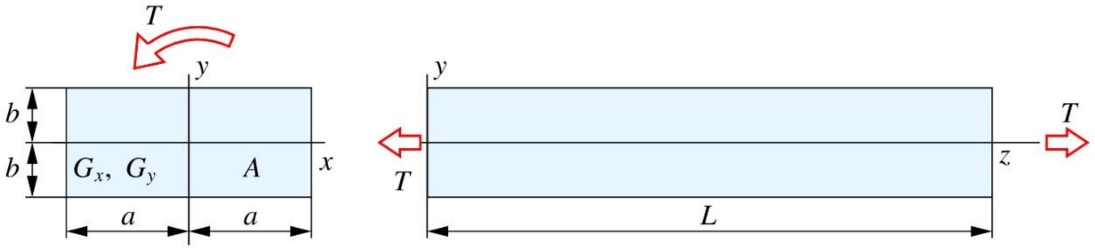

Figure 1 Beam with torsional load.

The Prandtl stress function formulation is used. The exact value of torsional rigidity is obtained as a limit value of an infinite series. Paper presents upper and lower bounds for the numerical value of torsional rigidity. The lower S_L and the upper S_U bounds of torsional rigidity with the exact value of torsional rigidity as a function of ratio of shear moduli is analyzed.

$$S_L = \frac{40}{9} \frac{G_x G_y a^3 b^3}{a^2 G_y + b^2 G_x}. \tag{1}$$

$$S_U = \frac{4 G_x G_y J_x J_y}{G_x J_x + G_y J_y} \leq R_U = G_x J_x + G_y J_y \tag{2}$$

Determination of the size of rectangular cross section whose torsional rigidity has maximum value for a given value of cross-sectional area is presented and it is illustrated by numerical example.

REFERENCES

[1] S.G. Leknitskii, Theory of Elasticity of an Anisotropic Elastic Body, Holdon Day Inc., San Francisco, 1963.
[2] S.G. Leknitskii, Torsion of Anisotropic and Non-Homogeneous Bars, Nauka, Moscow, 1971. (in Russian)
[3] M.L. Milne-Thomson, Anti-plane Elastic Systems, Springer, Berlin, 1962.
[4] O. Rand and W. Rowenski, Analytical Methods in Anisotropic Elasticity, Birkhäser, Zürich, 2005.

AN ANALYTICAL SOLUTION FOR THE TWO-LAYERED COMPOSITE BEAM-COLUMN WITH INTERLAYER SLIP AND CONSTANT AXIAL LOAD

ECSEDI István, BAKSA Attila, LENGYEL Ákos József, GÖNCZI Dávid
Institute of Applied Mechanics, University of Miskolc, Hungary
E-mail: mechecs@uni-miskolc.hu, mechab@uni-miskolc.hu, mechlen@uni-miskolc.hu, mechgoda@uni-miskolc.hu

Keywords: Composite Beam-Column, Axial Load.

Layered composite structures, especially layered composite beams are widely applied in building and bridge engineering since the advantages of the layers made of different materials can be well married, while their disadvantages can be reduced or eliminated. Therefore, it is very important to understand the mechanical behavior of the layered composite beams and the influence of the connection between the layers of composite beams which are joined to each other by different shear connectors such as nails, screws or rivets.

Because of the elastic deformation of those connectors can occur between the connected beam components the appearance of interlayer slip is possible. In this paper it is assumed that the normal direction of the connected layers is perfect. The connection in axial direction may be imperfect, which is described by the concept of interlayer slip. Paper presents an analytical solution for the two-layered composite beam-columns with imperfect shear connection.

The considered beam is simply supported at its both ends (see Figure 1). The beam is subjected to transverse load and constant axial load. The kinematic assumptions of the Euler-Bernoulli beam theory are used. The connection of the beam components is perfect in normal direction, but the axal displacement field may jump. The shear axial force derived from t the imperfect connection is proportional to the relative slip occurring between the layers. The determination of the analytical solution is based on Fourier method. The first theoretical and experimental studies analyzing the behavior of the composite beams with interlayer slip was published in the 1950s.

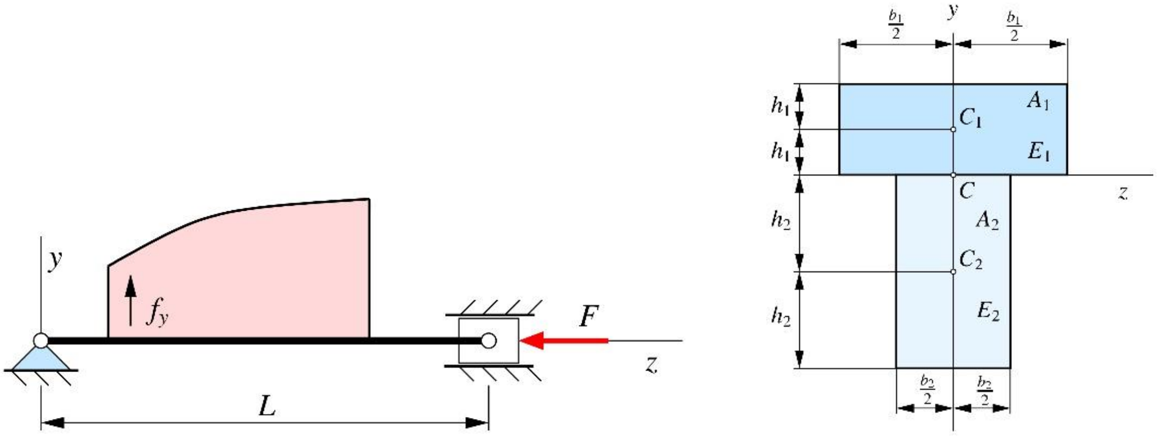

Figure 1 Layered composite beam-column, its applied load and cross section.

In paper [1] the Euler-Bernoulli beam theory was utilized to describe the static behavior of composite beams with interlayer slip. Since then, a lot of papers, studies have dealt with the problem of layered beams with partial shear interaction based on the results of Newmark et al [1]. In the present paper a slip-deflection formulation is presented to solve the statics problem of composite beams with imperfect shear connection and constant axial load. Lengyel and Ecsedi presented a second order analysis of composite beam-columns with interlayer slip. The considered beam carries the transverse load and constant axial load [2].

The beam-column at both end is simply supported, and its applied load is transverse load which depends on the axial coordinate and constant axial load. The presented close form solution is obtained by the Fourier series representation of the displacement and slip function. Two examples illustrate the application of the developed analytical method.

REFERENCES

[1] N.M. Newmark, C.P. Siess, I.M. Wiest, Test and analysis of composite beams with incomplete interaction. Proceedings of the Society of Experimental Stress Analysis, Vol. 8, No. 1, pp. 75-92, 1951.

[2] Á.J. Lengyel, I. Ecsedi, Second order analysis of composite beam-columns with interlayer slip. XXXII microCAD International Multidisciplinary Scientific Conference, Miskolc, Hungary, University of Miskolc, Paper ID D-1-5, 2018.

ANALYSIS OF THE QUALITY OF INCOMING ALUMINUM ALLOY INGOTS

GYARMATI Gábor, KÉRI Zoltán, MOLNÁR Dániel
Foundry Institute, University of Miskolc, Miskolc, Hungary
E-mail: ontgabor@uni-miskolc.hu , ontkeri@uni-miskolc.hu , daniel.molnar@uni-miskolc.hu

Keywords: Aluminum alloy, Metal quality, Bifilm, Defects, Reduced pressure test.

Regardless of the casting technology used for manufacturing cast components, liquid metal quality has an essential role in providing high structural integrity, mechanical performance, and the avoidance of casting defects like porosity, leakage, hot tears, and cracks [1]. Even the first of the well-known ten rules, created by Campbell [2] to provide the fundamental requirements for the manufacture of high-quality metal castings, emphasizes the importance of "starting with a good-quality melt". To accomplish this, the melting, melt-transfer, and melt-processing steps need to be carefully selected, executed, and controlled. However, as revealed by Erzi et al. [3] the quality of the ingots produced by different primary or secondary alloy suppliers can differ remarkably. In this way, the melt quality is affected by the impurity content of the ingots used as charge material. Among the impurities, double oxide films (or bifilms) and solute hydrogen have an overwhelmingly negative effect on the susceptibility to pore formation and the mechanical properties of cast parts, so the detection and quantification of these impurities present in ingots should be considered to be an important task when the supplier of the charge material is selected. There are different approaches available in the literature for this task [3-5]. In this work, we present our solution (Figure 1.) for this challenging and complex problem.

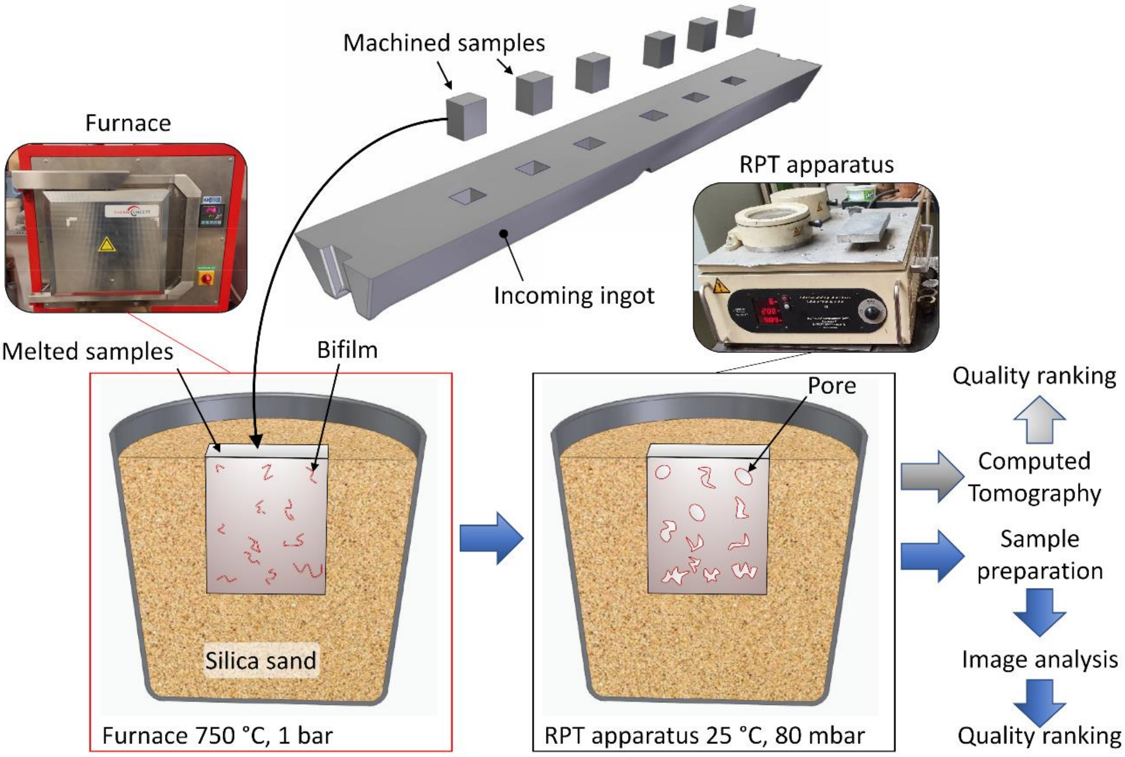

Figure 1 The scheme of the quality assessment of the ingot material

The reduced pressure test (RPT) is a valuable tool for liquid metal quality assessment, being able to reveal the presence of bifilms by utilizing the phenomenon of bifilm-initiated pore formation [6-9]. For this reason, a modified reduced pressure test, which is based on the work of Fox and Campbell [5] was used during our study for the quality evaluation of different ingot materials. The method itself consists of remelting alloy samples machined out of the incoming ingot material and allowing the samples to solidify in the vacuum chamber of the RPT apparatus at 80 mbar pressure (Figure 1). During melting and solidification, the specimen is supported in a steel cup containing silica sand. After the solidification of the specimen, the bifilm quantity can be evaluated by the means of computed tomography or image analysis of the cross-section of the specimens. Pore volume fraction, number density, specific pore surface area (pore area divided with sample volume), and Bifilm Index parameters can be evaluated and used for the evaluation of charge material quality. The sample geometry must be selected in a way that provides a similar solidification rate as in the case of traditional RPT samples. For this reason, solidification simulations were executed with different geometries and the one with the solidification rate closest to the simulated RPT samples' was selected.

The proposed ingot quality assessment technique was tested on primary aluminum alloy ingots produced with different technologies. The results were compared with the melt quality assessment of the as-melted batches made from the ingots. Based on the results, the recommended procedure for the analysis of ingot material quality is presented.

ACKNOWLEDGMENTS

Supported by the ÚNKP-22-3 New National Excellence Program of the Ministry for Culture and Innovation from the source of the National Research, Development and Innovation Fund.

REFERENCES

[1] Campbell, J. (2012), *Stop Pouring, Start Casting*. International Journal of Metalcasting, 6, 7–18.
[2] Campbell, J. (2004), *Castings Practice-The 10 Rules of Castings*. Elsevier Butterworth-Heinemann
[3] Erzi, E., Gürsoy, Ö., Yüksel, C., Colak, M., Dispinar, D. (2019), *Determination of Acceptable Quality Limit for Casting of A356 Aluminium Alloy: Supplier's Quality Index (SQI)*. Metals, 9, 957.
[4] Erzi, E. and Tiryakioğlu, M. (2020), *A Simple Procedure to Determine Incoming Quality of Aluminum Alloy Ingots and Its Application to A356 Alloy Ingots*. International Journal of Metalcasting, 14, 999–1004.
[5] Fox, S. and Campbell, J. (2002), *Liquid Metal Quality*. International Journal of Cast Metals Research, 14, 335–340.
[6] Fox, S. and Campbell, J. (2000), *Visualisation of Oxide Film Defects During Solidification of Aluminium Alloys*. Scripta Materialia, 43, 881–886.
[7] Dispinar, D. and Campbell, J. (2004), *Critical Assessment of Reduced Pressure Rest. Part 1: Porosity Phenomena*. International Journal of Cast Metals Research, 17, 280–286.
[8] Dispinar, D. and Campbell, J. (2004), *Critical Assessment of Reduced Pressure Test. Part 2: Quantification*. International Journal of Cast Metals Research, 17, 287–294.
[9] Gyarmati, G., Fegyverneki, G., Mende, T., Tokár, M. (2019), *Characterization of the Double Oxide Film Content of Liquid Aluminum Alloys by Computed Tomography*. Materials Characterization, 157, 109925.

NUMERICAL MODELLING AND SIMULATION OF SHEET METAL FORMING PROCESS

HABBACHI Marwen
Faculty of Mechanical Engineering and Informatics, University of Miskolc, Hungary
E-mail : marwen.habbachi@gmail.com

Keywords: Modelling and simulation, friction effect, mesh optimization, Sheet metal forming, Stainless steel

Simulation and modelling of sheet metal forming process are well common today in different industries (automotive, aerospace) and several research centers regarding its huge impact for both on production and reliability of the lifecycle of the equipment, and the quality of the product. However, to obtain the best configuration possible with the inputs parameters to achieve high level of production and increasing the durability of the tools needs some extra methods for the optimization for this problem using mostly finite element method cooperated with iterative algorithms based on Artificial Neural Network (ANN) [1]. Whereas this research is focused on modelling of stamping process of stainless steel AISI 304 to investigate to formability of the material, and studying the influence of the friction factor on the quality of the product as well the energy required for each set configuration.

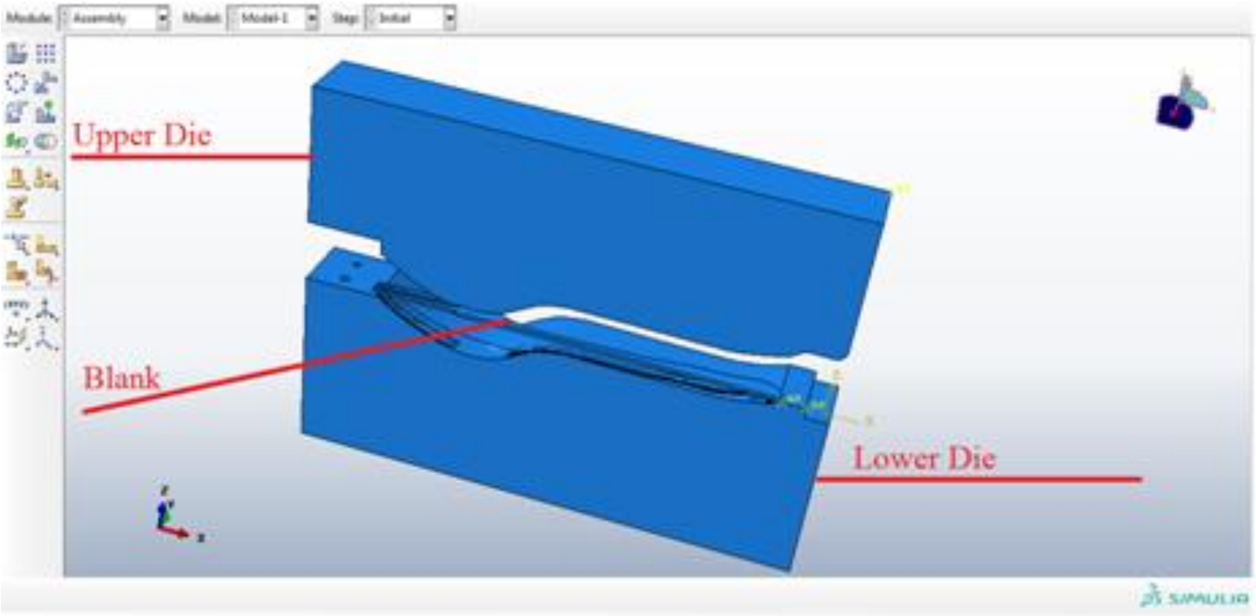
Module: Assembly
Model: Model-1
Step: Initial

Figure 1 Symmetric modelling of stamping process of stainless steel AISI 304

NUMERICAL MODELLING SETUP

The blank material is stainless steel AISI 304 It is an austenitic stainless steel composed of at least 18% chromium and 8% of nickel. It has the properties of being weldable and ductile. Its Young's modulus is E=200 GPa and its Poisson's ratio is ϑ=0.29. Several hardening laws have been tested and Ludwik's law seems the best suited to describe the behavior of AISI 304 by linking the flow stress σy to the plastic deformation εp [1]. This law is written in the form:

$$\sigma_y = \sigma_e + K.\varepsilon_p^n$$

Where σ_e , K and n are intrinsic characteristic related to material, they have the values defined in the Table 1.

Table 1: Hardening Parameters of AISI 304

Parameter	Σe	K	n
Value	197.3 (MPa)	1340.6 (MPa)	0.64

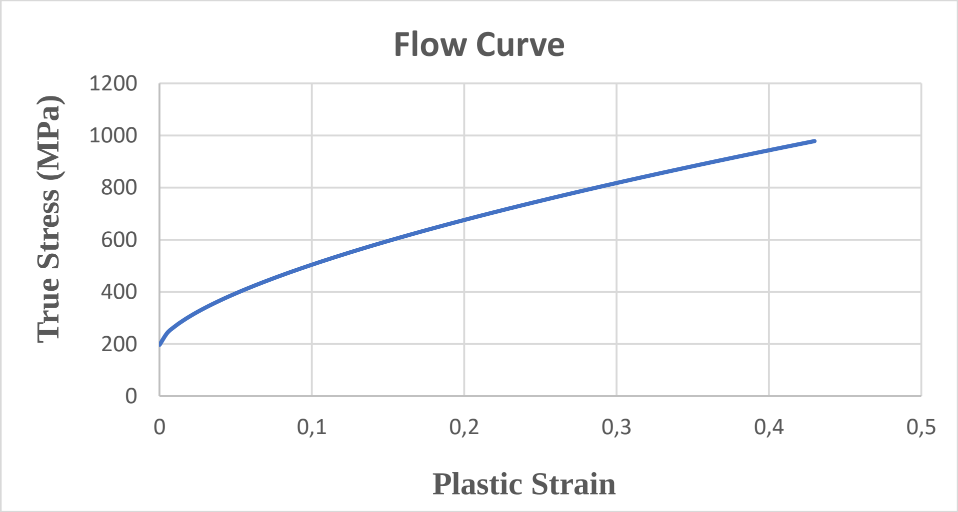

Figure 2 Flow Curve of AISI 304

Whereas, the blank is modeled as a deformed body, the other parts (Upper Die, Lower Die) are modeled as a rigid body to faster the calculation.
Since our model is symmetric, the half of the model was carried out in the simulation in order to decrease the time of calculation.
The calculation was done using Abaqus software.

RESULTS

Distribution in the deformed body has shown in Figure 3.

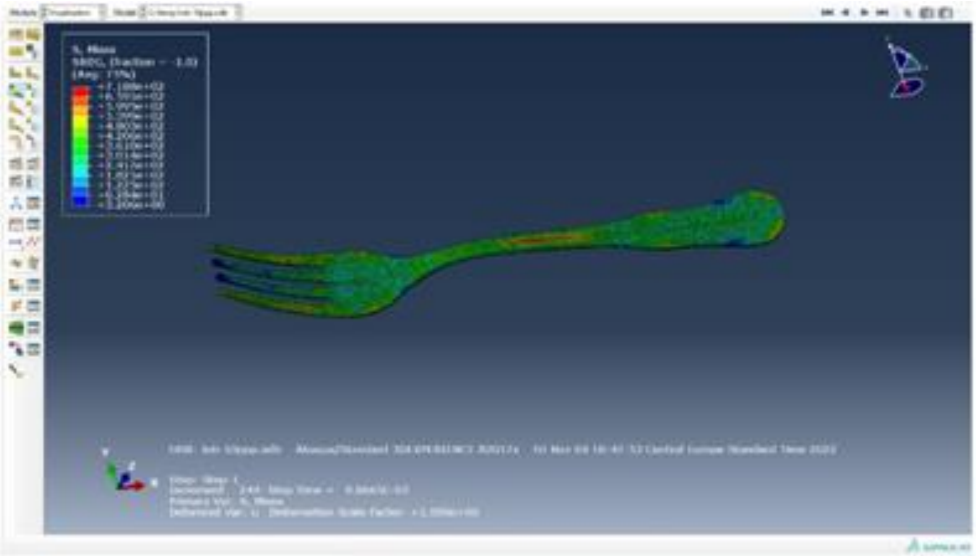

Figure 3: Von Mises Stress distribution in the deformed body

REFERENCES

[1] Wenqiong Zhang and Dongwei Wang, Optimization of Sheet Metal Forming Process.
[2] Parameters by Artificial Neural Network and Orthogonal Test Method, International Conference on Electrical, Mechanical and Industrial Engineering (ICEMIE 2016).
[3] Mohamed Azouazi, Modélisation et optimisation numérique de l’emboutissage de pièces de précision en tôlerie fine » ; thèse.

ULTRASONIC POWDER ATOMISATION FOR ADDITIVE MANUFACTURING

HALÁPI Dávid, VARGA László
Faculty of Materials and Chemical Engineering, University of Miskolc, Hungary
E-mail: ontdavid@uni-miskolc.hu , laszlo.varga@uni-miskolc.hu

Keywords: Ultrasonic atomisation, Atomisation, Powder, Metal powder, Additive manufacturing.

Ultrasonic atomization is used to obtain fine metallic powders to be used further in additive manufacturing. In this article, a metal powder production technology based on the ultrasonic sputtering method is presented, where the ultrasound frequency is 35 kHz. The medium particle size distribution of the metal powder that can be produced by the process based on this technology is 45-63 microns. The raw material is melted with an electric arc, which is pulverized with the help of ultrasound. Ultrasonic atomization methods are based on the capillary wave hypothesis. The produced metal powder particles may show differences in their tissue structure as a result of the different technologies. After atomization, the composition of the material does not change, as the entire process takes place in an inert atmosphere.

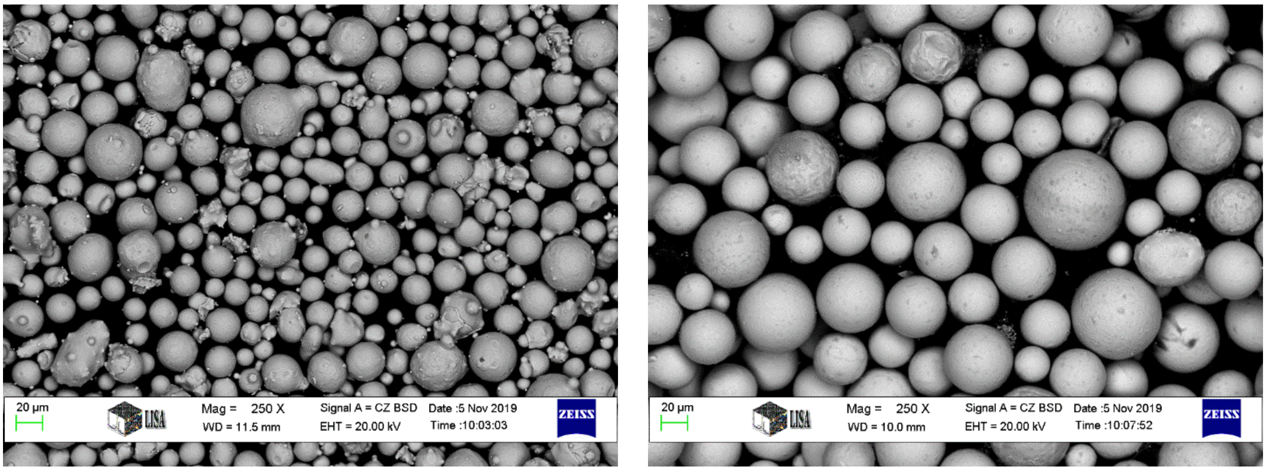

Sample_1: 17-4PH material

Sample_2: 1.4551 material

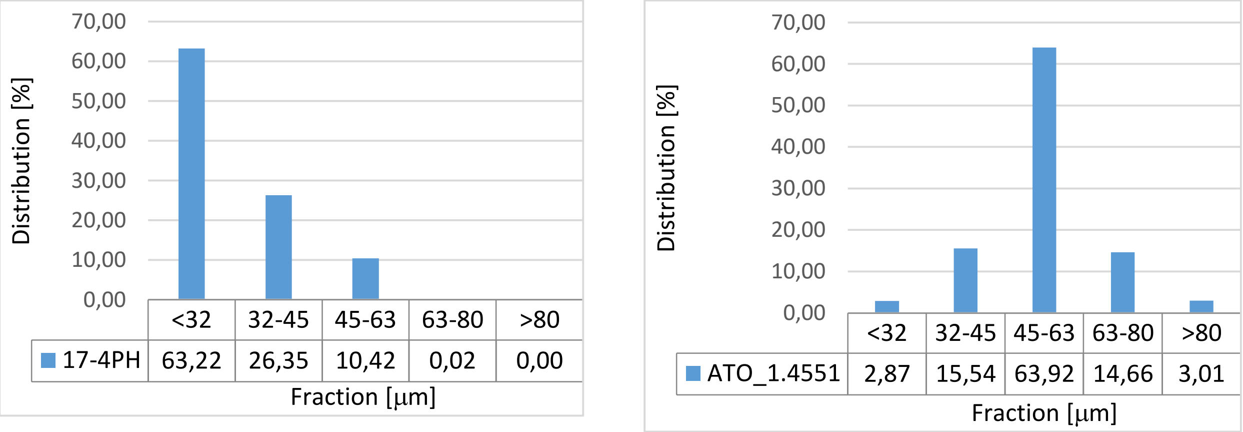

Figure 1 Different types of metal powder material sieve distributions

Different powder production technologies lead to powders of different quality, and their examination is extremely important in the field of 3D metal printing. Metal powder of the right size, shape and density is essential for printing, because these particles will be connected (fused, sintered) in the printing process.

The left side of the first figure shows the SEM image of a 17-4PH steel powder made by gas atomization and below it the grain size distribution, while the right side shows the grain size distribution and shape of a 1.4551 metal powder made by ultrasonic atomization.

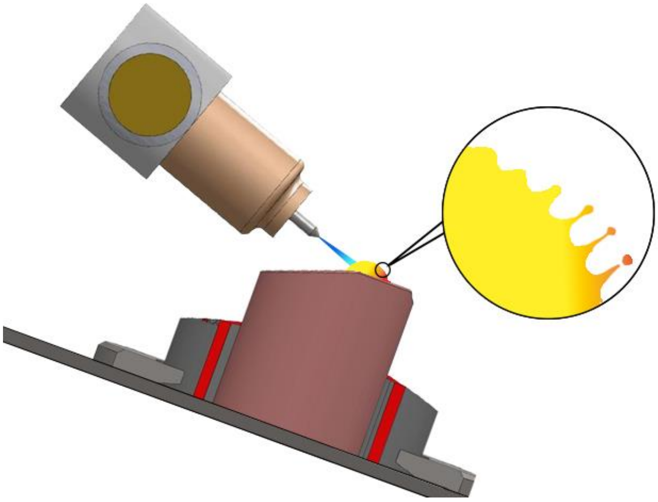

Figure 1 Schematic diagram of metal melting in ATO ultrasonic equipment

During the atomization process, capillary waves are formed on the surface of the liquid, the wavelength of which depends on the magnitude of the frequency, the energy distribution and the physico-chemical properties of the liquid. The most important factor is the density and surface tension of the liquid at the liquid-air interface. If the liquid begins to oscillate due to the vibration, the peaks of the capillary waves separate as droplets.

REFERENCES

[1] R. J. Lang, “Ultrasonic Atomization of Liquids,” Acustica, vol. 341, no. 1954, pp. 28–30, 1962.
[2] “The instability of liquid surfaces when accelerated in a direction perpendicular to their planes. I,” Proc. R. Soc. London. Ser. A. Math. Phys. Sci., vol. 201, no. 1065, pp. 192–196, Mar. 1950, doi: 10.1098/rspa.1950.0052.
[3] D. Sindayihebura, M. Dobre, and L. Bolle, “Experimental study of thin liquid film ultrasonic atomization,” … Exp. Heat pp. 1–7, 1997, [Online]. Available: http://sites.uclouvain.be/term/recherche/ultrasonique/art0197.pdf.
[4] J.W.S. Rayleigh, “The Theory of Sound (reprinted),” vol. 34, p. 1052, 1945, doi: 10.1017/CBO9781107415324.004.
[5] R. Rajan and A. B. Pandit, “Correlations to predict droplet size in ultrasonic atomisation,” Ultrasonics, vol. 39, no. 4, 2001, doi: 10.1016/S0041-624X(01)00054-3
[6] S. Alavi and S. Harimkar, “Ultrasonic vibration-assisted laser atomization of stainless steel,” *Powder Technol.*, vol. 321, 2017, doi: 10.1016/j.powtec.2017.08.007.
[7] Ł. Żrodowski *et al.*, “Novel cold crucible ultrasonic atomization powder production method for 3d printing,” *Materials (Basel).*, vol. 14, no. 10, 2021, doi: 10.3390/ma14102541.
[8] J. A. Slotwinski, E. J. Garboczi, P. E. Stutzman, C. F. Ferraris, S. S. Watson, and M. A. Peltz, “Characterization of metal powders used for additive manufacturing,” *J. Res. Natl. Inst. Stand. Technol.*, vol. 119, pp. 460–493, 2014, doi: 10.6028/jres.119.018.

PREDICTION OF ENERGY EFFICIENCY OF A SOLAR AIR COLLECTOR USING ARTIFICIAL NEURAL NETWORK TECHNIQUE

[1]HASAN Mustafa, [2]HRICZÓ Krisztián
[1]Faculty of Mechanical Engineering and Informatics, University of Miskolc, Hungary
E-mail: mustafa.hasan@stu.edu.iq, hasan.mustafa.moayad@student.uni-miskolc.hu
[2]Institute of Mathematics , Faculty of Mechanical Engineering and Informatics, University of Miskolc, Hungary
E-mail: mathk@uni-miskolc.hu

Keywords: solar air collector, artificial neural network, multi-layer perceptron, Levenberg-Marquardt algorithm.

Solar air collector (SAC) is a most commonly used solar energy system. It absorbs incident solar radiation, converts it into thermal energy, and releases this energy into circulating air. SACs are main components in many engineering applications, such as space heating and crop drying [1]. Various researchers have conducted experimental and analytical studies to improve the thermal performance of SAC [2]. These studies require a lot of time and are comparatively expensive. Therefore, soft computing techniques can be used to avoid these problems. Artificial neural network (ANN) technique is used to predict and optimize the performance of SAC[3]. İn recent years, ANN has becom increasingly popular in numerous engineering applications and has been used by many researchers in many fields [4]. The structure and behavior of this technique resemble the human nervous system. In general, the structure of ANN cosists of three layers, namely an input layer, a hidden layer, and an output layer. This network structure is the most common model and is called multi-layer perceptron (MLP). Each layer has a certain number of small, individual, and highly interconnected processing elements called neurons. ANN operates like a black box model and can predict the desired output of the system with limited training data. There are numerous algorithms for learning neural network models. Out of these algorithms, LM is the most popular due to its fast computing and minimum error rate [5].

The aim of this research is to predict the energy efficiency of a V- corrugated solar air collector using the actual weather data of Miskolc city, Hungary with the help of ANN. Six input parameters such as date, time, solar intensity, ambient temperature, mean plate temperature and air outlet temperature are used in the input layer. Energy efficiency is used as output parameter in the output layer. A total of 112 data samples are used for prediction, of which, 70% are used for training, 15% for validation, and the remaining 15% for testing the model. The number of neurons in the hidden layer is determined by trial and error. However, 2 to 14 neurons were examined. The lowest mean square error (MSE) value and the highest correlation coefficient (R) value indicate the optimal neuron model. From the statistical analysis, the lowest value of MSE for training, validation, and testing is 1.23E-04, 1.518E-04, and 6.33E-04, respectively, and the highest value of R for training, validation, and testing were 0.99917, 0.99936, and 0.99468, respectively. These values were found for a number of 3 neurons compared with the values of other neurons. Thus, the 6-3-1 structure is the optimal neuron model. The regression plot for this structure is shown in Figure 1.

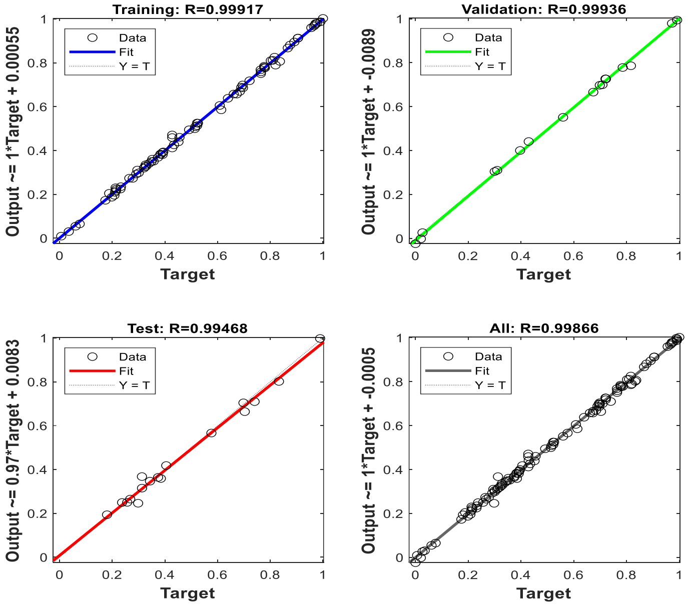

Figure 1 Regression plot of 6-3-1structure

The best validation performance occurred in epoch 87, where the MSE during validation was 0.0001518. in addtion, the training process was terminated in epoch 93 because the minimum gradient error was reached.

The prediction accuracy of ANN is also observed from the histogram error graph (see Fig. 2). It can be observed that most of the errors are near the 0 point error line. Therefore, it can be concluded that the neural structure 6-3-1 with LM learning algorithm is the optimal model for accurately predicting the efficiency of SAC.

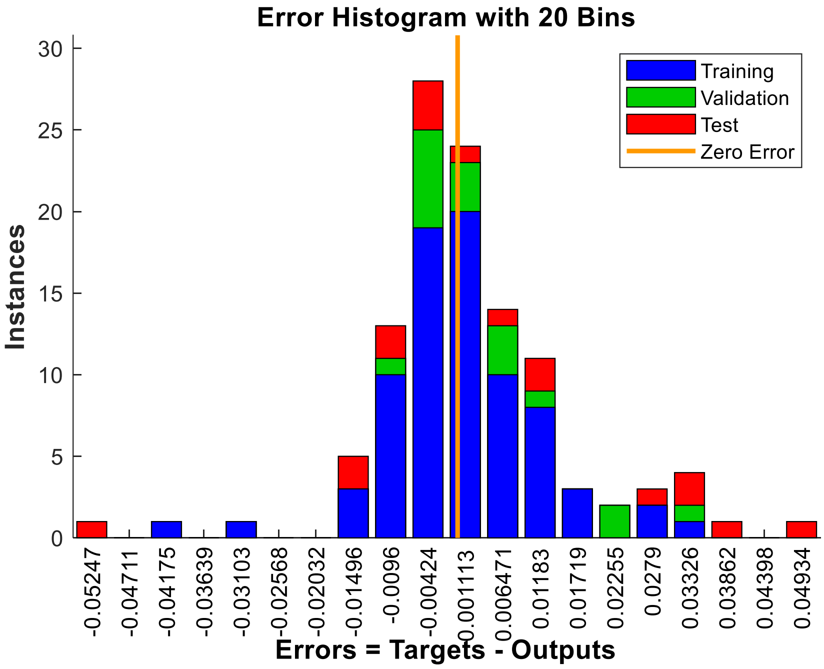

Figure 2 Error distribution graph

REFERENCES

[1] Hasan, M.M., Hriczó, K. (2023). A Literature Review of a Dual-Purpose Solar Collector. Vehicle and Automotive Engineering 4. VAE 2022. Lecture Notes in Mechanical Engineering. Springer, Cham. https://doi.org/10.1007/978-3-031-15211-5_26.

[2] Caner, M., Gedik, E., Keçebas, A. (2011). Investigation on thermal performance calculation of two type solar air collectors using artificial neural network. Expert Syst Appl, 38, 1668–1674.

[3] Ghritlahre, H.K., Prasad, R.K., (2018a). Application of ANN technique to predict the performance of solar collector systems - a review. Renew. Sustain. Energy Rev., 84, 75-88.

[4] Ghritlahre, H.K., Chandrakar, P., Ahmad, A. (2021). A comprehensive review on performance prediction of solar air heaters using artificial neural network. Annals of Data Science, 8 (3), 405-449.

[5] Benli, H., (2013). Determination of thermal performance calculation of two different types solar air collectors with the use of artificial neural networks. Int. J. Heat Mass Tran., 60, 1-7.

DIMENSIONAL ANALYSIS OF MIXING POWER REQUIREMENT IN AGITATED DRUM

HORVÁTH Dániel, POÓS Tibor
Department of Building Services and Process Engineering, Faculty of Mechanical Engineering, Budapest University of Technology and Economics, Hungary
E-mail: horvath.daniel@gpk.bme.hu , poos.tibor@gpk.bme.hu

Keywords: mixing power requirement, dimensional analysis, agitated drum.

In industry, mixing is a common operation. Mixing granular materials can be done for several purposes: e.g., homogenisation or segregation of the granular materials, but also during coating or drying. Different designs, layouts, and operating parameters are available depending on the mixing purpose and the mixed materials. The apparatus requires sizing of the electric motor power that performs the mixing. Underestimating the power of the mixing motor will result in the apparatus being unable to perform the mixing operation, and overestimating it by a significant amount may result in unnecessary additional investment and operating costs. The mixing power requirement depends on the quality, physical properties and quantity of the material to be mixed, as well as the geometry of the mixing apparatus.

The analysis of the literature shows that researchers have carried out measurements and simulations of mixing power requirements, but there are few literature equations ([1]–[4]) available for the determination by calculation. These equations differ in terms of equation form, range of validity, type of apparatus and mixed materials. *Table 1* summarises the literature equations.

*Table 1. M*ixing power equations in the literature for mixing granular materials.

No.	Ref.	Equation	Test facility	Material	Validity range
1	[1]	Experimental: $P\ =\ 1.03\ (\rho_b\mu_bV_IL_Inlg)^{0.93}$ Dimensional analysis: $\frac{P}{\rho_b{D_o}^3n^5}=K_p\left(\frac{\rho_b{D_o}^4n^2}{F_c}\right)^{-1}$ $K_p\ =1.884l+0.324$	Segmented curved-ribbon impeller	corn scratch and icing sugar	$0.25\frac{1}{s}\leq n\leq 1.67\frac{1}{s}$ $0.08\leq l\leq 0.58$
2	[2]	Experimental: $P\ =\ 0.21\ \rho_b\mu_bV_IL_Inlg$ Dimensional analysis: $\frac{P}{\rho_b{D_o}^3n^5}=K_p\left(\frac{\rho_b{D_o}^4n^2}{F_c}\right)^{-1}$ $K_p\ =0.267l+4.261$	horizontal helical double-ribbon impeller	corn scratch and icing sugar	$0.25\frac{1}{s}\leq n\leq 1.67\frac{1}{s}$ $0.08\leq l\leq 0.50$
3	[4]	$P=0.383\cdot 10^{-6}LD^{0.351}{\alpha_{AoR}}^{1.293}(n\rho_b)^{0.117}\left(\frac{m}{\beta}\right)^{0.883}$	rotary kiln	$\rho_b\ =1200\frac{kg}{m^3}$ and $1300\frac{kg}{m^3}$	$0\leq l\leq 0.15$ $25°\leq\alpha_{AoR}\leq 50°$
4	[3]	Double helical ribbon impeller: $P=114.3\left(\frac{H}{D}\right)^{1.19}n^{1.085}$ Pitched blade ribbon impeller: $P=160.1\left(\frac{H}{D}\right)^{1.553}n^{1.106}$	stirred tank	glass particles	$0.5\frac{1}{s}\leq n\leq 1\frac{1}{s}$ $0.633\leq\frac{H}{D}\leq 0.739$

The literature equations were created by fitting functions to measured data ([1]–[3]), by mechanical derivations [4] or by dimensional analysis ([1], [2]). For mixing element installations with horizontal layouts, rows 1 and 2 of *Table 1* summarise the equations found in the literature. The equations include the geometric dimensions $(V_I;L_I;D_o)$ specific to the apparatus, operating parameters $(n;l;g)$ and some material properties of the mixed materials $(\rho_b;\mu_b;F_c)$. Their range of validity is given by the range of loading factor (l) and rotational speed (n) tested for the different mixed materials. Row 3 of *Table 1* summarises the case where the mixing is performed by the rotating drum rather than by rotating mixing elements. The literature equation considers only the bulk density of the material (ρ_b), the mass of the material (m) mixed in the drum and the angle of repose (α_{AoR}) as material specific parameters. In addition, it includes some geometric parameters of the rotating drum $(L;D;\theta;\beta)$ and the rotational speed (n). The equation is validated at two bulk densities and the range of validity is given by a range of loading factor and a range of repose angle (α_{AoR}). An equation for a vertical layout of mixing apparatus was also created for two types of mixing elements and is presented in *Table 1*, row 4. The equation and the range of validity are given by two parameters: the ratio of the diameter of the tank (D) to the height of the bulk in the tank (H) and the rotational speed.

The literature mixing power equations listed in *Table 1* are not applicable to an agitated drum. Thus, one of the objectives was to collect parameters influencing the mixing power requirement. Another objective was to create an equation using dimensional analysis which is able to describe the mixing power requirement in the agitated drum shown in *Figure 1*.

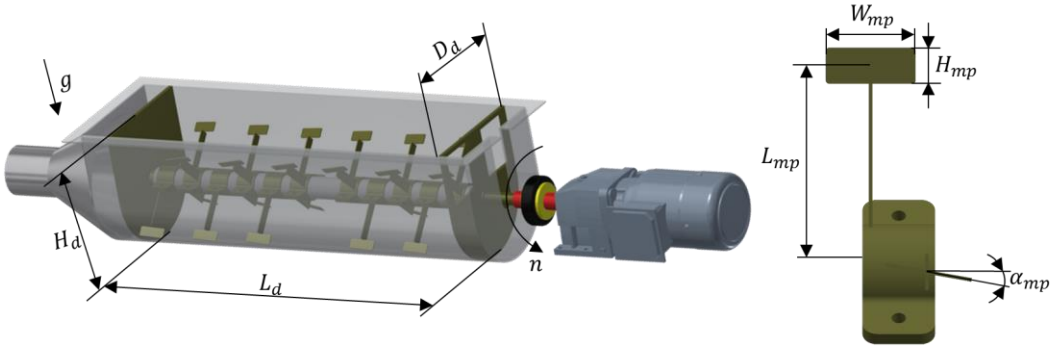

Figure 1. 3D model of the mixing drum on the left and the mixing paddle on the right with the dimensions. (L_d: drum length, D_d: drum width, H_d: drum height, W_{mp}: mixing paddle width, H_{mp}: mixing paddle height, α_{mp}: mixing paddle inclination angle, L_{mp}: mixing paddle force lever, n: rotational speed, g: gravity)

Based on the literature, 17 pcs parameters influencing the mixing power requirement were collected. These were the parameters describing the geometry of the mixing drum (drum length, drum width, drum height, mixing paddle width, mixing paddle height, mixing paddle inclination angle, mixing paddle force lever, number of mixing paddles, apparatus wall friction coefficient), parameters specific to the mixed material (typical particle size, bulk density, bulk friction coefficient, static angle of repose, bulk cohesive force) and operating parameters (drum loading factor, rotational speed, gravity). Then, using dimensional analysis, the equation of the mixing Power number for the agitated drum was created. To determine the unknown exponents in the equation, laboratory measurements were performed with air-dry hulled millet. Using the measured data and a nonlinear solver, and based on literature data, the unknown exponents were determined. The created Power number equation is as follows:

$$N_{P,pred} = 43.4 l^{1.04} N_C^{-1} {Fr_M}'^{1/6}\ .$$

The l in the equation denotes the drum loading factor, N_C the dimensionless Cohesion number and Fr_M the mixing Froude number. Multiplier 43.4 contains the parameters that can be taken as constant, i.e. the geometric dimensions of the apparatus and the unchanged parameters specific to the granular material. The mixing power requirement can be determined from the Power number equation:

$$P_{pred} = N_{P,pred} {L_{mp}}^5 n^3 \rho_b .$$

ACKNOWLEDGMENTS

This paper was supported by Gedeon Richter's Talentum Foundation (H-1103 Budapest, Gyömrői str. 19-21, Hungary) and the Hungarian Scientific Research Fund (NKFIH FK-142204).

REFERENCES

[1] I. Gijón-Arreortúa and A. Tecante, 'Mixing Performance of a Curved-Ribbon Impeller during Blending of Food Powders', *Chem. Eng. Technol.*, vol. 38, no. 4, pp. 734–740, 2015, doi: 10.1002/ceat.201400682.

[2] I. Gijón-Arreortúa and A. Tecante, 'Mixing time and power consumption during blending of cohesive food powders with a horizontal helical double-ribbon impeller', *J. Food Eng.*, vol. 149, pp. 144–152, Mar. 2015, doi: 10.1016/j.jfoodeng.2014.10.013.

[3] Y. Bao, Y. Lu, Z. Cai, and Z. Gao, 'Effects of rotational speed and fill level on particle mixing in a stirred tank with different impellers', *Chin. J. Chem. Eng.*, vol. 26, no. 6, pp. 1383–1391, 0 2018, doi: 10.1016/j.cjche.2017.11.010.

[4] X. Liu, X. Xu, W. Wu, F. Herz, and E. Specht, 'A simplified model to calculate the power draw for material movement in industrial rotary kilns', *Powder Technol.*, vol. 301, pp. 1294–1298, Nov. 2016, doi: 10.1016/j.powtec.2016.08.005.

TRANSFORMATION OF AN INTERNAL COMBUSTION ENGINE VEHICLE TO AN AUTONOMOUS ONE THROUGH MODULAR SYSTEM DESIGN

HUNYADY Gergely, FODOR Dénes
Széchenyi István University, Hungary
E-mail: hunyady.gergely@hallgato.sze.hu , fodor.denes@ga.sze.hu

Keywords: autonomous vehicle; modular system design; internal combustion engine; robustness;

Recent vehicle development concepts are focusing on functionalities instead of components, therefore new solutions are required to define the architecture of systems which are becoming more and more complex. This is especially true for driverless vehicles, for which high quality requirements are combined with the need for reliable, easily maintainable solutions. One of the most applied solutions for handling this complex task is to define each functionality as a module and therefore narrow down the system concept for blocks with inputs and outputs combined with the related requirements. This also facilitates the application of V-model in systems engineering regarding the testing and validation of functionalities. Defining the system on a high-level as simple as possible is inevitable for defining lower level requirements. This solution was also applied for designing electric driverless car’s mostly from the beginning, but one should also consider the configuration of motors due to the difference in control algorithm for an electric drive with 1, 2 or 4 motors considering also the exact placement (eg. drive shaft or wheel-hub configuration). Richard Matthaei and Markus Maurer [2] already developed a top-down approach with three-level design based on functional requirements to manage the high complexity of environment modeling based on the system architectures of the DARPA Urban Challenges. They made high efforts defining the functional parts of “perception” with the focus of application independence which in these terms means that no platform specific requirements are included for e.g. cruise control.

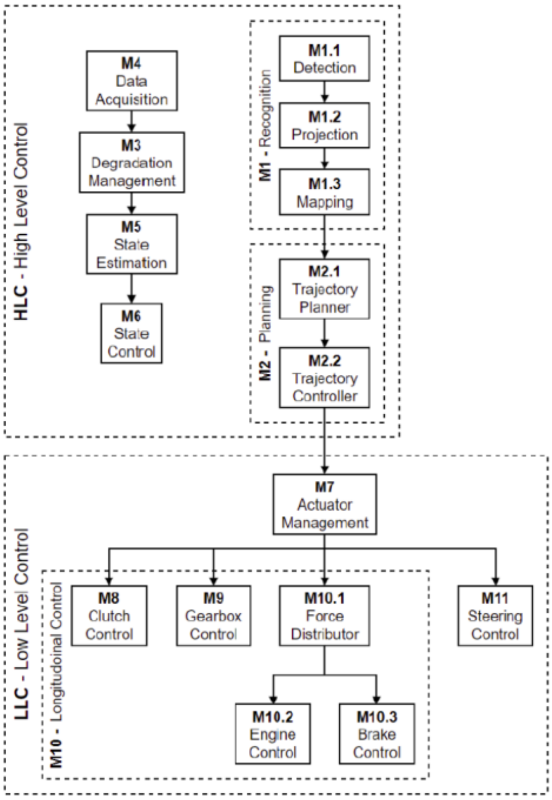

Figure 1: Separation of High-Level and Low-Level functions with modular design

The suggested solution in this article replaces the three-level design from [2] with a two-level one, named according to their level of abstraction: high- and low-level control. This separation was done in order to differentiate between vehicle-independent (e.g. mapping) and vehicle-dependent (e.g. actuation) functionalities. Following the same top-down approach, beginning from environment recognition and mapping functionalities, the two levels of abstraction were separated at the vehicle control targets based on the predecessor thesis [1]. This means the high-level control is responsible for perception and route calculation alongside with state control functionalities and low-level control is responsible for platform dependent functionalities like steering and brake control based on the calculated targets like yaw rate.

Module	Input	Output	EV	CV
M1 - Recognition	**Camera image**	**Reference lines**	**x**	**x**
M1.1 - Detection	Camera image	Cone image coordinates	x	x
M1.2 - Projection	Cone image coordinates	Cone xy positions	x	x
M1.3 - Mapping	Cone xy positions	Reference lines	x	x
M2 - Planning	**Reference lines**	**High-level commands**	**x**	**x**
M2.1 - Trajectory planner	Reference lines	Car trajectory	x	x
M2.2 - Trajectory controller	Car trajectory	High-level commands	x	x
M3 - Data acquisition	**Signals, commands**	**Component data**	**x**	**x**
M4 - Degradation management	**Component data**	**Component state**	**x**	**x**
M5 - State estimation	**Component state**	**Vehicle state**	**x**	**x**
M6 - State control	**Vehicle state**	**State machine commands**	**x**	**x**
M7 - Actuator management	**High-level commands**	**Low-level commands**	**x**	**x**
M8 - Clutch control	**Clutch target position**	**Clutch actual position**		**x**
M9 - Gearbox control	**Gear target**	**Actual gear**		**x**
M10 - Longitudinal control	**Acceleration target**	**Vehicle speed**	**x**	**x**
M10.1 - Force distributor	Acceleration target	Brake and motor torque	x	x
M10.2 - Motor control	Motor torque	Car acceleration	x	x
M10.3 - Brake control	Brake torque	Car braking	x	x
M1 - Steering control	**Steering angle target**	**Actual steering angle**	**x**	**x**

The goal besides differentiating between vehicle dependent and independent functionalities was to create an universal architecture which can handle both conventional drivetrain with internal combustion engine and electric ones. The key role in this development is to discretize the main functionalities which are drivetrain dependent and the ones which are not. As an example, actuator management is needed to generate reference values for steering control and gearbox control as well if the drivetrain has an internal combustion engine. For electric drivetrains, steering control and force distributor target calculation is sufficient but with different motor control setup. The aim of this article is to define the modules of a driverless car with internal combustion engine with respect to compatibility with electric drivetrain and capability to drive the car both in manual, and in driverless mode without modification.

ACKNOWLEDGMENTS

This work has been supported by Project no. TKP2021-NKTA-48 which has been implemented with the support provided by the Ministry of Technology and Industry of Hungary from the National Research, Development and Innovation Fund, financed under the TKP2021-NKTA funding scheme.

REFERENCES

[1] Gergely H. (2022), *Longitudinal Control for Autonomous Racing with Internal Combustion Engine*. Master's thesis in Vehicle Engineering, 29-31.
[2] Richard M. and Markus M. (2015), *Autonomous driving – a top-down-approach*. Automatisierungstechnik 2015; 63(3): 155–167
[3] Behrooz M., David C. (2012), *Vehicle Powertrain Systems*, Wiley
[4] Rolf I. (2014), *Engine Modeling and Control*. Springer.
[5] Rajesh R. (2006), *Longitudinal Vehicle Dynamics*, Springer.
[6] Craig C. (1997), *Autonomous Speed Control for Conventional Vehicles*
[7] Michal P. (2017), *Autonomous vehicle with internal combustion drive based on the homogeneous charge compression ignition technology*

EFFECTS OF ELEVATED TEMPERATURE ON THE MECHANICAL BEHAVIOR OF ACSR TYPE CONDUCTORS

JAWABREH Anas, SEPSI Máté, BARKÓCZY Péter
Metal Forming and Nanotechnology, Institute of Physical Metallurgy, Faculty of Materials and Chemical Engineering, University of Miskolc, Hungary
E-mail: anasjawabreh0012@gmail.com , femsepsi@uni-miskolc.hu , fembarki@uni-miskolc.hu

Keywords: High voltage, Conductor, Aluminium, Heat resistant

The operating temperature of the standard steel-reinforced aluminum conductors (ACSR) of high-voltage transmission systems is limited to 80°C due to the annealing effect of the elevated temperature [1]. This means a limit in the current carrying capacity of the conductors [2]. Higher operating temperatures could mean larger capacity [3]. This is the basis of the high-temperature low sag (HTLS) conductors [4]. One basic type of HTLS conductor contains wires produced from heat-resistant aluminum alloys [5] to increase the temperature of annealing processes. This proves the larger strength of the conductor in elevated temperatures. So, the operating temperature of the HTLS conductors is larger than 80°C (150-210°C). The overloading or emergency cases can cause a larger temperature than the maximal operating temperature. The scope of the presentation is to examine and compare the changes in the mechanical behavior of different conductors.

The temperature of the conductor during operation is mainly determined by the resistivity of the aluminum wires which originates from the alloy and its state. Next to the resistivity, the environmental conditions have another important effect, where the surface conditions of the wires in the outer layer have a decisive role [6]. The stranded steel-reinforced aluminum conductors are complex structures themselves. There are complex methods for the evaluation of phase transformation in metals [7] or examining the surface or surface layers [8], but the testing of the power of complex structures usually uses simple destructive mechanical tests of samples [9]. The evaluation of these tests needs a complex interpretation. The introduced tests and comparisons follow this scheme.

Three types of steel-reinforced aluminum conductors are tested: I. ACSR 264-AL1/34-ST1A, II. AACSR 185-AL4/43-ST6C, III. AACSR 264-AT1/34-A20SA. AL1 denotes cold-drawn wires (H16) from unalloyed grade (EN AW 1370). ST1A means heavily galvanized high carbon, high strength steel wire. AL4 is the designation of stabilized alloyed aluminum wires (EN AW 6101). ST6C is the designation of the heavily galvanized ultrahigh-strength steel wires. the AT1 denotes the cold-drawn heat-resistant wires. A20SA means the aluminum-cladded steel wires, where the aluminum layer is used as a corrosion protective layer. The materials of the wires determine the strength and the resistivity of the conductors next to the construction. The standards show that the conductors’ elastic moduli mainly depend on the construction. Therefore, those constructions which have the same calculated elastic moduli are chosen.

The standards (e.g., EN 50182:2001) use the tensile testing of the wires to evaluate the mechanical properties of the conductors. For example, the rated tensile strength of the conductor is calculated from the measured tensile strength of the wires. But to evaluate the whole complex stranded structure the testing of the conductor is used. The most important mechanical property of the stranded conductors is elastic behavior. This is described well by the stress-strain test where the conductor is loaded with different stress levels for a certain time (EN 50182:2001). The result of the test is evaluated by a polynomial which contains next to the stress-strain function contains the effect of the short-term creep (Fig. 1.). This polynomial is used in the modern calculation methods of the span, sag, and clearance.

Samples of the chosen conductors are heated up by current to 230°C and held at this temperature for 3 hours. Additionally, other samples were heated up also by the current to 400°C. At this temperature, the soaking was just 0.5 hours. The tensile strength of all conductors was tested, and the rated tensile strength was calculated. The different conductors are compared after the different treatments. The comparison shows that in all cases the strength of the wires is decreased but to a different extent. This decrement in strength is due to the annealing of the aluminum wires.

Isothermal heat treatments were performed on the wires at the same temperature as a reference. Here the tensile strength was measured too. These results show the maximum extent of the strength loss due to annealing. The results can show the effect of the tempering of the conductor samples. Additionally, the microstructure of some wires from the conductor samples was also examined. Partial recrystallization was observed in some cases here, the recrystallization and the recovery together were reduced the strength of the wires. In other cases, the deformed grain structure was observed, which suggests the recovery process only which meant the annealing of the wires.

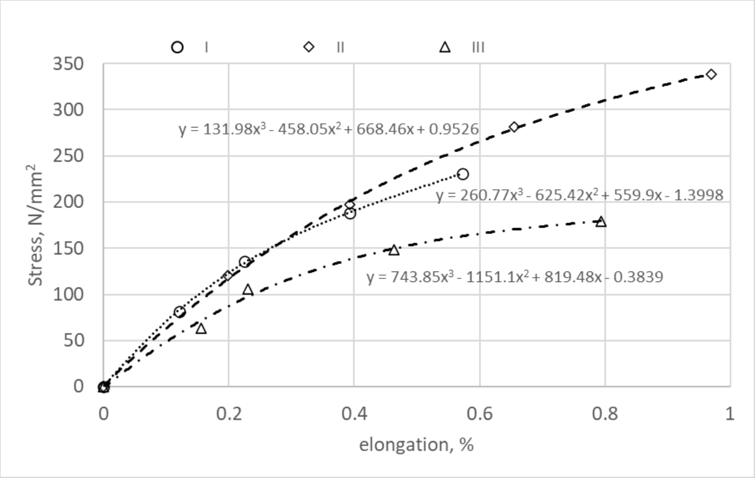

Figure 1 Stress-strain polynomials of the reference conductors without any heat treatment.

Next to the wire testing the stress-train test also was performed on the tempered conductor samples. The polynomial functions have contained the effect of tempering on the steel wires too. The comparison of the polynomials as the elastic behavior shows an interesting picture of the heat resistivity of the conductors.

Conductor type III shows the smallest extent of changes in tensile strength due to the heat-resistant aluminum alloy. The largest decrement in tensile strength was measured in the case of unalloyed wires. The same difference can be seen in the changes in the polynomials. But the changes of the polynomial of the conductor type II show an interesting result due to the high strength of the steel wires. The lecture shows the results and the comparisons in detail.

ACKNOWLEDGMENTS

M. Sepsi contributed with the professional support of the Doctoral Student Scholarship Program of the Co-operative Doctoral Program of the Ministry of Innovation and Technology financed by the National Research, Development, and Innovation Fund.

REFERENCES

[1] CTC Global: *Engineering Transmission Lines with High Capacity Low Sag ACCC Conductors*, Engineering Manual, CTC Global, 2011

[2] A. A. P. Silva, J. M. B. Bezerra: *Applicability and limitations of ampacity models for HTLS conductors*, Electric Power Systems Research, vol. 93, pp. 61-66, 2012

[3] Konstatin O. Papailiou ed.: *Overhead Lines*, Cigré Green Books, Springer, 2017

[4] J.-R. Riba, S. Bogarra, Á. Gómez-Pau, M. Moreno-Eguilaz: Uprating of transmission lines by means of HTLS conductors for a sustainable growth: Challenges, opportunities, and research needs, Renewable and Sustainable Energy Reviews, vol. 134, pp. 1-13, 2020

[5] J. D. Robson: *A new model for prediction of dispersoid precipitation in aluminium alloys containing zirconium and scandium*, Acta Materialia, vol. 52 (6), pp. 1409-1421, 2004

[6] Z. Engel, T. Wszolek: *Audible Noise of Transmission Lines Caused by the Corona Effect: Analysis, Modelling, Prediction*, Applied Acoustics, vol. 47 (2), pp. 149-163, 1996

[7] R. L. Kovács, G. Langer, Sz. Gyöngyösi, Z. Erdélyi: *A Versatile Technique for In-situ Investigation of the Effect of Thin Film Cracking on Gas Permeation of Coated Flexible Polymers*, Review of Scientific Instruments, vol. 92, pp. 1-4, 2021

[8] L. Daróczi, Sz. Gyöngyösi, L. Z. Tóth, D. L. Beke: *Effect of the martensite twin structure on the deformation induced magnetic avalanches in Ni2MnGa single crystalline samples*: Scripta Materialia vol. 114, pp. 161-164., 2016

[9] Sz. Gyöngyösi, A. Gábora, G Balogh, G. Kalácska, T. Bubonyi, T Mankovits: *Effects of Additives on the Mechanical Properties of Aluminum Foams*, Mechanisms and Machine Science vol. 109, pp. 307-313, 2022

OPTIMISATION OF METHANOL RECOVERY BY SURROGATE MODELS: INFLUENCE OF PRICES

KARAMAN Ömer Faruk, HÉGELY László, LÁNG Péter
Department of Building Service and Process Engineering, Faculty of Mechanical Engineering, Budapest University of Technology and Economics, Hungary
E-mail: karaman@edu.bme.hu , hegely.laszlo@gpk.bme.hu , lang.peter@gpk.bme.hu

Keywords: optimisation, batch distillation, simulation, surrogate model, solvent recovery.

INTRODUCTION

Batch distillation (BD) is one of the most commonly used methods to treat waste solvent mixtures. Components of these mixtures often form azeotropes, which make the separation more difficult. For BD, a dynamic optimisation problem has to be formulated and solved. A feasible path approach is often used to evaluate the objective function (OF) by solving the process model iteratively within the range of optimisation variables. However, when a flow-sheet simulator is used, the optimisation is typically carried out by an external tool utilizing an evolutionary (typically genetic) technique. These techniques require a large number of OF evaluations, which increases the computational intensity of the optimisation.
Hegely and Lang [1] investigated the use of a genetic algorithm to optimise the recovery of methanol (in a purity of 99.5 mass%) from a five-component waste solvent mixture: acetone (A, 0.07 %), methanol (B, 37.4 %), tetrahydrofuran (C, 4.89 %), water (D, 56.34 %) and toluene (E, 1.56 %). Several azeotropes are formed: A-B, B-C, B-E, C-D and D-E. C and E are removed in two fore-cuts (fc1,fc2) causing a considerable loss of B, which is obtained as main cut (mc). An after cut (ac) is also taken and recycled to decrease the loss of B and purify the residue D.
For this process, Hegely et al. [2] suggested a surrogate model-based optimisation (SMBO) technique to decrease the computational load. The evaluation of surrogate models (SMs), which are simplified models built from the inputs and outputs of rigorous models whose behavior they mirror, requires significantly less computer power. Simulations were run by a flow-sheet simulator (Chemcad) in a set of points in the space of the optimisation variables that were produced via Latin Hypercube Sampling (LHS). The ALAMO machine learning technique was then used to fit algebraic SMs to the simulation results in order to describe OF and the constraints. SQP solved the ensuing optimisation problem with ease. The simulation's outcomes were accurately reproduced by the SMs. The number of simulations was reduced from 3000 to 1000, the profit obtained by the SMBO was by 5% higher than that of Hegely and Lang [1]. The flow chart of SMBO method is as follows:

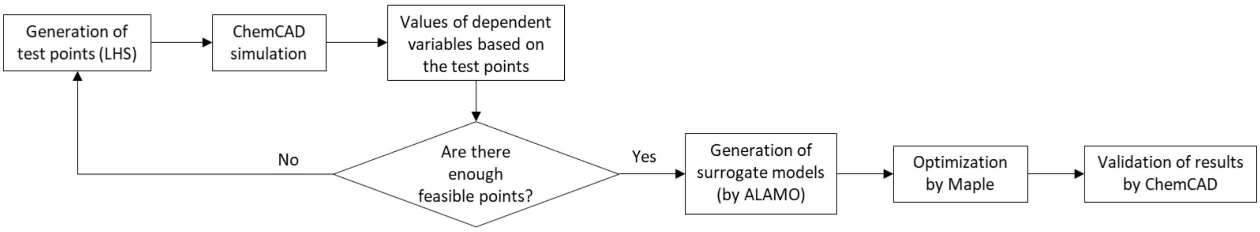

Reoptimisation for different prices of methanol (p_B) is possible with SMBO without further simulation. p_B plays a crucial role in the profitability of the process. Therefore, the goal of this work is to study the influence of the p_B on the optimal operation of the BD process.
The treatment of a batch consists of five steps. In Step 0, the column is heated with total reflux to approach steady-state conditions, which takes 360 min. At this point, the condensate contains mainly B and C, with a composition close to the azeotropic one. A first fore-cut with reflux ratio R_1 is taken in Step 1. Here, most of the C and E is removed with the considerable loss of B. This step ends when $x_{d,C}<Cr_1$ where $x_{d,C}$ is the instantaneous mass fraction of C in the distillate, and Cr_1 is the stopping criterion for Step 1. This fore-cut is incinerated. In Step 2, a second fore-cut with reflux ratio R_2 is taken. Since the pollutant concentration of the cut is still very high and there is a considerable amount of B in the second fore-cut, it is recycled to the next batch. This step ends when $x_{d,C}<Cr_2$.
Step 3 is the main cut (B product) with reflux ratio R_3. This step ends (because of the increasing $x_{d,D}$) when $x_{mc,B}<0.9952$ where $x_{mc,B}$ is the mass fraction of B in the main cut. In Step 4, an ac with R_4 is taken to eliminate B from the still residue so that it can be sent to biological treatment. The ac has a considerable B content, and it is recycled to the next batch. Taking of the cut is finished when the B content of the still residue ($x_{sr,B}$) becomes lower than 0.25%.

CALCULATION METHOD

The column contains 27 theoretical plates (including the reboiler and the total condenser) [1]. The top pressure is 1.013 bar, the total pressure drop is 0.25 bar. The volume of the charge is 25 m^3. Hold-ups: condenser: 0.45 m^3, column: 0.05 m^3/plate. Reboiler heat duty (Q_{st}=1800 MJ/h), provided by steam of 3 bar (heat of condensation: r_{st}=2263.5 MJ/t). OF is the profit of a single batch.

$$OF = p_B m_{mc} - p_{inc} m_{fc1} - p_{st} \frac{Q_{st}}{r_{st}} t$$

where: p_B: price of methanol, 0.46 US$/kg, m_{mc}: mass of the main cut, kg, p_{inc}: price of incineration, 0.21 $/kg, m_{fc1}: mass of Fore-cut 1, kg, p_{st}: price of steam, 57.6 $/t, t: duration of the whole process, h.

The optimisation problem is subject to the inequality constraints: 1: $x_{mc,B} \geq 0.9952$, 2: $x_{fc2,C}/x_{fc2,B} \leq 0.107$, 3: $x_{fc2,E}/x_{fc2,B} \leq 0.12$, where $x_{fc2,B}$, $x_{fc2,C}$ and $x_{fc2,E}$ are mass fractions of B, C and E in fc2, respectively.

Constraint 1 guarantees the required purity of the product. Constraints 2 and 3 are needed to ensure that the organic pollutants C and E are not accumulated in fc2 so that it can be recycled to the next batch. The optimisation variables are: R_1, R_2, R_3, and Cr_1, Cr_2. Influence of R_4 on OF is negligible. As an example of the SMs, model of t is:

$$t = 95.93 \cdot R_1 + 16.04 \cdot R_2 + 78.61 \cdot \ln R_2 - 0.89 \cdot e^{R_3} + 939.52 \cdot e^{Cr_1} - 3{,}59 \cdot R_1^2 + 24.95 \cdot R_3^2 - 4531 \cdot Cr_1^2$$

Reoptimisation is studied by using Maple where OF is optimised for different p_B values between 0.4 to 0.6 US$/kg. Influence of p_B on optimisation variables is studied. Model accuracy is calculated by comparing the OF value of SMs and the one obtained with simulation. (At the methanol price of 0.46 $/kg, Hegely et al. obtained: R_1: 5.68, R_2: 2.49, R_3:3.09, Cr_1: 0.2138, Cr_2: 0.0255, OF: 493 $)

RESULTS

Influence of methanol price on the OF (a) and the optimal values of operational parameters (b) is as follows:

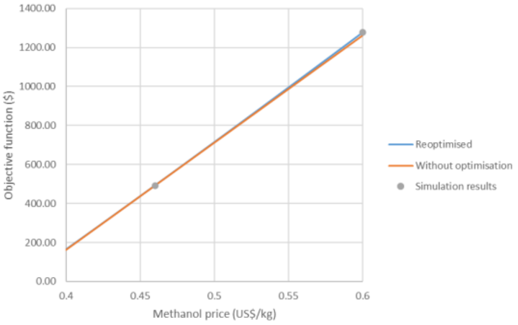

a.

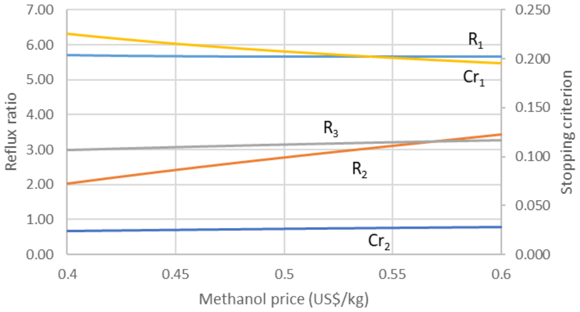

b.

On the increase of p_B, Cr_1 decreases, while R_1 hardly changes. More fc1 is taken, which increases the cost of incineration. m_{fc2} decreases. The increase in Cr_2 also contributes to the decrease of the m_{fc2}. R_3 and m_{mc} increase.

Due to the increase of m_{mc}, the profit becomes higher. OF increases from 490 to 1277 $ when p_B increases from 0.46 to 0.6 $/kg. Duration of the process increased from 2080 to 2158 min. In an extreme case (p_B=0.60 $/kg), OF obtained from SMs and simulation is compared to determine the model error which is low (1.6 $). OF is slightly underestimated by the SMs. OF is also calculated without optimisation for different p_B values. Difference between the OF obtained without and with reoptimisation is small.

CONCLUSION

Surrogate models (SMs) were used to reoptimise the batch distillation (BD) of a a five-component azeotropic solvent mixture for different methanol prices (p_B).The influence of p_B on the operational parameters (R_1, R_2, R_3, Cr_1, Cr_2) of the process was studied. Within the range studied, the increase of p_B increased the profit. More first fore-cut and less second fore-cut are taken. Duration of the process also increased. Difference between the profit obtained without and with reoptimisation is small.

ACKNOWLEDGMENTS

The research reported in this paper was supported by the National Research, Development, and Innovation Fund of Hungary under Grants TKP2021-EGA-02, FK-143059, by the János Bolyai Research Scholarship of the Hungarian Academy of Sciences, and by the ÚNKP-22-5-BME-325 New National Excellence Program of the Ministry for Culture and Innovation from the source of the National Research, Development and Innovation Fund.

REFERENCES

[1] Hegely, L. and Lang P. (2016), *Optimization of a batch extractive distillation process with recycling off-cuts.* Journal of Cleaner Production, 136, 99-110.

[2] Hegely, L., Szucs M.T., Karaman O.F., Lang P. (2022), *Optimisation of a Batch Distillation Process by Applying Surrogate Models*. Proceedings of the 12th International Conference Distillation & Absorption 2022, Paper 1264.

HEAT TRANSFER CHARACTERISTICS OF WATER-CUO NANOFLUID FLOW INSIDE 2D PIPE

[1]KHALILI NAJAFABADI Mohsen, [2]HRICZÓ Krisztián, [1]BOGNÁR Gabriella
[1]Department of Machine and Product Design, University of Miskolc, Hungary
E-mail: mohsenkhll@gmail.com, v.bognar.gabriella@uni-miskolc.hu
[2]Institute of Mathematics, University of Miskolc, Hungary
E-mail: mathk@uni-miskolc.hu

Keywords: Nanofluid, CuO, Water, Convective Heat Transfer, CFD

INTRODUCTION

The velocity distribution and heat transfer improvement in a two-dimensional channel filled with a water–CuO nanofluid are numerically studied. The nanofluid flow is assumed laminar and one-phase with Newtonian behaviour. Pure water is considered as the base fluid, and water-CuO nanofluid with four different volume fractions of CuO nanoparticles is examined. A constant heat source–sink is considered to cover the entire length of the bottom wall of the channel while the upper wall is assumed thermally insulated. The control volume technique is used to discretize the governing differential equations, and the SIMPLE algorithm is used to solve the velocity-pressure coupling. A CFD simulation is applied to nanofluid flow utilizing ANSYS FLUENT to solve the governing equations of the flow. The effects of nanoparticle volume fraction on the heat transfer, velocity profile, wall shear stress, skin friction coefficient, and Nusselt number along the channel have also been examined. The results confirm that the volume fraction of nanoparticles plays an important role in heat transfer enhancement and hydrodynamic behaviour of the flow. The results are presented in figures and tables.

The velocity distribution and heat transfer improvement of water-CuO nanofluid in a laminar 2D flow within a horizontal channel are investigated numerically in this study. The influence of the volume fraction on heat transfer, velocity, wall shear stress, skin friction coefficient, and Nusselt number have also been studied along the channel. The model is explained along with the governing equations that describe the model. The geometry generated, the mesh independency study, and the numerical solution method are presented. Finally, the results are presented.

THERMOPHYSICAL PROPERTIES OF THE BASE FLUID AND THE STUDIED NANOFLUID

As a function of the volume fraction, the thermal properties of the nanofluid are calculated. Therefore, the density, thermal capacity, viscosity, and thermal conductivity are estimated based on the concentration of nanoparticles in the base fluid [1]. thermo-physical properties for CuO-water nanofluid at different values of φ are presented in Table 1.

Table 1 Thermophysical properties CuO-water at different values of φ [2], [3]

Volume Fraction (φ)	(1%)	(2%)	(3%)	(4%)
ρ_{nf} (kg/m^3)	1053.218	1108.236	1163.254	1218.272
C_{pnf} (J/kg K)	3956.96017	3754.264391	3570.74227	3403.796118
k_{nf} (W/m K)	0.616623822	0.633557563	0.650809972	0.668390129
μ_{nf} (N s/m^2)	0.00102852	0.001054959	0.00108236	0.001110767

MODEL DESCRIPTION

The single- phase approach for solving the flow of nanofluid problem is adopted in this numerical study. In this approach the following assumptions are used:

- The nanoparticles and the base fluid (water) are to be perfectly mixed and treated as a homogenous mixture. Moreover, the fluid phase and the solid particles are assumed to be in thermal equilibrium and move with the same velocity.
- Steady, Newtonian, and incompressible fluid flow is considered.
- Thermophysical properties of the nanofluid are assumed to be dependent on the volume fraction of the nanoparticles.
- No-slip boundary condition is also considered on the walls.

RESULTS

Numerical results for the thermal boundary layers at different locations along the channel are presented. Figure 1 depicts the impact of nanoparticle volume fraction on the temperature profile for CuO-water nanofluid flow at three different cross sections (X=0.1,0.5, and 2 m) along the channel. The Y-axis shows diameter of the channel while the X-axis shows temperature. Thermal boundary layer thickness increases with an increase in the parameter φ which is nanoparticle volume fraction. Comparison of the temperature profiles for different nanofluid concentrations shows that CuO-water at 4% has the thickest thermal boundary layer. Therefore, it is observed that the nanoparticles change the flow and heat transfer characteristics and causes an increase in the thermal boundary layer. Moreover, the graph shows that the temperature near the lower wall at cross section X=0.1m is around 475K while it rises to 650K and 950K at cross sections X=0.5m and X=2m, respectively. This is due to existence of a constant heat flux at the bottom wall along the channel when the nanofluid reaches the end of the channel, it receives more heat from the lower wall. However, the increase of temperature near the upper wall along the channel length is not as rapid as that of for the lower wall since the upper wall is thermally insulated and is receiving heat only from the nanofluid flowing inside the channel.

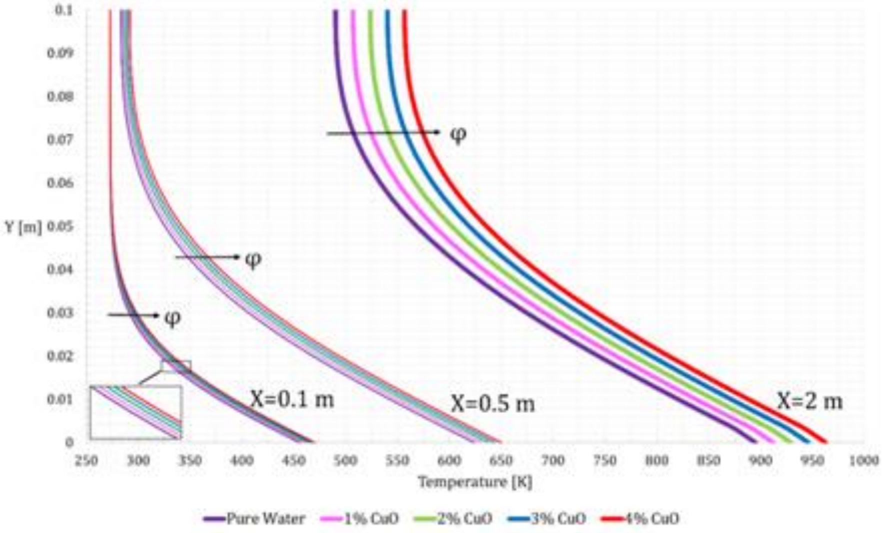

Figure 2 Temperature distribution at different cross sections for different nanoparticle volume fractions

CONCLUSIONS

Nanofluid flow within a horizontal channel was numerically investigated using CFD simulation. The influence of CuO nanoparticles on water base fluid has been highlighted in this work. It has been examined how the velocity distribution, the wall shear stress, skin friction coefficient, the temperature distribution, and Nusselt number vary with volume fraction of the nanoparticles. The maximum velocity shows an increase with increasing volume fraction. It is obtained that the temperature increased with increasing the volume fraction of CuO everywhere along the channel. Moreover, it is observed that when the volume fraction increases, the wall shear stress and skin friction coefficient, and Nusselt number along the channel increase as well. The goal is to see how the concentration of nanoparticles affects the velocity and temperature profiles of nanofluid flow in a horizontal channel. Further study is recommended in the transition and turbulent flow for the same model.

ACKNOWLEDGMENTS

This work was supported by project no. 129257 implemented with the support provided from the National Research, Development and Innovation Fund of Hungary, financed under the K_18 funding scheme.

REFERENCES

[1] Khanafer, K. and Vafai, K. (2011), *A critical synthesis of thermophysical characteristics of nanofluids.* International Journal of Heat and Mass Transfer, 54(19), 4410–4428.

[2] Xuan, Y. and Li, Q. (2000), *Heat transfer enhancement of nanofluids*. International Journal of Heat and Fluid Flow, 21(1), 58–64.

[3] Mahbubul, I. and Amalina, M. A. (2012), *Latest developments on the viscosity of nanofluids*. International Journal of Heat and Mass Transfer, 55(4), 874–885.

BUBBLE POSITION CONTROL BY PHASE-CONTROLLABLE ULTRASONIC STANDING WAVE

KLAPCSIK Kálmán
Department of Hydrodynamic Systems, Faculty of Mechanical Engineering, Budapest University of Technology and Economics, Hungary
E-mail: kklapcsik@hds.bme.hu

Keywords: acoustic cavitation, bubble dynamics, translational motion, bubble position control

The keen interest of chemistry is to utilize ultrasound in chemical reactions. Its physical background is the acoustic cavitation induced by ultrasonic irradiation. Due to the high amplitude acoustic waves, thousands of micron-sized radially pulsating bubbles are formed in the liquid domain. The collapse of the individual bubble can be strong enough to reach the temperature several thousands of degrees of Kelvin inside the bubble at the minimum radius [1]. This extremely high temperature is beneficial for various kinds of chemical reactions [2]. Despite the exhaustive research in the last decades, the biggest challenge of sonochemistry, which is to scale up the applications feasible for industrial size, is still unsolved. One of the main barriers of scalability is the attenuation of the sound wave [3] due to the high-density bubble clusters (acoustic shielding [4]). One of the possible solutions to overcome this difficulty is to control the position of bubbles in the cluster by manipulating the acoustic field. Acoustic manipulation methods provide unique contactless material handling in various applications, such as particle manipulation [5], pattern formation [6] and micro-assembly [7]. Traditionally, acoustic manipulation devices create simple standing wave patterns on a surface, chamber, or channel. In a standing wave pattern, there are trapping points (e.g., pressure antinode) or lines, where the acoustic radiation force is zero. The interplay of acoustic radiation force and drag force drives the particles to these trapping points. By transforming the force field, either by controlling the phase or intensity of the transducers or by switching between resonance modes, the trapping points can be modified; thus, the position of the particles can be controlled.

Despite its simplicity, acoustic manipulation methods have not been used to control the position of the bubbles in the clusters. The present paper aims to numerically demonstrate the possibility of bubble position control by using phase-controllable ultrasonic irradiation. Thus, a numerical model that is capable to describe the coupled radial oscillations and translational motion of the bubble is applied. The radial oscillation of the bubble is described by the Keller—Miksis equation [8]

$$\left(1-\frac{\dot{R}}{c_L}\right)R\ddot{R}+\left(1-\frac{\dot{R}}{3c_L}\right)\frac{3}{2}\dot{R}^2=\left(1+\frac{\dot{R}}{c_L}+\frac{R}{c_L}\frac{d}{dt}\right)\frac{p_L-p(x,t)}{\rho_L}+\frac{\dot{x}^2}{4},$$

where R and x are the instantaneous bubble radius and bubble position; respectively. Furthermore; $\rho_L = 998\ kg/m^3$ is the liquid density, $c_L = 1500\,m/s$ is the speed of sound in the liquid and $p(x,t)$ is the local pressure at the bubble position. The dots stand for the derivatives with respect to time. p_L denotes the pressure at the bubble wall, which is written as

$$p_L=\left(\frac{2\sigma}{R_0}+P_\infty\right)\left(\frac{R_0}{R}\right)^{3\gamma}-\frac{2\sigma}{R}-4\mu_L\frac{\dot{R}}{R}$$

where $\sigma = 0.0725\,N/m$ is the surface tension, $\mu_L = 0.001\,Pas$ is the liquid dynamic viscosity and R_0 is the equilibrium radius of the bubble. According to Doinikov [9], the equation of the translational motion is written as

$$R\ddot{x}+3\dot{R}\dot{x}=\frac{3F_{ex}(x,t)}{2\pi\rho_L R^2},$$

where $F_{ex}(x,t)$ is the external force acting on the bubble, which is the sum of the primary Bjerknes force $F_B = -V(t)\nabla p(x,t)$ and the drag force $F_D = -12\pi\mu_L R(\dot{x}-v_{ex}(x,t))$. Note that $V(t)$ is the bubble volume, $\nabla p(x,t)$ is the pressure gradient of the acoustic field and $v_{ex}(x,t)$ is the liquid velocity induced by the acoustic irradiation.

The manipulation method presented in this paper is based on the principle that a standing wave is the superposition of two counter-propagating waves $p_i(x,t) = P_0\cos(\omega t \pm kx - \varphi_i)$ generated by opposing transducers. Here, P_0 is the common pressure amplitude, $\omega = 2\pi f$ is the excitation frequency, $k = \omega/c_L$ is the wave number and φ_i is the phase shift of the first or second component. Thus, the total pressure field can be written as

$$p(x,t)=P_A\cos\left(kx+\frac{\varphi_1-\varphi_2}{2}\right)\sin\left(\omega t-\frac{\varphi_1+\varphi_2}{2}\right),$$

where $P_A = 2P_0$ is the pressure amplitude of the standing wave. By varying the phase difference $(\varphi_1-\varphi_2)$ between the counter-propagating waves the standing waveform can be altered in space.

Two test cases are presented in Fig. 1, where the relative displacement x/λ of the bubble as a function of the dimensionless time $\tau = t/(2\pi/\omega)$ is plotted. The blue, red and green curves are obtained for bubbles with equilibrium sizes of $40\,\mu m$, $30\,\mu m$ and $20\,\mu m$, respectively. In both cases, the excitation frequency is $f = 25\,kHz$ and the pressure amplitude is $P_A = 1\,bar$ (left) and $P_A = 1.3\,bar$ (right). The dashed black curves denote the actual position of the pressure antinode, which is altered by varying the phase shift difference between the counter-propagating waves. In the first case (left), the antinode position is fixed at $x/\lambda = 0$ for 1000 acoustic period, and the bubbles are initialized at position $x/\lambda = 0.1$.

It is known that bubbles with a size below the resonance size corresponding to the excitation frequency are attracted by the antinode; thus, these bubbles approach the antinode located at $x/\lambda = 0$. After the first 1000 acoustic cycles, the antinode is moved to $x/\lambda = 0.25$, see the dashed black curve. This antinode shift is followed by these bubbles. In the second case, the antinode is moved between $x/\lambda = -0.5$ and $x/\lambda = 0.5$ according to a sine function. This acoustic field manipulation is followed by the bubbles also.

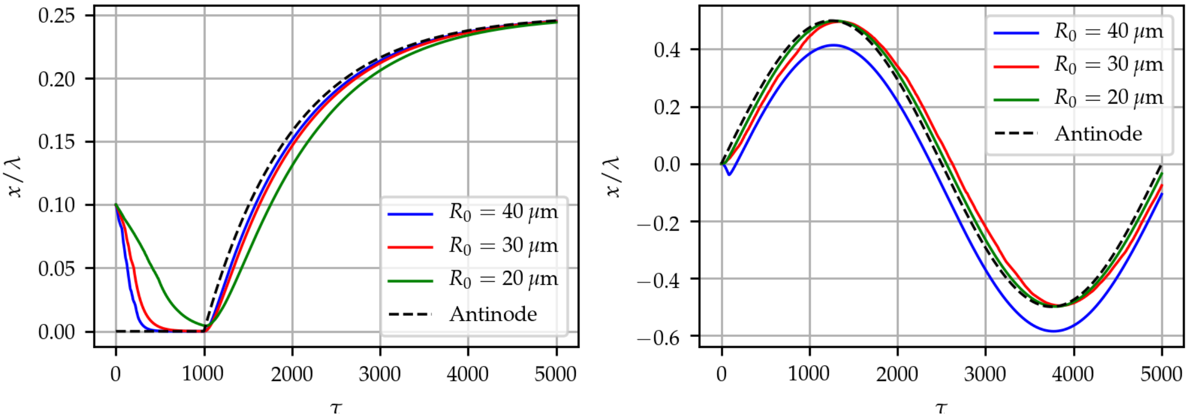

Figure 1 Bubble position in terms of relative displacement as a function of the dimensionless time for bubbles with different sizes. The dashed black curves denote the actual position of the pressure antinode.

Based on the results, the acoustic manipulation method is a feasible option to control the bubble position. However, in a real cluster, thousands of interacting bubbles are present; thus, further improvement of the model and investigations are required to seek control that can be feasible in practice. The adequate control of cluster structure can be an important advancement to face one of the biggest challenges in sonochemistry. which is to scale up the production feasible for real industrial applications.

ACKNOWLEDGMENTS

Supported by the ÚNKP-22-5-BME-310 New National Excellence Program of the Ministry for Culture and Innovation from the source of the National Research, Development and Innovation Fund

REFERENCES

[1] Brennen, C.E. (1995), *Cavitation and Bubble Dynamics*, Oxford University Press, New York.
[2] Yasui, K., Tuzizuti, T., Lee, J., Kozuka, T., Towate, A., Iida, Y. (2008), *The range of ambient radius for an active bubble in sonoluminescence and sonochemical reactions*, J. Chem. Phys., 128(18), 184705.
[3] Sutkar, V. S., Gogate, P. R. (2009), *Design aspects of sonochemical reactors: Techniques for understanding cavitational activity distribution and effect of operating parameters*, Chem. Eng. J., 155, 26-36.
[4] van Iersel, M. M., Benes, N. E., Keurentjes, J. T. (2008), *Importance of acoustic shielding in sonochemistry*, Ultrason. Sonochem., 15(4), 294-300.
[5] Ding, X., Lin, S.-C.-S., Kiraly, B., Yue, H., Li, S., Chiang, I.-K., Shi, J., Benkovic, S. J., Huang, T. J. (2012) *On-chip manipulation of single microparticles, cells, and organisms using surface acoustic waves*, Proc. Nat. Acad. Sci., 109(28), 11105-11109.
[6] Vuillermet, G., Gires, P. Y., Casset, F., Poulain, C. (2016), *Chladni patterns in a liquid at microscale*, Phys. Rev. Lett., 122(18), 184501.
[7] Goldowsky, J., Mastrangeli, M., Jacot-Descombes, L., Gullo, M. R., Mermoud, G., Brugger, J., Martinoli, A., Nelson, B. J., Knapp, H. F. (2013), *Acousto-fluidic system assisting in-liquid self-assembly of microcomponents*, J. Micromech. Microeng., 23(12), 125026
[8] Keller, J. B., Miksis, M. (1980), *Bubble oscillations of large amplitude*, J. Acoustc. Soc. Am., 68(2), 628-633
[9] Doinikov, A. A. (2002), *Translational motion of a spherical bubble in an acoustic standing wave of high intensity*, Phys. Fluids, 14(4), 1420-1425.

EFFECT OF THE FLOW CURVE DETERMINATION ON THE THINNING OF DRAWN PARTS

KÖLÜS Martin László, BORBÉLY Richárd, SZŐKE Dániel, BÉRES Gábor József
John von Neumann University, Hungary
E-mail: kolus.martin@gamf.uni-neumann.hu, borbely.richard@gamf.uni-neumann.hu, beres.gabor@gamf.uni-neumann.hu

Keywords: Flow curve, Thinning, Cupping test, Sheet metal

This study presents the results of finite element simulations based on different variations of the flow curve of DC04 automotive thin sheet. Nowadays the importance of sheet metals in the industry is increasing. Many sheet forming technologies are used every day with one very important input parameter being the flow curve. The most common method for flow curve definition is the tensile test, which is not reliable for high strains due to the necking phenomenon. For this reason, we used compression test as well, that resulted two-or- three magnitude higher strains than in case of tension test. The aim of our research is to investigate how different flow curve equations affect the variation of sheet thickness in cupping tests. In order to exclude other influencing factors in the experiment, both the sheet material and the geometric properties of the specimen, as well as the external state factors were considered to be the same in all cases. The finite element simulations were performed using Simufact 2021.1 software.

As mentioned before, an accurate knowledge of the flow curve for the material is a prerequisite for running finite element simulations. The Hockett-Sherby equation [1]:

$$\sigma = \sigma_s - \exp(-(N\varepsilon)^p)\,(\sigma_s - \sigma_y)$$

was used in the simulation environment, which is well-known and used worldwide among other theories related to the stress strain behaviour of metallic materials. The equation includes four material parameters such as the yield strength (σ_y) and the saturation stress (σ_s). In the first case, using data obtained purely from tensile testing, the flow curve equation for the DC04 sheet metal was determined. In the second case, we complemented our tensile test results with results obtained from compression test. This resulted in a flow curve covering a larger range of deformation, with an equation that differs from the flow curve obtained from the tensile test. Figure 1 shows the flow curves obtained with both tensile and compression test.

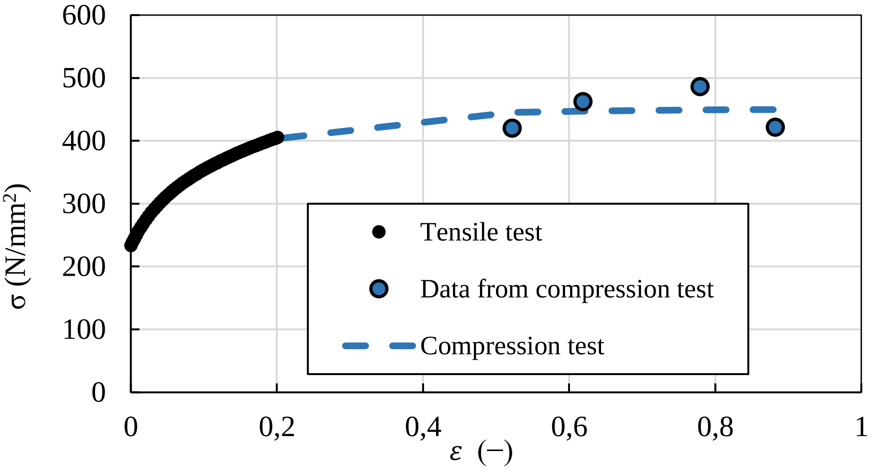

Figure 1 The flow curve of the DC04 thin sheet

The input parameters for both cases are described in Table 1.

Table 1 The input parameters used for the simulations

	σ_y	σ_s	N	p	ε
Tensile	240	456	8,60	0,89	0,20
Compression test	240	450	7,56	0,96	0,88

As an example, simulation results can be seen in Figure 2. The initial element size was 1,4 number was 6744 type was hexahedral and Coulomb friction model was estimated with the value of 0.12. Forming limit curve was considered as the failure criterium obtained by literature results and Hill’48 yield criterion using the average Lankford coefficient was applied. The validation of the simulations is in progress, however this study deals with the comparison of the numerical results only.

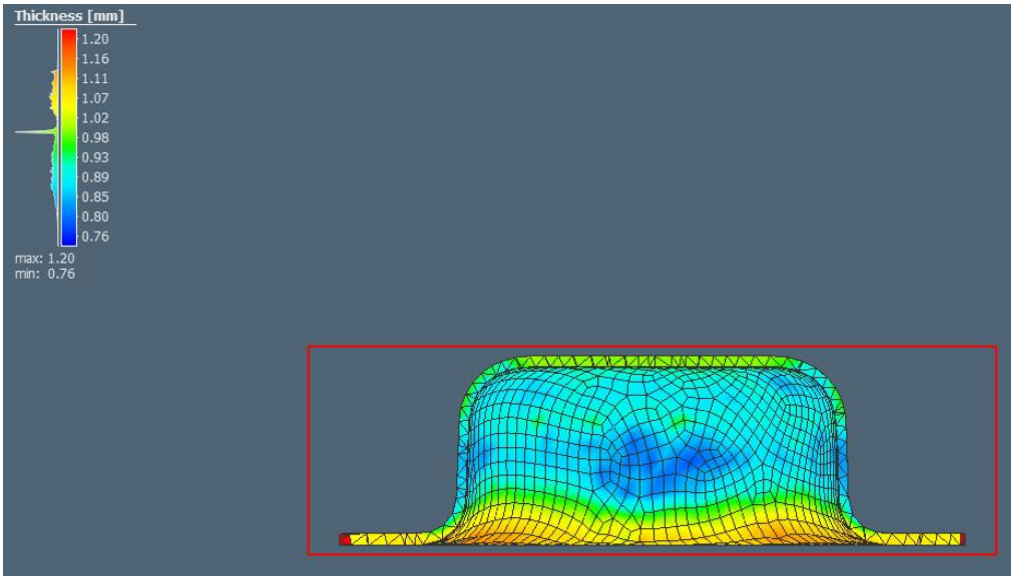

Figure 2 Finite element simulation of cupping test

It can be observed according to our results (Figure 3) that the two curves are almost identical, however an essential difference can be spotted at the zone of double necking.

Observing Table 1, it is clear that there is a difference of about 10% for the *N* and *p* factors. In the range of the double necking where the plate is thinned, there is also a difference of 10% with a good approximation.

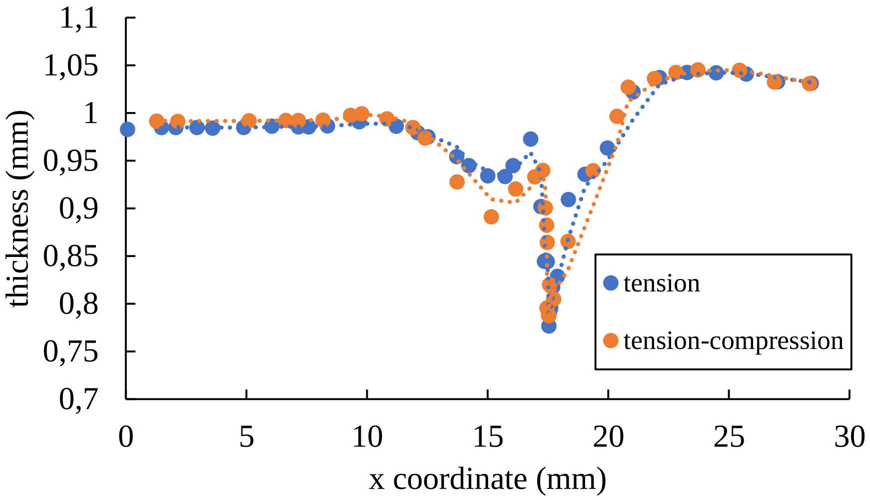

Figure 3 The change of thickness

ACKNOWLEDGMENTS

We would like to thank John von Neumann University for providing us with the tools and materials essential for this research, and we would like to thank all our colleagues who contributed in some way to the research.

REFERENCES

[1] Xin-cun Zhuang et al., Determination of Flow Curve and Plastic Anisotropy of Medium-thick Metal Plate: Experiments and Inverse Analysis, Journal of Iron and Steel Research, International, 2015.

THE IMPORTANCE OF PERPENDICULARITY DURING THE SCANNING ULTRASOUND EXAMINATION

[1]KOROKNAI László, [1]KUZSELLA László, [2]PÓR Gábor
[1]Institute of Material Science and Technology, University of Miskolc, Hungary
E-mail: korok.laci16@gmail.com ; kuzsella@uni-miskolc.hu
[2]Institute University of Dunaújváros , Dunaújváros, Hungary
E-mail: porg@uniduna.hu

Keywords: Ultrasound, Non-Destructive Testing, Perpendicularity

It is a well-know fact that ultrasound is suitable for detecting material defects and cracks. Conventional manual-type tests would be very tedious during a series production and would be too time-consuming and subjective. In the Hungarian Acoustic Industrial Diagnostic Laboratory at the University of Dunaújváros. we deal with nondestructive material testing, so we test solid products, components or even complete systems without damaging them.My Colleagues developed an ultrasonic scanning system with a unique examination method. The biggest advantage of which is that the results will be free of subjectivity and reproducible. In addition, I would like to present the most important problem.

In our laboratory, we deal with non-destructive material testing, so we test solid products, components, or even complete systems without intervention, even during operation. One of the most suitable methods for examining the internal structure of materials is ultrasonic examination, in which the body to be examined is illuminated with sound beams that are in the ultrasonic range. Traditionally, this test was performed manually moving a test probe by a person who specialized in it. In our laboratory, however, my colleagues are developing an automated scanning method for these manual tests, which allows us to perform more stable movements with smooth progress, resulting in much more repeatable measurements.

Figure 1 The main components of Scanning Ultrasound equipment

An ultrasonic head is fixed into a multi-axis actuating mechanism to scan the object to be examined (Fig.1.). During the scan, measurements are performed with a predetermined step resolution, to which the current coordinate points are added. To perform the measurements, we use an Olympus-branded ultrasonic measuring device, which produces one dimensional ultrasonic images for each for each coordinate points and transmits them to a computer. From the collection of these results, we can construct two-dimensional diagrams and three-dimensional pictures.

During the examinations, it is possible to observe what happens when the ultrasound and the examination surface don’t close a 90 degrees angle with each other (Fig.2.).

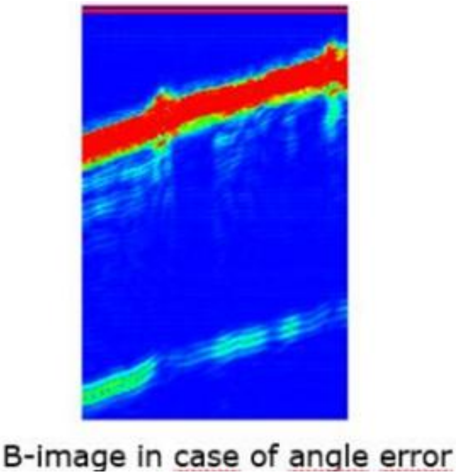

Figure 2 B-image with angle error

You can see the angle error on the second image. This is important problem, because all the defects will move in the material because of angel error and we will get an incorrect results.

REFERENCES

[1] László Koroknai: Design and Construction of a Leveling Table for Scanning Ultrasonic Testing Equipment, University of Dunaújváros, Dunaújváros, 2021.
[2] László Koroknai: Porosity test on a machined surface using a camera method, University of Dunaújváros, Dunaújváros, 2019

TUBE-TO-TUBE JOINING BY FORMING

[1]*KOVÁCS Péter Zoltán*, [2]*JÓNÁS Szabolcs*
[1]*Department of Materials Science and Technology, Faculty of Mechanical Engineering, University of Miskolc, Hungary*
E-mail: metkpz@uni-miskolc.hu
[2]*Department of Machine and Product Design, Budapest University of Technology and Economics, Hungary*
E-mail: jonas.szabolcs@gt3.bme.hu

Keywords: tube joining, joining by forming, FEA

ABSTRACT

Several technologies have been developed for joining tubes. In this study an innovative technology has been shown, which is purely using metal forming process. The technology is using the phenomenon of plastic instability. In this study the tool design phase for the further experimental tests is shown by finite element analyses.

INTRODUCTION

There are several different methods to join tubes as welding, gluing or threaded connections. The present study is dealing with an innovative technology for tube joining from the FE simulation point of view. The goal is to find a proper tool geometry for tube joints. The basic phenomenon of the presented technology is the plastic instability. In recent studies the technology is introduced as a challenging way of joining of tubes, although the benefit of the technology is dissimilar materials can be joined together and cost effective compared to other methods [1][2][3]. A few variants have been developed, however in this study we are dealing with the most basic one, the axial joining.

MATERIALS AND METHODS

The main goal is to determine a proper tool design for joining tubes by plastic forming. The first decision is to define the diameter, wall thickness, and the length of the tubes, so far, the available ones at the University of Miskolc is 100 mm in length with the outer diameter of 32 mm and 1.5 mm of wall thickness made by aluminium alloy.

For the simulations the applied material was the EN AW-5754 type of aluminium alloy, for which the flow curve is measured, and extrapolated according to the Hockett-Sherby material law for higher strain regimes (Figure 1). The applied FE simulation software was the MSC.Marc/Mentat 2019 Academic. Due to the geometry, the model is considered as axisymmetric. The applied boundary conditions and the FE mesh can be seen in Figure 2. The chamfer of the tubes is 70° in all cases; however the forming load is highly depending on it.

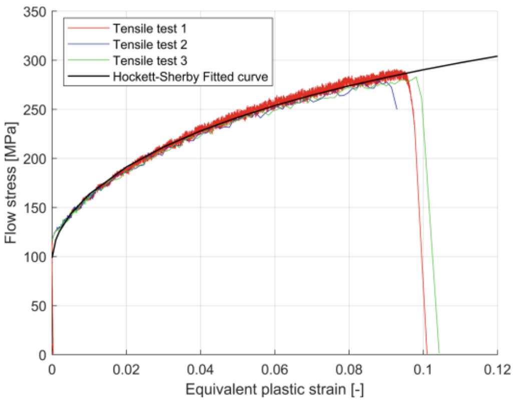

Figure 1 Flow curve of the EN AW-5754

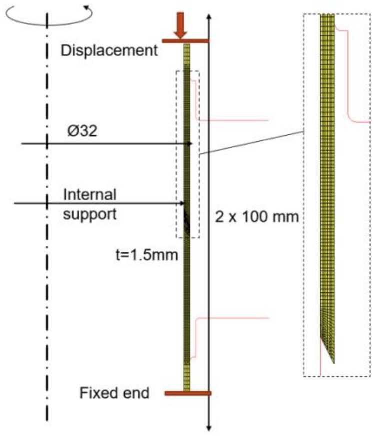

Figure 2 FE model and mesh distribution

The investigated parameters of the tools are the distance between the dies, the depth, and the width of the grooves. The frictional condition in between the tubes and the tools are also analysed.

RESULTS

The force-displacement curves and the residual geometry for each design variants are compared and evaluated in order to determine the final tool design for the experiments. The process of the joining simulation can be seen in Figure 3.

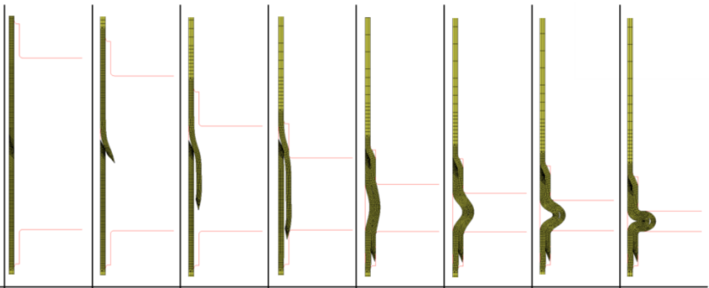

d [mm]	0	4.85	19.38	29.07	36.33	38.76	41.18	44.09
F [kN]	0	7.99	10.56	12.91	30.72	30.72	30.72	30.73

Figure 3 Joining process

A typical force-displacement curve for the process is presented in Figure 4. The joints' geometrical parameters which are the basics of the comparison can be seen in Figure 5. The Table 1 and 2 show the numerical results of the simulations.

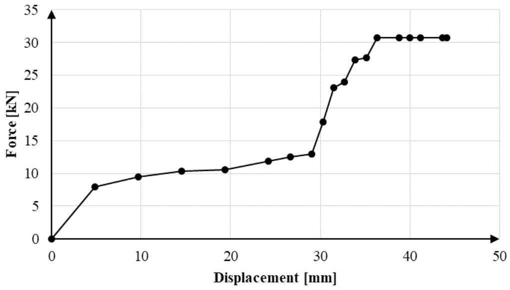

Figure 4 Force-displacement curve

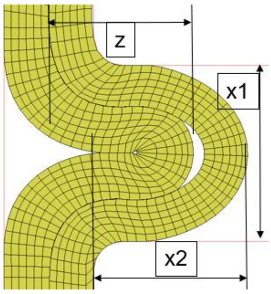

Figure 5 Joint geometrical parameters

Table 1 Effect of the tool design on the geometrical parameters

	x1 [mm]	x2 [mm]	z [mm]	Fmax [kN]
h50b10c1.5	5.91	5.17	4.83	30.7
h45b10c1.5	5.27	4.63	4.16	29.4
h40b10c1.5	4.97	3.70	3.26	27.3
h50b5c1.5	*6.05*	*6.46*	*6.27*	*31.1*
h50b15c1.5	5.39	5.40	3.06	33.06
h50b10c2	5.42	4.32	4.19	31.8
h50b10c2.5	4.32	3.36	2.08	31.9

Table 2 Effect of the friction coefficient on the geometrical parameters

μ	x_1 [mm]	x_2 [mm]	z [mm]	F_{max} [kN]
0.1	*6.05*	*6.46*	*6.27*	*31.1*
0.3	6.15	6.40	6.88	37.2
0.5	6.15	6.40	6.43	40.9
0.7	6.15	6.39	6.42	41.3

REFERENCES

[1] Alves, L.M., Silva, C.M.A., Martins, P.A.F. (2017), Joining of tubes by internal mechanical locking, Journal of Materials Processing Technology, 242, 196-204

[2] Goncalves, A., Alves, L.M., Martins, P.A.F. (2014), Tube joining by asymmetric plastic instability, Journal of Materials Processing Technology, 214, 132-140

[3] Agrawal, A.K., Narayan, R.G. (2020), Experimental and numerical studies on joining steel tubes by end forming, Journal of Construction Steel Research, 167, 105792

MECHANICAL TESTING OF 3D PRINTED STAINLESS STEEL SPECIMENS

KOVÁCS Sándor Endre, VARGA László
Institute of Foundry Engineering, Faculty of Materials and Chemical Engineering, University of Miskolc, Hungary
E-mail: ontendre@uni-miskolc.hu , ontvlaci@uni-miskolc.hu

Keywords: 3D metal printing, stainless steel, mechanical testing, additive manufacturing

Additive manufacturing is one of the most rapidly growing industry of our time, which includes all kinds of rapid prototyping and manufacturing methods, or in a more widespread way, 3D printing. The name is based on the decision of the ASTM F42 committee, to distinguish it from conventional crafting methods, which are based on the subtraction of material to reach the final shape of the product. In this way, the shape is only being formed by material addition [1].
The 3D printing process of metals evolved from both conventional powder metallurgy and polymer-based additive manufacturing, and by today it is capable of making parts, with a high-level of complexity, which would require extreme preparations otherwise, in a relatively short period of time. However, the 3D printing machine operates on higher energy levels, and more sensitive to the purity of the base material, thus it is still more expensive than the conventional counterparts.
To ensure the quality of a 3D printed metal part, the simplest and cost-effective way is to test them by creating tensile test specimens [2][3]. This way we can gather information about the strength and ductility of materials under uniaxial tensile stresses. This data can be compared to other alloys, printing orientations and methods. The key to this type of measurement is that it is easy to replicate, and fast to measure, also the diversity of the deployed specimens can be used to gain information in various forms. Typical tensile specimen types are shown in Fig.1.

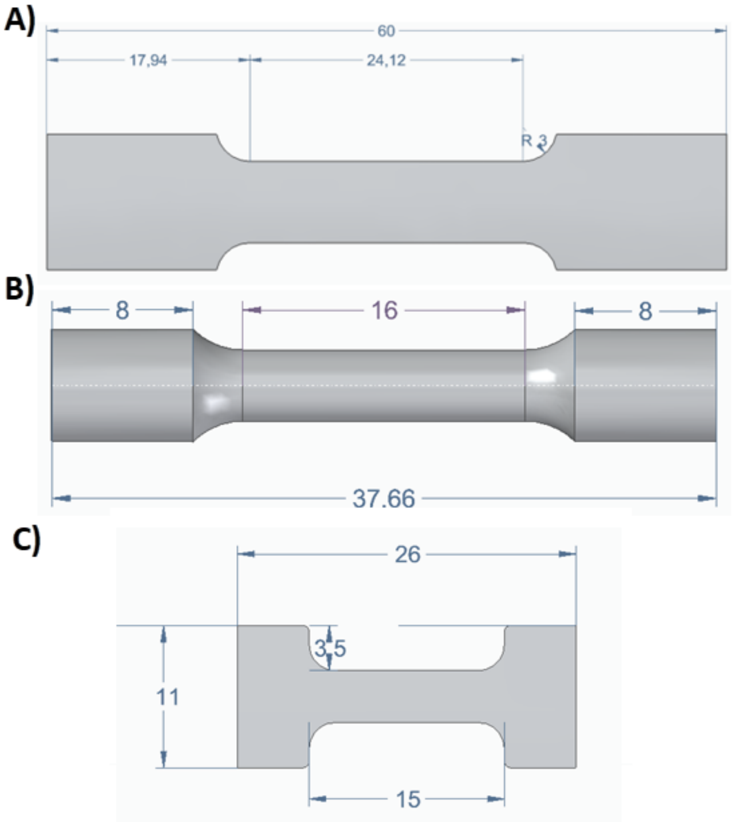

Figure 1 Different types of tensile test specimens used by our measurements: A) Rectangular specimen B) Round specimen C) Modified, small-sized rectangular specimen

As Fig 1. shows, regarding additive manufacturing, size and shape does not matter. All kinds of specimens can be created, and these samples can be customized in any desired way.
The goal of this study is to show that during 3D printing, size, shape, orientation, and layer creator is an extremely critical factor, in a product quality point of view. Additive manufacturing is a rather powerful tool, however not omnipotent, overseeing the production and setting an optimal printing job is also a huge part of the process. Also, it is one of the weaknesses, because in most cases if something goes wrong during the production it means immediate failure, which is not desired in a cutting-edge environments.

To have a good comparison of the 3D printing we used the same alloy, namely 17-4ph stainless steel powder, we only modified the specifications of the tensile test specimens, as shown in Fig. 1. We also modified the thicknesses, and surface area to measure that how the mechanical properties change regarding these modifications.

While making these modifications, it was also important, that we have information about the inner stresses, which build up during the 3D printing process. Additive manufacturing is highly susceptible to residual stresses, which can be harmful for future use. To determine these stresses, we used X-ray diffraction (XRD) on different specimens, which is shown on Fig. 2.

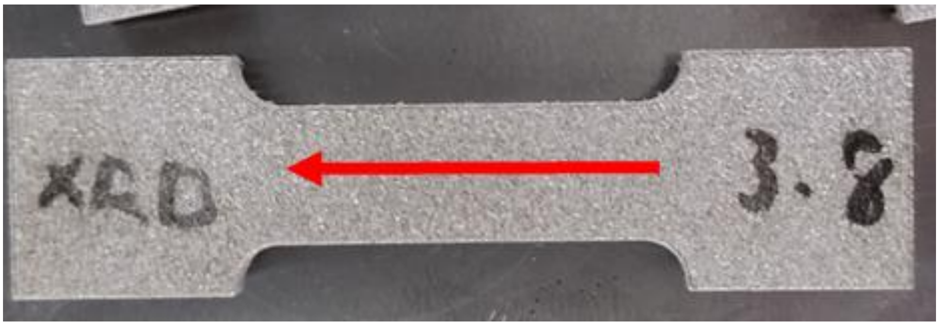

Figure 2 XRD measurement of a rectangular tensile test specimen

The results then were collected and compared with the datasheet values, made from the same material's specimens, with conventional manufacturing methods.

REFERENCES

[1] William E. Fraizer – Metal Additive Manufacturing: A review – ASM International 2014

[2] Chanun Suvanpreecha, Phanuphak Seensattayawong, Vorawat Vadhanakovint and Anchalee Manonukul – Influence of Specimen Layout on 17-4PH Alloys Fabricated by Low-Cost Additive Manufacturing

[3] Haolin Jia, Hua Sun, Hongze Wang, Yi Wu, Haowei Wang - Scanning strategy in selective laser melting (SLM): a review

DESIGN OF AN UNIQUE CLAMPING DEVICE FOR THE DEVELOPMENT OF PRESSING TECHNOLOGY

LADÁNYI Ramóna, BODZÁS Sándor
Department of Mechanical Engineering, Faculty of Engineering, University of Debrecen, Hungary, Debrecen
E-mail: ramiladanyi2000@gmail.com , bodzassandor@eng.unideb.hu

Keywords: test manufacturing, 3D printing, Alufix, assembly, finite element analysis

In my project I designed a device to clamp a custom workpiece for press machining. My chosen component is a protective cover for a switch sensor. The purpose of the protective cover is to protect the sensor foil inside the coverage part from dirt, foreign materials and oil leakage. The product is currently running in test production, so there is no final fixture, as the shape, size and material of the product. It can change at any moment, so there is no possibility to use a fixed mould (e.g. cast mould) for fixing due to changes, it would be too time consuming and expensive to change it every time. As a first step, I modelled the part using Solid Edge software and then I printed with Ultimaker 3D printer. I printed out 3 alternatives, showing that the properties of the product can change during the manufacturing process, so the 3 models changed in geometry and material as well.

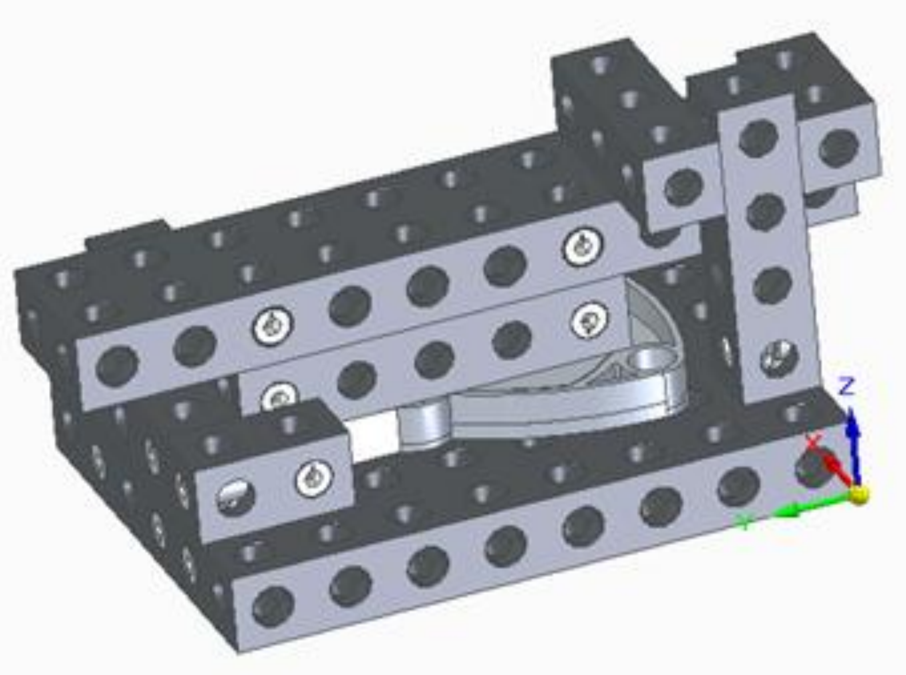

Figure 1 Clamping device with the product

It is important that the clamping device is properly fixed so that the pressing can be done without breaking, destroying or deforming the workpiece. I design the fixtures using the Alufix system, which is a precision modular clamping system for clamping reproducible workpieces. I chose the Alufix system because when product properties change, I can easily disassemble the fixture and assemble a new one in seconds. I imported the Alufix parts in Solid Edge, then assembled the fixture there and I performed finite element simulation on the assembled clamping device and product with the appropriate press values and the result showed that the press can be performed perfectly under the given conditions. After the evaluation, I performed the pressing on all 3 models and both visually and in terms of compression force, there were clear differences, which can easily represent how we can improve the final product to be perfect.

Figure 2 Pressing test results

After the pressings were done, I prepared production documentation (parts list, assembly instructions) for the production technicians and SWI (Standard Work Instruction) for the operators to assemble correctly and use the equipment properly.

Overall, the implemented device is suitable for the implementation of the press. The aim of my research is to investigate how effective the Alufix system is in the production of a custom part sample and to use these results to design a permanent device for series production.

REFERENCES

[1] K. Krisztián -Dr Líska János -Nagy József, "'A Neumann János Egyetem duális képzésfejlesztése a Kecskemét és térsége kiemelt járműipari központ környezetében'".

[2] Bálint, Ó. Egyetem, B. Donát Gépész És Biztonságtechnikai, and M. Kar, "Műszakiak Tudományos Ülésszaka," pp. 95–98, 2017, doi: 10.33895/mtk-2017.07.

[3] Horváth Richárd and Dr. Mikó Balázs, "Perifériális Technológiák," 2009. Accessed: Jun. 06, 2022. [Online]. Available: http://old.bgk.uni-obuda.hu/ggyt/targyak/seged/bagca15nlc/15.pdf

[4] Ducsai János, Alapmérések Geometriai Mérések. Budapest: Műszaki Könyvkiadó, 2020.

[5] W. Barskamp, "ALUFIX Main Catalogue." Accessed: Jun. 05, 2022. [Online]. Available: https://www.witte-barskamp.de/assets/downloads/Kataloge/Modulare-Spannsysteme/ALUFIX/ALUFIX-Main-Catalogue-2022-E.pdf

[6] Terdik János and Zeller László, Szerszámkészítő mestervizsgára felkészítő jegy. Budapest: Magyar Kereskedelmi és Iparkamara, 2014.

ANALYSIS OF STRUCTURAL STRENGTHS FOR THE CABLEWAY GROUP

DANIEL Lates, CALIN Alfianu
SC IRUM SA, Romania
E-mail: daniel.lates@irum.ro , calin.alfianu@irum.ro

Keywords: cableway, structural strengths, forestry.

DESCRIPTION OF FOREST CABLEWAY

Forestry cableways are cable transport equipment used in forestry operations for wood collection operations (see Fig.1). They are used to collect wood in hard-to-reach, steep and remote areas. These installations are composed of power units placed on sleds that serve to move them by self-traction to the place of operation.

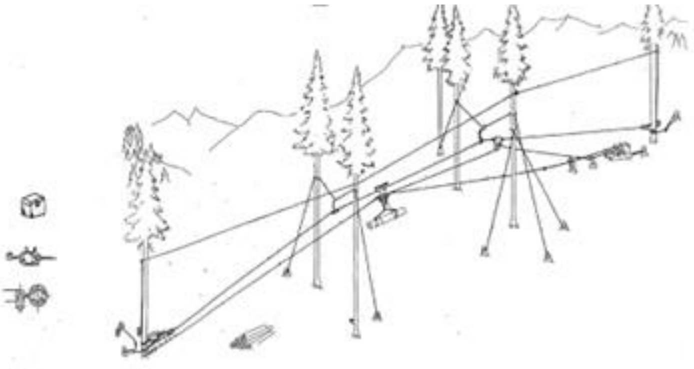

Figure 1 The basic drawing of the sleigh-type cableway

I. Loading scenarios:

Lifting into working position

The scenario tries to determine the constraints and loads for the static analysis in case the funicular group is self-propelled uphill to be taken to the work location. The soil is modeled to create the mathematical model: **Constraints:** sliding contact on the sole of the sled with the ground; cable end blocked; solidification contacts between welded components; sliding contacts without friction in bearings (radial or axial); gear sliding contacts. **Loads:** on the ground plane, in the direction opposite to the direction of the cable Friction force:

$$Ff = \mu \cdot \text{Gn} = 0.35 \cdot 24{,}000\ \text{N} = 8{,}400\ \text{N}$$

distributed over the entire surface of the two skis; in the ground plane, in the direction opposite to the direction of the cable Tangential gravitational force Gt=23,000 N, (see Fig.2).

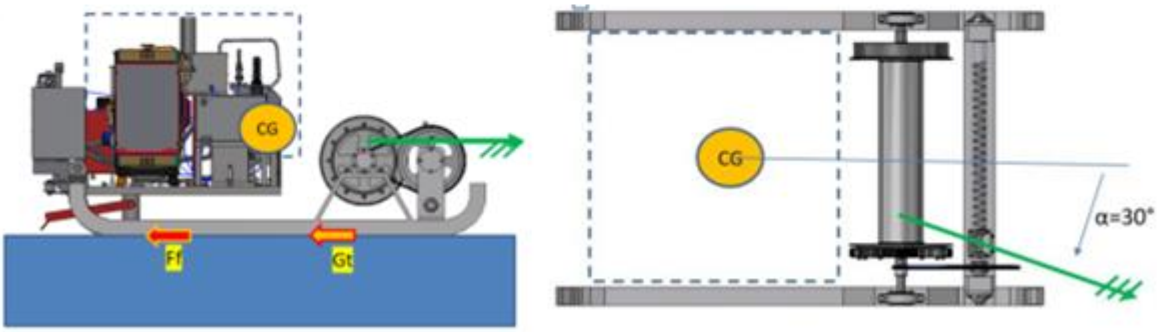

Figure 2 The scenario of lifting into working position

II. Brake support in the absence of the traction cable

The scenario tries to determine the constraints and loads for the static analysis if the cableway group rests on its brakes (hoe) when the cable is disconnected. It is important that the funicular is stable (does not roll back). The soil is modeled to create the mathematical model:

Constraints: sliding contact on the sole of the sled with the ground; solidification contacts between welded components; sliding contacts without friction in bearings (radial and axial); gear wheel sliding contacts; embedding the brake (hoe) in the ground

Loads: In the center of gravity, the tangential component of the weight of the funicular Gt=23,000 N; in the ground plane, in the direction opposite to the direction of the cable tangential gravitational force Gt=23,000 N, (see Fig.3).

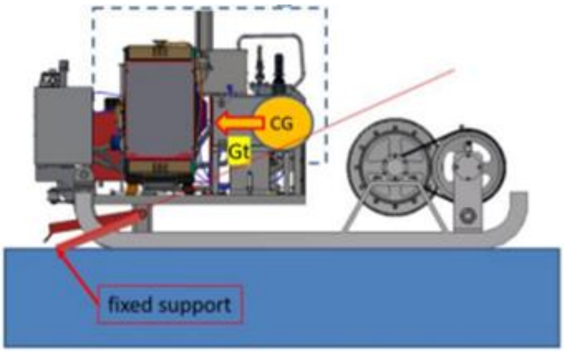

Figure 3 Braking scenario without traction cable

III. Lifting the maximum load

The scenario tries to determine the constraints and loads for the static analysis in the situation where the cableway group is fixed in the place of exploitation and pulls the maximum load including the weight of the traction cable considering an overload factor 2. Th To calculate the tension in the cable, the angles formed between the cableway's drum and the cable must be considered: inclined 30° to the longitudinal plane of the funicular group and 20° upwards. The soil is modeled to create the mathematical model:

Constraints: sliding contact on the sole of the sled with the ground; ground group connection embedment contacts; solidification contacts between welded components; sliding contacts without friction in bearings (radial or axial); gear sliding contacts.

Loads: vertically downwards in the center of gravity, the normal component of the gravitational force Gn= 66,000 N; in the ground plane opposite the projection of the load, the friction force 8,400 N, (see Fig.4).

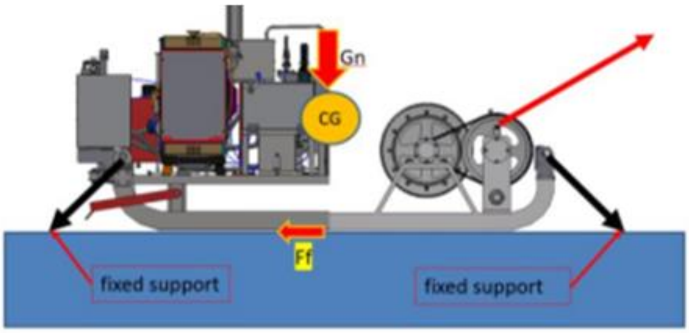

Figure 4 Maximum load lifting scenario

ACKNOWLEDGMENTS

This work was supported by the project: Forestry funicular with hybrid drive and energy recovery, MySMIS: 120499. Priority axis 1: Research, technological de-velopment and innovation (CDI) in support of economic competitiveness and business development Action: 1.2.1 Stimulating the demand of enterprises for innovation No. financing contract: 353/390029/27.09.2021.

REFERENCES

[1] Lates, D., Inte, R., A., Chirca, M., Dranca, M., Oprea, C. (2022), Initial evaluation of the performances of a sledtype forest cableway, International Conference INTER-ENG 2022, Interdisciplinarity in Engineering, Targu Mures. [2]

[2] Lates, D., Moica, S., Veres, C., Pozdirca, P., Harpa, E. (2019), Design of Smart Forestry Cableway, Elsevier, Procedia Manufacturing 32,79-86. [3]

[3] Barbu, M. C., (2013), Forest And Wood Industry In Romania, ISSN 2069-7430 ISSN-L 1841-4737, Pro Ligno, 9(4). [4]

[4] Dragan, I.C., Bora, L., Cerchez, G., Comanescu, A., Stan, I. (1971) Funiculare Forestiere (cableway forestry), Ceres, Bucuresti. [5]

[5] Naftali S. (1958), Funiculare (cableway). Editura Tehnica, Bucuresti.

USING ARTIFICIAL NEURAL NETWORK IN THE DESIGN OF COMPOSITE SANDWICH STRUCTURES

[1]MOHAMMED SAHIB Mortda, [2]KOVÁCS György, [1]SZÁVAI Szabolcs
[1]Institute of Machine and Product Design, University of Miskolc, Hungary
E-mail: mortdamohammed@gmail.com, szavai.szabolcs@uni-miskolc.hu
[2]Institute of Manufacturing Science, University of Miskolc, Hungary
E-mail: altkovac@uni-miskolc.hu

Keywords: Honeycomb sandwich composite structure; Artificial Neural Network; Monte Carlo Algorithm.

The need to evolve the behavior of advanced sandwich structures is forcing the industry to investigate new design approaches for these types of structures. Honeycomb sandwich composites are ideal alternatives instead of traditional materials such as metals in aerospace and automotive industries. Using the Artificial Neural Network (ANN) technique in this study provides an effective model for the structural design of honeycomb sandwich composite structures. The data for training ANN were obtained by combining the equations applicable to sandwich structural elements with the Monte Carlo algorithm. The functional relationship between the design and output variables was then established using the BackPropagation (BP) neural network. The face sheets of the sandwich structure were constructed as a Carbon Fiber Reinforced Plastic (CFRP) composite laminate with a cross-ply layup; furthermore, the core of the sandwich structure was an aluminum (Al) honeycomb core. The sandwich structure dimensions length and width (l, b), the applied load (p), the core density (ρ_c), and the total deflection limit (δ_{Req}) specified by the designer were all input variables. The output of the neural network included the core thickness (t_c), face sheet thickness (t_f), core safety factor (SF_C), and face sheet safety factor (SF_F). The results demonstrated that ANN is capable of accurately predicting the design parameters of sandwich structures. The ANN model provides a reduction in effort and time in the design and redesign of sandwich structures.

PURPOSE AND METHODOLOGY OF THE RESEARCH

The components of the investigated sandwich structure are laminated CFRP face sheets and a low-density AL honeycomb core bonded with adhesives as it can be seen in Fig.1. The core layer provides high stiffness and load bearing capacity with relatively low weight [1-2]. ANN has been identified as one of the outstanding techniques for modelling complex nonlinear relationships. ANN is a bioinspired computational approach that mimics human brain behavior and learning. This method does not require explicit knowledge of the physics phenomena being investigated. However, it relies entirely on the historical input-output data set (example set) to establish the relationship between the data through the training process. The main aim of the research is to develop a novel model that can predict the design variables of the sandwich structure based on the desired deflection limit. This model can be referred to as a reverse design approach [3].

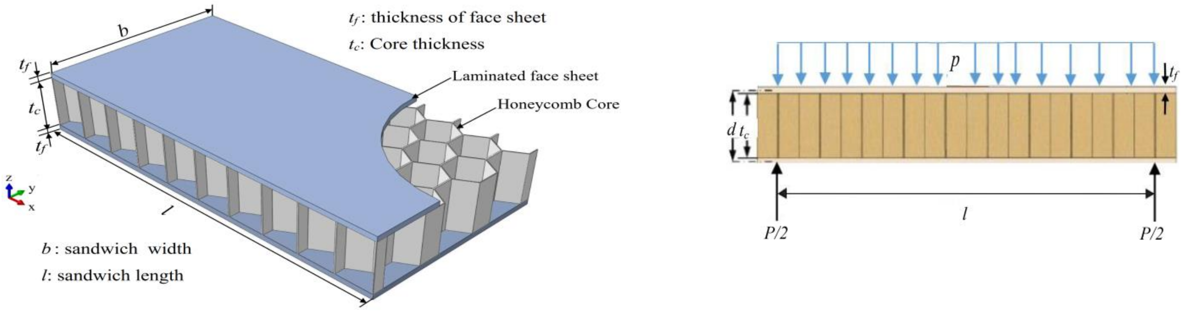

(a) Sandwich structure's dimensions *(b) Loading and boundary conditions*

Figure 1 The investigated sandwich structure

APPLICATION OF ARTIFICIAL NEURAL NETWORK MODEL

In our research the FeedForward Back-propagation Network (FFBN) was chosen because it is often used to solve complex problems [4]. In FFBN, the network learns the relationship between the data in the input and output layers through a training process that consists of several steps depending on the training algorithm used. During our research the Levenberg-Marquardt (LM) training algorithm was used. When using the LM algorithm, training is done in three phases: Training, Validation and Testing. Therefore, the input data were randomly divided into three groups: 70% for training, 15% for testing, and 15% for validation. In this study, the number of hidden layers was 3 layers, and the neurons were 12, 5, and 5 with (tansig) transfer functions in the respective three layers. The linear transfer function (purelin) is used in the output layer. The input and output data used in the creation of ANN are shown in Fig.2.

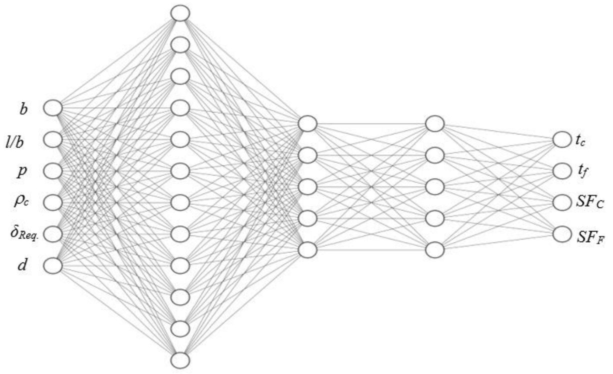

Figure 2 Neural network structure design model of the investigated sandwich structure

RESEARCH RESULTS

The performance of the elaboration ANN model can be investigated by comparing the analytical solution with ANN prediction. Fig. 3 compares the values of a core thickness (t_c) and face sheet thickness (t_f) obtained from the analytical model with those predicted by the model ANN. It shows that the results of the model ANN agree very well with the analytical values. Therefore, the neural network model exhibited good predictive ability with high accuracy, which increases our confidence in its use in further analysis, especially when using neural networks in sandwich structure optimization problems.

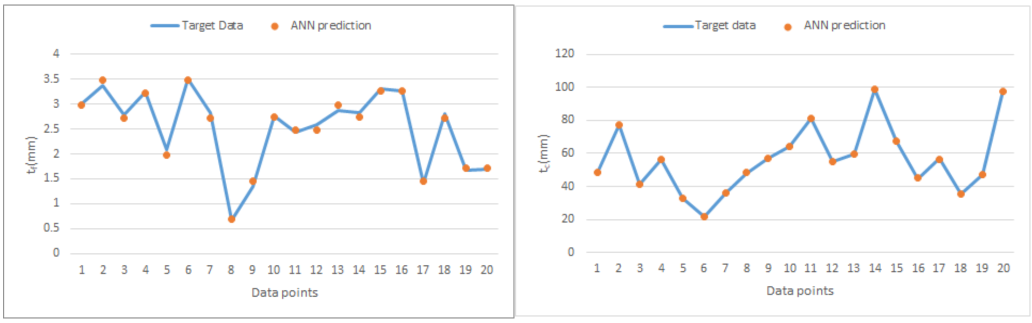

Figure 3 ANN prediction for some of the design points

The present study was conducted to investigate the application of artificial neural network technique to build a novel ANN prediction model to predict the structural design parameters of honeycomb sandwich composites based on deflection limits. We began by solving analytical equations organized by the Monte Carlo algorithm to obtain the required data set.

The research represented an advance in the design of sandwich structures with lower computational cost and reasonable accuracy. In this context, the designer has to select the dimensions, load value, core density and maximum deflection of the sandwich structures. While, the proposed intelligent model is able to predict the core thickness, the thickness of the face sheets, and the safety factors of the honeycomb core and face sheets. In conclusion, this model has the potential to go a step further in elaborating sandwich structure optimization problems.

REFERENCES

[1] Dababneh, O., T. Kipouros, and J. F. Whidborne. (2018), *Application of an efficient gradient-based optimization strategy for aircraft wing structures.* Aerospace, 5 (1): 1–27

[2] Harizi, W., J. Anjoul, V. A. Acosta Santamaría, Z. Aboura, and V. Briand. (2021), *Mechanical behavior of carbon-reinforced thermoplastic sandwich composites with several core types during three-point bending tests.* Compos. Struct., 262 (October 2020): 113590.

[3] Basheer, I. A. and Hajmeer, M. (2000), *Artificial neural networks: Fundamentals, computing, design, and application*, Journal of Microbiological Methods, 43(1), pp. 3–3.

[4] Basu, J. K., Bhattacharyya, D. and Kim, T. (2010), *Use of Artificial Neural Network in Pattern Recognition*, International Journal of Software Engineering and its Applications, 4(2), pp. 23–34.

EXPERIMENTAL ANALYSIS OF BUS DRIVER BEHAVIOR AND COGNITIVE LOAD

NAGY Viktor, KOVÁCS Gábor
Széchenyi István University, Hungary
E-mail: nviktor@sze.hu , kovacsg@sze.hu

Keywords: Human Factor, Driver Behavior, Driver Monitoring, Public Transport.

The complexity of the road transport system – elements of the transport infrastructure, traffic density and on-board systems of the vehicles – imposes an increasing cognitive load on drivers. This is especially true for bus drivers working in public transport. The increasing physical and mental strain can cause a decrease or loss of attention, which poses a high traffic safety risk. Professional bus drivers' working conditions mainly differ from private vehicle users. Complex driving circumstances, and operations conditions are responsible for work stress and fatigue. The main reasons are complicated driver cockpit interfaces, irregular working hours, disruptive passenger behavior and the need of traffic adaption [1].

The advanced driving aid systems (ADAS) are partially suitable to replace the driver's active intervention in certain emergency situations. At the same time, it can be observed that in the case of ADAS and autonomous vehicles, if the computer is unable to handle the given emergency situation, it "returns" driving and responsibility to the driver [2]. Therefore, a detailed examination of the human factor within the human-machine relationship is still extremely important. Examining the driver's attention level provides an opportunity to apply effective accident prevention steps and/or interventions. Furthermore, the progressive ergonomic design of increasingly complex vehicle onboard systems and interfaces also help to keep attention, control, and concentration [3].

The aim of the investigation of the driver's attention during present work is to assess the elements and effects of the cognitive load with the sensors temporarily installed in the vehicle and detecting the driver's activity, considering on-board instruments and interfaces.

LITERATURE

The literature examines this topic in extremely diverse perspective. The appearance of sleepiness at bus drivers is a critical area of traffic safety. Participants were tested by simulating long driving distances with the help of a simulator, and the degree of drowsiness (ORD) was evaluated on a 4-point scale. The automated elements of the monitoring system detected the signs of drowsiness but could not adequately filter out all critical situations and the author predicted the need for further tests [4].

Our test method planned to run on a public road and/or a closed track (not in a simulator), so we must operate with sensors that do not interfere with driving. A research team analyzed wearable and non-contact based sensor systems. In addition, the driver's cognitive load level was deduced from the analysis of the vehicle data. After synchronizing the data, the analysis was done using software, and the classicization was done with an artificial intelligence (AI) supported system. The results showed that the reliability and accuracy of the camera monitoring is superior to that of the sensors placed on the driver. So, in a real driving environment, these sensors and their systems can be used safely [5]. In order to involve more participants and examine real world situations less wearable sensors should be used.

A multi-participant survey, in which truck drivers were examined, included Maintenance of Wakefulness Tests (MWT). The apnea phenomenon was present among the half of participants, and it became clear that it is also necessary to measure other effects related to sleep and alertness [6]. The NHTSA characterized driver distraction of four categories: visual distraction (e.g. looking away from the road); auditory distraction (e.g. responding to a ringing cell phone); biomechanical or manual distraction (e.g. manually adjusting the radio volume); cognitive distraction (e.g. being lost in thought) [7].

EXPERIMENT

The data collection involved the vehicle – currently operating bus used in urban transport –, and operator – the bus driver. During the static examination of the vehicle, a structured assessment of the design of the driver's compartment and the controls was carried out. During the (test) operation, the operating method, control processes and typical environmental effects, planned and unexpected situations were identified. Two drivers were involved in the pilot test, and in-depth interview was conducted. The driver's cognitive load was examined on a 15 kms long city/suburban (80%/20%) route carried out in Debrecen, Hungary, with random traffic and simulated, low-rate passenger flow. Quite accurate tracking of the driver's gaze was possible with the eye-tracking glasses of the Pupil-Labs [8, Fig. 1]. Light-shadow changes of the environment and reflections caused medium level of accuracy in the recording of raw data, but these can be eliminated in post processing. Three compact GoPro cameras were used to record the exterior views: one gave a forward view (looking on the dashboard and windshield); two had direct view of the driver (side, front-low). Professional 4G/GPS based data logger made possible to record vehicle telemetry and position data.

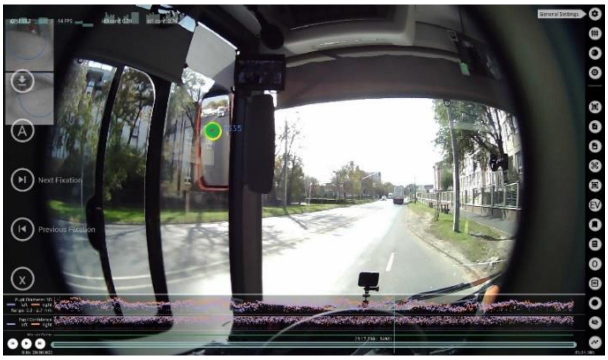

Figure 1 Eye-tracking software analysis with Pupil Player

RESULTS

The conscious perception or working memory usage and the distraction of the driver's attention are increased in urban traffic, due to the vehicle's complex signaling, control and communication interfaces, as well as the presence of the external environment (passengers, noises) of constant and variable intensity [9]. In the case of our experiment manual, visual and auditory, cognitive distraction was detected and simulated, in real world circumstances. The speciality of the urban bus driver distraction is the combination of visual and auditory distraction when communication with the passenger is in progress. More attention is needed when approaching and leaving bus stops and managing boarding and disembarking of passengers.

Our research work was focusing on monitoring driver behavior by using advanced wearable sensors, and using camera technology, in combination of telemetry data and in-depth interview. The experiments are showing that complex and multimodal distraction elements and human behavior effects make the measurement concept and methodology hardly definable, thus further optimization is required. If driver behavior, situation awareness and attention could be monitored and registered precisely, accident prevention could be set on higher level. Advanced camera technology and AI based post processing, later real-time processing methods are to be developed for achieving the best bus drivers' monitoring results.

ACKNOWLEDGMENT

The described work was carried out as part of a Cooperative Doctoral Program (KDP) supported by the National Research, Development and Innovation Office (NKFIH) and Ministry Of Culture and Innovation (KIM).

REFERENCES

[1] Montoro L, Useche S, Alonso F, Cendales B. (2018). *Work Environment, Stress, and Driving Anger: A Structural Equation Model for Predicting Traffic Sanctions of Public Transport Drivers*. International Journal of Environmental Research and Public Health, 15, 497.

[2] Kovács, G., Hőgye-Nagy, Á., Kurucz, Gy. (2021). *Human Factor Aspects of Situation Awareness in Autonomous Cars – A Psychological Approach*. Acta Polytechnica Hungarica, 18 (7), 7–24.

[3] Pickering, C. A., Burnham, K. J., & Richardson, M. J. (2007). *A review of automotive human machine interface technologies and techniques to reduce driver distraction.* IET Conference Publications, 532 CP, 223–228. https://doi.org/10.1049/cp:20070468

[4] Schwarz, C., Gaspar, J., Miller, T., & Yousefian, R. (2019). *The detection of drowsiness using a driver monitoring system.* Traffic Injury Prevention, 20 (sup1), 157–161. https://doi.org/10.1080/15389588.2019.1622005

[5] Rahman, H., Ahmed, M. U., Barua, S., & Begum, S. (2020). *Non-contact-based driver's cognitive load classification using physiological and vehicular parameters.* Biomedical Signal Processing and Control, 55, 101634. https://doi.org/10.1016/j.bspc.2019.101634

[6] Huhta, R., Hirvonen, K., & Partinen, M. (2021). *Prevalence of sleep apnea and daytime sleepiness in professional truck drivers.* Sleep Medicine, 81, 136–143. https://doi.org/10.1016/j.sleep.2021.02.023

[7] Ranney T.A., Garrott W.R., Goodman M.J. (2001). NHTSA Driver Distraction Research: Past, Present, and Future. Technical Report, SAE Technical Paper.

[8] Kassner, M., Patera, W., & Bulling, A. (2014). Pupil: *An open source platform for pervasive eye tracking and mobile gaze-based interaction.* UbiComp 2014 - Adjunct Proceedings of the 2014 ACM International Joint Conference on Pervasive and Ubiquitous Computing, 1151–1160. https://doi.org/10.1145/2638728.2641695

[9] Nilsson, H., Mullaart, M., Strand, N., & Eriksson, A. (2021). *The effects of information relevancy on driving behavior: A simulator study on professional bus drivers.* Cognition, Technology and Work, 23(3), 429–437, 2021, https://doi.org/10.1007/s10111-020-00644-x

A SOLUTION FOR CREATING A SUBMODEL OF AN ELECTRIC MOTOR IN A VEHICLE DYNAMICS MODEL BY USING MATLAB SIMULINK

NEMES Dániel, HAJDU Sándor
Department of Mechanical Engineering, Faculty of Engineering, University of Debrecen, Hungary
E-mail: nemes.daniel@eng.unideb.hu , hajdusandor@eng.unideb.hu

Keywords: vehicle, Matlab, BLDC, dynamic simulation, submodel, electric motor

Two questions arise during the simulations. The first one is the method of simulation the second is the accuracy of the model parameters. A vehicle was modelled by using Matlab Simulink. This model has several submodels, which were created with little information available. To bridge this gap some restraints were required. In this article, a solution was introduced for creating a submodel of an electric motor by using Matlab Simulink. For a later optimization task, it is important to simulate the efficiency map of the BLDC motor because, in this way, the location of the optimum can be authentically demonstrated. If the physical motor is available, what is simulated, there is an opportunity to measure the efficiency map. R. Wang and his colleagues measured the driving and braking efficiency map of a pure electric ground vehicle [1]. This method is unavailable to us, so another solution must be used. H. Patel and H. Chandwani simulated a BLDC motor in Matlab Simulink and verified it [2]. The detailed simulation of the electric motor gives odds to get a higher accuracy but for this, it is necessary to verify the simulated model. Without this, it is just an unnecessary computation capacity-guzzler. The combined FEM simulations also have too much simulation time. A good example of this can be seen in the research of R. Caramia and his colleagues [3]. The goal is to create a flexible submodel that can be easily modified and can be run quickly. In the book of L. James and L. John can be found a simple method to parameterise the electric motor losses based on the physical base [4]. This method helps us model a series of BLDC motors. Table 1 contains the main parameters of created motor series.

Table 1 Main parameters of created motor series

Maximum torque	Maximum power
60 Nm	20 kW
100 Nm	40 kW
150 Nm	60 kW
200 Nm	80 kW
250 Nm	100 kW

A framework in Matlab was used for the test which represents a measuring bench. This framework in addition to the motor, it also contains the battery, DC/DC converter, speed controller, inertial moment load, and sensors. Figure 1 contains this framework and the motor.

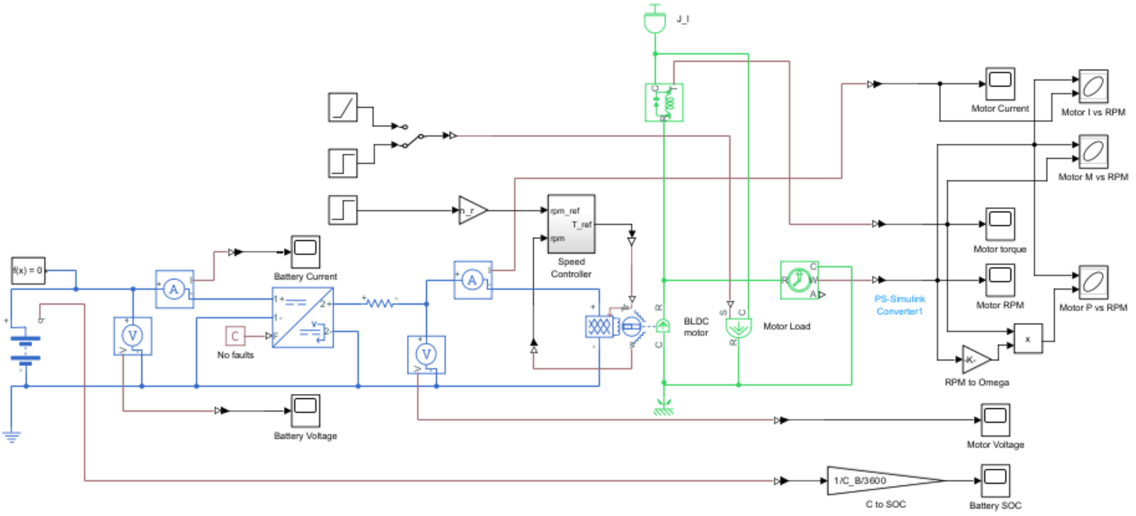

Figure 1 Created framework and the electric motor

It was used the follow equations to calculate the losses, and the efficiency of motor [4].

$$\eta_{\mathrm{m}} = \frac{\text{output power}}{\text{optput power} + \text{losses}} = \frac{\mathrm{T} \cdot \omega}{\mathrm{T} \cdot \omega + \mathrm{k_c} \cdot \mathrm{T}^2 + k_i \cdot \omega + k_w \cdot \omega^3 + C}$$

Where:

$\mathrm{k_c}\left[\frac{W}{Nm^2}\right]$ – copper losses coefficient

$\mathrm{k_i}\left[\frac{W}{\frac{rad}{s}}\right]$ – iron losses coefficient

$\mathrm{k_w}\left[\frac{W}{\left(\frac{rad}{s}\right)^3}\right]$ – windage losses coefficient

C [W] – constant power losses

T [Nm] – motor torque

$\omega\left[\frac{rad}{s}\right]$ – motor speed

The aim of this research is to tune these parameters to generate efficiency maps will similar like a catalogue efficiency map. The generated maps were shown in Figure 2.

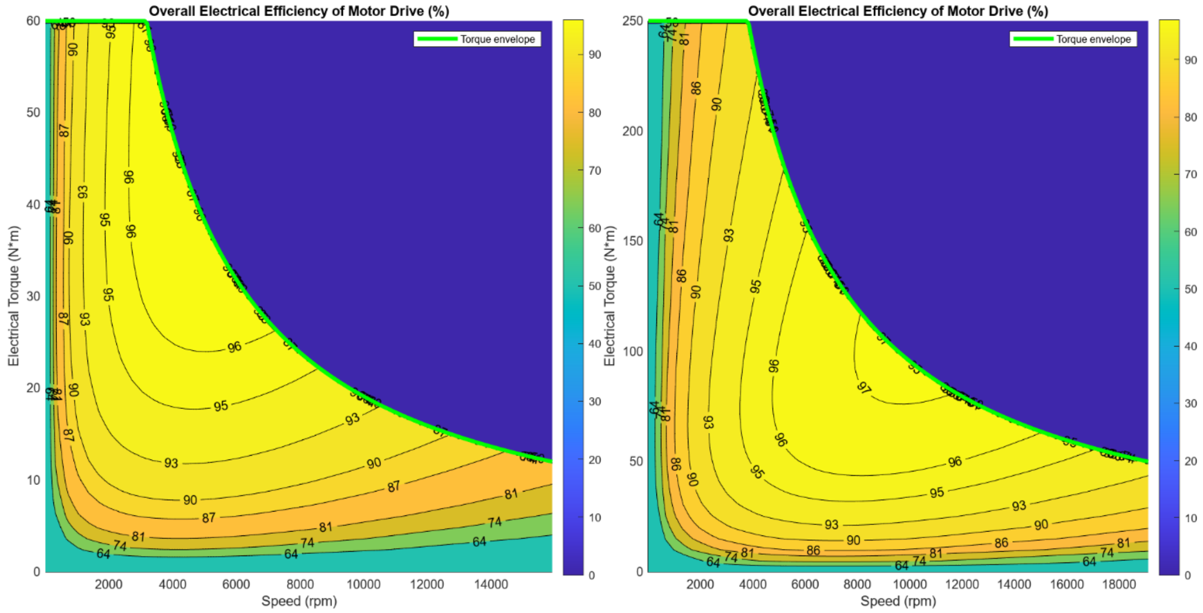

Figure 2 Generated efficiency maps
(Maximum torque 60 Nm and maximum power 20 kW on left,
Maximum torque 250 Nm and maximum power 100 kW on right)

ACKNOWLEDGMENTS

The research was supported by the Thematic Excellence Programme (TKP2020-NKA-04) of the Ministry for Innovation and Technology in Hungary, within the framework of the (Automotive Industry) thematic program of the University of Debrecen.

REFERENCES

[1] R. Wang, Y. Chen, D. Feng, X. Huang, and J. Wang, “Development and performance characterization of an electric ground vehicle with independently actuated in-wheel motors,” *J. Power Sources*, vol. 196, no. 8, pp. 3962–3971, 2011, doi: 10.1016/j.jpowsour.2010.11.160.

[2] H. Patel and H. Chandwani, “Simulation and experimental verification of modified sinusoidal pulse width modulation technique for torque ripple attenuation in Brushless DC motor drive,” *Eng. Sci. Technol. an Int. J.*, vol. 24, no. 3, pp. 671–681, 2021, doi: 10.1016/j.jestch.2020.11.003.

[3] R. Caramia, R. Piotuch, and R. Pałka, “Multiobjective FEM based optimization of BLDC motor using Matlab and Maxwell scripting capabilities,” *Arch. Electr. Eng.*, vol. 63, no. 1, pp. 115–124, 2014, doi: 10.2478/aee-2014-0009.

[4] J. Larminie and J. Lowry, *James Larminie, John Lowry(auth.)-Electric Vehicle Technology Explained, Second Edition (2012).pdf*. 2012.

INVESTIGATING THE EFFECT OF SURFACE ROUGHNESS TYPE ON THE CONVECTION AND RADIATION HEAT TRANSFER INSIDE THE ENCLOSURE

[1]OMLE Issa, [2]ASKAR Ali Habeeb, [3]KOVÁCS Endre
[1]Department of Power Mechanical Engineering, Al-Baath University, Syria
E-mail: issa.j.omle@gmail.com
[2]Department of Fluid and Heat Engineering, University of Miskolc, Hungary
E-mail: 20156@uotechnology.edu.iq
[3]Institute of Physics and Electrical Engineering, University of Miskolc, Hungary
E-mail: kendre01@gmail.com

Keywords: Enclosure, Convection, Radiation, Nusselt, ANSYS.

In the current work, we investigate the convection and radiation heat transfer in a small space as shown in Figure 1, we study two types of wall roughness, triangular and circular, and compare them with the wall without roughness, then we study their effect on the thermal environment of the closed space. We use ANSYS Fluent simulations to do the thermal and dynamic modeling of the two-dimensional cavity, where the left wall is warmer than the right wall, but the upper and lower horizontal walls are adiabatic as shown in Figure 2. We compare the Nusselt numbers in both roughness cases and for two values of the Rayleigh number 10^4 and 10^6 shown in Table 1, which change depending on the characteristic length of the cavity. The results show the temperature contours and Nusselt number curves. In general, it was observed that the roughness had a strong effect on the thermal behavior of the air inside the closed cavity, where the Nusselt number decreases in both cases of roughness, but the largest decrease occurs in the case of triangular roughness and for angles less than 90, which leads to a decrease in the amount of total heat transfer.

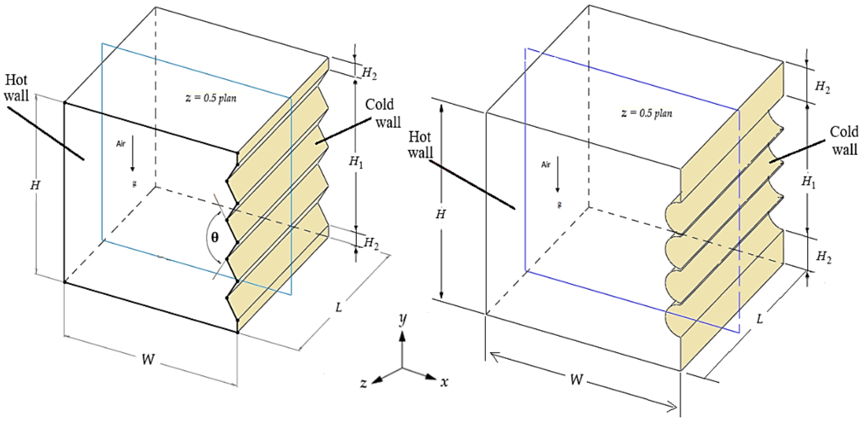

Figure 1 Diagram (3D) of the geometry.

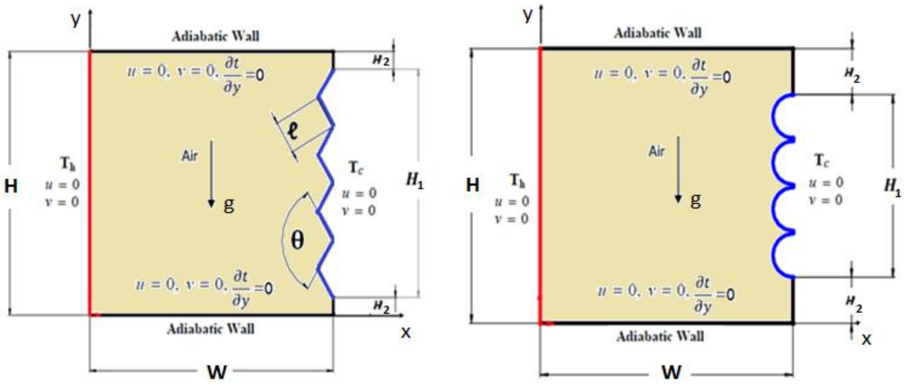

Figure 2 Schematic diagram 2D of the enclosures with boundary conditions.

The Rayleigh number:
$$Ra = \frac{g\beta \Delta T W^3}{\nu\alpha}$$

The total Nusselt number:
$$Nu_{tot} = Nu_{rad} + Nu_{conv}$$

Table 1 Depending on the characteristic length *W*, Rayleigh numbers.

Ra	Width (W) cm	Height (H) cm
10^4	2.1	2.1
10^6	9.7	9.7

One of the results concluded that in the case of radiation with emissivity ε=0.4 and for both Rayleigh numbers 10^4, 10^6, the total Nusselt number of circular rough is smaller than traingular with angles bigger than 90° as shown in Figure 3.

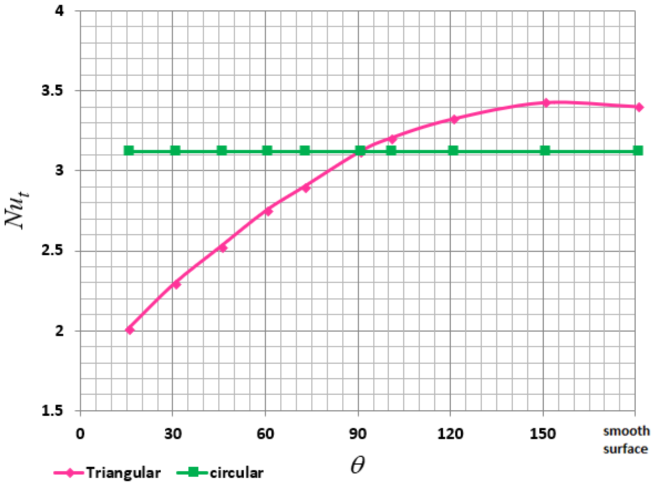

Figure 3 Comparing the Nu_t according to the type of roughness surface in case of ε = 0.4 and for Rayleigh number 10^4

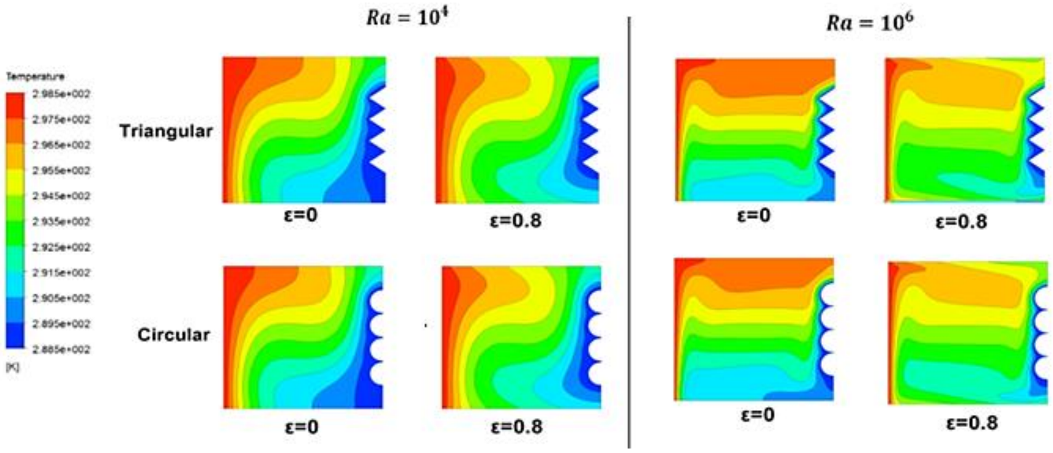

Figure 4 Temperature contours for circular and triangular roughing at the angle 72 °.

The effects of the roughness type can be explained by looking at the temperature contours as shown in Figure 4, where we notice the effect of the roughness on impeding the flow of air, especially inside the rough elements.

REFERENCES

[1] Iyi, D., & Hasan, R. (2015). Natural Convection Flow and Heat Transfer in an Enclosure Containing Staggered Arrangement of Blockages. United Kingdom: ELSEVIER,ScienceDirect.

[2] Altaee, A. H., Ali, F. H., & Mahdi, Q. A. (2017). Natural Convection Inside Square Enclosure Containing Equilateral Triangle with Different Orientations. Babylon: Journal of Babylon Univ ersity/Engineering Sciences/ No.(4)/ Vol.(25): 2017.

[3] Kane, M. K., Mbow, C., Sow, M. L., & Sarr, J. (2017). A Study on Natural Convection of Air in a Square Cavity with Partially Thermally Active Side Walls. Dakar, Senegal: Open Journal of Fluid Dynamics , 7, 623-641.

[4] Thakur, S., & Kumar, S. (2016). Impact Of Radiation Models In CFD Simulations Of Natural Convection Heat Transfer In A Side Heated Square Cavity. INDIA: International Journal for Research in Applied Science & Engineering Technology (IJRASET).

EXAMINATION OF HYDROLYSIS-RESISTANT POLYKETONE AND ITS APPLICATION POSSIBILITIES IN THE INDUSTRY

POLYÁKNÉ KOVÁCS Annamária, TAMÁSI Kinga, SZABÓ Tamás József
Hungary Ceramic and Polymer Engineering Department. University of Miskolc, Hungary
E-mail: kovacs.annamaria.uni@gmail.com , polkinga@uni-miskolc.hu , polsztam@uni-miskolc.hu

Keywords: polyketone, glass fiber, hydrolysis, chemical resistence, polyamide

The polyketone is a very promising engineering plastic wich is very enviroment-friendly since carbon monoxide is also used during production. Polyketone belongs to the group of high-performance plastics, a type of material with a partially crystalline structure and excellent technical properties. Several types of composites are known: without reinforcement, - graphite, carbon and fiberglass, and a variant containing a combination of these. It is also used in the aerospace, nuclear and chemical industries. In the automotive industry, the replacement of metals with plastic is still current. Today, this is encouraged not only by increasingly strict regulations on fuel consumption and weight reduction, but also by the greater freedom in terms of design and shapes, as well as the reduction of production costs, which can be achieved by using plastics. Many types of reinforced plastics and composites are used in the automotive industry. By combining different base polymers and reinforcing fibers, the desired mechanical and other properties can be well adjusted.

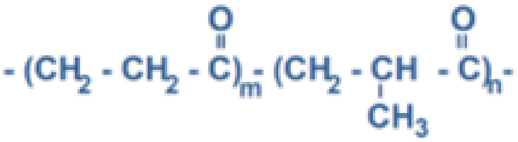

$$-(CH_2-CH_2-\overset{\overset{O}{\|}}{C})_m-(CH_2-\underset{CH_3}{CH}-\overset{\overset{O}{\|}}{C})_n-$$

Figure 1 Chemical formula terpolymer polyketone [1]

Among my tests was the moisture absorption test, which I carried out for 500 hours and 70 °C / 62 % relative humidity. The evaluated results are illustrated in Figure 2. There are polymers capable of absorbing moisture (1- 5% by weight) that affects their properties (e.g. polyamides, polyesters, natural polymers, some fiber-reinforced composites). These polymers are called hydrophilic polymers. Moisture has a softening effect, i.e. it reduces the modulus of elasticity, strength and increases the elongation at break [2].

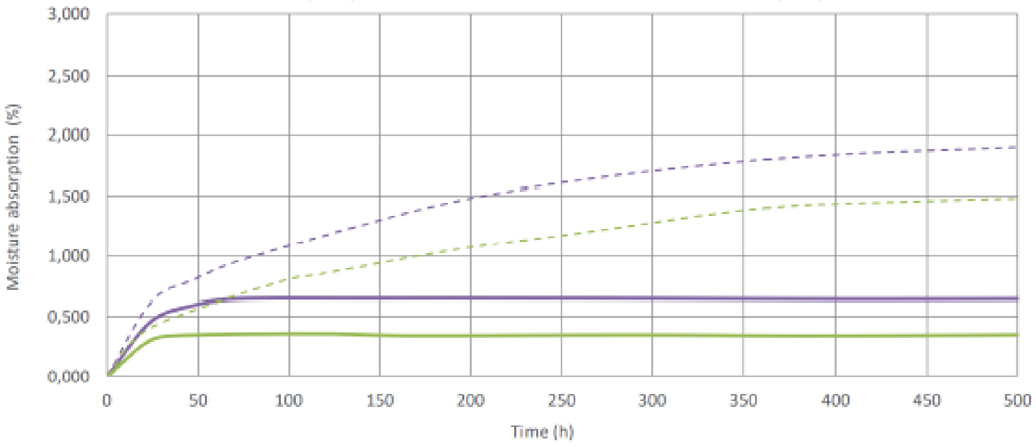

Figure 2 Moisture absorption 500 h 70 °C / 62 % rel. humidity [2]

Chemical resistance test: During the above test, I examined and compared the chemical resistance between polyamide and polyketone. After 25 days at 80 °C, it is clearly visible that the yield stress in the case of polyamide was significantly reduced under the influence of all media. In all cases, the polyketone showed almost the same value as after reaction with the solutions, as shown in Figure 3.

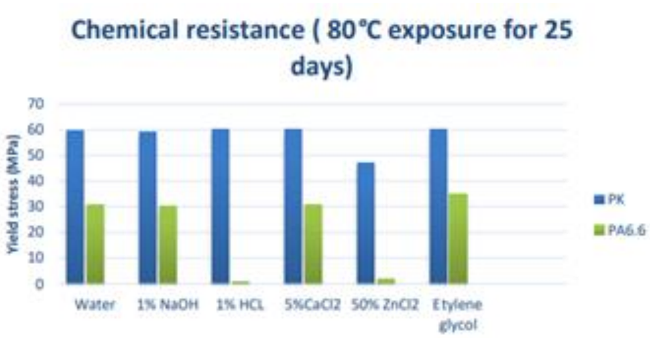

Figure 3 Comparison of the yield stress of Polyketone and Polyamide after reacting in different chemical solutions

VW TL 52682 test : Ethylene glycol is used as cooling water that removes heat from the environment in applications such as radiator end tanks, cooling pipes, oil filters, gas caps and expansion tanks. The most important parameter to consider when choosing the materials used in these critical components is the component aging in the presence of ethylene glycol at temperatures between 120-140 °C. Therefore, appropriate material selection is the most important requirement for cooling system applications. [3.]

Test parameters:
- *Temperature: 135 °C*
- *Coolant: G12evo/water (50/50)*
- *Requirement: Flexural strength after 1000 hours > 25 MPa*

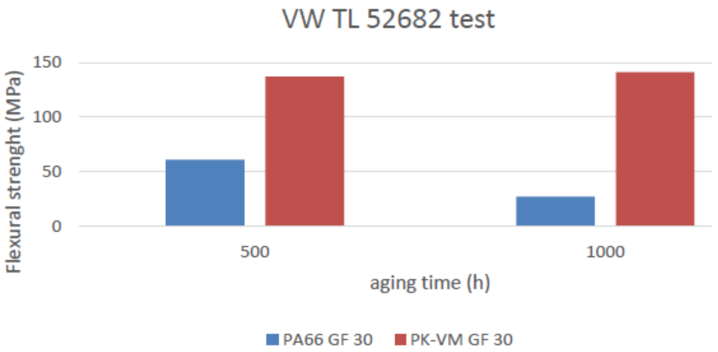

Figure 4 Examination of the change in flexural strength based on VW TL 52682 test in g12evo/water medium polyketone and polyamide

During the VW TL 52682 test, the most important requirement is that after 1000 hours the bending strength reaches a minimum of 25 MPa. Figure 4 shows that the polyamide specimen has just reached the desired value after 1000 hours. The polyketone produced an even higher value after the test time than the result measured after 500 hours. [4.]

REFERENCES

[1] https://www.pslc.ws/mactest/ketone.html
[2] Baschek, G., Hartwig, G., & Zahradnik, F. (1999). Effect of water absorption in polymers at low and high temperatures. Polymer, 40(12), 3433–3441. doi:10.1016/s0032-3861(98)00560-6
[3] Hydrolysis Resistance and Mechanical Property Changes of Glass Fiber Filled Polyketone Composites Upon Glass Fiber Concentration Sung Min Kim and Kwang-Jea Kim, Elastomers and Composites Vol. 52, No. 1, pp. 1~8 (March 2017).
[4] M. Lee, H. Kim, and M. Y. Lyu, "A Study on Warpage of Glass Fiber Reinforced Plastics for Part Design and Operation Condition: Part 2. Crystalline Plastics", Polymer(Korea), 36, 677 (2012).

CONTINUOUS CONCENTRATION MEASUREMENT OF ORGANIC AIR POLLUTANT COMPONENTS IN GAS STREAM

POÓS Tibor, SZÁVICS Nikolett
Department of Building Services and Process Engineering, Faculty of Mechanical Engineering, Budapest University of Technology and Economics, Hungary
E-mail: poos.tibor@gpk.bme.hu , szavnik@gmail.com

Keywords: organic air pollutants, measuring instrument, ethanol, methanol, ethyl-acetate

Monitoring air quality is extremely important regarding environmental protection and human health protection. For this reason, gases have become the defining quantities to be measured in industrial and domestic activities. From an examination point of view, the possible places of the flow of air pollutants into the environment should be distinguished.

A typical source of air pollution from industrial work is the point source [1], a source with concentrated parameters, mostly high chimneys and vents located at power plants and industrial sites. A gas concentration measuring device installed here can calculate the volume flow of the outgoing gas stream and the concentration of air pollutants, and thusly the number of harmful components entering the environment can be determined from the data. The authority orders continuous measurement and data recording if the emitted pollutant concentration regularly exceeds the limit value. The sensors' task in concentration measurement is to provide an electrical signal proportional to the concentration, received by an evaluation instrument and converted into a readable signal, accompanied, where appropriate, by an acoustic and visual sign. To measure the concentration of gases belonging to the group of volatile organic compounds (VOCs), the following measuring sensors are widely used: photoionization meter (PID), infrared gas concentration meter, flame ionization (FID) device, sensor operating on the principle of catalytic combustion, and occasionally metal-oxide (MOS) sensors.

In our research, we had to propose continuous and online measurements of the concentration of ethanol, methanol, and ethyl acetate released into the environment in the fermentation technology of an industrial alcohol-producing distillery. Table 1 shows the pollutant concentration values and mass flows measured by the control authority at the point source of the distillery at a given time. The environmental protection limit values for both concentration and mass flow are given in the table. The indices in concentrations and mass flows refer to the serial number of the measurement.

Table 1. Measured and limited values of VOCs measured in point source

Components	***Limit values***		***Values measured at the point source***					
	c	$\dot{m}$	c_1	$\dot{m}_1$	c_2	$\dot{m}_2$	c_3	$\dot{m}_3$
	mg/m^3	*kg/h*	*mg/m*^{3}	*kg/h*	*mg/m*^{3}	*kg/h*	*mg/m*^{3}	*kg/h*
1. methanol	100,0	2	2,93	0,025	0,85	0,053	20,22	0,097
2. ethanol + ethyl-acetate	150,0	3	265,95	2,261	341,83	2,123	323,39	1,552
3. methanol + ethanol + + ethyl-acetate	150,0	3	268,88	2,286	342,68	2,176	343,61	1,649

The values marked red in Table 1 exceeded the permissible limit. It can be seen that the concentrations are around very low values. Thus, an effective concentration meter is necessary for their continuous monitoring, even at low values.

Based on official regulations, calculations, and available data, the expectations and conditions for the measuring device are summarized in Table 2.

The table does not contain recommendations and specifications for the installation and maintenance of the instrument, so the list of requirements should be supplemented by the following:

- Regular preventive maintenance of the measuring systems shall be carried out by the operator at the frequency specified by the manufacturer.
- The measuring system must be operated so that it prevents unauthorized access and changes in results.
- The control calibration of the measuring instruments belonging to the continuous measuring instrument must be carried out annually. After the commissioning, conversion, or repair of measuring devices and measuring systems, a control calibration must be carried out in all cases, which can also be carried out on-site.

Table 2. List of requirements for instrument selection

No.	***Appellation***	***Depiction***	***Value***
1.	Measured components	methanol,	CH_3OH
		ethanol	C_2H_5OH
		ethyl-acetate	$C_4H_8O_2$
2.	Accuracy	instrument sensitivity	0,1 *ppm*
3.	Sampling	averaging multiple measurements	~5 *min*
4.	Measured parameters	concentrations:	minimum range:
		methanol	0-100 mg/m^3 0- 77 *ppm*
		ethanol	0-150 mg/m^3 0-80 *ppm*
		ethyl-acetate	0-150 mg/m^3 0-42 *ppm*
5.	Alarm	At exceeded limit value	>77*ppm* (metanol) >80 *ppm* (etil-alkohol) >42 *ppm (*etil-acetát)
6.	RH%	relative humidity	0-100%
7.	Auditing	audited instrument	Type-Approval Certificate

In Hungary, gas analyzers and dust measuring devices used for measuring air pollution and air pollution levels, suitable for continuous measurement, must have a type of approval certificate [2]. By studied the list of type-approved instruments [3] can be classified into the following areas of application:

- Continuous concentration measurement devices for flue gas emissions from combustion equipment, waste incinerators, and other power plants.
- Equipment for continuous measurement of the PM10 and PM2.5 fractions of airborne dust in ambient air.
- Stationary emission sources (stoker power plants, waste incinerators, and other power plants) emission meters.
- Measurement of ambient air components.
- Multi-component emission measuring systems.

The type list of 220 instruments offered few options for measuring volatile organic compounds with such a low minimum limit of measurement. Two devices were selected from the list that meets specific criteria, these are the SICK MCS100 FT and the ABB ACF5000. They provide continuous monitoring, not only for organic gases. The disadvantage of their application is that they cannot be used in the case of gases with saturated or near-saturation humidity content, which in this case is prevailing at the point source. The relative humidity can be reduced, but this requires the installation of an additional unit, which makes the measurement process more expensive.

In the case of the examined components, the instruments aggregate the VOC concentration in the gas stream, so other components are also included in the final concentration value. No instrument fully meets the requirements in the list of instruments with a type approval certificate. Therefore we also looked for instruments that are not on the list but can be found commercially. Infrared, PID, FID, and the catalytic principle are what can measure the required alcohol concentrations in the smallest possible measurement range. During the search, we found that there is no adequate instrument that, in addition to the low measurement limits, could continuously measure the concentration of each component in a gas stream saturated with humidity. Thus, it could be a solution if the National Authority for Environment and Nature Conservation does not request the concentration of each component separately but prescribes the limit value in total VOC because there are already audited measuring devices for this case.

ACKNOWLEDGEMENT

This work was supported by the Hungarian Scientific Research Fund (NKFIH FK-142204).

REFERENCES

[1] Endre D. D., „Levegőtisztaságvédelem” (Air quality protection), p. 247.

[2] W. K. H. Kft, „6/2011. (I. 14.) VM rendelet a levegőterheltségi szint és a helyhez kötött légszennyező források kibocsátásának vizsgálatával, ellenőrzésével, értékelésével kapcsolatos szabályokról - Hatályos Jogszabályok Gyűjteménye”. https://net.jogtar.hu/jogszabaly?docid=A1100006.VM (08/23/2022).

[3] „OLM - Típusjóváhagyási (korábban: Típusalkalmassági felülvizsgálati) igazolással rendelkező gázelemzők és pormonitorok (2002-2021)”. http://www.levegominoseg.hu/tipuslista (08/31/2022).

CHARACTERISTIC FUNCTIONS OF A BATCH, CONVECTIVE DRYING

POÓS Tibor, SZABÓ Viktor, RASHED A. Rashed
Department of Building Services and Process Engineering, Faculty of Mechanical Engineering, Budapest University of Technology and Economics, Hungary
E-mail: poos.tibor@gpk.bme.hu , szabo.viktor@gpk.bme.hu , rashed@edu.bme.hu

Keywords: convective drying, drying rate, drying periods

By graphing experimentally established rates of drying N versus the solid's moisture content X, the drying kinetics are assessed (Doran, 2013). A drying rate curve is the end outcome, as seen in Figure 1/d. The drying material's size, thickness, and drying conditions all impact how the drying rate curve looks. Moreover, constant drying conditions, such as constant air temperature, flow rate, humidity, and flow direction, are used to determine drying rate curves. However, under constant drying conditions — which only apply to the gas phase — the moisture content and other solid properties change (Doran, 2013), which defines the steady state. It may be thought of as remaining constant throughout the whole drying process. Internal heat and moisture diffusivities substantially impact the process during the period of falling drying rate. Therefore, it is also important to determine these coefficients.

Figure 1 shows the drying rate curve with constant drying conditions of three cases for different initial solid material temperatures represented by A, B and C curves based on lower initial temperature to wet bulb temperature and the higher initial temperature according to constant drying conditions. The solid material have a significant water content once drying gets started. The first water to evaporate after a warming-up comes from the wet solid's surfaces that are in direct touch with the air stream passing across them, represented on the drying curve as the initial period (I) as shown in Figure 1. The temperature of the drying material approaches the equilibrium temperature while cooling or heating, where the wet bulb temperature is formed, represented in Figure 1/b of the drying operation where the three curves of A, B and C meet. This period can usually be ignored because it is the shortest in thorough drying.

The surface remains saturated with water if water is supplied via mass transfer from within the solid to the surface at a fast enough rate. A period of constant drying rate is represented by the second period (II) of Figure 1. Heat and mass transfer occur at the surface of the solid during the constant drying rate period because the surface is continuously moist, allowing free water always to be accessible for evaporation. As a result, the material's external gas boundary layer is where the heat and mass transfer resistances are placed. In contrast, the wetted mass in means of the moisture content of the particle will keep decreasing with time, as shown in Figure 1/a and 1/c of the second period (II). Under constant drying conditions, the heat and mass transfer coefficients on the gas side are constant. It should be noted that the constant decrease in the material's vapor diffusivity at the surface layer causes the transport coefficients on the gas side to vary likewise during this time.

A critical moisture content X_{cr}, is attained with further drying as the solid's water content declines, as shown in Figure 1/c, which depicts the beginning of the third period (III). At this moment, the process enters the period of falling drying rate in the third period (III) of Figure 1, and the drying rate starts to slow down. A change in the system's mass and/or heat transfer conditions can be seen in the decrease in the drying rate below X_{cr} at the beginning of the falling drying rate period. There is no longer a continuous or almost continuous liquid coating at the surface of the solid during the initial stages of the falling rate period as the drying surface becomes partially unsaturated. This would be the last stage of drying over time. Here comes the fourth period of the drying curve (IV) until the surface is completely dry where the three curves go to the maximum drying point. Still, before this, the evaporating surface effectively moves deeper into the material as drying progresses as a solid layer of dried material accumulates at and then below the surface, requiring heat to be carried by conduction to the remaining water farther inside the solid. The heat transfer rate decreases over time because the dried solid near the surface is often a poor heat conductor.

The drying rate of the fourth period (IV) decreases, and the process is known as hindered drying or diffusion, as internal resistances restrict heat and mass transfer entirely. Consequently, the material's temperature rises to a level equivalent to the drying gas's inlet temperature T_G. Up until it gets close to the equilibrium moisture content X_{dP}, where the material dries at an ever-slower rate. The solid's moisture content declines even more. This is the lowest moisture content produced at the drying process's chosen temperature and relative humidity at the end of the fourth period (IV).

The drying curve N of each different initial temperature of the three cases has one drying rate curve after the end of the first period (I), which is seen in Figure 1/e.

When the drying rate curves are calculated for a given material under various conditions, they appear to be geometrically similar. They are only a function of how much drying has taken place (Mujumdar, 2006).

All these curves may frequently be approximated to a single curve, or "characteristic," as shown in Figure 1/f. of a particular substance if they were normalized with respect to the beginning drying rate and average moisture content.

To calculate the characteristic drying rate:

$$f = \frac{N}{N_{const}} \tag{1}$$

and the characteristic moisture content:

$$\Phi = \frac{X - X_{dP}}{X_{cr} - X_{dP}} \tag{2}$$

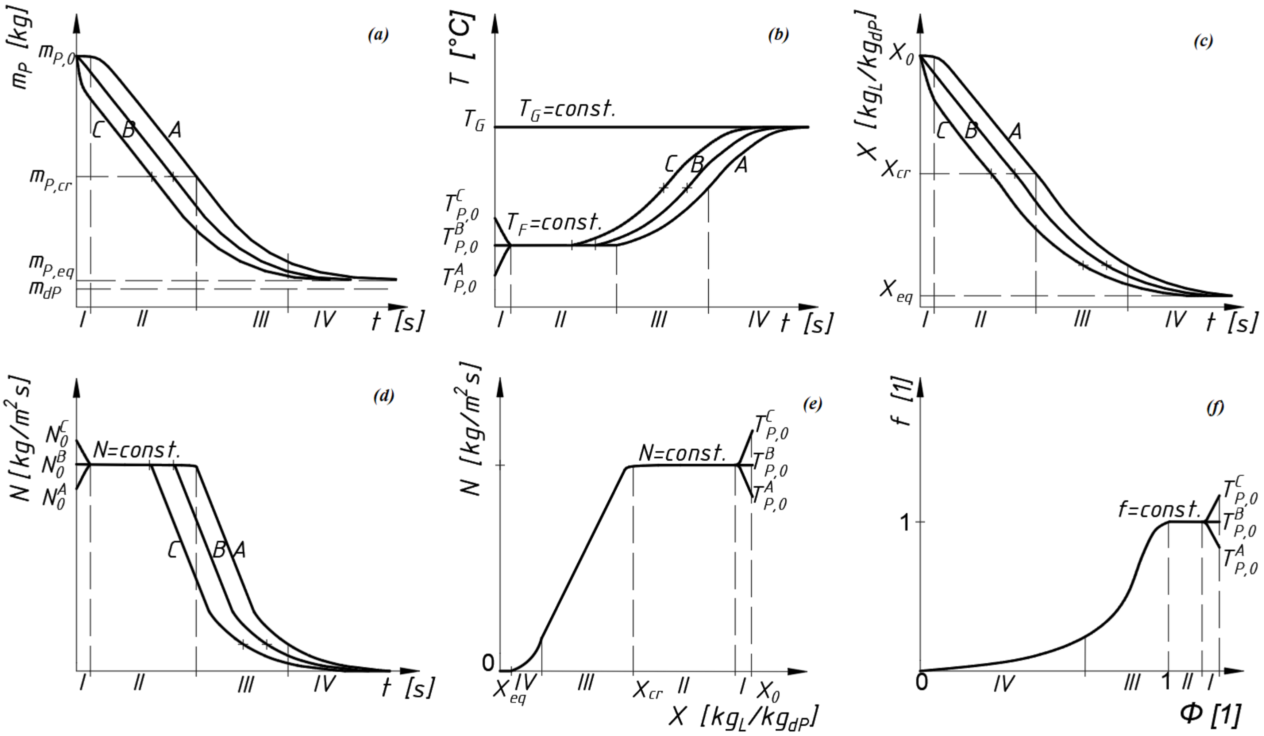

Figure 1 Drying curves of a batch, convective drying for constant drying conditions of three cases for different initial solid material temperature: a) change of the wet mass of the material with drying time, b) change of the temperatures with drying time, c) change of the material's moisture content with drying time, d) change of the drying rate with drying time, e) change of the drying rate with moisture content on wet basis, f) change of the characteristic drying rate with characteristic moisture content

ACKNOWLEDGMENTS

This work was supported by the Hungarian Scientific Research Fund (NKFIH FK-142204).

REFERENCES

[1] Doran, P. M. (2013). *Unit Operations.* Bioprocess Engineering Principles, Academic Press. 445–595.
[2] Mujumdar, A. S. (2006). *Handbook of Industrial Drying.* CRC Press, Bota Racon.

EFFECT OF SURFACE-MODIFIED NANOPARTICLES ON OIL RECOVERY EFFICIENCY AND THE MECHANISM UNDERLIES THIS EFFECT

QASEM Rabea Hussein Mohammed
Institute of Physical Metallurgy, Metal Forming and Nanotechnology, University of Miskolc, Hungary
E-mail: rabeagasem@gmail.com

Keywords: Nanoparticles, Petroleum, Surface-Modified Nanoparticles, Enhanced Oil Recovery

PROBLEM STATEMENT

Most oil fields around the world have achieved the stage where the total production rate is nearing the decline phase. According to the International Energy Agency (IEA), crude oil is expected to contribute approximately with 26% of the world's energy supply by 2040. Nanoparticles (NPs) have the potential to profoundly change EOR and to improve mechanism of recovery.

Although application of (NPs) has proven an effective role as an agent to recover more oil trapped in the reservoir, the necessity of their modification with some additives for improvement oil recovery is not fully highlighted yet. There is a lack of fundamental understanding- from view of some studies- about the efficiency of surface-modified nanoparticles in Enhancing Oil Recovery. In addition, the nature of the interactions that occur between these surface-modified NPs and the porous media in the oil fields is still a thorny issue. Therefore, this paper reviews the most recent studies related to the effect of surface-modified NPs on Enhance Oil Recovery and their interactions with rock properties and reservoir fluid.

OBJECTIVE

The objective of the current research is to know the effect of surface–modified NPs in EOR. Particularly, the study has the following sub-objectives:

- To clarify the effect of surface-modified NPs on the efficiency of oil recovery.
- To show the difference between efficiency of surface- modified NPs/and unmodified NPs in EOR.
- To know the mechanism underlies effect the surface – modified NPs on EOR.
- To understand the interactions among surface–treated NPs, rock properties and reservoir fluid.

RESEARCH SIGNIFICANCE

The significance of this paper is to show how the use the surface-modified NPs can achieve higher results in the oil recovery, unlike the unmodified ones. This can lead to achieve better oil recovery. This study also will try to clarify the importance of modifying NPs before they are injected into reservoir to overcome the limiting conditions of the reservoir, such as pressure, temperature, and salinity, which prevent NPs from achieving more oil recovery.

RESEARCH QUESTIONS

The research is conducted to answer the following questions:

- What are the challenges that limit the use of NPs in EOR?
- Do the surface-modified NPs assist to meet reservoir conditions to improve oil recovery?
- Is oil displacement by surface- modified NPs more efficient than using unmodified NPs?
- What are the mechanisms leading to increase oil recovery by surface-modified nanofluids?

CONCLUSION

This study reviewed the summary of previous studies on the effect of surface-modified nanoparticles on the enhanced oil recovery. Based on these studies results the following conclusions can be drawn:

(1) Surface-modified nanoparticles have more oil recovery efficiency than unmodified ones
(2) The mechanism underlies this effect is that the modification of the nanoparticles in the surface helps to change the properties of the injected fluid.
(3) Modifying the nanoparticles before injecting, makes them more stable and thus the results more effective.
(4) Surface-modified nanoparticles are more capable in the reduction of IFT and the alteration of wettability.

We recommend conducting further studies and expanding the laboratory experiments, taking into consideration the necessity of linking them in field applications.

Table 1 Summary of Studies on Oil Recovery Using Surface- Modified Nanoparticles

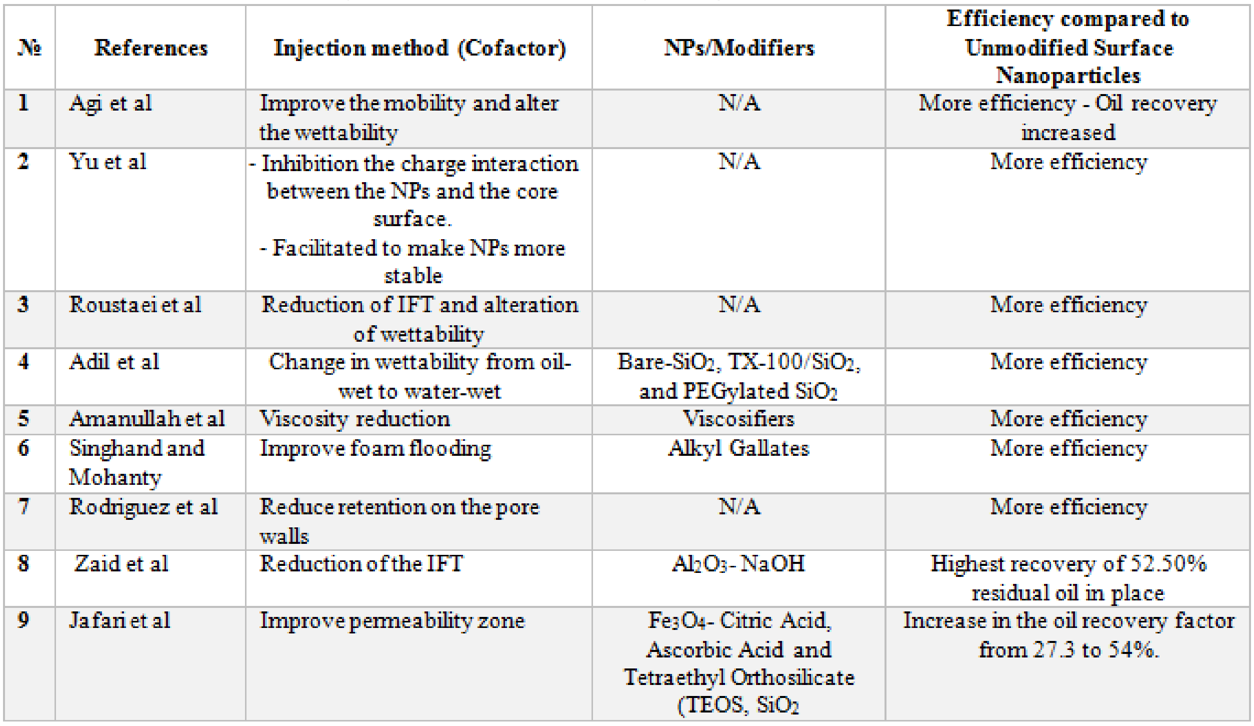

№	References	Injection method (Cofactor)	NPs/Modifiers	Efficiency compared to Unmodified Surface Nanoparticles
1	Agi et al	Improve the mobility and alter the wettability	N/A	More efficiency - Oil recovery increased
2	Yu et al	- Inhibition the charge interaction between the NPs and the core surface. - Facilitated to make NPs more stable	N/A	More efficiency
3	Roustaei et al	Reduction of IFT and alteration of wettability	N/A	More efficiency
4	Adil et al	Change in wettability from oil-wet to water-wet	Bare-SiO_2, TX-100/SiO_2, and PEGylated SiO_2	More efficiency
5	Amanullah et al	Viscosity reduction	Viscosifiers	More efficiency
6	Singhand and Mohanty	Improve foam flooding	Alkyl Gallates	More efficiency
7	Rodriguez et al	Reduce retention on the pore walls	N/A	More efficiency
8	Zaid et al	Reduction of the IFT	Al_2O_3- NaOH	Highest recovery of 52.50% residual oil in place
9	Jafari et al	Improve permeability zone	Fe_3O_4- Citric Acid, Ascorbic Acid and Tetraethyl Orthosilicate (TEOS, SiO_2	Increase in the oil recovery factor from 27.3 to 54%.

REFERENCES

[1] Adil, M., Mohd Zaid, H., Raza, F. and Agam, M.A., 2020. Experimental evaluation of oil recovery mechanism using a variety of surface-modified silica nanoparticles: Role of in-situ surface-modification in oil-wet system. PloS one, 15(7), p.e0236837.

[2] Agi, A., Junin, R. and Gbadamosi, A., 2018. Mechanism governing nanoparticle flow behaviour in porous media: insight for enhanced oil recovery applications. International Nano Letters, 8(2), pp.49-77.

[3] Amanullah, M., AlArfaj, M.K. and Al-abdullatif, Z.A., 2011, January. Preliminary test results of nano-based drilling fluids for oil and gas field application. In SPE/IADC drilling conference and exhibition. Society of Petroleum Engineers.

[4] Jafari, A., Hasani, M., Vafaei-Sefti, M., Fakhroueian, Z. and Baghbansalehi, M., 2020. Surface modification of synthesized Fe 3 O 4 super-paramagnetic NPs and performance investigation in gelation parameters enhancement: application in enhanced oil recovery. Applied Nanoscience, 10(3), pp.955-969

[5] Rodriguez Pin, E., Roberts, M., Yu, H., Huh, C. and Bryant, S.L., 2009, January. Enhanced migration of surface-treated NPs in sedimentary rocks. In SPE annual technical conference and exhibition. Society of Petroleum Engineers.

[6] Roustaei, A., Saffarzadeh, S., Mohammadi, M.: An evaluation of modified silica nanoparticles, efficiency in enhancing oil recovery of light and intermediate oil reservoirs. Egypt. J. Petrol 22, (2013).

[7] Singh, R. and Mohanty, K.K., 2016. Foams stabilized by in-situ surface-activated NPs in bulk and porous media. SPE Journal, 21(01), pp.121-130.

[8] Sun, X., Zhang, Y., Chen, G. and Gai, Z., 2017. Application of NPs in enhanced oil recovery: a critical review of recent progress. Energies, 10(3), p.345.

[9] Yu, J., Berlin, J.M., Lu, W., Zhang, L., Kan, A.T., Zhang, P., Walsh, E.E., Work, S., Chen, W., Tour, J. and Wong, M., 2010, January. Transport study of NPs for oilfield application. In SPE International Conference on Oilfield Scale. Society of Petroleum Engineers.

[10] Zaid, H.M., Radzi, N.S.A., Latiff, N.R.A. and Shafie, A., 2014, October. Effect of morphology of aluminium oxide NPs on viscosity and interfacial tension (IFT) and the recovery efficiency in enhanced oil recovery (EOR). In AIP Conference Proceedings (Vol. 1621, No. 1, pp. 705-710). American Institute of Physics.

GEOMETRIC ANALYSIS OF SPLINE SHAFTS USING SURFACE ROUGHNESS PROFILOMETER AND 3D SCANNER

ROY Atosi, BODZÁS Sándor
Department of Mechanical Engineering, Faculty of Engineering, University of Debrecen, Hungary
E-mail: atosiroy@mailbox.unideb.hu, bodzassandor@eng.unideb.hu

Keywords: surface roughness, spline shaft, fretting wear, 3D scan, manufacturing accuracy.

Surface roughness is a strong quantitative indicator of manufacturing precision and wear of machine parts due to irregular operation, i.e., excessive friction, heat and electric current conduction, tightness of contact joints, and positional accuracy [1]. However, precise surface roughness measurement for characterization of wear in rotating machine parts, arising from lack of lubrication and misalignment, is difficult and often time-consuming. In this work, surface roughness parameters of two 21 cm spline shafts made of alloy steel through plain milling technology were measured using a profilometer OPT surface roughness measurement machine, and the findings were utilized to identify the capacity of a high-tech 3D scanner tool, the GOM 3D metrology high precision scanner, in identifying the manufacturing precision of those shafts. The profilometry was completed by traversing a 2-µm chisel stylus at 0.5 mm/s on the top and side surfaces of the spline shafts teeth (Figures *1 and 2*). In total, 12 surface roughness parameters were measured from the data, including eight amplitude parameters, one spacing parameter, one hybrid parameter, and two material ratio parameters. The roughness and spacing parameters provided information on the teeth's shape profile, while the material ratio parameters detailed the potential wear.

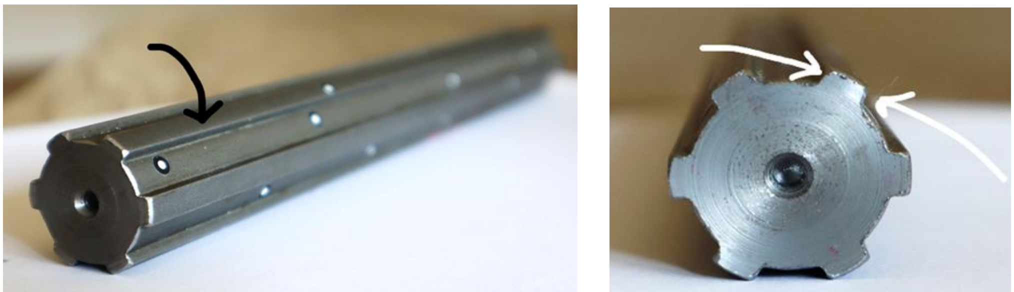

Figure 1 (left) Top surface and (right) left- and right-hand surfaces of the [specify material name] spline shaft, where profilometry was completed

Figure 2 OPT surface roughness measurement machine

Table 1 Average roughness, Ra comparison for top and side surfaces of both shafts

R_a (µm)	Teeth	1	2	3	4	5	6
Shaft 1	Top	3,232	3,220	3,095	3,122	2,960	3,096
	Side	1,503	1,629	1,627	1,794	1,860	1,354
Shaft 2	Top	3,920	3,117	3,510	3,703	4,304	3,556
	Side	1,307	1,689	1,854	1,536	1,600	1,789

Shaft-2 showed an overall higher surface roughness amplitude compared to shaft-1 highlighting better manufacturing precision (*Figure 3*). However, the average roughness of the side surfaces of the teeth (for both shafts) was significantly lower compared to the top, which could be attributed to the high-precision machine tools used for machining the tooth profile. This is also indicative of the less-used state of the shafts.

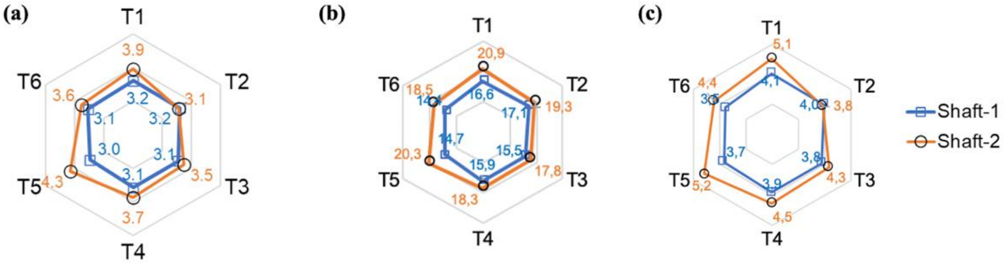

Figure 3 Comparison of the roughness amplitude parameters hinted at better manufacturing precision of Shaft-1; Polar plot of (a) average, (b) maximum, and (c) root-mean-square roughnesses of Shaft-1 and Shaft-2

Also, in order to determine the manufacturing precision of the spline shafts, they were scanned using a sophisticated and high-tech 3D scanner, and the deviation was compared to the standard CAD model of the shafts. Initial results show that surface roughness measurements can be used to improve the accuracy of manufacturing.

ACKNOWLEDGMENTS

The described work was carried out as part of a project supported by the TALENTUD council at University of Debrecen.

REFERENCES

[1] Gadelmawla ES, Koura MM, Maksoud TMA, Elewa IM, Soliman HH. *Roughness parameters*. J Mater Process Technol. 2002;123(1):133-145.

[2] Bodzás Sándor. *Manufacturing of the surfaces of spline fitting connection*. The International Journal of Advanced Manufacturing Technology. 2020;111(3-4):909-920.

[3] Cufaro V, Curà F, Mura A. *Surface characterization of spline coupling teeth subjected to fretting wear.* Procedia Engineering. 2014;74:135-142.

[4] He Y, Zhang W, Li Y, Wang Y, Wang Y, Wang S. *An approach for surface roughness measurement of helical gears based on image segmentation of region of interest.* Measurement. 2021;183:109905.

INFLUENCE OF ION IMPLANTATION ON TOOL STEEL

SKORIC Branko, TEREK Pal, KOVACEVIC Lazar, TEREK Vladimir, BOBIC Zoran, KUKURUZOVIC Dragan
Department for Production Engineering, University of Novi Sad, Novi Sad, Serbia
E-mail: skoricb@uns.ac.rs

Keywords: Nanomodification, ion implantation, Kr, ultra precision machining.

The importance of nanomodifications in technology development has been growing, especially in development of new generation of tools. The development trend of precision and ultra precision machining clearly shows that we are dealing with up to few tens of nanometers in size. Therefore, depth of modification of tools should be between 30-100nm. We will give some preliminary results of investigations of possibilities of nanomodification by Kr ion implantation.

This is simply the result of the technology development trend set by Taniguchi [1]. According to this reference, nanometer accuracy has already been achieved in ultra precision machining. Tool lifetime depends directly on the surface phenomena which occur during exploitation, mainly on adhesive and abrasive wear.

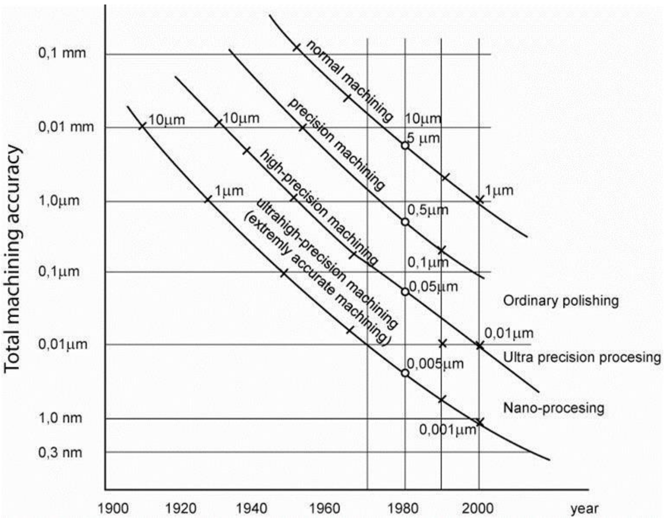

Figure 1 Trends in precision machining by Taniguchi [1]

If it is taken into account that ultra precision tools require nano modifications in the range of 100nm, ion implantation appears to be not only the most appropriate technique, but the only possible solution having in mind the type of machining, type of tools, as well as type of exploitation conditions. Ion implantation was believed to be a revolutionary surface treatment called to solve many wear and corrosion problems of metallic tools and components [2]. Krypton ions have been implanted in steel substrates using mVINIS Ion Source. The mVINIS Ion Source shown in Figure 2. The mVINIS Ion Source is an ECR (electron cyclotron resonance) ion source with multiple applications.

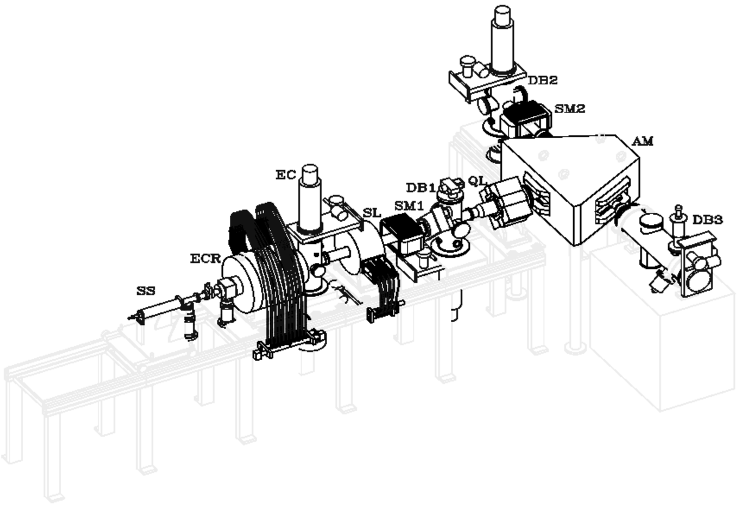

Figure 2 mVINIS Ion Source as a complete heavy ion injector

In our work we had used two different types of steel. The reason was that these steels have different machinability due to the difference in steel structure caused by the different percentage of carbon and alloying elements present. The base of the 100Cr6 steel is consisted of uniform martensite so we decided to present only these results in this paper. The stopping of ions in a material as uniform as steel 100Cr6 will be on a different depth comparing to the material with a non-uniform structure like for example high speed steel - M2.

In this paper Kr8+ ions with the energy of 120 keV and Kr11+ ions with the energy of 180keV were used. The Krypton spectrum is shown in Figure 3.

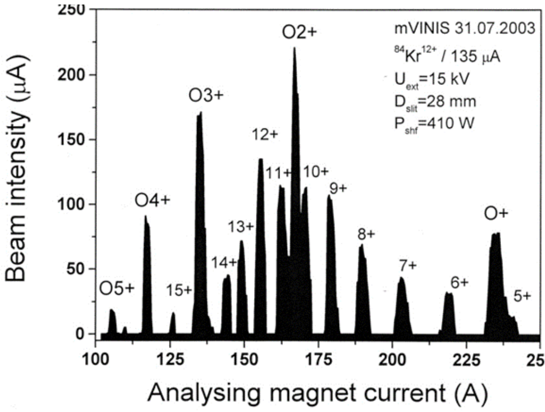

Figure 3 Krypton spectrum

The results of friction coefficient measurements are presented in the table 1. Two different loads were applied and significant differences in friction coefficients were obtained. Results presented in the table 1 are average values of several measurements. Hard metal was used as a counter material during measurements.

Table 1. Friction coefficients

Steel	Friction coefficient μ, F=10N	Friction coefficient μ, F=100N
100Cr6	0.035	0.09
100Cr6 implanted with Kr^{8+}	0.02	0.062
100Cr6 implanted with Kr^{11+}	0.03	0.075

On the basis of presented results, several conclusions can be drawn:

1. Ion implantation of Kr can decrease surface nano roughness of cold working steel 100Cr6, however results depend on the Kr ion energy.
2. Friction coefficient depends on applied load and significantly depends on type of applied Kr ions and their energy.

ACKNOWLEDGMENTS

The authors gratefully acknowledge research support by the project entitled „ Savremene proizvodne i informacione tehnologije u proizvodnom masinstvu“ in the Department of Production Engineering, Faculty of Technical Sciences Novi Sad, Serbia.

REFERENCES

[1] Taniguchi N.: Taniguchi Diagram, Nanotechnology, Oxford University Press, Oxford, 1996.

[2] Kakaš D., Škorić B., Novakov T., Kovačević L., Rakita M., Bohne W., Gregor M., Nešković N., Dobrosavljević A., Helle W.: Nanoimplantation of krypton into the surface layer of tool steels, 6th International Conference “Research and Development in Mechanical Industry” RaDMI 2006, pp. 13–17., Budva, Montenegro, September 2006.

EFFICIENCY OF MACHINING CURVED SURFACES THROUGH ELECTRICAL DISCHARGE TECHNOLOGY

STRAKA Ľuboslav, KUCHTA Patrik
Faculty of Manufacturing Technology with seat in Prešov, Technical University of Kosice, Kosice, Slovakia
E-mail: luboslav.straka@tuke.sk , patrik.kuchta@tuke.sk

Keywords: Accuracy, process efficiency, surface quality, Wire Electrical Discharge Machining (WEDM).

A significant negative of electrical discharge machining technology using a wire tool electrode is relatively low productivity, as well as the overall efficiency of the process. It is influenced by a whole range of accompanying phenomena [1]. The main accompanying phenomenon that participates in the decrease of the overall economic efficiency of electrical discharge machining are microgeometry errors, which occur due to the inhomogeneity of the electrical discharge process [2]. Another negative accompanying phenomenon are errors in the geometric accuracy of the machined surface, as a result of the frequent destruction of the wire tool electrode, faulty interpolation during its guidance and, last but not least, its vibrations. These aspects subsequently lead to the requirement of multiple application of additional finishing cuts, which significantly reduces the overall economic efficiency of the machining process. These reasons led us to conduct experimental research with the aim of defining the possibilities for achieving higher overall efficiency of the production process through WEDM technology.

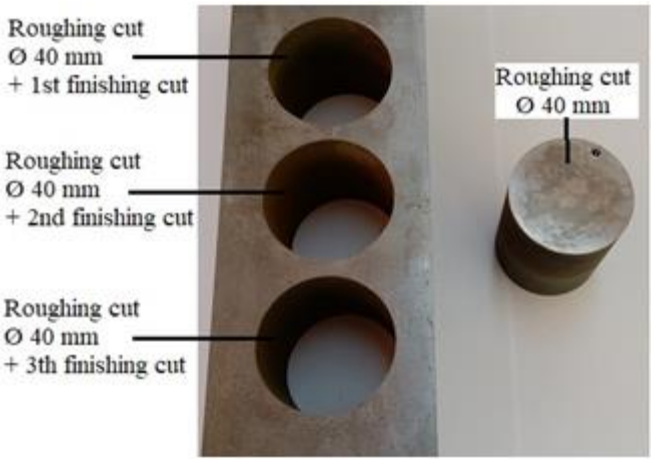

Figure 1 Experimental samples made by WEDM technology

Electrical discharge machining technology has extraordinary potential in the field of electrothermal process, mainly due to the possibility of achieving high quality of the machined surface [3]. In addition to the tool electrode, the selection of a suitable combination of the main technological and process parameters also plays a significant role in the quality of the machined surface and the productivity of the machining process. With their appropriate combination, it is possible to achieve not only high quality of the machined surface but also high production productivity. However, this task is a relatively demanding and complicated task in the conditions of electrical discharge machining technology due to the presence of a large number of process input parameters. Therefore, it is important to carefully prepare the machining process, which includes the choice of a suitable type of tool electrode, for the specific quantitative and qualitative requirements of the entire machining process [4,5]. As part of the experiment, a wire tool electrode with the trademark BEDRA MEGACUT type pro TWO was used. It is a second generation brass wire electrode. This electrode brings longer maintenance free machining cycles, ensures maximum safety of operation even in demanding typical serial production conditions and brings high tolerances for modern closed wire routing. The experimental samples were made of tool steel EN 40CrMnMoS8-6 (W.Nr.1.2312) using an Agiecut Classic 3S electroerosive machine. It is a tool steel that is supplied hardened and tempered with a tensile strength of 880-1080 MPa as standard. This tool steel can also be nitrided and has relatively good polishability. It is often used for the production of tools for processing plastics, but also for the production of molds for pressure casting. The surface roughness parameters *Ra* and *Rz* were measured on experimental samples with a diameter of 40.0 mm made by a full roughing cut and subsequent three finishing operations. These were recorded using a contact roughness meter Mitutoyo SJ 400.

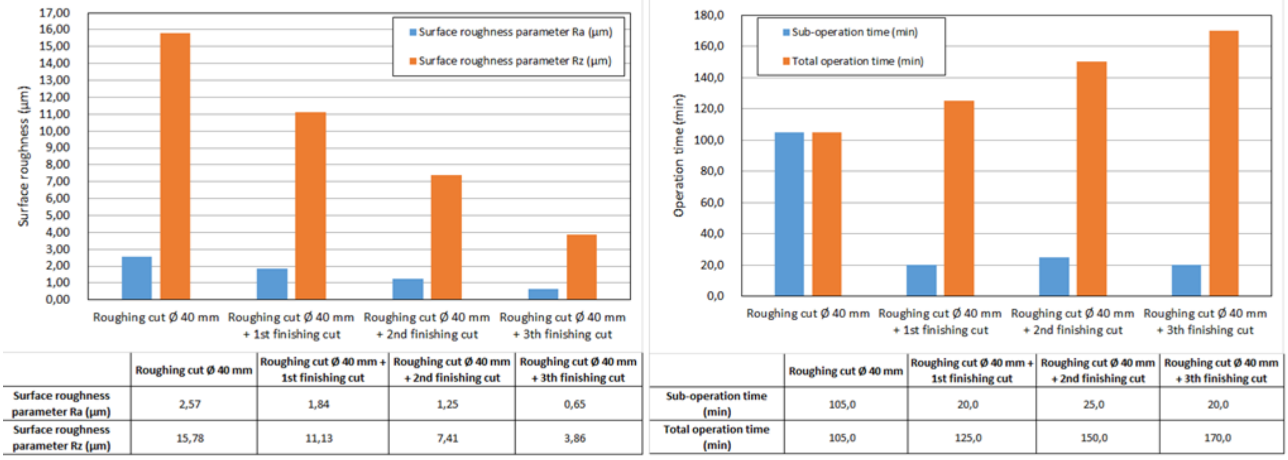

	Roughing cut Ø 40 mm	Roughing cut Ø 40 mm + 1st finishing cut	Roughing cut Ø 40 mm + 2nd finishing cut	Roughing cut Ø 40 mm + 3th finishing cut
Surface roughness parameter Ra (µm)	2,57	1,84	1,25	0,65
Surface roughness parameter Rz (µm)	15,78	11,13	7,41	3,86

	Roughing cut Ø 40 mm	Roughing cut Ø 40 mm + 1st finishing cut	Roughing cut Ø 40 mm + 2nd finishing cut	Roughing cut Ø 40 mm + 3th finishing cut
Sub-operation time (min)	105,0	20,0	25,0	20,0
Total operation time (min)	105,0	125,0	150,0	170,0

Figure 2 Qualitative and quantitative parameters of experimental samples made by WEDM technology

Based on the graphical dependencies shown in fig. 2, it can be concluded that the overall shortest WEDM time was recorded for a full roughing cut, and conversely, the operation consisting of a full roughing cut and three finishing cuts took the longest. At the same time, it can be observed that the best surface quality was achieved with the machined surfaces with a full roughing cut and three finishing cuts, and on the contrary, the worst when applying the operation with one full roughing cut [6]. Therefore, the choice of an acceptable quality level of the machined surface after WEDM is very important. Any unjustified qualitative increase in the level of the machined surface in terms of roughness parameters of the machined surface leads to an increase in the total production time, which has a very adverse impact on the overall economy of the cut [7]. At the same time, from the point of view of the objectivity of the comprehensive evaluation of the quality of the machined surface versus the economic efficiency of its production, it is necessary to focus further research on their mutual optimization.

ACKNOWLEDGMENTS

The described work was carried out as part of a project supported by the VEGA 1/0205/19.

REFERENCES

[1] Dzionk, S., Siemiatkowski, M.S. (2020), *Studying the effect of working conditions on WEDM machining performance of super alloy Inconel 617*. Machines, 8, 54.

[2] Jabbaripour, B., Sadeghi, M.H., Faridvand, S., Shabgard, M.R. (2012), *Investigating the effects of EDM parameters on surface integrity, MRR and TWR in machining of Tie6ALe4V*. Machining Science and Technology, 16, 419-444.

[3] Mouralova, K., Zahradnicek, R., Houska, P. (2016), *Evaluation of surface quality of X210Cr12 steel for forming tools machined by WEDM*. MM Science Journal, 5, 1366-1369.

[4] Oniszczuk-Swiercz, D., Swiercz, R., Chmielewski, T., Salacinski, T. (2020), *Experimental investigation of influence WEDM parameters on surface roughness and flatness deviation*. Metal 2020, 29, 611-617.

[5] Sanchez, J.A., Rodil, J.L., Herrero, A., De Lacalle, L.N.L., Lamikiz, A. (2007), *On the influence of cutting speed limitation on the accuracy of wire-EDM corner-cutting*. Journal of Materials Processing Technology, 182, 574–579.

[6] Straka, Ľ., Piteľ, J., Čorný, I. (2021), *Influence of the main technological parameters and material properties of the workpiece on the geometrical accuracy of the machined surface at WEDM.* International Journal of Advanced Manufacturing Technology, 115(9-10), 3065-3087.

[7] Yan, M.T., Wang, P.W., Lai, J.C. (2016), *Improvement of part straightness accuracy in rough cutting of wire EDM through a mechatronic system design.* International Journal of Advanced Manufacturing Technology, 84, 2623-2635.

MACHINING OF CARBIDE METALS BY ELECTRICAL DISCHARGE TECHNOLOGY

STRAKA Ľuboslav, KUCHTA Patrik
Faculty of Manufacturing Technology with seat in Prešov, Technical University of Kosice, Slovakia
E-mail: luboslav.straka@tuke.sk , patrik.kuchta@tuke.sk

Keywords: Electrical discharge machining, carbides, productivity, surface quality.

The growing qualitative and quantitative requirements for the machining of products with complex shapes from difficult-to-machine materials lead researchers to search for new alternative solutions through which relatively favourable results can be achieved in their machining [1]. Well, it's not always an easy task. Moreover, in combination with the requirement of the complexity of the shape of the machined surface, only a limited number of production technologies are able to fulfill this condition [2,3]. Therefore, due to the high demands placed on current modern production and the required high standard of the machined surface, progressive electrical discharge machining technology is increasingly being used. And it is through this progressive technology that it is possible to achieve relatively good success in the machining of hard metals [4]. The aim of the contribution was therefore to describe in detail the results of experimental research aimed at comparing the achieved roughness of the eroded surface after electrical discharge machining depending on the specific properties of the machined material.

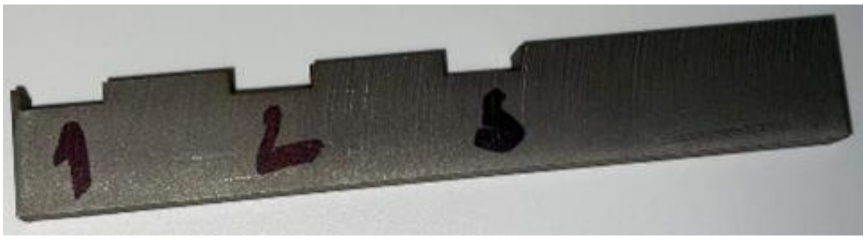

Figure 1 Carbide specimen machined through progressive electrical discharge machining technology

The primary goal when machining hard metals is to achieve the required quality level of the machined surface while simultaneously maintaining high production productivity. All of this, of course, also taking into account the economy of the electrical discharge process itself. The experimental research carried out was therefore aimed at comparing the qualitative indicators of the machined surface in terms of roughness parameters when machining selected types of hard metals using wire electrical discharge machining (WEDM) technology [5]. Despite the fact that carbides can be machined relatively effectively with electrical discharge machining technology, certain problems are associated with their machining. The most significant problem is the electrical conductivity of cobalt, which exceeds that of tungsten [6]. Thus, the cobalt binder in tungsten carbide erodes earlier, while the carbide particles fall out of the base material during electroerosion without melting. It follows that the amount of cobalt binder determines the speed of electroerosion, and at the same time, the amount of applied energy during machining determines the intensity of removal of the base material. Three types of hard metals were used in the experiment, namely K10F, K06F and Ti6Al4V. Experimental samples were made on an AgieCharmilles CUT 20P electrical discharge machine. A brass coated wire with a diameter of 0.25 mm and a tensile strength of 900 N.mm^{-2} was used as a tool for making experimental samples. Using the AgieCharmilles CUT 20P electrical discharge machine, 15 mm long cuts with different surface roughness were made on K10F, K06F and Ti6Al4V carbide samples. In total, three variants of the settings of the main technological and process parameters were applied to each type of carbide, thus achieving three qualitative levels of the machined surface in terms of roughness parameters. The measurement of the quality indicators of the machined surface in terms of roughness parameters of the machined surface of the experimental samples was carried out using a Mitutoyo SJ 400 contact measuring device.

Figure 2 Electrical discharge machine AgieCharmilles CUT 20P on which experimental samples were made

The results of experimental measurements of roughness parameters during machining of hard metals with designations K10F, K06F and Ti6Al4V using WEDM technology with identical settings of the main technological and process parameters are shown in Table 1.

Table 1 Measured values of the surface roughness of the cuts made on experimental samples made of carbide K10F, K06F a Ti6Al4V

Type of material	**Measured surface roughness values (Ra a Rz) of cuts**					
	1st cut		***2nd cut***		***3rd cut***	
	Ra (μm)	*Rz* (μm)	*Ra* (μm)	*Rz* (μm)	*Ra* (μm)	*Rz* (μm)
K10F	2.05	13.47	1.39	8.17	0.32	2.09
K06F	1.87	11.47	1.06	6.92	0.30	1.97
Ti6Al4V	2.73	16.48	1.96	12.73	0.75	5.14

Based on the results of the experimental measurements, it was found that even with the identical setting of the main technological and process parameters, the best quality of the eroded surface of the samples was achieved when machining the K06F carbide, and for all three quality cuts. At the same time, the lowest value of the roughness parameters *Ra*=0.30 μm and *Rz*=1.97 μm was achieved at the 3rd cut. On the contrary, the worst quality when machining Ti6Al4V carbide was achieved in the 1st cut with the value of the roughness parameters of the eroded surface of the samples *Ra*=2.73 μm and *Rz*=16.48 μm. On the basis of the experimentally obtained data, it can be concluded that even with identical settings of the main technological and process parameters in electroerosive machining with a wire electrode, when the type of machined material is changed, the quality of the machined surface differs in terms of surface roughness parameters *Ra* and *Rz*. Therefore, further research needs to be focused on finding the causes of these differences in the quality of the machined surface after WEDM in terms of roughness parameters.

ACKNOWLEDGMENTS

The described work was carried out as part of a project supported by the VEGA 1/0205/19.

REFERENCES

[1] Jabbaripour, B., Sadeghi, M.H., Faridvand, S., Shabgard, M.R. (2012), *Investigating the effects of EDM parameters on surface integrity, MRR and TWR in machining of Tie6ALe4V*. Machining Science and Technology, 16, 419-444.

[2] Mouralova, K., Zahradnicek, R., Houska, P. (2016), *Evaluation of surface quality of X210Cr12 steel for forming tools machined by WEDM*. MM Science Journal, 5, 1366-1369.

[3] Oniszczuk-Swiercz, D., Swiercz, R., Chmielewski, T., Salacinski, T. (2020), *Experimental investigation of influence WEDM parameters on surface roughness and flatness deviation*. Metal 2020, 29, 611-617.

[4] Sanchez, J.A., Rodil, J.L., Herrero, A., De Lacalle, L.N.L., Lamikiz, A. (2007), *On the influence of cutting speed limitation on the accuracy of wire-EDM corner-cutting*. Journal of Materials Processing Technology, 182, 574–579.

[5] Straka, Ľ., Piteľ, J., Čorný, I. (2021), *Influence of the main technological parameters and material properties of the workpiece on the geometrical accuracy of the machined surface at WEDM.* International Journal of Advanced Manufacturing Technology, 115(9-10), 3065-3087.

[6] Zhu, Z., Guo, D., Xu, J., Lin, J., Lei, J., Xu, B., Wu, X., Wang, X. (2020), *Processing Characteristics of Micro Electrical Discharge Machining for Surface Modification of TiNi Shape Memory Alloys Using a TiC Powder Dielectric*. Micromachines, 11, 1018.

COMPONENT DEVELOPMENT USING TOPOLOGICAL METHODS

SZABÓ Kristóf
Faculty of Mechanical Engineering and Informatics, Department of Machine Tools and Mechatronics, University of Miskolc, Hungary
E-mail: szgtszab@gmail.com

Keywords: Topology Optimization, Product Design Methodology, Generative Design.

INTRODUCTION

The article aims to briefly summarize the design aids which can be used nowadays, such as topology optimization and generative design, which are common in integrated CAD systems. A case study is used to present the results and comparisons provided by the previously mentioned methods. In case of designing machines and structures, the design task can be accomplished in different ways. These methods include the continuous development of the steps of design methodology developed in the last century. Various procedures and techniques related to the University of Miskolc play an important role in terms of machine design [1], [5] - [7]. Each design method has its own advantages and disadvantages, but the most appropriate one is determined by the qualification of the design staff and the type of task in question. The process is greatly influenced by its resource requirements, although efforts must be made to maintain the technical and technological level of the present age and to create the best use of it. It can be observed that in many areas of industry, the proportion of human labour is decreasing compared to the work of machinery and other means of production. This is inherent in the development process, in the hope of which we can provide a solution to a given task faster, more accurately and, if necessary, at less cost. A system where one merely communicates information and makes decisions while the equipment is working, seems to be a favourable way. Similar processes are taking place in the field of product design, thanks to the generative design module that became widespread in integrated CAD systems, as it serves as an example of the philosophy mentioned above. Design engineering is limited to provide accurate information and select from the results obtained.

THE SELECTED COMPONENT

The case study demonstrates the design of a component made up of simple geometric elements using design methods, such as generative design, provided by the present age.

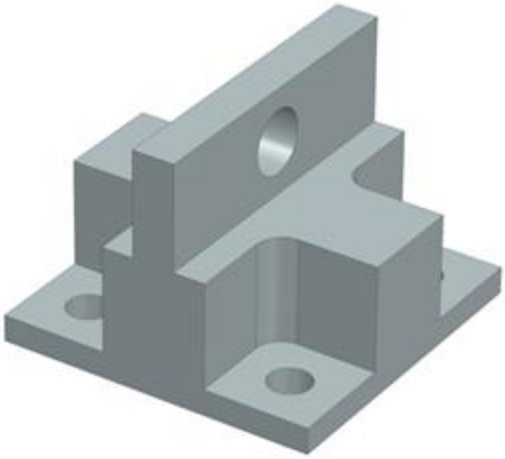

Figure 1 Modified model of the reference part.

The initial part, which is a console, is screwed to a specific plane. A load can be hung in the mortise in the part, so the console is subjected to tensile stress. The part is fixed to the horizontal plane with four screws and during the test, it is assumed that the screw connection used is suitable to withstand the resulting stress states.

A hook or pin can be inserted into the hole in the bottom of the part. In order to make the results comparable, a preliminary finite element simulation is performed on the initial workpiece, so that the load capacity of the part becomes known. For finite element analysis Autodesk Inventor was used. During the test the maximum stress and maximum displacement arising under the load was searched. The point of attack of the load force and its direction were recorded on the part. Based on the geometric properties of the component, the direction of the specified load is considered critical. The load can be stated as static, the magnitude of which is 50 [kN]. The design of the part continues with the definition of the fixing points, which have been defined on the surfaces of the holes. The material selected during the operation was 1.4125(440C) stainless steel.

The software gives the option of specifying a plane of symmetry or minimum meshing settings, the appropriate selection of which can reduce the calculation time. It is worth to mention that many materials and manufacturing technologies can be selected, so the number of solutions is quite large. It is advisable to filter the various solutions as soon as possible [8] – [11]. If the generation of solutions starts in a certain direction, it should be treated as a component, so after opening the result of iterations on that logical thread can be treated as a possible solution. It is possible to monitor the stress state, which allows obtaining information concerning the mechanical properties of the given iteration results without further investigation.

Figure 2 Results of the generative design process.

The course of the generation resulted in three components shown in Figure 2, during which the software mapped two hundred and thirty iteration steps, each of which is a complete component, after which the most suitable variant was selected. The program has a built-in comparison function in which different conditions can be assigned to each coordinate axis and the program is capable of evaluating every solution.

REFERENCES

[1] Takács Gy., Zsiga Z., Szabóné Makó I., Hegedűs Gy. Gyártóeszközök módszeres tervezése, Nemzeti Tankönyvkiadó, (2011), Miskolc
[2] Szabó K., Hegedűs Gy.: A generatív tervezést támogató szoftverek rövid áttekintése, Multidiszciplináris Tudományok (2020), doi: 10.35925/j.multi.2020.3.39
[3] Szabó K., Hegedűs Gy.: A generatív tervezés lépései integrált CAD rendszerekben, Multidiszciplináris Tudományok (2020), doi.org/10.35925/j.multi.2020.4.43
[4] Szabó K.; Hegedűs Gy.: Brief Overview of Generative Design Support Software, Design of Machines and Structures 10: 2 pp. 123-132., 10p. (2020), doi: 10.32972/dms.2020.023
[5] Hegedűs, Gy. A módszeres géptervezés alkalmazása ipari mérőgép fejlesztése estén, Doktoranduszok Fóruma 2002: Gépészmérnöki Kar szekciókiadványa. (2002)
[6] Kamondi, L. – Sarka, F. – Takács, Á. (2011). Fejlesztés- módszertani ismeretek, Nemzeti Tankönyvkiadó, Miskolc
[7] Pahl, G., Beitz, W., Feldhusen, Grote, K. - H. (2007). Engineering Design – A Systematic Approach, London: Springer-Verlag, ISBN 978-1-84628-318-5
[8] Stejskal, T., Dovica, M., Svetlík, J., Demec, P., Hrivniak, L., Šašala, M. - Establishing the Optimal Density of the Michell Truss Members, Materials (2020) doi:10.3390/ma13173867
[9] Zuo, K., Chen, L., Zhang, Y., Yang, J.: Study of key algorithms in topology optimization, Int J Adv Manuf Technol, 787–796 (2007), doi: 10.1007/s00170-005-0387-0
[10] Bendsøe, M.: Optimization of Structural Topology, Shape, And Material, Springer, Berlin, 1995, ISBN 978-3-662-03117-9, doi: 10.1007/978-3-662-03115-5
[11] Trautmann, L.: Product customization and generative design, Multidiszciplináris Tudományok (2021), doi: https://doi.org/10.35925/j.multi.2021.4.10

APPLICATION OF TOPOLOGICAL METHODS IN THE DEVELOPMENT OF VEHICLE COMPONENTS

SZABÓ Kristóf
Faculty of Mechanical Engineering and Informatics, Department of Machine Tools and Mechatronics, University of Miskolc, Hungary
E-mail: szgtszab@gmail.com

Keywords: Product Design Methodology, Topology Optimization, Generative Design.

INTRODUCTION

Engineering design is intended to produce an acceptable result to a formulated problem both technically and economically. Before manufacturing a physical prototype, the part pre-inspected in a virtual context, the end of which is to reduce time and costs. This way is called virtual prototyping, which can be related to the parallelization of methodical design [1,2,3]. Likewise, additive manufacturing now is an arising technology that can be considered the next industrial revolution. In fact, the use of this technology is projected to expand steadily [4,11]. Compared to traditional manufacturing technologies, additive technology offers lesser design freedom for both prototype and finished products and doesn't bear precious tools and molds. Likewise, computer-aided design CAD technologies, similar as generative design, can further extend the applicability of additive manufacturing. Generative design tools are also showing growth and expansion in numerous areas of the industry. The main CAD system providers have also developed their own generative design systems, conforming to the trends [5,6,10]. Interactive design seems to connect with different engineering cultures [7]. Considering the freshness of additive manufacturing and generative design technologies, the methodology is presently allowed to be deficient. This paper seeks to answer the following research question (RQ): how effectively can the generative design methodology be applied to an appropriately designed part based on the methods explored?

THE BASIS OF THE STUDY

The case study in this article is based on a previous competition development proposal, the main theme of which is an experiment in the development of chassis components for vehicles. The study aims to reduce the weight of the components in case of the wheel suspension system. In case of vehicles designed for racing, this demand is even more emphasized as increasing the acceleration potential of the vehicle can be understood by increase of the traction force and/or reduce of the mass. The chosen topic may be appropriate for several reasons to examine the applicability of the given design method, as the role of mass reduction, especially the reduction of unsprung masses, is particularly important in case of vehicles designed for racing. The expected attributions can be provided by the chassis if the parts are rigid enough. The individual connection points were determined during the entire chassis design, which are located on different planes and axes capable of each other, which can generate complex and spectacular results.

THE SELECTED COMPONENT

The 3D model of the part under consideration was designed on the base of traditional design styles. The raw material of the element is 6061 aluminum with a density of 2.7 [g / cm3], a yield point of 275 [MPa] and a tensile strength of 310 [MPa]. The overall size of the stump stand is 280x150x60 [mm] and the weight of the current design is 1.25 [kg]. The indicated axis can be manufactured using traditional cutting operations. The entire element features cuts, and pockets, which are said to be the tools of traditional design and manufacturing methodologies. Generative design is a design process in which an algorithm optimizes the shape of the element for a particular boundary condition. The design of the shape is not a manual design task. The developer determines the functional boundary conditions of the part, adds it into the software, which calculates the shape of the optimized part according to the specified criteria during iteration processes [6, 10]. Lately, several papers have been devoted to the description of generative design processes [8, 9], on the base of which the outlined task is answered.

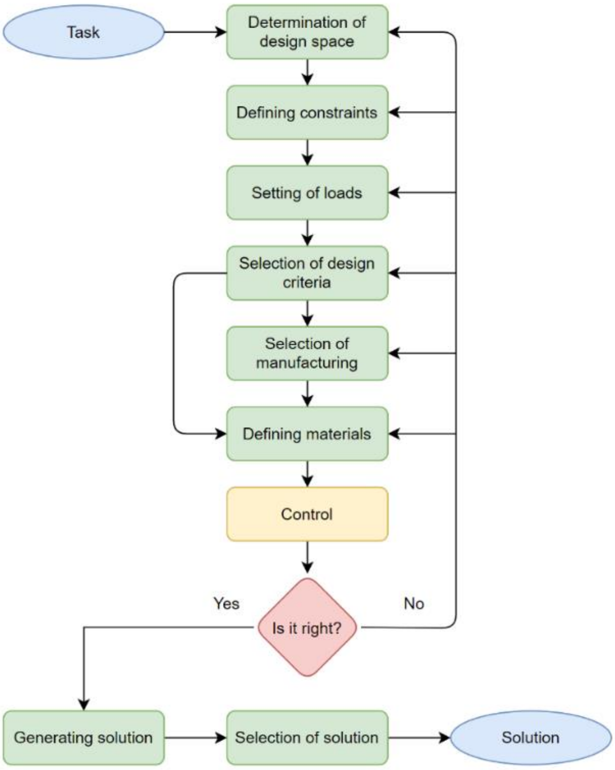

Figure 1 Steps of the generative design process [9].

It is advisable to carry out the design process step by step on the basis of the indicated flowchart, as this is the only way to get an effective result based on preliminary exploration. The presented case study in the paper is answered in the Generative Design Support module of the Fusion 360 Integrated Design System. Examination of the installation environment of the chassis parts is analysed in the Design Module, while the mass optimization task is performed using the Generative Design Module and the final check of the results can be carried out in the Simulation Module.

REFERENCES

[1] Takács, Gy., Zsiga, Z., Szabóné Makó, I., Hegedűs, Gy.: *Methodical design of production tools*, Nemzeti Tankönyvkiadó, (2011), Miskolc (in Hungarian)
[2] Hegedűs, Gy.: *Application of Knowledge-Based Design in Computer Aided Product Development* Lecture Notes in Mechanical Engineering, pp. 109-114., (2017)
[3] Hegedűs, Gy.: *The application of methodical design to industrial measuring machine development*, PhD Students Forum, 2002: Proceedings of Faculty of Mechanical Engineer-ing (2002), Miskolc (in Hungarian)
[4] Wohlers, T., Campbell, R. I., Huff, R., Diegel, O., & Kowen, J.: Wohlers report 2019: *3D printing and additive manufacturing state of the industry*. Wohlers Associates (2019)
[5] Szabó, K.; Hegedűs, Gy.: *Brief Overview of Generative Design Support Software*, DESIGN OF MACHINES AND STRUCTURES 10: 2 pp. 123-132., 10 p. (2020), doi: 10.32972/dms.2020.023
[6] Szabó, K., Hegedűs, Gy.: *Brief Overview of Generative Design Support Software*, MULTIDISZCIPLINÁRIS TUDOMÁNYOK (2020), (in Hungarian) doi: 10.35925/j.multi.2020.3.39
[7] Fischer, X., Nadeau, J.-P.: *Research in Interactive Design* (Vol. 3): Virtual, Interactive and Integrated Product Design and Manufacturing for Industrial Innovation. Springer, Berlin (2011)
[8] Szabó, K., Hegedűs, Gy.: *Steps of Generative Design in Integrated CAD Systems*, MULTIDISZCIPLINÁRIS TUDOMÁNYOK (2020), (in Hungarian) doi.org/10.35925/j.multi.2020.4.43
[9] Szabó, K., Hegedűs, Gy.: *Steps of Generative Design in Integrated CAD Systems* DESIGN OF MACHINES AND STRUCTURES 11, No. 1 (2021), pp. 53-58. DOI: 10.32972/dms.2021.007
[10] Gönczi, D.: *Essential features of topological Optimization tasks in Abaqus Final Program System*, MULTIDISZCIPLINÁRIS TUDOMÁNYOK 11. (2021) 4 sz. pp. 177-187 (in Hungarian) doi.: 10.35925/j.multi.2021.4.22
[11] Frazier, W.E.: *Metal additive manufacturing: a review. J. Mater. Eng. Perform*. 23, 1917–1928 (2014)

ASSESSMENT OF PULSATING FLOW

SZODRAI Ferenc
Department of Building Services and Building Engineering, Faculty of Engineering, University of Debrecen, Hungary
E-mail: szodrai@eng.unideb.hu

Keywords: low Reynolds; laminar; pulsating; solenoid; thermal analysis; iso-flux; large-eddy simulation; water flow

Almost every scale in thermal engineering requires performance optimization to lessen energy demand. The possibility of using pulsating flow for water cooling was investigated both experimentally and numerically. The abstract and the presentation that is made for the conference summarize the work published in the previous study [1]. The experiments were conducted below a 60 $mL \cdot min^{-1}$ flow rate and frequencies of 3.3, 4, 5, 6.6, and 10 Hz. The flow rate and temperatures were monitored while the solenoid valve was actuated and cooled with thermoelectric coolers. The observations were recreated using commercially available software (Ansys Fluent 2022R1) that can do large-eddy simulations with associated thermal modelling. Thermal boundaries were formed by employing a constant input temperature and iso-flux conditions. The numerical and experimental findings were compared and analysed. The results demonstrate that the Nusselt number of the investigated pulsating flow was lower than the Nusselt number of the constant flow scenarios at the equivalent averaged flow rate.

The lumped heat capacitance model was assessed for the iso-flux scenario.

Because the convective heat transfer coefficient is not constant, but rather evolves over time, a numerical correction is necessary.

A minor peak was identified at $Nu = 9.3$ at $St = 0.756$, but no significant increase was found in the measured range.

Nu was lower at the comparable average Re when compared to constant flow conditions.

The findings of both experiments and simulations correspond well.

New optimum ranges can be discovered using simulation and validated using the shown experimental technique [1].

ACKNOWLEDGMENTS

Project no. TKP 2020-IKA-04 was implemented with the support provided by the Ministry of Innovation and Technology of Hungary from the National Research, Development, and Innovation Fund, financed under the 2020-4.1.1-TKP2020 funding scheme. Project no. TKP2021-NKTA-34 has been implemented with the support provided by the Ministry of Innovation and Technology of Hungary from the National Research, Development, and Innovation Fund, financed under the TKP2021-NKTA funding scheme.

REFERENCES

[1] F. Szodrai, “Experimental and Numerical Assessment of Iso-Flux Cooling with Low Reynolds Pulsating Water Flow,” *sensors*, vol. 22, no. 7487, 2022, doi: https://doi.org/10.3390/s22197487.

INVESTIGATION OF THE ADHESION PROPERTIES OF POTTINGS

TAJTI Ferenc, BERCZELI Miklós
Department of Innovative Vehicles and Materials, GAMF Faculty of Engineering and Computer Science, John Von Neumann University, Kecskemét, Hungary
E-mail: tajti.ferenc@gamf.uni-neumann.hu , berczeli.miklos@gamf.uni-neumann.hu

Keywords: Laser, surface treatment, adhesive, high temperature wetting, aluminium sheet.

With the increase in the number of electrical devices, there is a growing demand for adhesives and sealants. In electrical devices, potting plays an important role in sealing electronic components from environmental humidity and moisture. In many cases, these adhesive materials have a dual function. On the one hand, they have to provide a strong bond between the materials, and on the other hand, they have to insulate the component from external environmental factors. Special potting adhesives can be used to achieve such requirements. Potting materials are adhesives that soften and spread over the surface to be sealed and glued when exposed to heat. However, sealing will only be satisfactory if the potting has good adhesion to the surface [1-2].
We can test the spreading of the potting material with a high-temperature wettability measuring device. A sample plate is placed in the furnace of the device, and the required amount of potting is placed on it. The furnace is used to heat the sample to a temperature where the potting softens. The furnace is viewed with a camera during the measurement. This allows us to monitor live the melting of the adherent. For the potting materials, a one-hour heat treatment is required. After that we check how far the potting has spread over the surface using the camera image. The smaller the contact angle between the adhesive and the surface, the more it spreads, the better the adhesion between them [3-5].

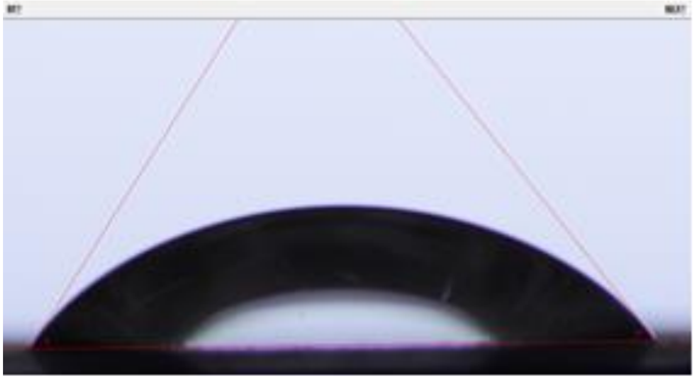

Figure 1 Bad wetting of the adhesive on aluminium sheet

As shown in the Fig 1., the adhesive does not spread much on the surface after melting, indicating that the adhesion properties are weak. The Fig 2. shows a small contact angle, indicating that adhesion between the adhesive and the surface is good.

Figure 2 Good wetting behaviour of potting on aluminium sheet

Potting requires a thorough cleaning of the surface to be bonded and, in some cases, surface treatment to achieve better adhesion. For aluminium, there are several options for surface treatment. Traditional mechanical surface treatments such as sanding, or sandblasting can be used. We can also treat the surface with chemical agents. However, laser surface treatment is an outstanding and well-optimized technology for surface treatment. For the surface treatment of the aluminium sheet, a femtosecond laser was used Fig 3.

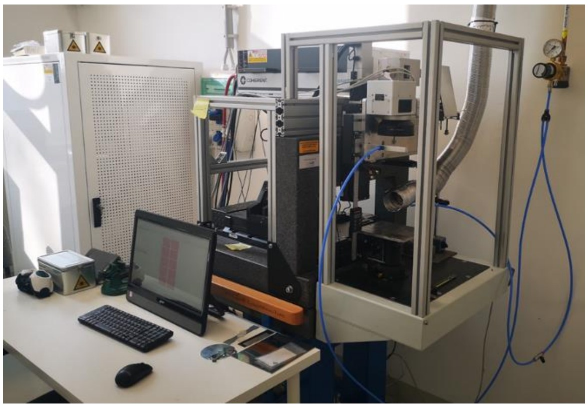

Figure 3 Coherent Monaco 1035 nm wavelength femtosecond laser system

The laser beam creates a special structure (Fig 4.) on the surface that can increase the adhesion properties of the surface.

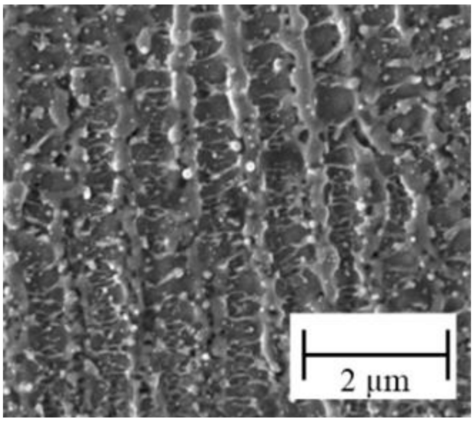

Figure 4 Laser beam created surface structure

Nowadays, adhesive technology is becoming an important bonding technology. To create high-strength bonded joints, properly prepared surfaces are required. The tests have shown that the structure formed on an aluminium surface treated with a laser beam can improve the adhesion of the surface.

In the following we will investigate several types of potting material for wetting. In addition, the behaviour of potting materials at higher temperatures will be investigated.

ACKNOWLEDGMENTS

This research is supported by 2020-1.1.2-PIACI-KFI-2021-00260 project.

REFERENCES

[1] F. Cavezza, M. Boehm, H. Terryn, T. Hauffman, A Review on Adhesively Bonded Aluminium Joints in the Automotive Industry, Met. 2020, Vol. 10, Page 730. 10

[2] R.F. Wegmanand, J. Van Twisk, Surface Preparation Techniques for Adhesive Bonding: Second Edition, Surf. Prep. Tech. Adhes. Bond. Second Ed. (2012) 1–148.

[3] F. Moroni, L. Romoli, M.M.A. Khan, Design of laser-textured surfaces to enhance the strength of adhesively bonded joints, Int. J. Adhes. Adhes. 85 (2018) 208–218.

[4] A. Rudawska, Selected aspects of the effect of mechanical treatment on surface roughness and adhesive joint strength of steel sheets, Int. J. Adhes. Adhes. 50 (2014)

[5] L. Romoli, F. Moroni, M.M.A. Khan, A study on the influence of surface laser texturing on the adhesive strength of bonded joints in aluminium alloys, CIRP Ann. - Manuf. Technol. 66 (2017) 237–240.

CELLULAR CERAMIC AND POLYMERIC MATERIALS FOR DEFENCE AND MILITARY APPLICATIONS- A REVIEW

[1]TAMÁSI Kinga, [2]POLYÁKNÉ KOVÁCS Annamária, [2]BORDÁS Viktor, [2]SIMON Andrea
[1]University of Public Service, Hungary
[1]E-mail: tamasi.kinga@admatis.hu
[2]University of Miskolc, Hungary
[2]E-mail: kovacs.annamaria.uni@gmail.com , v.bordas1992@gmail.com , femandi@uni-miskolc.hu

Keywords: cellular materials, foams, defence, military

Foam structures are one of the most exciting and complex structures in materials science, due to their advantageous properties. Foam materials are generally featured by high strength to weight ratio as well as excellent acoustic and thermal insulation properties compared with other engineering materials. Foams can be classified into three main types including two dimensional (2D) honeycombs, three dimensional (3D) with open cell configuration, and 3D with closed cell configuration. The use of cellular materials allows the simultaneous optimisation of stiffness, strength, energy absorption, overall weight, thermal conductivity, surface area, and gas permeability (the last two for open-cell foams). As such, these materials are highly desirable for a wide range of engineering applications and can be found commonly in the natural world (e.g., wood and bone). Foams offer a wide combination of properties, depending upon the foam material, pore volume and nature of cell structure. The range of properties includes high energy absorption, impact force reduction, blast amelioration, thermal insulation, electromagnetic shielding, etc. [1].

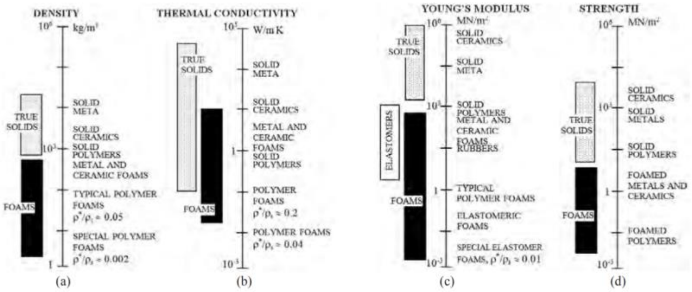

Figure 1 The range of properties of different foams
a.) density b.) thermal conductivity c.) Young's modulus d.) Strength [1]

One of the most traditional foam applications is also one of the most vital for the military. Secure packaging ensures that goods and products, imperative to simple activities or the most specialized operations, are delivered safely. Precision instruments, computers, supplies and weaponry all need to be transported across the globe and the potential for arriving in anything less than working order is not an option. Because of the remote locations they are often sent to and the fact that lives may depend on what is arriving, military packaging needs to be as secure as possible. Part of what goes into securing these shipments is polyethylene (PE) case foam [2].

Figure 2 Polyethylene produced foams for military application [2]

Technical ceramics exhibit several useful properties that make them the most common application for armour systems within the military and defense industry. These properties include having a relatively low weight, high-performance during ballistic-scale impacts, ability to withstand extremely high temperatures, low friction and resistance to wear, corrosion, and hardness. Some of the ceramic materials that have been the most useful for military armour applications include Al_2O_3 (alumina), B_4C (boron carbide) and SiC (silicon carbide), as well as several ceramic matrix composites (CMCs), such as Al_2O_3/ZrO_2 systems.

Of these materials, alumina is the most utilized technical ceramic for body armour, as it exhibits hardness, refractoriness, and modulus of elasticity at a much lower cost when compared to other commercially available technical ceramics [3].
Some other defense and commercial applications of transparent ceramics within the military sector include:
Aircraft, Missle domes, Transparent armors, IR windows, Hyper-hemispherical domes, Laser windows, Military aircraft lenses, Semiconductor processing applications, Scanner windows [3].

Figure 3 High-resilient technical ceramics (left: SKYDEX; right: composite armour system) [4]

Similar developments have also started at the University of Miskolc in 2021, where experts are producing glass and PU-based foam composite materials. Here the foaming agent was in all cases a substance of natural origin: raw materials, minerals pine, pinecones, coffee grounds or bark of some plants. Improvements are constantly being made, formulations need to be optimised and the additives chosen are changing. In all cases, the aim is to develop thermal insulation panels with favourable thermal and mechanical properties for military use.

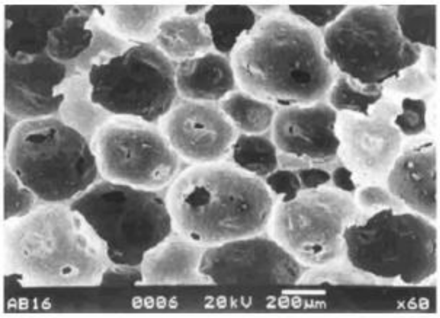

Figure 4 Microstructure of alumina foam using protein coagulation casting of ceramics [1]

ACKNOWLEDGMENTS
„SUPPORTED BY THE ÚNKP-22-4 NEW NATIONAL EXCELLENCE PROGRAM OF THE MINISTRY FOR CULTURE AND INNOVATION FROM THE SOURCE OF THE NATIONAL RESEARCH, DEVELOPMENT AND INNOVATION FUND."

REFERENCES

[1] A. Gokhale; B. Sudhakar; N.V.R Kumar; S. N. Sahu (2011): *Cellular Metals and Ceramics for Defence Applications (Review Paper),* Defence Science Journal, pp. 1-10., DOI: 10.14429/dsj.61.640
[2] Military Uses For Foam - Part I - Foam Factory, Inc. Blog (foambymail.com) (Download: 04.10.2022)
[3] M. Silva, D. Stainer, H. A. Al-Quershi, O. R. K. Montedo & D. Hotza (2014): *Alumina-Based Ceramics for Armor Application: Mechanical Characterization and Ballistic Testing*, Journal of Ceramics, DOI: 10.1155/2014/618154.
[4] https://idstch.com/technology/materials/ceramics-materials-for-military-body-and-vehicle-armor-and-aerospace-applications/ (Download: 12.10.2022)

CREATING POROUS METAL PARTS BY FUSED DEPOSITION MODELING AND SINTERING

THALMAIER Gyorgy, VIDA-SIMITI Ioan, SECHEL Niculina, BATIN Gabriel
Technical University of Cluj-Napoca, Romania
E-mail: Gyorgy.Thalmaier@sim.utcluj.ro

The Fused Filament Fabrication process (FFF) was first introduced and patented under the name of Fused Deposition Modelling (FDM®) in the 1990s, when it was as a free-form fabrication method for three-dimensional solid objects [1] At first the FDM was designed as a method to produce 3D printed parts made of polimeric materials. Starting from the last decade a significant number of decisive FDM patents expired [2] so a new development of the available filaments started. The emphasis was now on the diversification. The new direction of interest is the particle loaded filaments, and it's properties concentrated on the requirement of good extrudability at high particle loading while providing necessary mechanical strength with metal particles of 316 L steel, 17-4PH, Ti6Al4V, NdFeB, ceramics, hard metals or cermets [3– 7].

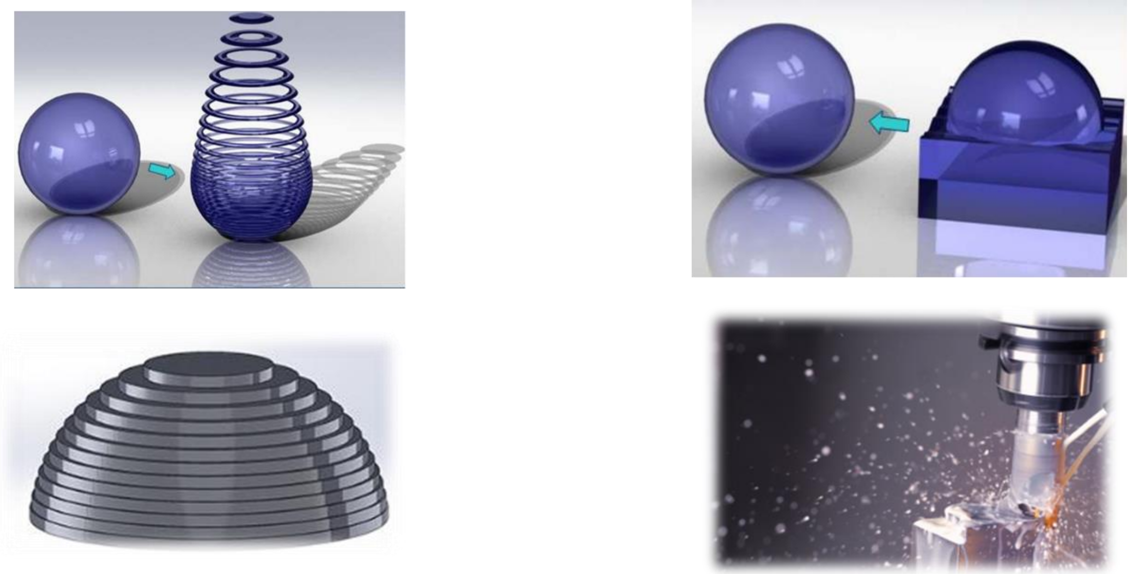

Additive fabrication   Subtractive fabrication

Figure 1 Additive vs Subtractive fabrication [8]

Today, commercial metal loaded filaments are available, nevertheless, only BASF is already offering a product called UltraFuse range of filaments to be printed on a typical desktop FFF printer and subsequently processed using an industry standard debinding and sintering route [17]. Only two commercial systems (by Desktop Metal and Markforged) seek to implement the complete process routine for automation of metal 3D printing all aim at simplifying the shaping, debinding and sintering process (SDS) and making it available at low cost and without the need for special infrastructural requirements, however other systems are capable of handling these filaments.
The CreatBot DX2 system was tested for using BASF's Ultrafuse Ph 17-5 filaments. Samples with different internal structures were printed, debinded and sintered and used as thermal conductivity enhancers for paraffin-based phase change materials.
The obtained smples were compared with other conductivity enhancement methods from the literature.

Figure 2 Additive fabrication steps a. -3D image; b.-printed part and c.- sintered part

REFERENCES

[1] S.C. Danforth, M. Agarwala, A. Bandyopadghyay, N. Langrana, V.R. Jamalabad, A.Safari, R. Van Weeren (1998), Solid freeform fabrication methods, US Patent 5738817,April 14,.

[2] I.H. Lee, Y.G. Kim (2015), The recent patent analysis and industrial trend of 3D printing, Indian J. Sci. Technol. 8 70–73,

[3] J. Gonzalez-Gutierrez, S. Cano, S. Schuschnigg, C. Kukla, J. Sapkota, C. Holzer (2018), Additive manufacturing of metallic and ceramic components by the material extrusion of highly-filled polymers: a review and future perspectives, Materials 11, 11(5), 840;

[4] J. Gonzalez-Gutierrez, I. Duretek, C. Holzer, F. Arbeiter, C. Kukla (2017), Filler content and properties of highly filled filaments for fused filament fabrication of magnets, Proceedings of SPE ANTEC,

[5] A. Bose, C.A. Schuh, J.C. Tobia, N. Tuncer, N.M. Mykulowycz, A. Preston, A.C. Barbati, B. Kernan, M.A. Gibson, D. Krause, T. Brzezinski, J. Schroers, R. Fulop, J.S. Myerberg, M. Sowerbutts, Y.-M. Chiang, A. John Hart, E.M. Sachs, E.E. Lomeli, A.C. Lund, (2018), Traditional and additive manufacturing of a new Tungsten heavy alloy alternative, Int. J. Refract. Met. Hard Mater. 73 22–28,

[6] S. Cano, J. Gonzalez-Gutierrez, J. Sapkota, M. Spoerk, F. Arbeiter, S. Schuschnigg, C. Holzer, C. Kukla, (2019), Additive manufacturing of zirconia parts by fused filament fabrication and solvent debinding: selection of binder formulation, Addit. Manuf. 26 117–128,

[7] W. Lengauer, I. Duretek, M. Fürst, V. Schwarz, J. Gonzalez-Gutierrez, S. Schuschnigg, C. Kukla, M. Kitzmantel, E. Neubauer, C. Lieberwirth, V. Morrison, (2019), Fabrication and properties of extrusion-based 3D-printed hardmetal and cermet components, Int. J. Refract. Met. Hard Mater. 82 141–149,

[8] J. Ramkumar Additive Manufacturing, lecture notes, Department of Mechanical Engineering IIT Kanpur, http://home.iitk.ac.in/~jrkumar/download/Lecture-5.pdf

TORQUE MEASUREMENT ON A CYLINDER TYPE MAGNETORHEOLOGICAL CLUTCH USING STRAIN GAUGES

TÖRŐCSIK Dávid, NAGY Attila
Széchenyi István University of Győr, Hungary
E-mail: torocsik@sze.hu , nagy.attila@ga.sze.hu

Keywords: Torque, current, cylindrical design, strain gauge, transducer.

In this study, we describe the construction of a torque measuring device developed by us, the measurement procedure we have carried out and the results of our measurements. The torque to be measured is transmitted by a clutch, filled with two types of magnetorheological fluid (MRF). The liquid consists of three elements: oil, metal particles and additives to prevent sedimentation. The first liquid contains 70%, and the second 80% of metal particles. The size of the metal particles are on average 1-10µm. The liquid can change its state under the influence of a magnetic field. In the unexcited state, the liquid has low viscosity like water or oil. As the force increases, it first takes on a honey-like state and then a solid state. There are two main types of magnetorheological clutches: cylindrical and disc designs. To measure the torque, we chose the cylindrical version. The magnetorheological clutch is mounted on an aluminium base (Fig. 1). The torque to be measured is provided by an electric motor controlled by a frequency converter.

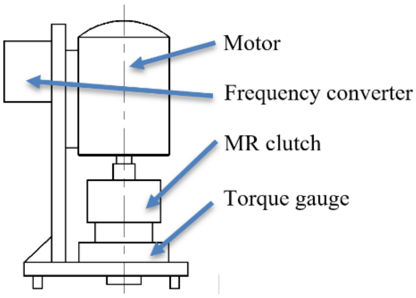

Figure 1 Construction of the measuring station

Preliminary calculations suggest a maximum torque of 2-2.5 Nm. For this reason, we had scaled the torque transducer to 5Nm. These dimensions had to be modified minimally for feasibility reasons, and the transducer was made with the modified dimensions. To measure the torque, we used a low profile hollow type reaction torque sensor that was designed by us. The outer and inner rings of the torque gauge consist of 4 parts. These segments are fastened together with screws. Spokes are located between the inner and outer rings. The reaction torque is measured by the deformation of these spokes which are made of two pieces of spring steel. The dimensions of this spring are 1mm thick, 30mm high and 150mm long (Fig. 2). The strain gauge was applied near to the highest bending stress area. A 24-bit resolution HBM QuantumX data logger was used for the measurement. The torque is generated by an electric motor with an inverter. The excitation of the fluid can be created by increasing the current within a measuring range of 0-5A. Based on the measured data, the maximum load capacity of the measuring device is determined.

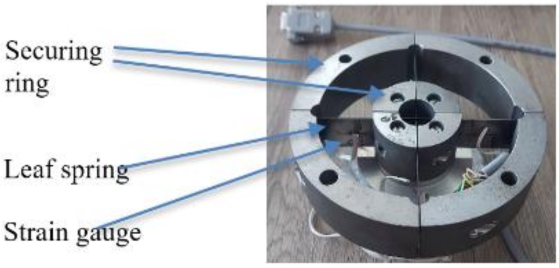

Figure 2 Torque measurement device

Before starting the measurement, it is necessary to check and set a few factors. The first parameter is the engine speed setting. The speed does not affect the torque transmitted by the clutch, so the speed was set to a medium range, i.e. 700 1/min. 50 cl of magnetorheological fluid is placed in the magnetorheological coupling, in order to equalize the temperature more easily. Anti-sediment substances prevent metal particles from settling, but it is worth stirring the liquid at the beginning of the measurement. The excitation current was varied between 0-5A in steps of 0.5A. We set a limit voltage of 10V on the power supply. The measured data can be seen in the table below (Table 1).

Table 1 Data on the measured torque

Leaf spring torque meter		
Amperage [A]	Fluid 1 (70%) - Torque [Nm]	Fluid 2 (80%) - Torque [Nm]
0	0	0
0,5	0,45	0,58
1	0,9	1,04
1,5	1,2	1,39
2	1,45	1,61
2,5	1,6	1,73
3	1,72	1,84
3,5	1,8	1,91
4	1,83	1,98
4,5	1,62	1,76
5	1,66	1,74

It can be read from the measured data that, unfortunately, the current design of the measuring equipment can only be used with 4A excitation. In case of higher excitation, uniaxiality error occurs between the clutch components. As a result of the attraction of the magnet, the outer surface of the measuring disc in the coupling rests on the hole made of C10 material.

In conclusion, the torque measuring device is designed to give reproducible results with an excitation in a range of 0-4A. When current between 4.5-5A is introduced into the coil, the measured torque drops to 1.7Nm by both fluids. The high magnetism makes the disc mounted on the shaft attract the outer part of the magnet, which creates eccentricity between the parts and the fluid gap gets reduced to 0. To create sufficient inertia, the thickness of the leaf springs need to be increased or the springs to be preloaded. However, more inertia results in less deformation, which affects the magnitude of the signal level emitted by the strain gauge.

REFERENCES

[1] Bansbach, E. E, Torque Transfer Apparatus Using Magnetorheological Fluids. US Patent, No: 5,779,013, 1998.
[2] Thamm-Ludvig-Huszár-Szántó, A szilárdságtan kísérleti módszerei, Műszaki könyvkiadó, Budapest, 1968
[3] LAMPE, D, Anwendung von Magnetorheologischen Fluiden in Kupplungen, www.donnerflug.de/publikationen/antrieb.pdf
[4] Gratzer, F, Steinwender, H, Kusej, A, Magnetorheologische Allradkupplungen. ATZ, Jahrgang 10, 2008. p. 902-909
[5] HBM QuantumX Operating manual. https://www.manualslib.com/manual/1455703/Hbm-Quantumx-Mx840.html, M. Jaindl, A. Köstinger, Ch. Magele, W. Renhart, Optimal design of disk type magnetorheologic fluid clutch

PROPANE GAS DIFFUSION FOR PROPANE-PROPYLENE SEPARATION COLUMNS WITH DIFFERENT OUTFLOW DIRECTIONS

TUGYI Levente, SIMÉNFALVI Zoltán, SZEPESI L. Gábor
Department of Chemical Machinery Institute, University of Miskolc, Hungary
E-mail: levente.tugyi@uni-miskolc.hu, zoltan.simenfalvi@uni-miskolc.hu, gabor.szepesi@uni-miskolc.hu

Keywords: CFD, explosive atmosphere, hazardous area classification, propane, source of release

High purity propylene is produced using a two-column process, with the columns operating at different pressures. The C3 mixture to be separated is first introduced into a high-pressure column operating at approximately 20 bar. The overhead is propylene, the bottom product of the column is propane. Propane is an explosion hazard and causes a dangerous fire when vapors are ignited from heat, spark, open flame or other source of ignition. Propane is heavier than air and may travel long distances. The aim of the study is to investigate the propagation of heavier-than-air gas - propane - around different leakage points under given boundary conditions. Cracks or holes can be caused by material fatigue, lack of maintenance or even human error. These points can be identified as sources of release, in the vicinity of which an explosive atmosphere can be formed. The literatures used to identify explosive atmospheres gives an approximation of the extent of the potential hazard, but using CFD simulation, a more informative result can be obtained on the potential propagation of propane gas at different times and different concentration values. In the model shown in the first figure, propane is certainly present as a bottom product in the lower third of the unit. For three sources of release of the same shape size, the propagation due to different outflow directions is modelled using ANSYS-CFD.

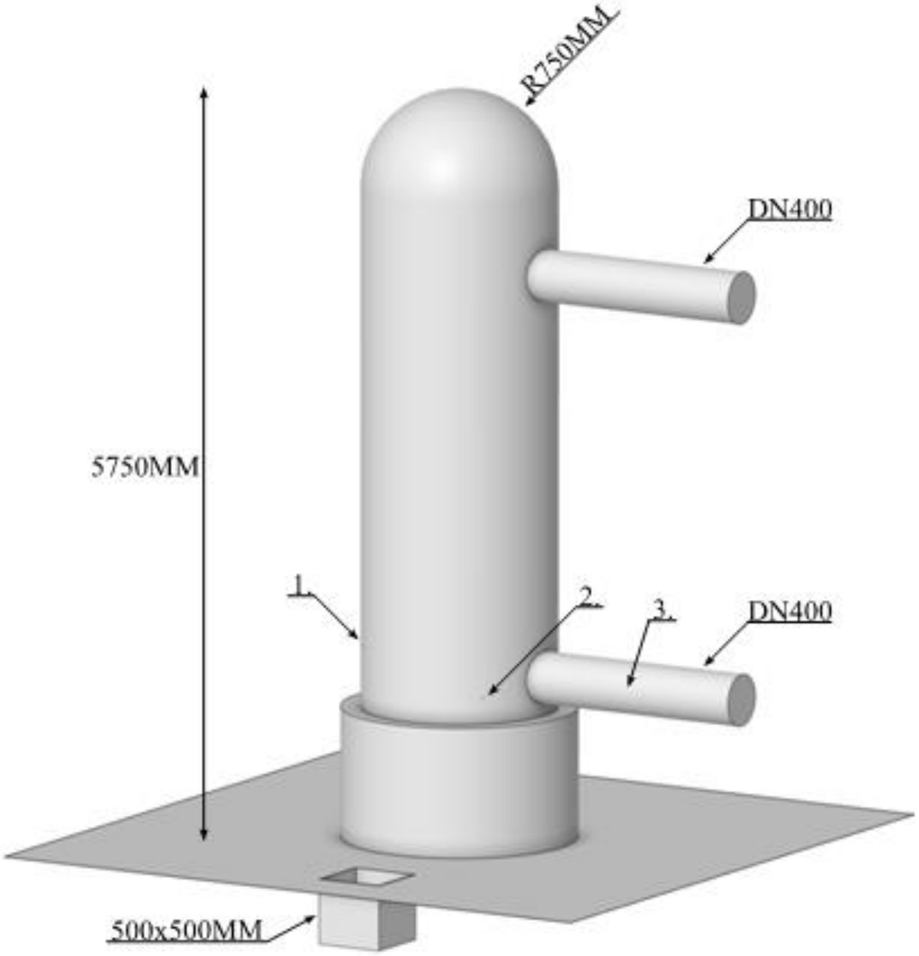

Figure 1 Propane propylene model for CFD analysis of sources of release 1., 2., 3.

Based on the literature and studies, it is clear that propane, as a heavier-than-air gas, will propagate downwards, but different gas volumes may be produced for the three different angular outflows (upward, normal and downward). The aim of the study is to analyse these propagation possibilities separately and also to compare them together at the lower explosive limit concentration or ARH20% and ARH40% and at the diffusion-induced conical distribution.

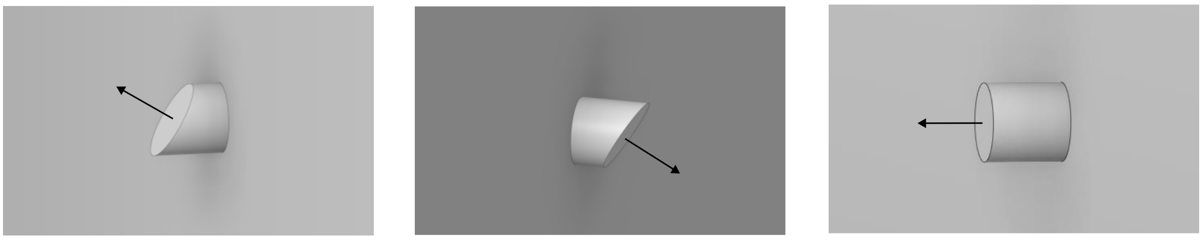

1. 2. 3.

Figure 2 1. upward outflow, 2. downward outflow, 3. normal outflow

EXPERT INVESTIGATION OF THE INSTALLATION AND MAINTENANCE OF A COMMUNICATION CABLE CUT WITH AN AGRICULTURAL MACHINE

VARGA Attila Károly
Institute of Automation and Infocommunication, Faculty of Mechanical Engineering and Informatics, University of Miskolc, Hungary
E-mail : attila.varga@uni-miskolc.hu

Keywords: communication network, fibre optic cable, overhead line, trail-type structure, common pole row, right of way

In 2009, a telecommunications services company, as a land user registered in the real estate register, built its optical cable line, which passes through an agricultural land in Borsod-Abaúj-Zemplén county, based on a lease agreement. The network is planned for reverse data transmission, which, in addition to program distribution, also enables the introduction of digital TV, IP-TV, broadband Internet, and VOIP telephone services. The line was placed on the already existing support structure on electricity supplier poles with the consent of the electricity supplier and with the permission of the National Media and Communications Authority.

In the design documentation, the designer specified a minimum height of 4.5 m. The construction had to be carried out in such a way that the minimum distance between the signal transmission network and the overhead line belonging to the power supplier is 2 m. The minimum height above the roads was set at 5.5 m, at 4.5 m above the entrances, and at least 6 m above the national road. It was a requirement that only non-conductive, maintenance-free optical cable with a Kevlar structure can be run on the medium-voltage, 20 kW network. The cable had to be placed 2 m from the element under the lowest voltage, under the power line.

In 2009, the construction could be completed according to the plans. The standards referred to in the technical description allow us to conclude that the construction was carried out in accordance with the regulations, and based on the commissioning and technical handover documentation at the time, they were found to be adequate. In the handover procedure, reference is made to standards MSZ 151-8 and MSZ 2364. [1][2][3][4][5]

In the 17,000-hectare arable area involved in the lawsuit, the agricultural operations related to crop cultivation were regularly carried out with machines of standard dimensions. In 2015, in a field on the outskirts of Borsod-Abaúj-Zemplén county, an agricultural machine (tractor) got caught in the optical overhead cable belonging to the plaintiff, stretched under the overhead air line, and severed it. As a result of this action, the internet, TV and telephone services operated by the plaintiff were interrupted for 26 hours. As a result of this event, the owner of the optical cable, as a plaintiff, submitted a claim to the territorially competent District Court to assert a claim for compensation. In 2017, the District Court of Miskolc declared the defendant guilty of the offense of disrupting the operation of a public interest enterprise and put him on probation for 2 years.

The company engaged in agricultural cultivation on the field, as defendant, and the legal representative appointed by it were convinced that the placement of the optical cable cannot be legal when it obstructs the proper use of the legally used property. In view of this, the defendant and his legal representative appealed against the court verdict. According to their point of view, if the optical cable had been properly placed, a standard-sized machine should have been able to fit under it. In the court proceedings, the application for the license to use the optical cable was available, with which the plaintiff wanted to prove that the placement was legal. In this regard, the defendant's legal representation is of the opinion that when this optical cable was built, this type of activity was not yet subject to a permit, but only to a notification, which was brought to the attention of the National Media and Communications Authority.

In view of the fact that the trial court classified the issue as a professional matter, it obliged the defendant to request a professional opinion as a motion for proof, in connection with which the legal representation of the defendant contacted the Institute of Automation and Infocommunication of the University of Miskolc, and ordered a forensic examination.

According to the plaintiff's claim, the optical cable was installed legally and regularly based on permits, in compliance with the design specifications. The line was placed on a support structure that is protected by a security zone, secured by a line right visible to anyone in the real estate register.

According to the claimant, the minimum height of the cable is 4.5 m. According to the plaintiff's point of view, it is covered by the protective strip for the power supply line, within which it is not possible to drive. Regardless of the electricity supplier's regulations, it is a requirement for optical cables that no work can be carried out within 0.3 m of them, only after prior consultation and under professional supervision. In view of this, he requests compensation for the damage related to the replacement of the severed line, and requested the issuance of a payment order against the defendant. The defendant objected to the payment order within the deadline, in which he disputed both the legal basis of the claim and its amount.

When determining the height above the ground of the track communication equipment to be installed on the support structure of the common column using the existing electricity supplier infrastructure - road crossings, gate entrances, outside areas, etc. in case of - the required height for high-current networks must be ensured. The definition of the minimum heights is detailed in the MSZ151-8 standard.

Therefore, it can be concluded that the common column line communication line involved in the case could only be broken by a vehicle with a height of 4.62 m measured at the highest point passing under it, if the maximum vertical distance of the tangent contact point parallel to the string connecting the mounting points of the wire hanging between the columns is the largest vertical distance from the string (largest overhang) was such that the 4.7 m height between the ground level and the above-ground communication line specified in the technical specifications of the power supplier for the outside area was not ensured.

When establishing a communications network, it is important that the governing standards and technical regulations are taken into account, but at the same time, continuous technical inspection and maintenance, compliance with technical and legal regulations are binding on the network operator. It is important to note that although the legal regulations and standards in force were taken into account during the compliance test during the licensing procedure, the standards referred to in the licensing procedure became mandatory with the licensing, so maintenance and inspection of the establishment is mandatory.

During the on-site inspection, the forensic expert examined the fertilizer spreading equipment, with particular regard to the height of the highest protruding structure during work, which was recorded in the on-site inspection report and the accuracy of the measurement was certified by the signatures of those present. The highest elevation measured with the hydraulic equipment at a wheel pressure of 2.2 bar on flat concrete terrain (which does not allow sinking into the ground) was 4.7 m, the working height was 4.3 m. The height of the optical cable measured in relation to the ground in the area in question was certified by those present with their signatures. The height of the optical cable was 4.45 m at an ambient temperature of 28 °C. The optical cable would have been in accordance with its commissioning (licensing) state, then the result of the measurement would have been a minimum height of 4.7 m. So, if the hydraulics of the machine (fertilizer spreader) are not in working position, but in the highest so-called it would have been in the service position, even in that case it would not have gotten caught in the optical cable, since under load, together with the ground subsidence, it was located almost 6-8 cm, i.e. 0.06 - 0.08 m lower (4.62 - 4.64 m) than the prescribed height (4.7 m according to MSZ 151-8).

The expert confirmed the defendant's claim that, in accordance with the MSZ 151-8 standard, in the case of the installation of track telecommunication equipment mounted on a common column row with a low-voltage overhead line, the minimum distance measured from the ground in the area under litigation, i.e. outside, usually in a garden or vineyard, is 4.7 m. In his expert opinion, the expert raised the need for cable maintenance. The court found it to be evidence that the condition in accordance with the regulations at the time of installation must be maintained throughout as long as the cable is stretched. [6]

It is clear that the disputed area, over which the cable broke, was already under agricultural cultivation when the cable was installed. It is natural that soil conditions can change as a result of agricultural cultivation or any other factor. This factor should not be ignored because it could also have caused the cable to be stretched at an incorrect height when the cable was cut. The expert investigation pointed out. that the cutting of the cable occurred due to the irregularly hanging optical cable, during which the employee demonstrated the behavior normally expected in the given situation.

REFERENCES

[1] MSZ 151-1:2000 szabvány, Magyar Szabványügyi Testület: Erősáramú szabadvezetékek. 1 kV-nál nagyobb névleges feszültségű szabadvezetékek létesítési előírásai, www.mszt.hu (dokumentumazonosító: 073524)

[2] MSZ 151-8:2002 szabvány, Magyar Szabványügyi Testület: Erősáramú szabadvezetékek. A legfeljebb 1 kV névleges feszültségű szabadvezetékek létesítési előírásai, www.mszt.hu (dokumentumazonosító: 121584)

[3] Magyar Igazságügyi Szakértői Kamara, https://miszk.hu/index.php/tudastar/torvenyek

[4] Az elektronikus hírközlési építmények egyéb nyomvonalas építményfajtákkal való keresztezéséről, megközelítéséről és védelméről szóló 8/2012. (I. 26.) NMHH rendelet, net.jogtar.hu

[5] MSZ 7487/3-80 szabvány, Magyar Szabványügyi Testület: Közmű- és egyéb vezetékek elrendezése közterületen. Elhelyezés a térszint felett, www.mszt.hu (dokumentumazonosító: 008971)

[6] A Kazincbarcikai Járásbíróság ítélete, valamint az azzal kapcsolatos perdokumentumok

[7] Märcz László (műszaki szakértő, ELMŰ-ÉMÁSZ): Közös oszlop létesítés kérdései, 2017, http://mknonprofitkft.hu/oktafile.php?file_id=1688&p=1, 2017.

INVESTIGATION OF HEAT TRANSFER COEFFICIENT AT EVAPORATION FROM A HEATED VESSEL

VARJU Evelin, POÓS Tibor
Department of Building Services and Process Engineering, Faculty of Mechanical Engineering, Budapest University of Technology and Economics, Hungary
E-mail: varju.evelin@gpk.bme.hu , poos.tibor@gpk.bme.hu

Keywords: evaporation, heat transfer, heat transfer coefficient.

When air and liquid come into contact, simultaneous heat and mass transfer occur at the liquid's surface, called evaporation. In the case of air flowing over an evaporating surface, the heat transfer coefficient determined from the Nusselt equations for heat transfer will be greater than for pure heat transfer [1]. This phenomenon has been observed in drying. The increase in the heat transfer coefficient is caused by cross-effects due to vertical evaporation flux, which breaks the boundary layer and intensifies the heat transfer. The aim of our research is to investigate the heat fluxes generated by the evaporation of water in a heated vessel and to determine the heat transfer coefficients for the evaporation processes shown in Figure 1.

During evaporation, heating the liquid is necessary to keep the temperature of the liquid surface constant and different from the wet bulb temperature. Figure 1/a, shows the case of evaporation when the surface temperature of the liquid $\left(T_f\ [°C]\right)$ is the same as the bulk air temperature $(T_G\ [°C])$, and there is no heat flux within the flowing air. In Figure 1/b, the temperature of the flowing air is greater than the surface temperature, so the resulting liquid surface temperature is determined by the sum of the heat flux from the air and the heating of the liquid. In Figure 1/c, the air temperature is lower than the surface temperature of the liquid, so the heat flux introduced by the heater is not only used to maintain the surface temperature of the liquid but also to heat the air.

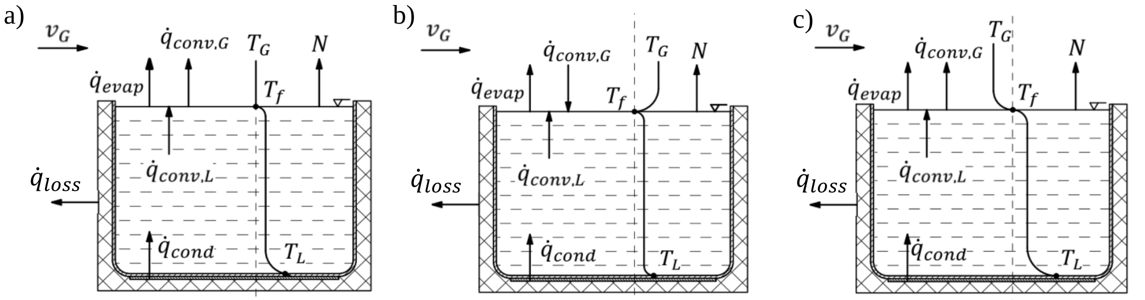

$\dot{q}_{evap} = \dot{q}_{cond} - \dot{q}_{loss}$ $\quad$ $\dot{q}_{evap} = \dot{q}_{cond} + \dot{q}_{conv,G} - \dot{q}_{loss}$ $\quad$ $\dot{q}_{evap} = \dot{q}_{cond} - \dot{q}_{conv,G} - \dot{q}_{loss}$

Figure 1. Investigated cases of evaporation from heated vessels and the heat fluxes under the process

(a) $T_f = T_G$, b) $T_f < T_G$, c) $T_f > T_G$)

For the surface of the liquid shown in Figure 1, the heat balance equation can be written as:

$$\dot{Q}_{evap} + \dot{Q}_{conv,G} + \dot{Q}_{conv,L} = 0, \tag{1}$$

where $\dot{Q}_{evap}\ [W]$ is the heat flux for evaporation, $\dot{Q}_{conc,G}\ [W]$ is the heat flux removed or transferred by air, $\dot{Q}_{conv,L}\ [W]$ is the heat flux from the main body of water to the water surface or from the surface to the main body.

Similarly, for the bottom liquid layer of a vessel heated from below, the heat balance equation can be written

$$\dot{Q}_{cond} + \dot{Q}_{conv,L} + \dot{Q}_{loss} = 0, \tag{2}$$

where $\dot{Q}_{cond}\ [W]$ is the heat flux to heat the vessel, $\dot{Q}_{loss}\ [W]$ is the heat loss on the side walls of the vessel. By expressing the term $\dot{Q}_{conv,L}$ from Eq. (2) and substituting it into Eq. (1), the heat balance equation of the heated vessel can be described by the following correlation:

$$\dot{Q}_{evap} + Q_{cond} + \dot{Q}_{conv,G} + \dot{Q}_{loss} = 0. \tag{3}$$

The Department of Building Processes and Process Engineering has a measuring equipment for measuring the evaporation rate, which can also be used to investigate heat transfer processes during evaporation [2]. Measurements were made of the evaporation of water in an electrically heated vessel, the liquid surface of which can be fitted to the bottom plane of the air duct. The velocity and temperature of the air flowing in the duct and the surface temperature of the liquid can be controlled during the measurements. The aim is to calculate the heat transfer coefficient between air and the liquid. In Eq. (3), the heat flux for evaporation:

$$\dot{Q}_{evap} = NrA_{evap}, \tag{4}$$

where $N\ (kg/(m^2s)$ is the evaporation rate, $r\ [J/kg]$ is the heat of evaporation and $A_{evap}\ [m^2]$ is the surface area of the liquid.

The heat flux used to heat the water is determined from the electrical power absorbed by the electric filament. The heat loss was estimated by the heat flux through the multi-layered wall (stainless steel vessel wall, 20 mm rock wool insulation, external steel sheet):

$$\dot{Q}_{loss} = k(T_L - T_{amb})A_{vessel}, \tag{5}$$

where $k\ [W/m^2K]$ is the overall heat transfer coefficient, $T_L\ [°C]$ is the bulk temperature of the liquid, $T_{amb}\ [°C]$ is the ambient temperature and $A_{vessel}\ [°C]$ is the external surface of the side walls of the vessel. The heat flux transmitted/abstracted by the air $\left(\dot{Q}_{conc,G}\right)$ can be determined from Eq. (3) for the cases shown in Figure 1. The heat transfer coefficient can be calculated from the heat flux expressed from the following correlation:

$$\dot{Q}_{conv,G} = \alpha_G \left|T_f - T_G\right| A_{evap}, \tag{6}$$

where $\alpha_G\ [W/(m^2K)]$ is the heat transfer coefficient between air and water.

The evaporation cases shown in Figure 1 were measured at different air temperatures and liquid temperatures for the same air velocity $(v_G = 2\ m/s)$, the results are shown in Table 1. The table shows the setting parameters, the evaporation rate and the heat fluxes. The table also gives the heat transfer coefficient between air and water and the value of the pure heat transfer coefficient $\left(\alpha_{plate}\right)$ under the same conditions of flow over the flat plate [3].

Table 1 Data for evaporation measurements, heat fluxes and heat transfer coefficients

Fig.	T_G	φ_G	T_f	N	$\dot{Q}_{evap}$	$\dot{Q}_{cond}$	$\dot{Q}_{loss}$	$\dot{Q}_{conv,G}$	α_G	α_{plate}
	$[°C]$	$[\%]$	$[°C]$	$[kg/(m^2h)]$	$[W]$	$[W]$	$[W]$	$[W]$	$[W/(m^2K)]$	$[W/(m^2K)]$
1/a	30,2	19,8	29,9	0,881	58,0	56,1	5,4	0	11,8	9,6
	39,9	20,0	39,8	1,340	87,3	108,6	7,7	0	10,4	9,6
	49,4	17,1	49,6	2,627	169,5	193,6	17,7	0	11,9	9,5
1/b	39,6	14,1	29,6	0,860	56,6	34,0	5,6	28,2	28,9	9,9
	40,1	18,3	35,0	1,149	75,2	64,4	8,0	18,8	37,8	9,8
	39,6	14,1	29,6	0,860	56,6	34,0	5,6	28,2	28,9	9,9
	44,5	10,2	30,0	0,891	58,7	37,1	10,6	32,1	22,7	10,1
	49,3	8,9	29,8	0,965	63,5	25,8	5,0	42,7	22,5	10,2
	54,0	6,5	29,6	0,989	65,1	13,1	3,4	55,4	23,3	10,3
1/c	34,7	27,6	39,2	1,506	98,2	120,4	8,6	13,5	30,5	9,3
	35,4	18,9	55,0	3,798	243,7	314,2	23,2	47,3	24,7	9,0
	30,2	33,1	50,1	2,824	182,2	228,5	21,4	25,0	12,8	9,0
	35,2	33,7	50,0	2,584	166,7	223,6	18,0	38,9	27,0	9,1
	39,7	15,2	49,2	2,872	185,4	211,9	16,0	10,4	11,3	9,2

Notations: $\varphi_G\ [°C]$ the relative humidity of the air.

It can be established that, for the same air temperature, as the water temperature is increased, the heat input for heating increases; whereas, if the air temperature is increased while maintaining the same water temperature, the heating demand decreases; and the higher the temperature difference between the fluid and the environment, the higher the heat loss. The heat flux removed by evaporation increases as the air and liquid temperatures increase. It can be observed that the heat transfer coefficient between air and water takes a higher value than the heat transfer coefficient determined for the flat plate, so that heat transfer with the mass transfer is more intense than heat transfer alone.

ACKNOWLEDGMENTS

This work was supported by the Hungarian Scientific Research Fund (NKFIH FK-142204).

REFERENCES

[1] B. M. Smolsky and G. T. Sergeyev, ‘Heat and Mass Transfer with Liquid Evaporation’, *Int. J. Heat Mass Transf.*, vol. 5, pp. 1011–1021, 1962.
[2] T. Poós and E. Varju, ‘Dimensionless Evaporation Rate from Free Water Surface at Tubular Artificial Flow’, *Energy Procedia*, vol. 112, pp. 366–373, Mar. 2017, doi: 10.1016/j.egypro.2017.03.1069.
[3] T. Környei, *Hőátvitel*. Budapest: Műegyetemi Kiadó, 1999.

APPLICATION OF LASER SURFACE TREATMENT IN SURFACE-ENHANCED RAMAN SPECTROSCOPY

[1,2]WINDISCH Márk, [1]MALOVECZKY Anna, [3]VERES Miklós, [3]RIGÓ István, [4]FÜRJES Péter, [2]DANKHÁZI Zoltán, [1]VIDA Ádám
[1]Bay Zoltán Nonprofit Ltd. for Applied Research, Budapest, Hungary
E-mail: mark.windisch@bayzoltan.hu, anna.maloveczky@bayzoltan.hu, adam.vida@bayzoltan.hu,
[2]Department of Materials Physics, Eötvös Loránd University, Budapest, Hungary
E-mail: zoltan.daknhazi@ttk.elte.hu
[3]Institute for Solid State Physics and Optics Wigner Research Centre for Physics, Budapest, Hungary
E-mail: veres.miklos@wigner.hu, rigo.istvan@wigner.hu
[4]Microsystems Laboratory, Centre for Energy Research, Budapest, Hungary
E-mail: furjes@ek-cer.hu@wigner.hu

Keywords: SERS, Silicon, Laser surface treatment

There are many types of laser processing that are suitable to control and tune the physical and chemical properties of solid surfaces [1]. Traditional laser surface treatments, such as surface melting and surface hardening are usually performed with a continuous laser beam [2]. Laser devices with ultrashort pulse durations are used for modern laser material processing. One of the advantages of ultra-short pulse laser treatment is the material removal combined with small heat effected zone. Additional benefit is that surface structures of different shapes and sizes can be created relatively easily.

One of the possible products of the applied ultrashort pulse laser processing is the SERS substrate which is used in Surface-enhanced Raman spectroscopy [3,4]. In our work, silicon monocrystal surface was structured by a femtosecond laser beam to fabricate a surface morphology built up from 50-100 nm units. The structured surface was coated with an 80 nm gold layer to create the SERS substrate with a plasmonic surface.

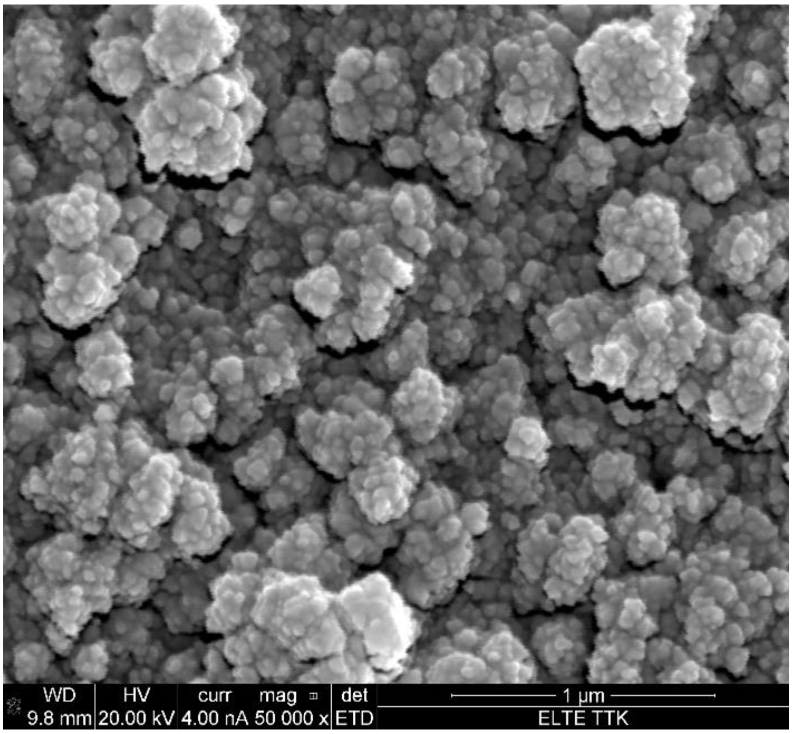

Figure 1 The surface of the fabricated SERS substrate

The SERS enhancement of the fabricated substrate was investigated using different concentrations of Rhodamine B and Rhodamine 6G solutions. The limit of detection for Rhodamine B and Rhodamine 6G of the SERS substrate was determined during Raman measurements. Furthermore, SERS enhancement of the commercially available products was compared with the prepared substrate.

During the presentation, the applied laser setup and the industrial use of surface-enhanced Raman spectroscopy will be introduced [4]. Finally, further possible development of SERS substrate will be discussed.

ACKNOWLEDGMENTS

Supported by the KDP-2021 Program of the Ministry of Innovation and Technology from the source of the National Research, Development and Innovation Fund.

REFERENCES

[1] Kannatey-Asibu E (2009), *Principles of laser materials processing*. John Wiley & Sons.
[2] Steen W. M., Mazumder J. (2010), *Laser Material Processing*. Springer
[3] Diels J-C., Rudolph W. (2006), *Ultrashort Laser Pulse Phenomena*. Elsevier
[4] Le Ru E. C., et al. (2008), *Principles of Surface-Enhanced Raman Spectroscopy: and related plasmonic effects.* Elsevier

POTENTIODYNAMIC STUDY OF THE EFFECTS OF NICKEL ON THE ELECTRODEPOSITION OF ZINC FROM CHLORIDE MEDIA

ZAKIYYA Hanna, KÉKESI Tamás
Institute of Metallurgy, University of Miskolc, Hungary
E-mail: zakiyya.hanna@student.uni-miskolc.hu , kekesi@uni-miskolc.hu

Keywords: Potentiodynamic study, Zn electrodeposition, Spent pickling liquor, Ni impurities, Chloride electrolyte.

INTRODUCTION

The recycling process of spent pickling liquor (SPL) from the hot dip galvanization technology has currently become attractive, as it does not only solve the environmental problem but also provide a secondary resource of metals, particularly zinc (Zn) and iron (Fe). The current research focused on the recovery of pure Zn. This liquid may contain 25 to 125 g/dm3 zinc, 90 to 200 g/ dm3 iron, and 70 to 100 g/dm3 free HCl and approximately 7 to 10 M total Clion [1] [2] [3] [4] [5] [6]. Therefore, the cathodic deposition of zinc should be considered in a wide range of concentrations of Zn and the main impurities. The detrimental effect of impurities on current efficiency (CE) or the morphology of the zinc deposited from acidic chloride solutions can be severe [7]. Therefore, the concentration of nickel, as an impurity, may be practically important to produce a pure zinc cathode. Nickel with higher reduction potential interferes with the deposition of zinc in two conditions. Firstly, its more noble nature tends to be deposited in favour of zinc, which later impacts the purity of the deposit. Furthermore, like iron, its lower overpotential to hydrogen also promotes more hydrogen evolution. Nickel may have no practical corrosive attack since its electrode potential (- 0.25 V) is significantly higher than that of zinc. However, – as discussed above – the lower hydrogen overpotential may result in more current loss and the preferential nickel deposition may cause unwanted impurity in the zinc cathode. The electrode potential of nickel is however less negative than that of iron as the major SPL impurities, therefore this effect can be even more disturbing if Ni is also contained in the electrolyte solution. At extreme cases, when the hydrogen evolution is intensive and the solution is close to neutral, the locally increasing pH may trigger the formation of hydroxide particles. Thus, an inhibiting layer can even be formed hindering the deposition of the less noble zinc. All these aspects of impurity co-deposition emphasize the importance of examining the effects of nickel contained in the purified zinc electrolyte.

EXPERIMENTAL METHODS

The potentiodynamic experiments of the Ni effects on the Zn electrodeposition process have been done in a series of 1-minute runs at 40 mV/s polarization speed with or without agitation (Fig.1). During the observation, several anode materials had been tested. Model solutions containing 90 g/dm3 Zn contaminated by a range of Ni concentration (1:100, 1:200, 1:300, 1:400, 1:500, 1:1000 and 1:10000) was prepared as the electrolyte solution. At the end of the experiment series, the deposit composition was analyzed by atomic adsorption spectroscopy (AAS).

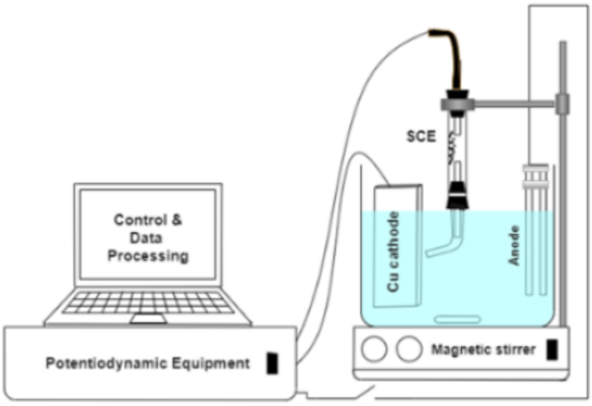

Figure 1 Schematic of the potentiodynamic electrodeposition equipment

RESULTS

The effect of nickel concentration in the electrolyte – even at lower levels than 1 g/dm3 - was found to influence the purity of the obtained Zn deposit. The structure of the deposited zinc is also influenced by the nickel contamination, making it more inclined to form rougher crystals or even longer dendrites. It could be observed at the end of the polarization cycle, some dendrites were grown in the 90 g/dm3 nickel electrolyte. The fine outgrowths were formed at the edges of the active cathode surface where a better nickel ion supply could be produced. Dendrite formation also occurs from the zinc solution of high (90 g/dm^3) concentration, but nickel dendrites tend to grow with more extended tips, reaching further into the solution and appearing in a relatively uniform pattern at the cathode edge. However, Zn dendrites develop more branches and side-arms (Fig 2).

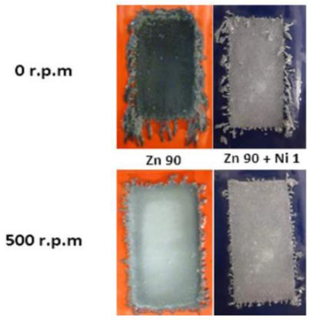

Figure 2 The final deposits from the 90 g/dm3 Zn and from the mixed 90 g/dm3 Zn + 1 g/dm3 Ni solutions at different stirring rates.

It was found that introducing Ni to the Zn electrolyte also change the nature of H+ reduction. More hydrogen reduction was observed in the mixed solution. This is supported by visual observations, and it results in the shifting of the characteristic polarization curve to the right after the intensive hydrogen evolution starts at about – 1V overpotential. The importance of electrolyte agitation also has been proved by the potentiodynamic results. Increased stirring rates result in denser zinc deposits and depressed hydrogen evolution at the cathode. The mass of nickel deposited from the mixed solutions significantly decreases as the Ni concentration decreases in the electrolyte, while the mass of deposited zinc is relatively constant from the agitated solutions (Fig 3). It means that the purity of the produced Zn is appreciably higher – with respect to Ni – if nickel is efficiently eliminated from the solution before electrowinning.

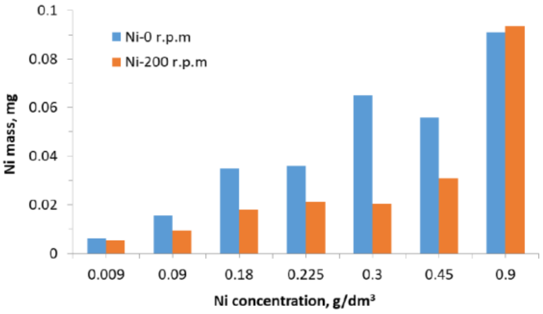

Figure 3 The mass of Ni impurities on the deposit of 90 g/dm3 Zn – pH 4.3 mixed electrolyte.

Stirring at a rate of higher than 200 r.p.m increases the rate of zinc electrodeposition – almost equally compared to the rate from stationary solution. This may be attributed to the virtual elimination of hydrogen evolution. However, the electrodeposition of Ni from the solutions of low concentrations had little response to the effect of stirring. The main effect was the Ni concentration, which determined the contamination of the deposited zinc layer. Nickel concentration did not influence the electrodeposition of Zinc in the examined ranges of concentrations. Anode gases evolved at the inert surface can cause added turbulence in the whole cell virtually enhancing the beneficial effects of forced electrolyte circulation. The strongest effect of stirring was seen in the change of the deposit morphology, efficiently eliminating the growth of long dendrites.

REFERENCES

[1] M. Regel-Rosocka, A review on methods of regeneration of spent pickling solution from steel processing, Journal of hazardous material, vol. 177, pp. 57-69, 2010.
[2] K. H Lum, G. W Stevens and S. E Kentish, Development of a process for the recovery of zinc sulphate from hot-dip galvanizing spent pickling liquor via two solvent extraction steps,Hydrometallurgy, vol.142, pp.108-115, 2014.
[3] U. Kerney, "Treatment of spent pickling acids from hot dip galvanising, Resources, Conservation and Recycling, vol. 10, pp. 145-151, 1994.
[4] G. Csicsovszki, T. Kekesi and T.I. Torok, Selective recovery of Yn and Fe from spent pickling solutions by the combination of anion exchange and membrane electrowinning techniques,Hydrometallurgy,vol.77,pp.19-28, 2005.
[5] I. Ortiz, E. Bringas, M. Fresnedo Sn Roman and A. Miren Urtiaga, Selective separation of zinc and iron from spent pickling solutions by membrane-based solven extraction: process viability, Separation Science and Technology, vol. 39, no. 10, pp. 2441-2455, 2004.
[6] A. Arguillarena, M. Margallo, A. Arruti-Fernandez, J. Pinedo, P. Gomez and A. Urtiga, Scale-up of membrane-based zinc recovery from spent pickling acids of hot-dip galvanizing, Membranes, vol. 10, p. 444, 2020.
[7] M. Sider and D. L. Piron, "The effect of metallic impurities and 2-butyne-1.4-diol on yinc electrowinning from chloride solutions," Journal of Applied Electrochemistry, vol. 18, pp. 54-61, 1988.

APPLICATION OF ADDITIVE MANUFACTURING TECHNOLOGY FOR THE PRODUCTION OF INJECTION MOLDING TOOLS IN ORDER TO REDUCE THE CYCLE TIME

TAKÁCS Zoltán, KÁLLAI Imre
KTS Metalltechnik Kft., Bátonyterenye, Hungary
E-mail: info@ktsmetalltechnik.hu , imrekallai21@gmail.com

Keywords: Additive manufacturing, Injection molding, Polymer, Cooling, Conformal tool

INTRODUCTION

We investigated how, by using additive manufacturing technology, productivity can be cost-effectively improved during injection molding, thereby producing more, better-quality products in a given time. During our development work, we looked for a possible area of use in which we can simultaneously achieve quality improvement and value growth on several fronts by applying additive manufacturing technology. Our goal during the research was to develop smart technology injection molding tool elements that are suitable for performing cooling, removing the product from the mold and forming. We recommend the use of our innovative, shape-following cooling technology and tool inserts for all products with a curved surface. In the case of cooling systems implemented with traditional technology, uniform tempering of the tool is difficult to solve, so the cooling processes take much longer than necessary During our experiments, the goal was to optimize the processes taking place in the tool, to maintain the balance between cooling and cavity filling, in order to achieve the shortest cycle time and obtain a product of adequate quality.

EXPERIMENTAL AND RESULTS

In order to optimize the heat balance of the injection molding tool, we had to develop a solution with the help of which we can reach the required tool temperatures as quickly as possible, even for components with a complicated design. For cooling, some kind of heat transfer liquid is used, which transfers the heat to the tool, and depending on how far the cooling channel is from the cavity, we can cool the polymer product after a time that varies in proportion to the distance. Based on this, it is clear that a cooling (tempering) channel system must be designed that runs as close as possible (ideally at a distance of 2-3 mm) from the forming cavity and can preferably hold this distance regardless of the surface of the product. In this way, we can minimize the formation of remaining stresses and deformations in the product resulting from the different cooling process. In the case of complex components with non-flat surfaces, it is clear that this is not feasible using traditional tool making technologies [1].

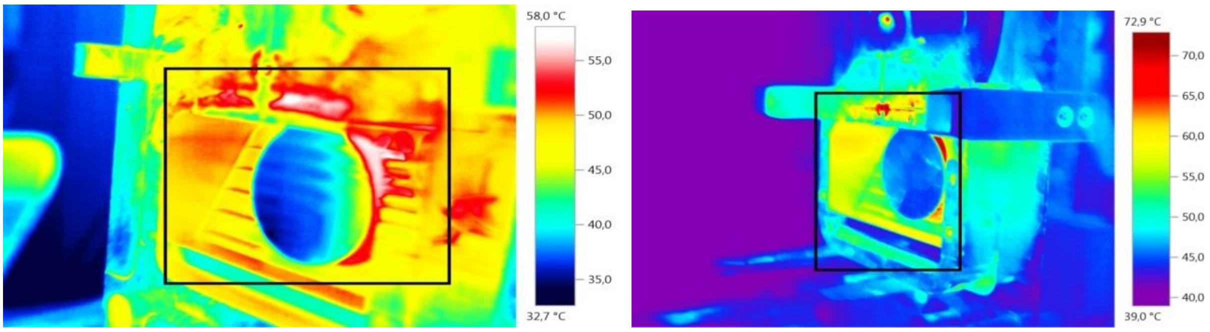

Figure 1 Results of a thermal camera test a.: conventional tool b.: conformal tool

With selective laser sintering, we can create any complex channel system by melting the fine metal powder layer by layer, which can be used to create tempering inserts suitable for each individual product. With the help of such an innovative tempering insert, the injection and ejection temperature of the tool can be achieved much more accurately, more homogeneously and faster, so there is no need to use overheated and cooled tempering fluid [2].

On Figure 2 it can be seen that the cycle times can be drastically reduced using additive manufacturing technology and conforming shape-following cooling channels. In the case of the first version of the tool design made with traditional technology, we were able to remove the product from the tool after 20 seconds cooling time, while with the inserts manufactured with additive technology, we were able to reduce the cycle time to 7 seconds at best. During the experiments, we have found that when determining the complexity of the cooling channel and the diameter of the tempering channel, it is better to prefer channels with a larger cross-section than an overly complicated and detailed cooling channel design. In the case of (long) channels with a small diameter and complicated geometrical design, the coolant turns more slowly in the tool, which reduces the cooling efficiency.

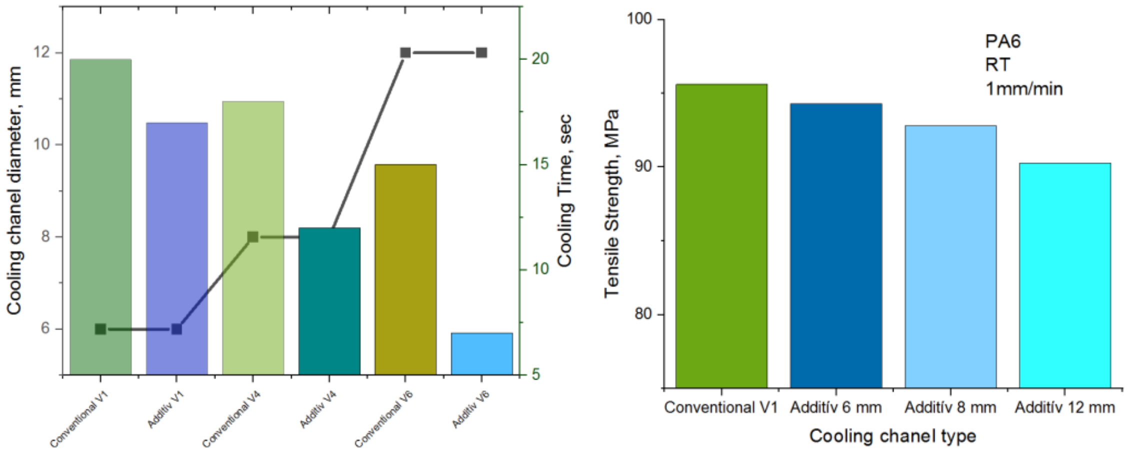

Figure 2. Effect of the cooling channel a.: on the cooling time, b.: on a crystallinity

An additional advantage of large-diameter cooling channels is that it reduces the use of raw materials, so the cost of raw materials also decreases. The efficiency of the cooling also affects the formation of the crystalline fraction of the polymers. Polyamide materials are partially crystalline amorphous polymers. A general feature of amorphous polymers is that the cooling rate used during formation, i.e. the intensity of cooling, affects the amount of crystalline fraction formed in the polymer. Figure 2 b shows the average tensile strength values. The design of the cooling channel, i.e. the increase in the intensity of the cooling, has a minimal but negative effect on the value of the mechanical strength. A difference of nearly 5.6% can be observed between the average tensile strength of the tensile test specimens produced from the conventional samples and those produced with the 12 mm diameter shape-following cooling channel providing the highest cooling intensity, which can be explained by the decrease in the crystalline fraction.

CONCLUSION

By significantly reducing cycle times, the price of products produced by injection molding can be significantly reduced. The investment cost of the injection molding tools (even higher at the moment) would be recouped sooner, which would also act as a catalyst for the design and production of newer products and prototypes. With the use of modern technology, more products can be produced in the same amount of time, this also reduces the price of the products, as a result of which the domestic plastic processors can offer their products at a competitive price, thus gaining a serious market potential compared to the Far Eastern manufacturers.

ACKNOWLEDGMENTS

This research and development project was supported by the European Union and the government of Hungary. GINOP-2.1.2-8-1-4-16-2017-00430.

REFERENCES

[1] Bruce Catoen, Herbert Rees; Injection Mold Design Handbook; ISBN:978-1-56990-815-0
[2] Sarker Dyuti; Metal Additive Manufacturing; Wiley 2021; ISBN:9781119210788